

# **Platinum-group elements within the Merensky reef, Western Limb, Bushveld complex: results of a high resolution mineralogical and geochemical study**

by

Justine Magson

For submission in accordance with the requirements for the degree Magister Scientiae in the Faculty of Natural and Agricultural Sciences, Department of Geology at the University of the Free State;

2016

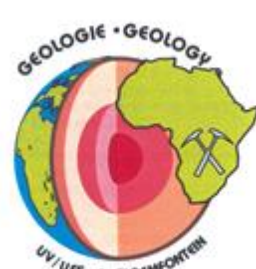
## **PART 1 (Main Text)**

**Supervisor: Prof. M. Tredoux, Department of Geology, UFS**  
**Co-supervisor: Dr. F. Roelofse, Department of Geology, UFS**



**Cardiff  
University**

UNIVERSITY OF THE  
FREE STATE  
UNIVERSITEIT VAN DIE  
VRYSTAAT  
YUNIVESITHI YA  
FREISTATA



**RHODES UNIVERSITY**  
*Where leaders learn*

## **DECLARATION**

I, Justine Magson, declare that this document is my own work, that it has not been submitted for any degree or examination in any other university, and that all the sources I have used or quoted have been indicated and acknowledged by complete references.

Justine Magson

.....  
Signed

.....  
Date

## **ACKNOWLEDGEMENTS**

I would like to thank my supervisor Prof M. Tredoux and my co-supervisor Dr F. Roelofse, both from the department of Geology at the University of the Free State, for assisting me with everything from lab work, travel arrangements, financial problems and for their expertise and guidance.

Thanks to:

The Department of Geology, University of the Free State, for the use of the facility, laboratories and for sample preparation.

The Inkaba YeAfrica Project for providing funding for the project.

Mr B. Cilliers and Mr C. Vermaak from Impala Platinum Mine for the samples, financial support and assistance. Without you this project wouldn't be possible.

Dr. I. McDonald, School of Earth and Ocean Sciences, Cardiff University, Wales, for the use of the inductively coupled plasma mass spectrometer, his assistance, patience and hospitality during my stay in Cardiff.

Mrs C. Cloete from the Council for Geoscience, South Africa, for her assistance and willingness to always help in sample preparations and for her advice.

Dr. G. Costin and the Geology Department of Rhodes University for the use of the Jeol JXA 8230 Superprobe, instrument sponsored by NRF/NEP grant 40113 (UID 74464) is kindly acknowledged.

Special thanks to Mrs R. Immelman for helping me with travel arrangements, administration and accountancy work.

## ABSTRACT

The formation of the Merensky reef still remains controversial despite of its economic importance and decades of research. Remaining questions like, the variability of the Merensky reef and how this effects the platinum distribution (e.g. whether the grade or distribution of platinum is influenced by the presence or not of pegmatoidal Merensky reef, whether PGE distribution are more associated with sulphides or with chromites) are still unanswered. Data were generated in order to address some of these questions. This study was undertaken in the south-western portion of the Western lobe of the Bushveld Complex on intersections of pegmatoidal and non-pegmatoidal Merensky reef from Impala Platinum Mine. The two non-pegmatoidal reefs correspond to the normal Merensky ‘A’ type reef and the pegmatoidal reef corresponds to the Merensky ‘B’ type reef according to the classification by Leeb-du Toit (1986).

The core was analysed in 2 cm intervals. Samples were analysed by optical microscopy. Quantitative analysis was done using scanning electron microproscopy and electron microprobe analysis. Major elements and trace elements were determined by using ICP-MS (inductively coupled plasma mass spectrometry). Platinum-group elements (PGE) were determined by Ni-S fire assay with an ICP-MS finish and sulphur by an Eltra Infrared Analyser.

Macroscopic investigation of the drillcores identified an anorthositic footwall with an overlying basal chromitite stringer and a pyroxenite hangingwall for the two non-pegmatoidal reefs. The pegmatoidal reef consists of an anorthositic footwall, a bottom chromitite stringer, a pegmatoidal layer with an overlying top chromitite stringer and a pyroxenite hangingwall.

Microscope analysis showed one sulphide inclusion visible in a chromitite grain which displayed a negative crystal shape imposed by the crystal structure of the host chromite. This could indicate the presence of sulphide liquid in the system at a very early stage. This might be an indication of PGE accumulation in a deeper staging chamber.

There is a correlation between the bottom chromitite stringer from the pegmatoidal Merensky reef and the single basal chromitite stringer from the non-pegmatoidal reef. There is also a Cr<sub>2</sub>O<sub>3</sub> correlation between the single basal chromitite stringer from the non-pegmatoidal reef and the top chromitite stringer from the pegmatoidal reef.

Whole rock geochemistry is strongly governed by the mutual influence and proportion of co-precipitating minerals competing for the same major cations like chromium, iron, aluminium and magnesium. Whole rock Mg# is the lowest in the chromitite layer, which is in contrast with what is seen in the mineral chemistry where Mg# is more primitive in the chromitite layer. This could be due to the subsolidus effect where the orthopyroxene within the chromitite layer is more enriched in Mg, due to the exchange with the chromite. The general evolution from bottom to top of the pegmatoidal reef is not so clear, with considerable irregularity.

Whole rock PGE content indicated that there is a close relationship between chromium and PGE enrichment, with the highest PGE content associated with the basal chromitite stringer in the case of the non-pegmatoidal reef and with the top chromitite stringer in the case of the pegmatoidal reef. Extremely high Pt/Pd ratios of up to 8.2 and Pt up to 40 ppm in the non-pegmatoidal chromitite stringer is noted but could be an artefact of the small sample sizes used.

Whether some of the results found are a local or a general characteristic, can only be determined by analysing more sections. The results of this study indicate that a combination of geochemical processes and multiple replenishments of magma with subsequent processes such as: crystallization of PGE as PGM, (Tredoux et al., 1995), collection of PGE by an immiscible sulphide liquid (Campbell et al., 1983 and Barnes and Maier, 2002b) and perhaps redistribution of PGE by late magmatic/hydrothermal fluids (Boudreau & Meurer, 1999). Trends of a deeper staging chamber as suggested by Hutchinson et al (2015) is supported by several of the observations made in this study and these processes could be responsible for the formation of the pegmatoidal and non-pegmatoidal Merensky reefs.

## TABLE OF CONTENTS

<b>Declaration</b>	i
<b>Acknowledgements</b>	ii
<b>Abstract</b>	iii
<b>Table of contents</b>	v
<b>List of tables</b>	viii
<b>List of figures</b>	x
<b>List of abbreviations</b>	xv
<b>List of mineral abbreviations</b>	xvi
<b>Part 1 (Main text)</b>	
<b>Chapter 1: Introduction</b>	
1.1 General geology	1
1.2 The Merensky unit	
1.2.1 General features of the Merensky Cyclic Unit	5
1.2.2 General features of the Merensky reef	6
1.2.3 The Merensky reef at Impala Platinum Mine	8
1.3 Models for PGE mineralisation and chromitite formation	9
1.3.1 Models for chromitite formation	9
1.3.2 Models for PGE mineralisation	9
1.3.3 Models for the formation of metalliferous (PGE) reefs	9
1.4 Previous studies on the Merensky reef and aim of the project	10
<b>Chapter 2: Material and methods</b>	
2.1 Sample description	12
2.2 Sample preparation	
2.2.1 Preparation of thin sections	17
2.2.2 Preparation of fusion discs	17
2.2.3 Preparation for PGE analysis	18
2.2.4 Preparation for REE, traces and majors	18

2.2.5 Preparation for sulphur analysis	18
2.3 Analytical procedures	
2.3.1 Optical Microscopy	19
2.3.2 Scanning electron microscope (SEM)	19
2.3.3 Electron microprobe analysis (EMPA)	20
2.3.4 X-ray fluorescence spectrometry (XRF)	21
2.3.5 Inductively coupled plasma mass spectrometry (ICP-MS)	22
2.3.6 Sulphur analysis: Eltra Infrared analyser	23
<b>Chapter 3: Results</b>	
3.1 Petrography	24
3.2 Mineral chemistry	37
3.2.1 Plagioclase	37
3.2.2 Orthopyroxene	41
3.2.3 Clinopyroxene	43
3.2.4 Chromite	44
3.2.5 Mica (phlogopite)	44
3.2.6 Base metal sulphides	45
3.3 Major element geochemistry	48
3.4 Trace element geochemistry	53
3.5 PGE geochemistry	55
<b>Chapter 4: Discussion</b>	59
4.1 Petrography	59
4.2 Whole rock major element data	67
4.3 Whole rock trace element data	73
4.4 PGE data	75
4.5 Comparison between mineral chemistry and whole rock major element data	80
<b>Chapter 5: Conclusions</b>	85
<b>References</b>	89

## **Part 2 (Appendices)**

<b>Table of contents</b>	<b>i</b>
<b>Appendix A: Description of core sets, standards and crystals used during analysis</b>	<b>A1 – A3</b>
<b>Appendix B: Petrography (modal mineral proportions)</b>	<b>B1 – B2</b>
<b>Appendix C: EMPA data sheets</b>	<b>C1 – C13</b>
<b>Appendix D: ICP-MS (whole rock: major element) data sheets</b>	<b>D1 – D14</b>
<b>Appendix E: ICP-MS (whole rock: trace element) data sheets</b>	<b>E1 – E12</b>
<b>Appendix F: PGE analysis data sheets</b>	<b>F1 – F2</b>
<b>Appendix G: Sulphur analysis</b>	<b>G1</b>
<b>Appendix H: Conference proceedings</b>	<b>H1 – H4</b>

## LIST OF TABLES

**Table 2.1:** Specifications of the microscope used in the study at the University of the Free State. Reflected and transmitted light was used to identify different mineral phases and to identify the best areas of interest for further quantitative analytical methods. (19)

**Table 2.2:** Characteristics of the scanning electron microscope (SEM). Energy dispersive X-ray spectrometry (EDS-SEM) was used to identify areas of interest and mineral phases for further quantitative analysis with the electron microprobe (EMPA). (20)

**Table 2.3:** Outline and characteristics of the electron microprobe (EMPA). Quantitative wavelength dispersive X-ray spectrometry was used to quantify phases and determine concentrations of elements in the different phases. (20)

**Table 2.4:** Outline and characteristics of X-ray fluorescent spectrometry done at the University of the Free State. X-ray fluorescence was used to determine concentrations of major elements in whole rock samples. (21)

**Table 2.5:** Instrumental parameters for inductively coupled plasma mass spectrometry (ICP-MS). Quantitative ICP-MS was used to determine whole rock trace elements and platinum group elements in core samples. (22)

**Table 2.6:** Instrumental parameters for the Eltra carbon-sulphur analyser. The quantitative Eltra analyser was used to determine sulphur (S) in the various core samples. (23)

**Table 3.2.1:** Average plagioclase chemistry in the different lithologies of the various boreholes. Major element oxides given in wt%. (38)

**Table 3.2.2:** Average orthopyroxene chemistry in the different lithologies of the different boreholes. Major element oxides given in wt%. (41)

**Table 3.2.3:** Average clinopyroxene chemistry in the different lithologies of the different boreholes. Major element oxides given in wt%. (43)

**Table 3.2.4:** Average mineral chemistry of chromite in the different lithologies of the different boreholes. Major element oxides given in wt%. (44)

**Table 3.2.5:** Average mineral chemistry of phlogopite in the different lithologies of the different boreholes. Major element oxides given in wt%. (45)

**Table 3.2.6a:** Average mineral chemistry of chalcopyrite in the different lithologies of the different boreholes. Given in wt%. (47)

**Table 3.2.6b:** Average mineral chemistry of pyrrhotite in the different lithologies of the different boreholes. Given in wt%. (47)

**Table 3.2.6c:** Average mineral chemistry of pentlandite in the different lithologies of the different boreholes. Given in wt%. (47)

**Table 3.2.6d:** Average mineral chemistry of pyrite in borehole 6259. Given in wt% (47)

**Table 3.3.1:** Average whole rock geochemistry (major element oxides and element ratios) of the various boreholes obtained from ICP-MS analysis. Major element oxides in wt%. (51)

**Table 3.4.1:** Average whole rock geochemistry (trace elements) of the various boreholes obtained from ICP-MS analysis. Trace element concentrations in ppm. (53)

**Table 3.4.2:** Average whole rock geochemistry (REE) of the various boreholes obtained from ICP-MS analysis. REE concentrations in ppm. (55)

**Table 3.5.1:** Average whole rock geochemistry (PGE) of the various boreholes obtained from ICP-MS analysis. PGE concentrations in ppm, S and Cr in wt%. (56)

**Table 4.1:** Average chromite chemistry data in the various chromitite layers for the various boreholes. Major element oxides in wt%.(Cr/(Cr+Al) calculated using molar values. (65)

**Table 4.4:** Pt/Pd ratios for the various lithological units in the three boreholes with Merensky reef intersection. (77)

## LIST OF FIGURES

**Figure 1.1:** Simplified locality map of South Africa, showing that the Bushveld Complex lies within the boundaries of South Africa, near the middle of the Kaapvaal Craton. The map also shows the various limbs, the Bethal limb that is covered with younger sediments, is not shown. The location of Impala platinum mine is the western Bushveld Complex is also indicated. (Map modified after Scoon and Mitchel, 2009 and Cawthorn et al., 2002a). (2)

**Figure 1.2:** Geology of the Western lobe of the Bushveld Complex. The stippled line indicates the outcrop of the Merensky reef. Map modified after Barnes & Maier, 2002b; Maier et al., 2013. (3)

**Figure 1.3:** Vertical section of the layered sequence from the Rustenburg Layered Suite (after Scoon & Mitchell, 2009; Clarke et al., 2009 and Cawthorn and Boerst, 2006). (5)

**Figure 1.4:** Schematic cross section showing the different footwall layers the Merensky reef can rest on depending on the depth of the pothole (after Leeb-du Toit, 1986; Cawthorn, 2002b; Cawthorn, 2005). (7)

**Figure 2.1:** a) Map showing Impala Platinum mining operations and the different shaft locations. (b) Drill core NP (non-pegmatoidal) from shaft 14; borehole SD14/90, drill core N (non-pegmatoidal) from near shaft 14; borehole BH6259 and drill core P (pegmatoidal) from shaft 20; borehole 20/0252. (12)

**Figure 2.2:** (Not to scale) Facies variation in the Merensky unit on Impala Platinum Mine. (a) and (b) shows non-pegmatoidal reef from the mine with the chromitite stringer varying in thickness (after Leeb-du Toit, 1986; Cawthorn, 2010); (c) pegmatoidal pyroxenite in which the thickness of both the pegmatoidal unit as well as the chromitite stringers can vary, traditionally viewed as ‘typical’ Merensky by Viljoen & Hieber (1986). (13)

**Figure 2.3:** Core log of borehole SD14/90 non-pegmatoidal Merensky reef indicating the different lithologies, drilling direction, samples analysed for PGE, depth of the core section and the location. (14)

**Figure 2.4:** Core log of borehole BH6259 non-pegmatoidal Merensky reef indicating the different lithologies, drilling direction, samples analysed for PGE, depth of the core section and the location. (15)

**Figure 2.5:** Core log of borehole 20/0252 pegmatoidal Merensky reef indicating the different lithologies, drilling direction, samples analysed for PGE, depth of the core section and the location. (16)

**Figure 3.1.1:** Photomicrographs of the rocks from the hanging wall (feldspathic pyroxenite) of borehole SD14/90. (25)

**Figure 3.1.2:** Photomicrographs of the rocks from the chromitite layer of borehole SD14/90. (25)

**Figure 3.1.3:** Photomicrographs of the rocks from the chromitite layer of borehole SD14/90. (26)

**Figure 3.1.4:** Photomicrographs of the rocks from the footwall (anorthosite) of borehole SD14/90. (27)

**Figure 3.1.5:** The average modal mineralogical composition of the hanging wall, chromitite layer and the footwall of the non-pegmatoidal Merensky reef (NP) borehole SD14/90. (27)

**Figure 3.1.6:** Photomicrographs of the rocks from the hanging wall (Feldspathic pyroxenite) of borehole BH6259. (29)

**Figure 3.1.7:** Photomicrographs of the rocks from the hanging wall (feldspathic pyroxenite) through the chromitite layer of borehole BH6259. (30)

**Figure 3.1.8:** Photomicrographs of the rocks from the footwall (anorthosite) of borehole BH6259. (31)

**Figure 3.1.9:** The average modal mineralogical composition of the hanging wall, chromitite layer and the footwall of the non-pegmatoidal Merensky reef (N) borehole BH6259. (31)

**Figure 3.1.10:** Photomicrographs of the rocks from the hanging wall (feldspathic pyroxenite) through the chromitite layer of borehole 20/0252. (33)

**Figure 3.1.11:** Photomicrographs of the rocks from the top chromitite layer of borehole 20/0252. (34)

**Figure 3.1.12:** Photomicrographs of the rocks from the pegmatoidal layer through the bottom chromitite layer of borehole 20/0252. (35)

**Figure 3.1.13:** Photomicrographs of the rocks from the bottom chromitite layer through the footwall (anorthosite) of borehole 20/0252. (36)

**Figure 3.1.14:** The average modal mineralogical compositions of the hanging wall, top chromitite layer, pegmatoidal layer, the bottom chromitite layer and the footwall of the pegmatoidal Merensky reef (P) borehole 20/0252. (37)

**Figure 3.2.1:** Composition of plagioclase in the ternary  $\text{CaAl}_2\text{Si}_2\text{O}_8$ ;  $\text{NaAlSi}_3\text{O}_8$  and  $\text{KAlSi}_3\text{O}_8$ . 14 analyses of samples from borehole SD14/90, 16 analyses of samples from borehole BH6259 and 13 analyses of samples from borehole 20/0252. (39)

**Figure 3.2.2:** Plot of depth versus An% (with error bars indicating the RSD ) in plagioclase of borehole a) SD14/90; b) BH6259; c) 20/0252. (40)

**Figure 3.2.3:** Composition of orthopyroxene and clinopyroxene in the ternary  $\text{Ca}_2\text{Si}_2\text{O}_6$ ,  $\text{Mg}_2\text{Si}_2\text{O}_6$  and  $\text{Fe}_2\text{Si}_2\text{O}_6$  system after Morimoto (1988). 15 analyses of samples from borehole SD14/90, 20 analyses of samples from borehole BH6259 and 19 analyses of samples from borehole 20/0252. (42)

**Figure 3.2.4:** Plot of depth versus Mg# (with error bars indicating the RSD) in orthopyroxene and clinopyroxene of borehole a) SD14/90; b) BH6259; c) 20/0252. (42)

**Figure 3.3.1:** Changing whole rock geochemistry, of a) SD14/90;b) BH6259 and c) 20/0252 illustrated by the Mg# and the Cr/(Cr+Fe<sup>3+</sup>) and Cr/(Cr+Al) metal ratios. Data are given in Appendix D. Chromitite stringer indicated by a red line. (49)

**Figure 3.3.2:** Changing whole rock An% of borehole a) SD14/90; b) BH6259 and c) 20/0252. Data are given in appendix D. Chromitite stringer indicated by a red line. (50)

**Figure 3.3.3:** From whole rock data CIPW norms was calculated and plotted in the ternary  $\text{CaAl}_2\text{Si}_2\text{O}_8$ ,  $\text{NaAlSi}_3\text{O}_8$  and  $\text{KAlSi}_3\text{O}_8$ . (52)

**Figure 3.4.1:** Chondrite-normalised REE diagrams for a) borehole SD14/90; b) borehole BH6259 and c) borehole 20/0252. (54)

**Figure 3.5.1:** PGE, Cr, S, Cu, Pt/Pd and Cu/Pd values vs depth for borehole A) SD14/90; B) BH6259 and C) 20/0252. (57)

**Figure 4.1.1:** Schematic diagram of A) the pegmatoidal Merensky reef, borehole 20/0252 (with two chromitite stringers) and the non-pegmatoidal reef (one chromitite stringer)

borehole BH6259; B) the pegmatoidal Merensky reef, borehole 20/0252 (with two chromitite stringers) and the non-pegmatoidal reef (one chromitite stringer) borehole SD14/90. (65)

**Figure 4.1.2:** The various chromitite stringer data plotted. (a) Mg# vs Cr<sub>2</sub>O<sub>3</sub>, (b) Mg# vs Al<sub>2</sub>O<sub>3</sub>, (c) Cr<sub>2</sub>O<sub>3</sub> vs Al<sub>2</sub>O<sub>3</sub>. NP5 – NP7: borehole SD14/90; N98: borehole BH6259; P11 – P13 and P48: borehole 20/0252. (66)

**Figure 4.1.3:** Composition of chromite in a ternary diagram. (66)

**Figure 4.2.1:** Major element oxides vs MgO for EMPA (orthopyroxene, clinopyroxene, plagioclase and chromite) and whole rock analysis from borehole SD14/90. (70)

**Figure 4.2.2:** Major element oxides vs MgO for EMPA (orthopyroxene, clinopyroxene, plagioclase and chromite) and whole rock analysis from borehole BH6259. (71)

**Figure 4.2.3:** Major element oxides vs MgO for EMPA (orthopyroxene, clinopyroxene, plagioclase and chromite) and whole rock analysis from borehole 20/0252. (72)

**Figure 4.3.1:** Chondrite-normalised multi element diagrams for borehole a) SD14/90; b) BH6259 and c) 20/0252. Normalisation values from Lodders, 2003. (74)

**Figure 4.4.1:** Chondrite normalized PGE patterns for borehole a) SD14/90; b) BH6259 and b) 20/0252. C1 chondrite normalized values are from Lodders, (2003). (79)

**Figure 4.4.2:** Binary variation diagrams of Pt, Pd, Ir, Cu and S for the non-pegmatoidal Merensky reef from borehole BH6259. (81)

**Figure 4.4.3:** Binary variation diagrams of Pt, Pd, Ir, Cu and S for the non-pegmatoidal Merensky reef from borehole SD14/90. (82)

**Figure 4.4.4:** Binary variation diagrams of Pt, Pd, Ir, Cu and S for the pegmatoidal Merensky reef from borehole 20/0252. (83)

**Figure 4.5.1:** a-c) Comparing depth versus An% for EMPA of plagioclase and whole rock analysis. The black dots with error bars represent the EMPA of plagioclase and the red dots represent the whole rock data. a) Borehole SD14/90; b) Borehole BH6259 and c) Borehole 20/0252. (84)

**Figure 4.5.1:** d-f) Comparing depth versus Mg# for EMPA of orthopyroxene and clinopyroxene and whole rock analysis. The black dots with error bars represents the EMPA of

clinopyroxene, the blue dots the orthopyroxene and the red dots the whole rock data. d) Borehole SD14/90; e) Borehole BH6259 and f) Borehole 20/0252. (84)

## LIST OF ABBREVIATIONS

An%	Anorthite content
BC	Bushveld Complex
BMS	Base metal sulphide
Chr	Chromitite layer
EDX	Energy dispersive X-ray spectrometry
EMP	Electron microprobe
En%	Enstatite content
FW	Footwall
HW	Hangingwall
ICP-MS	Inductive coupled plasma mass spectrometry
ICP-OES	Inductively coupled plasma-optical emission spectroscopy
LCZ	Lower Critical Zone
LG	Lower Group
LZ	Lower Zone
MR	Merensky reef
MaZ	Marginal Zone
MG	Middle Group
Mg#	Magnesium number = $(\text{Mg} / (\text{Mg} + \text{Fe}^{2+}))$
MZ	Main Zone
N.A.	Not applicable
n.d.	Not detected
Peg	Pegmatoidal layer
PGE	Platinum group elements
PGM	Platinum group minerals
REE	Rare earth elements
RLS	Rustenburg Layered Suite
RSD	Relative standard deviation
SEM	Scanning electron microscope
UCZ	Upper Critical Zone
UG	Upper Group
UZ	Upper Zone
XRF	X-ray fluorescence spectrometry

## **LIST OF MINERAL ABBREVIATIONS**

Amph	Amphibole
Biot	Biotite
Cpx	Clinopyroxene
Chr	Chromite
Cplag	Cumulus plagioclase
Iplag	Intercumulus plagioclase
Musc	Muscovite
Opx	Orthopyroxene
Phlog	Phlogopite
Plag	Plagioclase
Serp	Serpentine
Sul	Sulphide
Talc	Talc
Try	Tridymite
Qtz	Quartz

# Chapter 1: Introduction

## 1.1 General geology

The Bushveld Complex is the world's largest layered mafic intrusion and is part of the Paleoproterozoic Bushveld Igneous Province (Walraven et al., 1990). It is renowned for its deposits of Cr and platinum-group elements (PGE) (Cawthorn, 2010a). Situated in the northern parts of South Africa, it occurs in the North-West, Limpopo, Mpumalanga and Gauteng provinces. The Bushveld Complex lies within the northeastern portion of South Africa (Fig. 1.1) and occurs near the middle of the Kaapvaal Craton (Cawthorn et al., 2002a; Clarke et al., 2009) (Fig. 1.1). The Bushveld Complex was emplaced at 2.054 Ga into the supracrustal rocks of the Transvaal Supergroup, concordant in the Western lobe and discordant in the Eastern and Northern lobe in an intraplate setting (Clarke et al., 2009 and Walraven et al., 1990). The Transvaal Supergroup (ca. 2.5-2.1 Ga) (Scoon & Mitchell, 2009) comprises of: quartzite, a dolomitic and a banded ironstone sequence (Eales & Cawthorn, 1996) interlayered with volcanoclastic sediments and volcanic andesite (Barnes et al., 2009).

The complex is made up of five lobes, the fifth lobe doesn't outcrop but is hidden below younger sediments (Fig. 1.1). The five lobes are the Eastern lobe; the Southeastern or Bethal lobe, the Western lobe, the Far Western lobe and the Northern lobe (Cawthorn et al., 2002b). The Eastern lobe outcrops for ca. 200 km from Stoffberg to Chuniespoort and is well exposed. The Southeastern lobe doesn't outcrop and is only known from bore-core and geophysics information and its gravity and magnetic signature. The Western lobe which is not well exposed, extends from north of Pretoria to near Thabazimbi and was emplaced at the level of the Magaliesberg Quartzite (Eales and Cawthorn, 1996). The Far Western lobe is eroded and extends all the way to the Botswana border. The Molopo Igneous Complex is also part of the Bushveld Complex. The Northern lobe also known as the Potgietersrus lobe is partially covered with younger rocks (Eales and Cawthorn, 1996).

The Bushveld magmatic province can be divided into five major magmatic suites: (1) the bimodal Rooiberg Volcanic Suite (2.061 Ga, Walraven et al., 1990), (2) the Rustenburg Layered Suite (Eales et al., 1991) (3) a suite that comprises of marginal pre- and syn-

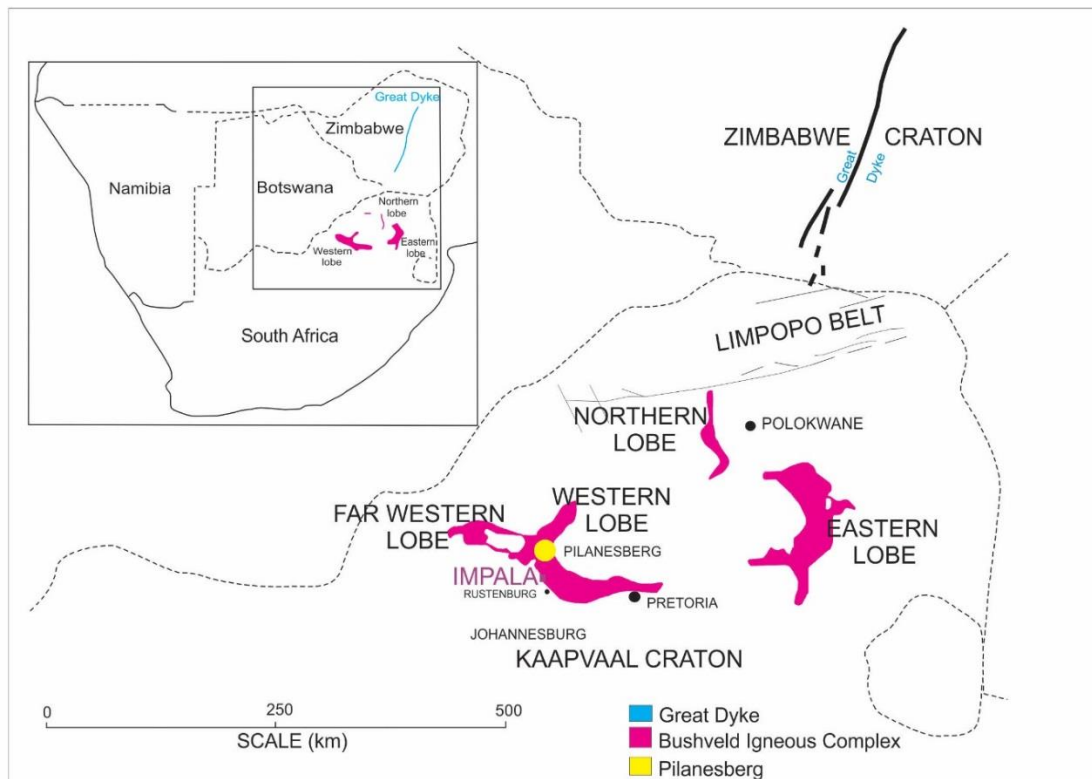


**Figure 1.1: Simplified locality map of South Africa, showing that the Bushveld Complex lies within the boundaries of South Africa, near the middle of the Kaapvaal Craton. The map also shows the various lobes. The location of Impala platinum mine in the western Bushveld Complex is also indicated. (Map modified after Scoon & Mitchell, 2009 and Cawthorn et al., 2002a).**

Bushveld sills and intrusions 4), the Lebowa Granite Suite and 5) the Rashoop Granophyre Suite (Fig. 1.2) (Kruger, 2005 & Naldrett et al., 2009). The Rustenburg Layered Suite is generally considered the “Bushveld Complex”. A variety of floor and roof rocks can be present in different parts of the complex. The Magaliesberg formation of the Pretoria Group forms the floor rocks in the Rustenburg area (Leeb-Du Toit, 1986). No regional metamorphism or extensive deformation can be seen in the Bushveld Complex, only minor or local alteration (Eales & Cawthorn, 1996). Kruger (2005) shows that the Bushveld Complex intruded as a flat, sill-like sheet at the boundary of the Rooiberg Group and the underlying Pretoria Group.

The Rooiberg Group has been dated (2.061 Ga by Walraven, 1997 & 2.057 Ga, Barnes & Maier, 2002b) and the close similarity in age and the position relative to the Rustenburg Layered Suite led to the suggestion that the Rooiberg Group be included in the Bushveld Complex as the earliest part of the Bushveld Complex sequence (Kruger, 2005). The Lebowa Granite Suite comprises of different sheeted intrusions of varying thickness from 1.5 to 3.5

km (Kleeman and Twist 1989). The Rashoop Granophyre Suite and the Lebowa Granite Suite represent the acid phase of the Bushveld Complex (Cawthorn et al., 2006b and Vermaak, 1976).

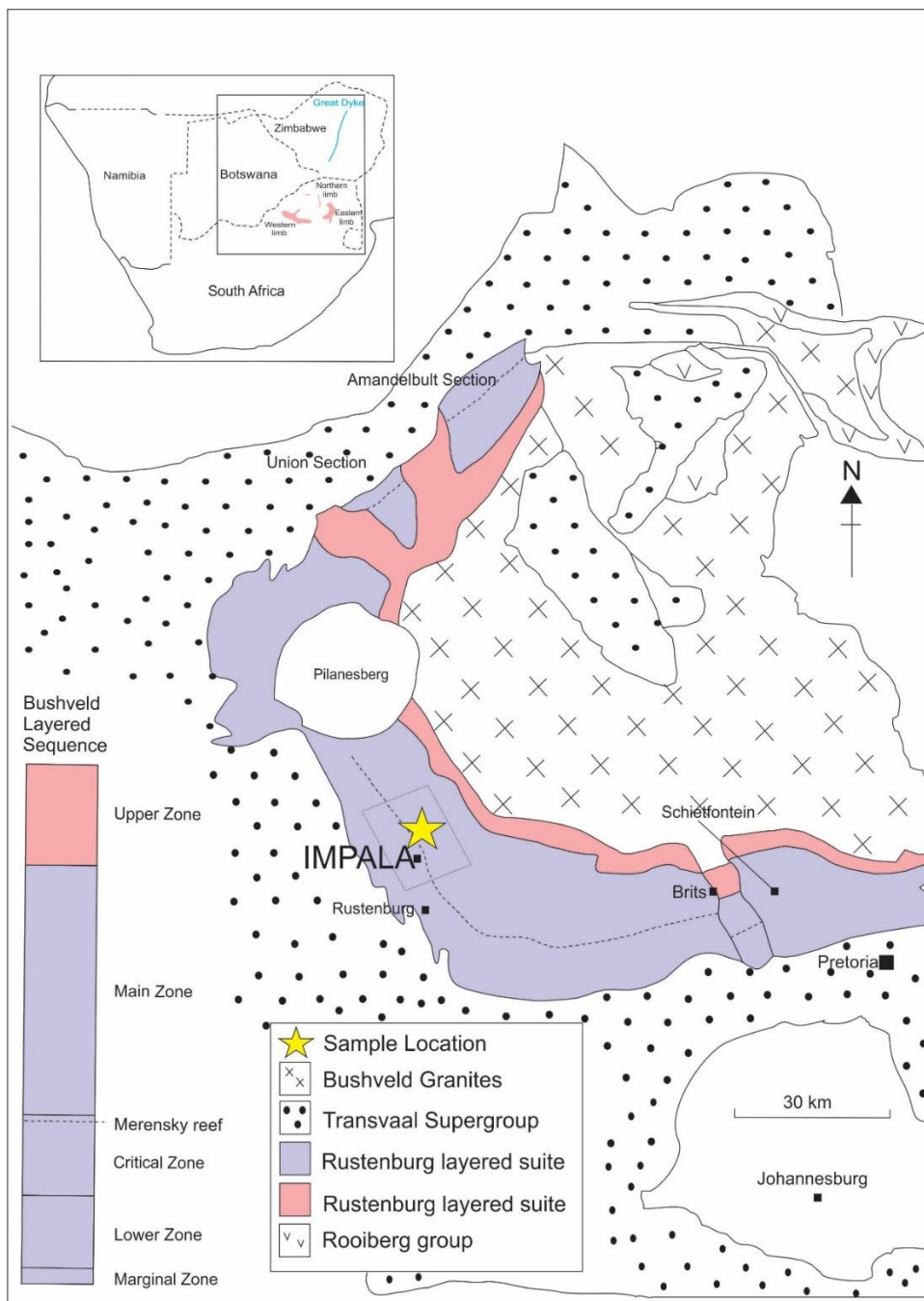


**Figure 1.2: Geology of the Western lobe of the Bushveld Complex. The stippled line indicates the outcrop of the Merensky reef. (Map modified after Barnes & Maier, 2002b; Maier et al., 2013).**

The mafic to ultramafic layered succession of the Rustenburg Layered Suite (RLS) contains 75% and 50% of the world's platinum and palladium resources, respectively (Barnes & Maier, 2002b). It has an aerial extent of more than 65000 km<sup>2</sup> and extends 450 km east-west and 350 km north-south with a thickness of 5-10 km (Eales & Cawthorn, 1996; Cawthorn et

al., 2006a, Kruger, 2005 and Walraven et al., 1990). The Rustenburg Layered Suite is stratigraphically subdivided into five different zones by SACS (1980). The Marginal zone (forms the base), which is overlain by the Lower zone, the Critical zone, Main zone and the Upper zone (Fig. 1.3) (Barnes and Maier, 2002a).

- The Marginal zone: ca 800 m in thickness and the result of multiple intrusions of magma and subsequent rapid crystallization. It consists of medium grained unlayered micro norite. Variable proportions of clinopyroxene, quartz, biotite, and hornblende occur as accessory minerals. The presence of quartz and biotite may reflect the assimilation of shale (Cawthorn et al., 2002b and Cawthorn et al., 2005).
- The Lower zone: up to 130 m in thickness although it has been influenced by floor topography and structure. The lower zone can also be subdivided into 3 sequences: 1) basal pyroxenite, 2) harzburgite and 3) an upper pyroxenite sequence, all of which contain less than 1% chromite and less than 4% interstitial plagioclase (Cawthorn et al., 2002b).
- The Critical zone: Within the Critical zone is the world's largest platinum bearing ore bodies: the UG2 reef and the Merensky reef as well as the largest deposit of chromitite. The Critical zone can be subdivided into two sub-zones: 1) Lower, 2) and the Upper Critical zone. These zones display excellent layering from chromitite, pyroxenite, and norite to anorthosite, in what are termed cyclic units (Cawthorn et al., 2006b). Chromitites are restricted to the Critical zone. Two stratigraphically delineated groups contain these chromitite layers (Kinnaird et al., 2002) and they are listed below.
  - 1) Lower Critical zone (LCZ): ca 800m thick layers of feldspathic pyroxenite and chromite with minor olivine. It can also contain up to seven layers of chromitite (LG1-LG7) which can reach up to 1m in thickness as well as MG 1-2 chromitites.
  - 2) Upper Critical zone (UCZ): Comprises of chromitite, pyroxenite, norite and anorthosite. Up to 7 cyclic units are recognized. Near the top of the UCZ the MG 3-4 occur as well as two thick chromitite layers namely the UG1 and UG2 (whereas the UG3 is restricted to the Eastern Bushveld). The Merensky cyclic unit and the Bastard cyclic unit are the top 2 cyclic units in the UCZ (Cawthorn et al., 2006b). The boundary between the LCZ and the UCZ is at the base of the MG2 chromitite layer where plagioclase-

rich rocks manifest. Between the MG2 and MG3 plagioclase becomes cumulus as opposed to intercumulus.

The Main zone: consists of norite and gabbronorite with minor amounts of anorthosite and pyroxenite layers. It is a thick succession (ca 3000 m) and isn't as well layered as the Critical zone (Cawthorn et al., 2006b).

The Upper zone: ca 2000 m thick and is well layered, and contains 24 magnetite layers, which are the most prominent feature of this zone (Cawthorn et al., 2006b).

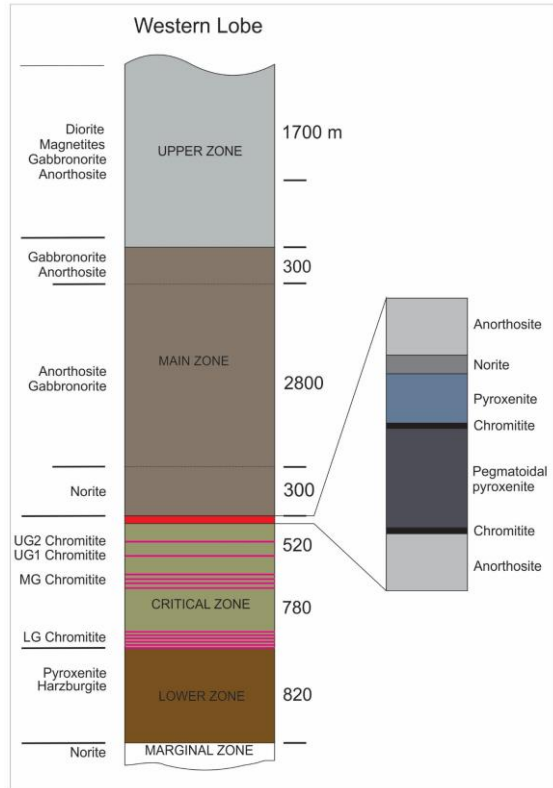


**Figure 1.3: Vertical section of the layered sequence from the Rustenburg Layered Suite (after Scoon & Mitchell, 2009; Clarke et al., 2009 and Cawthorn and Boerst, 2006).**

## 1.2 The Merensky unit

### 1.2.1 General features of the Merensky cyclic unit

According to Kruger (2010) the influx of a large volume of a new Main Zone magma occurred close to the Thabazimbi Murchison Lineament. The same magma influx also interacted with the Critical Zone rocks to the South of the Thabazimbi Murchison Lineament in the Eastern and Western lobes to form a broad unconformity with the Critical Zone, manifested by large-scale regional pothole and sharp local erosional depressions or potholes. A later sill like influx of Main zone magma intruded the Platreef in the north as the 'B' reef and south of the Thabazimbi Murchison Lineament as a thin intrusion which exploited the unconformity boundary between the Critical Zone and the Bastard cyclic unit to form the

Merensky cyclic unit (Kruger, 2010). This model of new magma entering the chamber would result in a sharp step-like increase in  $^{87}\text{Sr}/^{86}\text{Sr}$  ratio's, which was not observed by Kruger (1982). They suggested that the  $^{87}\text{Sr}/^{86}\text{Sr}$  ratios were modified by infiltration of intercumulus liquids from the footwall and that the intercumulus material would therefore vary with the proportion of Sr introduced from the footwall. Kruger (2010) suggested that sulphide in the Platreef and the Merensky reef was derived from highly sulphide rich sediments.

The Merensky cyclic unit forms the sixth unit in the Upper Critical zone, and is fairly consistent in thickness (9-10m) across the Rustenburg section (Viljoen & Hieber, 1986). The Bastard reef commences at the uppermost seventh cyclic unit in the Critical zone (Fig. 1.3) (Viljoen & Hieber, 1986). The Bastard cyclic unit is very similar to the Merensky cyclic unit, except for the sulphides at the base being less abundant and the Bastard cyclic unit having considerably lower PGE tenors (Naldrett et al., 2009). The Merensky cyclic unit is the thinnest of the cyclic units, being only a few meters thick (Cawthorn, 2005).

### **1.2.2 General features of the Merensky reef**

The Merensky reef is a composite sheet like body that varies in thickness and occurs at the top of the Critical zone (Leeb du Toit, 1986). The Merensky reef is the base of the sixth unit. A major change within the interval between the UG2 and the Merensky reef occur between the northern portion, north of Pilanesburg and the south western part. In the south western section the vertical separation between the Merensky reef and the UG2 is ca 120 m, compared to the north western section where it is only 40 m. Thus, in the north the more felsic intervals are thinner compared to the south. The mafic units are thicker and richer in olivine and pyroxene compared to the south (Naldrett et al., 2009).

The Merensky reef outcrops for ca. 140 km along the Western and Eastern lobes of the Bushveld Complex. The average dip of the Merensky reef ranges from  $9^\circ$ - $27^\circ$ , towards the centre of the Bushveld Complex. In the northern portion of the Eastern lobe, dips as high as  $65^\circ$  have been recorded (Cawthorn et al., 2002a).

The term “reef” is a mining term referring to a layer that is enriched in PGE, with a width of about 80 – 120 cm depending on whether it is pegmatoidal or non-pegmatoidal reef (Cawthorn et al., 2002a). Platinum concentration in the Merensky reef can vary from 5-15 ppm depending on the width and which sections are measured. The mafic to ultramafic magmas that formed the Bushveld Complex contain no more than several ppb platinum, it

can be said that the processes that produced this enrichment in the Merensky was responsible for a 1000-fold platinum enrichment (Cawthorn, 1999).

Platinum is one of six closely related elements, including palladium, iridium, ruthenium, rhodium and osmium and with gold and silver forming the noble metals. Platinum and palladium are the most abundant in most deposits, whereas others are usually by products (Cawthorn, 1999). Platinum group element mineralization within the Bushveld Complex occurs primarily in stratiform ore bodies known as the Merensky reef, the UG2 reef and the Platreef. Cawthorn (1999) and Naldrett et al. (2009) amongst others have estimated that the three main PGM reefs (ie. The Merensky, UG2 and Platreef) together contain about 200 million oz of PGM which is about 75% of the world's PGE. The grades of mineralization are uniform in the UG2 and Merensky in both the Eastern and Western Bushveld (Cawthorn, 2005).

There is considerable lateral facies variation of the Merensky unit. The Merensky reef can rest on different footwall layers which implies an erosional unconformity. Terminology used at Impala Mines are "A" reef where the reef can rest on various layers of the "Footwall 1" unit and where there is little to no erosion, and no potholes or they are very shallow. The "B" reef rests on the "Footwall 2" unit. The "B" reef is most commonly the pegmatoid type but in certain cases it could be the pyroxenite type, the potholes are deeper and erosion is present. The "C" reef rests on a "Footwall 3" anorthositic norite layer or any of the other lower footwall layers, the potholes are very deep (Leeb-Du Toit, 1986) (Fig. 1.4).

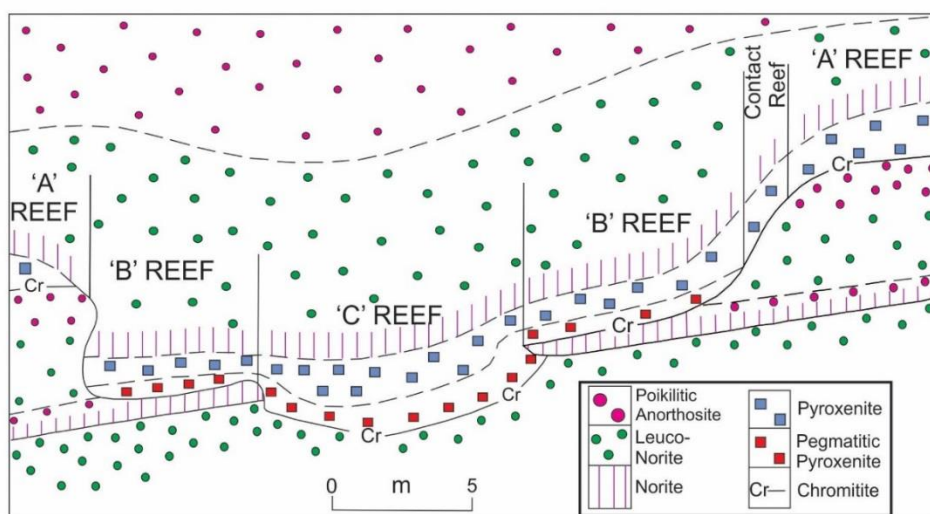


**Figure 1.4: Schematic cross section showing the different footwall layers the Merensky reef can rest on, depending on the depth of the pothole (after Leeb-du Toit, 1986; Cawthorn, 2002b; Cawthorn, 2005).**

### **1.2.3 The Merensky reef at Impala Platinum Mine**

The Merensky reef is exploited on the southwestern part of the Western lobe by Impala Platinum Mine (Fig. 1.2). Impala Platinum is situated 123 km from Johannesburg and 30 km north of Rustenburg. It is the second largest platinum producer in the western world (Leeb du Toit, 1986). To define the pegmatoidal Merensky reef: it starts 23 cm below the lower chromitite (in the anorthosite) and it goes all the way up, to end 23 cm above the top chromitite (in the pyroxenite); the non-pegmatoidal Merensky reef starts 40 cm below the chromitite stringer and ends 60 cm above the chromitite stringer (Barnes & Maier, 2002b). Reef lithologies observed for the pegmatoidal and non-pegmatoidal reefs are leuconorite, anorthosite, chromitite, pegmatoidal pyroxenite and pyroxenite/feldspathic pyroxenite. The vertical distribution of PGE in the Merensky reef is variable but it can to a certain extent be determined. The separation of the two chromitite layers, the thickness, or the absence of one chromitite layer plays a big role in the vertical distribution of PGE. If only one chromitite layer is present, mineralization will tend to concentrate more towards the lower part of the chromitite layer. In the case of two chromitite layers and a large separation between the two chromitite layers the mineralization tends to concentrate higher in the succession, more towards the upper chromitite layer. This is called a top loaded reef (Cawthorn, 2010a; Davey, 1992).

The Merensky reef can be referred to as either a pegmatoidal reef or a non-pegmatoidal reef. In the former case two chromitite stringers are separated by a pegmatoidal layer that can vary in thickness. In the latter case the chromitite layer rests on a footwall of anorthosite and above the chromitite layer is feldspathic pyroxenite (the hanging wall). In the northern parts of Impala Platinum Mine there is little to no pegmatoidal layers whereas in the southern parts of the mine pegmatoidal layers are present. In fact the pegmatoidal layer is only well developed on Wildebeesfontein North and South mines and also in potholes on Bafokeng South Mine (Leeb-Du Toit, 1986).

Mineralization of the Merensky reef at Impala Platinum Mine is generally the same as mineralization elsewhere in the Bushveld Complex. The general strike of the Merensky reef at Impala Platinum Mine is north-north-west to south-south-east, the average dip is about 9.5° towards the centre of the Bushveld Complex. Reef outcrop is mostly towards the western boundary of the lease area and at the eastern boundary the reef is ca. 900 m below the surface (Leeb-du Toit, 1986).

## **1.3 Different models for PGE mineralization and chromitite formation**

Chromitite layers can be traced over hundreds of km's along strike in the Eastern as well as the Western lobes of the Bushveld Complex and are associated with significant PGE mineralisation (Maier et al., 2013). Many thin layers of chromitite exist in the Bushveld Complex and they seem to merge with the major seams. There are 14 major seams recognised (LG1–7, MG1-4 and UG1-3) (Maier et al., 2013).

### **1.3.1 Models for chromitite formation**

Three models are proposed for chromitite formation: a) Pressure change: Both Cameron (1980) and Lipin (1993) suggested that pressure may be an important controlling factor in oxide formation, where stability fields may be shifted through pressure changes; b) Injection of chromite slurry suggested by Eales (2000): To overcome the problem of the chromium budget in the LZ and CZ; c) Magma mixing: The most popular model that was presented by Irvine (1975, 1976) from his work on the MuskoX Intrusion. In this model the injection of a primitive magma mix with the more evolved resident magma, within a magma chamber, to result in chromium supersaturation.

### **1.3.2 Models for PGE mineralisation**

In the Bushveld Complex PGE are so closely associated with chromitite that even the thinnest chromitite layers contain elevated PGE concentrations. Three models are proposed for PGE mineralisation a) Chromite association: Some authors have speculated that chromite may act as a potential host for PGE. Vermaak & Hendriks (1976) and recent work by McDonald & Holwell (2011) noted cases where sulphides occur within chromites in the Northern lobe. b) Sulphide association: Work by (Barnes & Maier 2002b) suggested that because PGMs are so closely associated with sulphide, such as in the Merensky reef, that a sulphide liquid was the principal phase in collecting the PGE. In this model, a fractionating body of magma may reach sulphide saturation and therefor form an immiscible sulphide liquid which is exsolved from the silicate magma. c) PGE Clusters: In the model presented by Tredoux et al., (1995). PGE are stabilized by surface absorption with either sulphur or iron, these clusters essentially preconcentrate the PGE.

### **1.3.3 Models for the formation of metalliferous (PGE) reefs**

The formation of metalliferous (PGE-bearing) reefs has been studied intensively and various

hypotheses have been proposed. Three models are proposed: a) Downward accumulation of PGE-bearing sulphide melts. PGE, present within the silicate melt have extremely high partition coefficients for sulphide and are effectively captured by the sulphide melt droplets. With time these PGE-bearing sulphide droplets will settle upon a cumulus pile to produce a metalliferous ore horizon. b) Upward infiltration of fluid. Following the model presented by Willmore et al. (2000) and Boudreau & Meurer (1999), Cl-rich intercumulus fluid percolates upward, through the cumulus pile and dissolves any PGE and sulphide present. The high fluid content of the magma can also act as a flux, where remelting would ultimately lead to the formation of a coarse grained pegmatite. Evidence for this model includes the presence of pegmatoidal unit of the Merensky reef and the enrichment of RRE in the pyroxenes of the Merensky reef. c) Lateral injection of a crystal-rich slurry has been proposed for the Merensky reef and other metalliferous reefs by Mitchell and Scoon (2007) and Kruger (2010). This model requires that magma, ascending through a mush column, migrates through conduits and inherits crystals from earlier crystallization events which may differ from one another. This model can provide explanations for many of the problems, which the other two models couldn't or had difficulty in answering. For example, the chromium budget is resolved by the introduction of chromite microphenocrysts sourced from a staging chamber.

## **1.4 Previous studies on the Merensky reef and aim of the project**

Comprehensive and detailed descriptions of the Merensky reef as well as the stratigraphic setting in the Western Bushveld have been given by Leeb-du Toit, (1986); Viljoen & Hieber, (1986); Maier & Bowen, (1996); Barnes & Maier, (2002a; 2002b); Cawthorn et al., (2002a & 2002b); Godel et al., (2007); Naldrett et al., (2009; 2011 and 2012) Wilson et al., (1999); Seabrook et al., (2005); Kruger & Marsh, (1982, 1985); Vermaak, (1976) and Brynard et al., (1976). However mechanisms for the formation of the Merensky reef still remains controversial despite decades of research.

In 1976 Vermaak & Hendriks gave a detailed review of the mineralogy of the Merensky reef. The Merensky reef comprises typically of postcumulus (interstitial) plagioclase and clinopyroxene while orthopyroxene and olivine are cumulate. Accessory minerals like hornblende, biotite, phlogopite and muscovite occur along with quartz, zircon, calcite and tourmaline. The rest of the primary mineralogy is made up by base metal sulphides (such as

chalcopyrite, pyrite, pyrrhotite and pentlandite), chromite, magnetite, ilmenite and rutile. Despite a modal proportion of 1 – 5%, these sulphides host the majority of precious metals occurring in the Merensky reef (Barnes & Maier, 2002b). However there is also a suggestion that chromite may act as potential host for PGE (Latypov et al., 2013). Various facies for the Merensky reef have been documented which may influence PGE distribution (Cawthorn et al., 2002a, Cawthorn 2010a, 2010b).

Cawthorn (2012) noted that PGE distribution in the Merensky reef in the vertical section is irregular. Typically non-pegmatoidal reef facies contain mineralization within the anorthosite underlying the lower chromitite unit and within pyroxenite layers. In the pegmatoidal reef facies a double peak PGE distribution is evident, though the mineralization tends to track the upper chromitite giving rise to the style known as “top loaded” (Davey, 1992; Cawthorn, 2010a and 2012). Barnes and Maier (2002b) proposed that the thickness of the pyroxenite unit within the Merensky reef is inversely proportional to the grade of the ore.

Despite heavy interest in recent years the control of PGE-partitioning within the Merensky reef still remains controversial. Remaining questions like, the variability of Merensky reef and how this effects the platinum distribution (e.g. whether the grade or distribution of platinum is influenced by the presence or not of pegmatoidal Merensky reef, whether PGE distribution are more associated with sulphides or with chromites), are still unanswered.

This research is based on doing detailed geochemistry and mineralogy on core samples from Impala Platinum Mine. Data were generated in order to address the following:

- Can vertical distribution of PGE be used to determine if PGE partitioning, in the Merensky reef, is controlled by chromite or sulphide?
- To supplement the PGE data, rock and mineral chemistry data will be used to determine if there are any vertical changes in the mineralogy and geochemistry at 2 cm intervals.
- Can these processes be used to help improve the understanding and constraints on the genetic processes of the Merensky reef?

In total 3 core samples ( $\pm$ 113 closely spaced samples) were analysed using high-precision analytical methods to determine the distribution of PGE, major elements, trace elements and mineral chemistry.

## Chapter 2: Material and methods

### 2.1 Sample description

The samples investigated originate from three drill cores, collected from Impala Platinum Mine in Rustenburg in the Western limb of the Bushveld Complex (Fig. 1.4). Drill core NP (non-pegmatoidal) from shaft 14; borehole SD14/90, drill core N (non-pegmatoidal) from near shaft 14; borehole BH6259 and drill core P (pegmatoidal) from shaft 20; borehole 20/0252 (Fig. 2.1) were collected for this research. In all three cases, samples were taken from the economically mineralized part of the reef. Borehole 20/0252 was drilled underground with an inclination of 90°. The mining width generally encompasses material from 70 cm above the chromite stringer to 30 cm below the chromitite stringer for the non-pegmatoidal Merensky reef and 70 cm above the top chromitite stringer to 30 cm below the bottom chromitite stringer for the pegmatoidal Merensky reef. For this project we concentrated on  $\pm 50$  cm above and below the chromitite stringer for borehole BH6259 and  $\pm 10$  cm above and below the chromitite stringer for borehole SD14/90. In the case of borehole 20/0252 we concentrated 20 cm above the top chromitite stringer and 10 cm below the lower chromitite stringer.

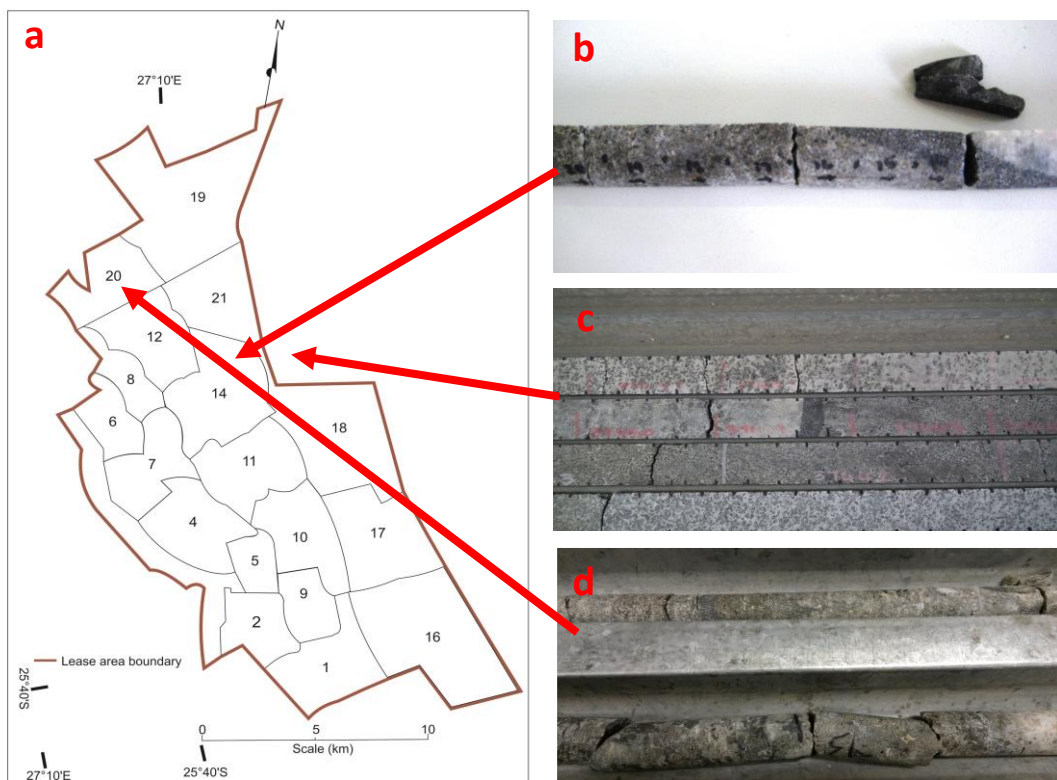


**Figure 2.1: a)** Map showing Impala Platinum mining operations and the different shaft locations. **(b)** Drill core NP (non-pegmatoidal) from shaft 14; **(c)** borehole SD14/90, drill core N (non-pegmatoidal) from near shaft 14; **(d)** borehole BH6259 and drill core P (pegmatoidal) from shaft 20; borehole 20/0252.

Drill cores SD14/90 & BH6259 correspond to the normal Merensky ‘A’ type reef using the nomenclature of Leeb-du Toit (1986). Reef lithologies observed in drill core SD14/90 (non-pegmatoidal; NP) are feldspathic pyroxenite, chromitite and anorthosite (Fig. 2.2a) (Fig. 2.3). The top 8 cm of the core is medium grained feldspathic pyroxenite. The feldspathic pyroxenite is underlain by an inclined thin chromitite layer ( $\pm 2.5$  cm) of irregular thickness (dip- $60^\circ$ ). The chromitite layer is underlain by a layer of medium grained anorthosite. Reef lithologies observed in drill core BH6259 (non-pegmatoidal; N) are feldspathic pyroxenite, chromitite (dip- $35^\circ$ ) and anorthosite (Fig. 2.2b) (Fig. 2.4). The top 50 cm of the core is medium grained feldspathic pyroxenite, which is underlain by a thin layer of chromitite. The chromitite is underlain by a layer of fine to medium grained anorthosite. Drill core 20/0252 corresponds to the normal Merensky ‘B’ type reef using the nomenclature of Leeb-du Toit (1986). Reef lithologies observed in drill core 20/0252 (pegmatoidal; P) are feldspathic pyroxenite, chromitite, pegmatoidal pyroxenite, chromitite and anorthosite (Fig. 2.2c) (Fig. 2.5). The top 22cm of the core is feldspathic pyroxenite which is underlain by a top chromitite layer ( $\pm 2$  cm). Pegmatoidal pyroxenite ( $\pm 68$  cm) lies between the top and bottom chromitite layer. The bottom chromitite layer is ( $\pm 4$  cm) underlain by anorthosite ( $\pm 8$  cm). In figure 2.3 - 2.5 detailed core sections are described with the different lithologies and lengths.

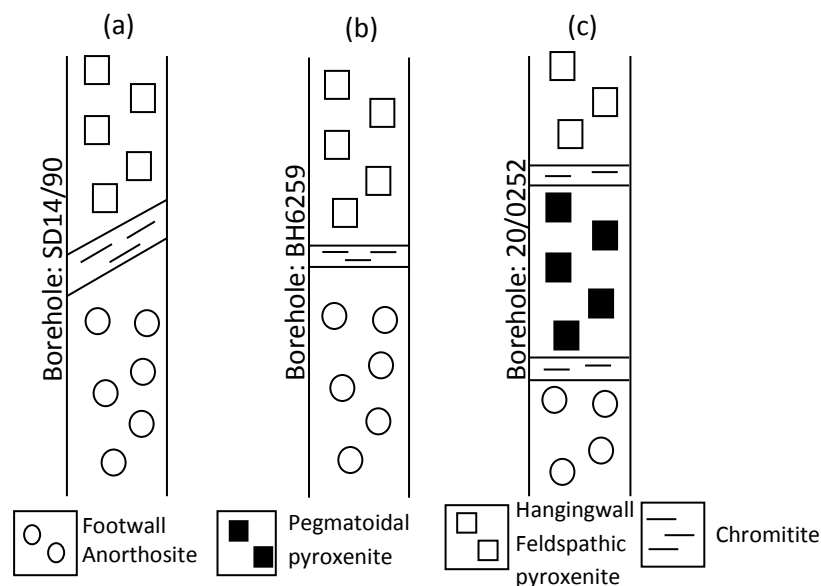


**Figure 2.2: (Not to scale) Facies variations in the Merensky unit on Impala Platinum Mine. (a) and (b) shows non-pegmatoidal reef from the mine with the chromitite stringer varying in thickness (after Leeb-du Toit, 1986; Cawthorn, 2010a); (c) pegmatoidal pyroxenite in which the thickness of both the pegmatoidal unit as well as the chromitite stringers can vary, traditionally viewed as ‘typical’ Merensky by Viljoen & Hieber (1986).**

## Non-Pegmatoidal Merensky reef Borehole: SD14/90

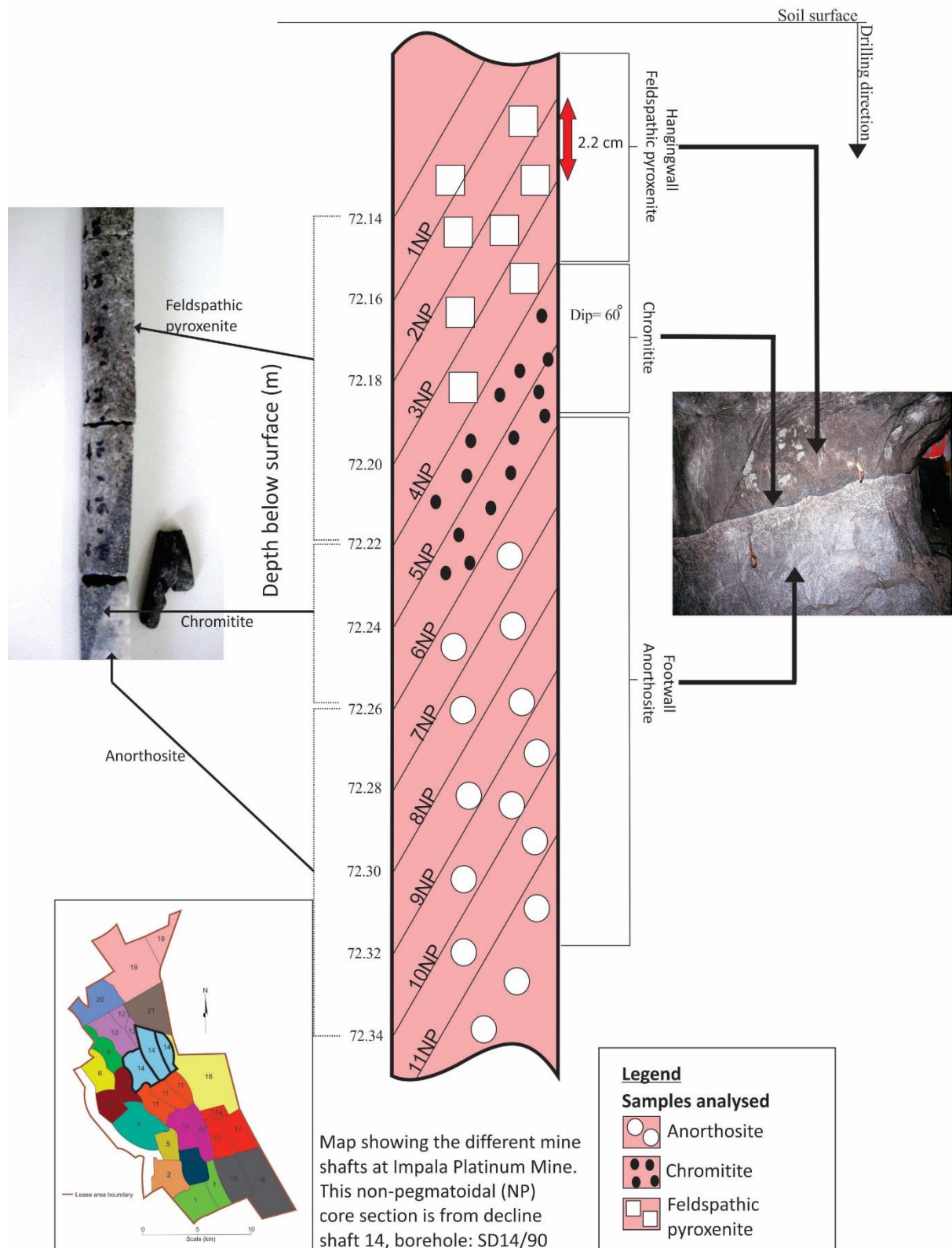


**Figure 2.3: Core log of borehole SD14/90 non-pegmatoidal Merensky reef indicating the different lithologies, drilling direction, samples analysed for PGE, depth of the core section and the location.**

## Non-Pegmatoidal Merensky reef Borehole: BH6259

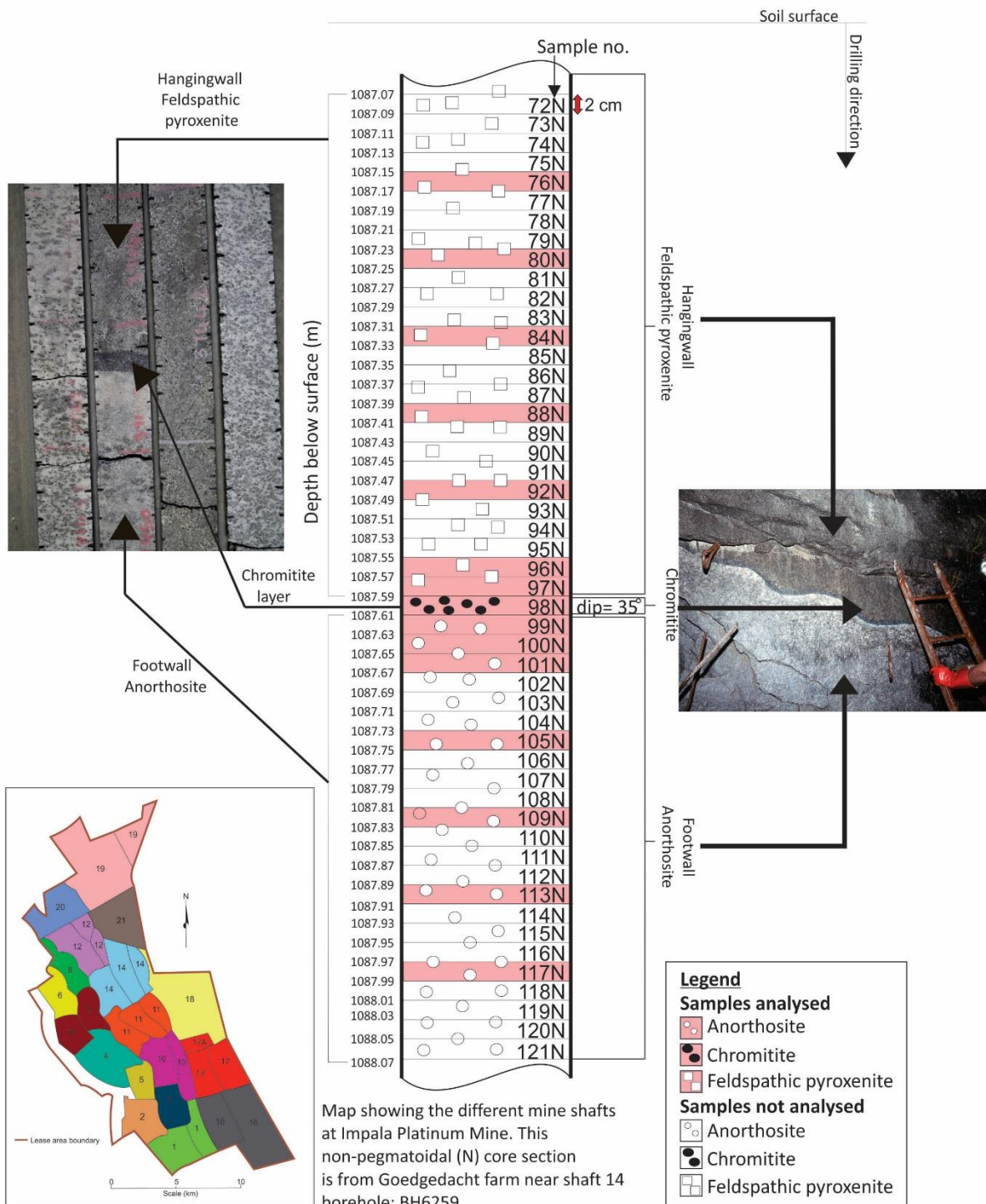


**Figure 2.4: Core log of borehole BH6259 non-pegmatoidal Merensky reef indicating the different lithologies, drilling direction, samples analysed for PGE, depth of the core section and the location.**

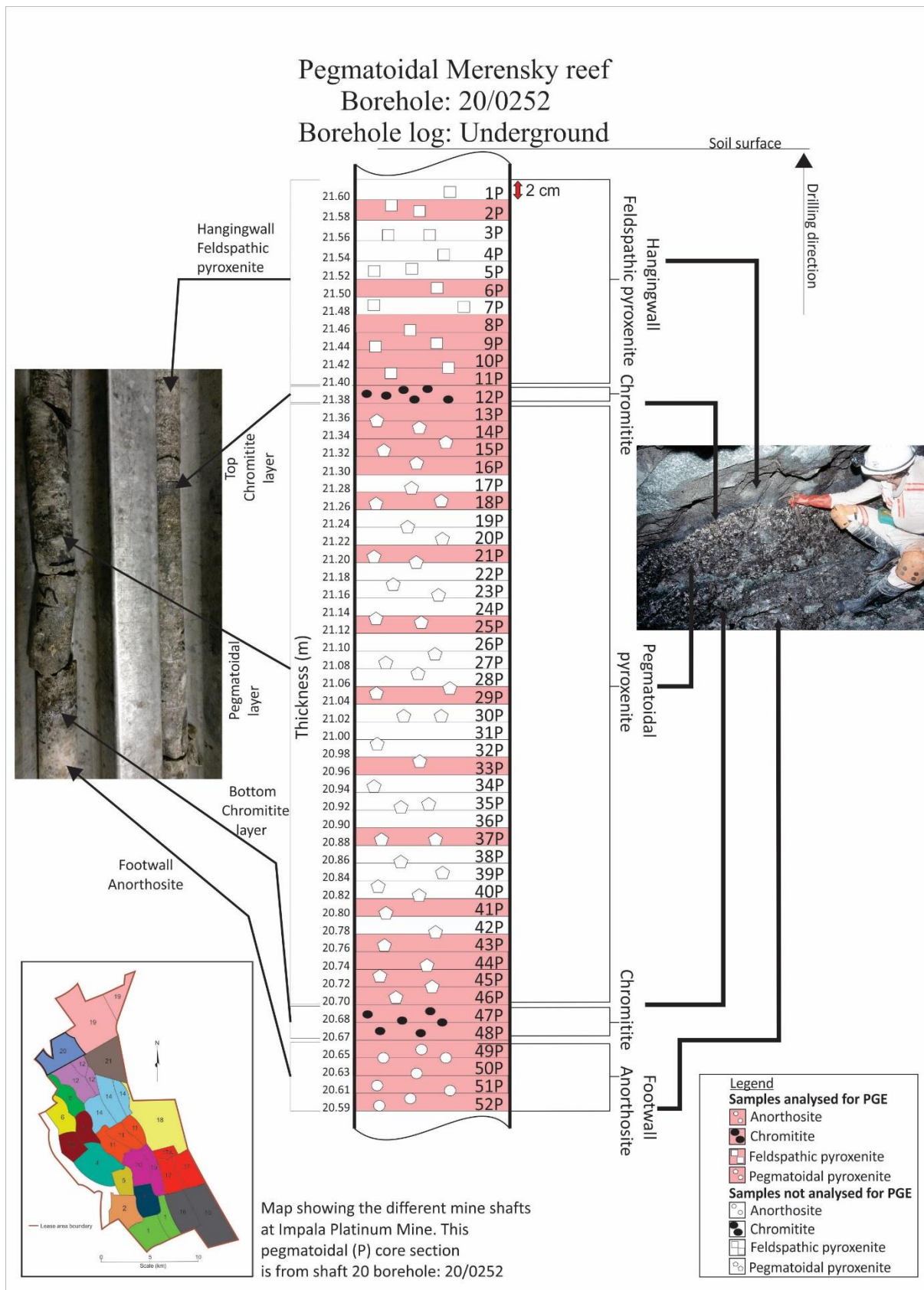


**Figure 2.5: Core log of borehole 20/0252 pegmatoidal Merensky reef indicating the different lithologies, drilling direction, samples analysed for PGE, depth of the core section and the location.**

## **2.2 Sample preparation**

In this study the core was sampled continuously and the length of each core section was restricted to availability of the borehole. Each core set was cut using a diamond saw into 2cm intervals parallel to the chromitite stringer and used for analysis. Details on each core set, are listed in appendix A (Table A.1). Figure 2.3 – 2.5 show each core sample, the location, the depth, the drilling direction, the lithologies and the different lithologies as well as the samples analysed. To ensure an even distribution of sample data along the length of the core, a sample was selected every 6 cm for PGE analysis in the footwall and hangingwall. Data was concentrated around the chromitite layers which are believed to be the more economically mineralized part, and every 2 cm, for about 6 cm was analysed. The selected pieces were then prepared for analysis. Preparation involved thin sections, fusion discs and powder material to be used for various analytical methods. All samples were analysed for major and trace element data.

### **2.2.1 Preparation of thin sections**

A total of 46 polished thin sections were prepared, from the different core sets for petrographic examination using transmitted and reflected light. A particular problem with polishing the thin sections was the loss of some of the grains. For example, pyroxene grains with well-developed cleavage, were easily lost during polishing.

### **2.2.2 Preparation of fusion discs**

Each 2 cm piece was initially reduced in a plastic bag with a hammer and then further reduced to a powder in an agate ring mill. Fusion discs were prepared at the Council for Geoscience. H<sub>2</sub>O<sup>-</sup> and L.O.I. were determined gravimetrically at 100 °C and 1000°C, respectively. Fusion discs were prepared by weighing off ± 1 g of sample and ± 10 g of flux. Claisse pure grade C-0620-60 flux was used to prepare the glass discs and it consists of 49.75% Li<sub>2</sub>B<sub>4</sub>O<sub>7</sub>, 49.75% LiBO<sub>2</sub> and 0.50% LiBr. The certified reference materials and the blank were prepared in the same way. The certified reference materials used to calibrate the X-ray fluorescence spectrometer are listed in Appendix A (Table A.2).

### **2.2.3 Preparation for PGE analysis by NiS fire assay**

Each 2 cm piece was initially reduced in a plastic bag with a hammer and then further reduced to a powder in an agate ring mill. Analysis of crushed high purity silica showed that the external contribution of elements such as Cr, Ni, Co and PGE during crushing was negligible. Samples were then prepared for PGE analysis by nickel sulphide fire assay pre-concentration and tellurium co-precipitation as described in McDonald & Viljoen (2006) and Huber et al. (2001). International certified reference materials (WMG-1 and WPR-1) and a blank was prepared in the same manner.

### **2.2.4 Preparation for REE, traces and majors by ICP-MS/ ICP analysis**

Following crushing, 1 g of each sample was weighed and then heated in a muffle furnace at 900°C to release H<sub>2</sub>O, CO<sub>2</sub> and other volatiles present. The mass of the ignited residue was determined and the LOI calculated. In a Claisse BIS Pt-Rh crucible, 0.1 g of the ignited residue was weighed and mixed with 0.6 g of Li metaborate flux (Alfa Aesar Spectroflux 100B). 0.5 ml of a solution of 25% (weight/volume) lithium iodide (Alfa Aesar) was added that acts as a non-wetting agent. The mixture was fused over a propane burner in a Claisse Fluxy automated fusion system, which automatically pours the melt into beakers after fusion. The 250 ml Teflon beakers contained 20 ml of 10% HNO<sub>3</sub> and 30 ml of deionised water. The beakers were then placed on magnetic stirrers, so that all glass fragments were stirred until dissolved. After dissolution 1 ml of a 100 ppm Rh spike solution was added as an internal standard and made up to 100 ml with deionised water. Blanks were prepared in the same manner as above, but excluding the sample. The international certified reference materials (MRG-1, NIM-P and JB1) was prepared in the same way. Using the JY Horiba ULTIMA2 ICP-MS, the solutions were then analysed for SiO<sub>2</sub>, TiO<sub>2</sub>, Al<sub>2</sub>O<sub>3</sub>, Fe<sub>2</sub>O<sub>3</sub>, MnO, MgO, CaO, Na<sub>2</sub>O, K<sub>2</sub>O, P<sub>2</sub>O<sub>5</sub> (McDonald & Viljoen 2006).

REE, Ti, V, Cr, Mn, Co, Ni, Ga, Rb, Sr, Y, Zr, Nb, Ba, Hf, Ta, Th and U were determined using the same solution, except that the initial rock solution was diluted 10 times with 2% HNO<sub>3</sub> and spiked with 5 ppb of In and Tl internal standards (McDonald & Viljoen, 2006).

### **2.2.5 Preparation for sulphur analysis**

Approximately 0.2 g of milled sample was weighed of and sent to the Council for Geoscience, South Africa, for sulphur analysis. No further preparation was necessary and

samples were directly analysed on an Eltra CS 800 double dual range carbon-sulphur analyser.

## 2.3 Analytical procedures

### 2.3.1 Petrography

Petrographic examination was aimed at differentiating between phases, identification of textures and structures and for determination of the modal mineralogical compositions of samples (Nesse, 2004). The modal mineralogy was determined by point counting 1000 points per thin section using a mechanical stage. Minerals observed microscopically but not encountered during point counting were assigned concentrations of less than 0.5% by volume. Characteristics of the microscope used at the University of the Free State are listed in Table 2.1.

**Table 2.1: Specifications of the microscope used in the study at the University of the Free State. Reflected and transmitted light was used to identify different mineral phases and to identify the best areas of interest for further quantitative analytical methods.**

Microscope: UFS	
<b>Model</b>	Reflective and transmitted light microscope: Olympus BX51 Camera used for pictures: Altra 20 soft imaging system Software: Analysis imager
<b>Analyse</b>	Differentiate between phases and to identify areas of interest for SEM and EMPA
<b>Sample preparation</b>	Polished thin sections
<b>Magnification</b>	2x, 4x, 10x, 20x magnification objective lenses

### 2.3.2 Scanning electron microscopy (SEM)

SEM is a non-destructive, reasonably precise and accurate and relatively fast analytical technique with rapid data acquisition. For SEM work the thin sections were coated with a thin layer of carbon of  $\pm$  15-100 nm. This conducting layer is necessary to produce a high energy electron beam (10-50 keV), evenly over the sample (Reed, 2005) and to prevent charging. The electron beam excites an electron which in return produces a characteristic fingerprint set of X-rays for each element in a phase (Reed, 2005). The specifications and operating conditions of the instrument used at the University of the Free State are in Table 2.2.

**Table 2.2: Characteristics of the scanning electron microscope (SEM). Energy dispersive X-ray spectrometry (EDS-SEM) was used to identify areas of interest and mineral phases for further quantitative analysis with the electron microprobe (EMPA).**

SEM: UFS	
<b>Model</b>	JOEL JSM 6610 Scanning Electron Microscope
<b>Analyse</b>	Qualitative analysis and quantitative identification of phases
<b>Detectors</b>	Thermo Scientific Ultra dry EDS spectrometer
<b>Data format</b>	Spot analysis, element and composition maps
<b>Acc. Voltage</b>	20 kV
<b>Probe current</b>	20 nA/ variable
<b>Beam size</b>	1 µm/ variable
<b>Sample preparation</b>	Polished thin sections with a carbon coating

### 2.3.3 Electron microprobe analysis (EMPA)

EMPA has high spatial resolution and sensitivity. EMPA is a fast, non-destructive, in-situ analytical method with rapid data acquisition. Thin sections were coated with a layer of carbon-coating to ensure a high energy electron beam evenly over the sample. Characteristic X-rays are detected at particular wavelengths and the intensities are measured to determine the concentrations (Reed, 2005). The outline of the EMPA work done at Rhodes University, Department of Geology is summarized in Table 2.3.

**Table 2.3: Outline and characteristics of the electron microprobe (EMPA). Quantitative wavelength dispersive X-ray spectrometry was used to quantify phases and to determine concentrations of elements in the different phases.**

EMPA: Rhodes University	
<b>Model</b>	Jeol JXA 8230 Superprobe
<b>Analyse</b>	Quantitative analysis on plagioclase, pyroxene, chromite, mica, sulphide
<b>Analysers</b>	4 WD spectrometers
<b>Data format</b>	Spot analysis
<b>Acc. Voltage</b>	15 kV
<b>Probe current</b>	20 nA
<b>Beam size</b>	<1 micron
<b>Correction method</b>	ZAF matrix correction method was employed for quantification
<b>Sample preparation</b>	Polished thin sections covered with carbon coating
<b>Detection limit</b>	100 ppm (depends on conditions and element)
<b>Detectors</b>	Scintillation detector

One of the biggest problems to compensate for are surface imperfections. During sample preparation special care need to be taken when polishing the thin section so that irregular surfaces can be avoided. Irregular surface topographies play a big role in getting good quality data. Natural standards were used for data quantification. The various standards employed for

the different oxides in the EMPA are described in Appendix A (Table A.3, A.4 and A.5). The various crystals used in the EMPA analysis are described in Appendix A (Table A.6).

### 2.3.4 X-ray fluorescence spectrometry (XRF)

XRF is used to identify and determine the bulk composition of for example a rock. XRF does not destroy the material analysed, but it removes all spatial information. Analysis of elements by XRF is made possible by the behaviour of atoms when they interact with high energy primary X-ray photons. Electrons are then ejected in the form of photoelectrons. This causes a hole in the orbital, which is then filled with electrons from the outer orbitals to create a stable state. During the electron excitation or replacement, the energy is released due to decrease in the binding energy of the electron. This is known as fluorescence. The energy of the emitted fluorescence photons is determined by the difference in energies between the individual and final orbitals for the individual transitions. Wavelength is inversely proportional to the energies and is characteristic for each element (Willis et al, 2011). Fused glass beads are the preferred method to introduce oxide samples into the spectrometer for X-ray fluorescence (XRF), the reason being that during the fusion process, factors like heterogeneity, particle size and mineralogical effects are eliminated (Bernstein, 1962 and LeHouillier & Turmel, 1974). The outline of the XRF work done at the University of the Free State is listed below in Table 2.4.

**Table 2.4: Outline and characteristics of X-ray fluorescence spectrometry done at the University of the Free State. X-ray fluorescence was used to determine concentrations of major elements in whole rock samples.**

XRF : UFS	
<b>Model</b>	AxiosPANalytical W-D XRF spectrometer
<b>Analyse</b>	Whole rock major elements
<b>Analysers</b>	Wavelength dispersive (WD) spectrometer
<b>Software</b>	Super Q software V.4.
<b>Acc. Voltage</b>	60 kV
<b>Probe current</b>	66 mA
<b>Tube</b>	Rh-tube
<b>Power level</b>	4 kV
<b>Sample preparation</b>	Fusion discs prepared by the Council for Geoscience
<b>Detection limit</b>	1 ppm
<b>Detectors</b>	Flow count and duplex detectors

One of the biggest problems encountered was during the preparation of the fusion discs. Non-homogeneous dissolution cannot be rectified by mathematical corrections (Bernstein, 1961; Bernstein, 1962, LeHouillier & Turmel, 1974; Vrebos & Helsen, 1983 and Gunn, 1960). So

care should be taken when deciding on the flux and during dissolution to ensure a homogeneous solution. The various crystals used in the X-ray fluorescence (XRF) spectrometer to measure the different whole rock major elements are described in Appendix A (Table A.7).

### 2.3.5 Inductively coupled plasma mass spectrometry (ICP-MS)

ICP-MS is a multi-element technique with excellent detection limits. An ICP plasma source is used to dissociate the sample into its atom or ion constituents. In the case of ICP-OES the light emitted by the ions are detected but with the ICP-MS the ions themselves are detected. The ions are passed through the mass spectrometer after they have been extracted from the plasma. In the mass spectrometer the ions are separated based on their atomic-mass-to-charge ratio by a quadrupole or magnetic sector analyser. The amount of ions produced and the low backgrounds gives the best detection limits available, usually in the parts-per-trillion range. (Gross, 2011). Typical limits of detection can be seen in McDonald & Viljoen, (2006). The instrumental parameters for the ICP-MS work done at Cardiff University are listed below in Table 2.6 for trace elements analysis and PGE analysis

**Table 2.5: Instrumental parameters for inductively coupled plasma mass spectrometry (ICP-MS). Quantitative ICP-MS was used to determine whole rock trace elements in core samples and platinum group elements in core samples.**

	<b>ICP-MS: Cardiff University</b>
<b>Model</b>	Thermoelemental X series (X7) ICP-MS
<b>Plasma gas</b>	Argon
<b>Forward power</b>	1200 W
<b>Nebuliser</b>	Meinhard with impact bead spray chamber
<b>Pump speed</b>	15 rev min <sup>-1</sup>
<b>Sample uptake</b>	~0.5 mL min <sup>-1</sup>
<b>Nebuliser gas flow rate</b>	0.95 L min <sup>-1</sup>
<b>Auxiliary gas flow rate</b>	0.7 L min <sup>-1</sup>
<b>Coolant gas flow rate</b>	13 L min <sup>-1</sup>
<b>Cones</b>	Nickel
<b>Lens parameters optimised to achieve</b>	>50 000 Hz/ppb for Rh <sup>103</sup> and In <sup>115</sup> and to achieve <1% CeO/Ce
<b>Analysis mode</b>	Peak jumping
<b>Dwell times (for trace elements)</b>	From 1 (for Ti and Mn) to 20 ms (for REE, Hf, Ta, Th and U)
<b>Dwell times (for PGE)</b>	20 ms for all PGE and Au isotopes

Calibrations were performed using solutions of the certified reference materials and a blank. The sample was spiked with 5 ppb In and Tl internal standards to correct for instrumental drift at high, medium and low masses respectively. After every 6<sup>th</sup> unknown sample the standard was also repeated for analysis to see if any instrumental drift occurred. Accuracy was

assessed by multiple analysis of the PGE reference materials and to check for instrumental drift.

### **2.3.6 Eltra carbon-sulphur analyser**

The Eltra carbon-sulphur analyser gives precise and quick measurements. The CS-800 is equipped with up to 4 independent infrared (IR) cells. This allows for simultaneous analysis at various concentrations (high and low sulphur concentrations) in one measurement. Sulphur dioxide ( $\text{SO}_2$ ) is formed when the sample is melted during exposure to pure oxygen gas. For purification the combustion gasses pass through a dust filter and a moisture absorber. The sulphur is then detected in infrared cells. After the sulphur measurement, oxidation of sulphur dioxide ( $\text{SO}_2$ ) to sulphur trioxide ( $\text{SO}_3$ ) takes place. The sulphur trioxide ( $\text{SO}_3$ ) is then removed with cellulose wool (Jordaan & Maritz, 2010). The instrumental parameters for the Eltra carbon-sulphur work done at the Council for Geosciences, South Africa, is listed below in Table 2.7.

**Table 2.6: Instrumental parameters for the Eltra carbon-sulphur analyser. The quantitative Eltra analyser was used to determine sulphur (S) in the various core samples.**

	<b>Eltra carbon-sulphur analyser: Council for Geoscience</b>
<b>Model</b>	Eltra CS 800 double dual range C-S analyser
<b>Balance</b>	Sartorius CP 64
<b>Detection limits for C and S</b>	0.017 g and 0.009 per 100g respectively
<b>Stability</b>	Monitored using the CGS laboratory in-house soil reference standards
<b>Furnace</b>	Induction furnace, above 2000°C
<b>Detection method</b>	Solid state infrared absorption
<b>Gas required oxygen supply</b>	Air liquid cylinder 3.5 purity
<b>Nitrogen supply</b>	Air liquid cylinder 5.0 purity
<b>Oxygen pressure</b>	2 - 4 bar
<b>Nitrogen pressure</b>	4 - 6 bar
<b>Oxygen flow rate</b>	180 l/h

Detection limits were obtained by repeat analysis of the blank samples. The instrument was calibrated using the standards listed in appendix A (Table A.8). CGS, in-house laboratory soil reference standards, was used to monitor the stability of the instrument.

## Chapter 3: Results

### 3.1. Petrography

Detailed petrographic descriptions of the Merensky reef in the Western limb have been presented by several researchers working at different mines: Impala Platinum Mine (Leeb-du Toit, 1986; Barnes & Maier, 2002a; Cawthorn & Boerst, 2006a; Cawthorn, 2002a and Cawthorn, 2010b); Rustenburg Platinum Mine (Viljoen & Hieber, 1986; Cawthorn, 2010b). In this project the international standard nomenclature (IUGS) was used to name and classify the different lithologies. The term feldspathic pyroxenite is used when no pegmatoidal textures are present and the grain size is (<20 mm) and pegmatoidal is used when the grain size exceeds 20 mm. In local mining terminology the term pegmatoidal is referred to as pegmatitic pyroxenite. In this section the value indicated below the scale bar indicate the length of the entire scale bar and not the length of the subdivisions.

#### 3.1.1 Borehole SD14/90

The first set of non-pegmatoidal Merensky reef core (NP) (shaft 14, borehole SD14/90) studied, corresponds to the normal Merensky ‘A’ type reef using the nomenclature of Leeb-du Toit (1986). Reef lithologies observed are melanorite, chromitite and anorthosite (See figure 2.3 for a detailed core log description of borehole SD14/90).

The top 8 cm of the core consists of medium grained feldspathic pyroxenite. Subhedral to anhedral orthopyroxene crystals (~65%) are densely packed and is the principle phase. Some of the orthopyroxene are interpenetrating (indented) on faces orientated at a high angle to the vertical (Fig. 3.1.1a), with parallel extinction. Orthopyroxene displays an abundance of narrowly spaced exsolution lamellae of clinopyroxene. In some cases the exsolution lamellae are thickened. Plagioclase (~25%) occurs as an intercumulus phase and exhibits undulose extinction and some show compositional zoning. Wedge shaped deformation twins and lamellar twinning are visible (Fig.3.1.1b). Clinopyroxene (~1%) forms anhedral grains that are included as minor inclusions in the orthopyroxene. Anhedral phlogopite (~4%) showing white to light greenish brown pleochroism are interstitial to pyroxene and is distinguished from the occasional biotite showing light brown to darker brown pleochroism occurring in certain sections. The sulphide phases present consist of intergrowths of phases like pyrrhotite, pentlandite and chalcopyrite (Fig. 3.1.2a). These sulphides occur interstitially to the cumulus phases. Larger sulphide grains ( $\pm 1.49$  mm) occur above the chromitite contact (Fig. 3.1.2.a),

with a decrease in size closer to the contact (Fig. 3.1.2.b). The contact with the underlying chromitite is sharp. The degree of alteration appears to increase towards the chromitite layer.

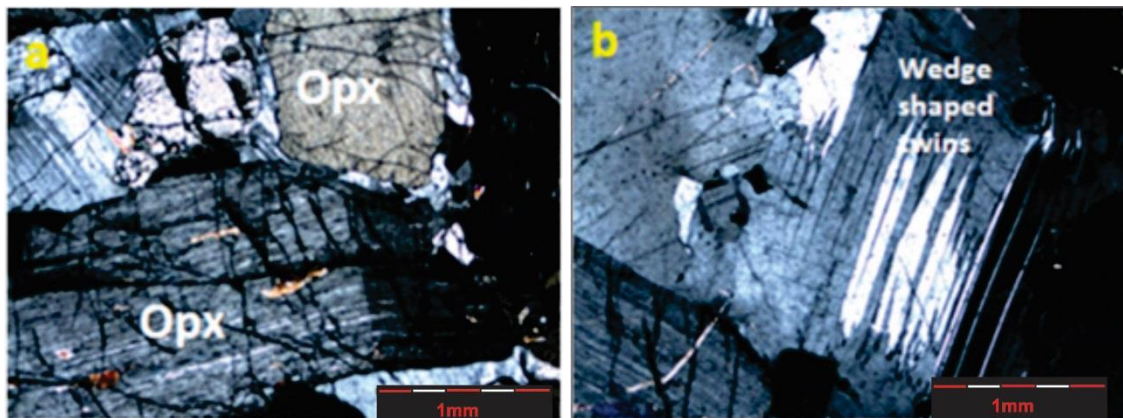


**Figure 3.1.1:** Photomicrographs of the rocks from the hangingwall (feldspathic pyroxenite) of borehole SD14/90. (a) Photomicrograph of orthopyroxene interpenetrating on faces orientated at a high angle to the vertical under cross-polarized light. (b) Intercumulus plagioclase showing wedge shaped deformation twins under cross-polarized light. Opx, orthopyroxene; Cpx, clinopyroxene. Scale bars indicate 0.2 mm divisions.

The feldspathic pyroxenite is underlain by an inclined thin chromitite layer ( $\pm 2.5$  cm) of irregular thickness. The chromitite consists of ~65% modal chromite which ranges in shape from cubic to amoeboidal. The chromite is poikilitically enclosed by plagioclase. Plagioclase (~25%) in the chromitite layer occurs as an intercumulus phase. The anhedral to subhedral plagioclase shows wedge shaped twins (Fig. 3.1.3a) with lamellar twinning and in some cases undulose extinction. Phlogopite occurs interspersed with the chromite (Fig. 3.1.3b) and plagioclase. Anhedral orthopyroxene (~5%) occurs as patches between the chromite. Sulphides ( $\pm 0.46$  mm) are visible throughout the thin section, with a decrease towards the lower contact, between the chromitite and the anorthosite. In some of the chromite, sulphide droplets are preserved that have the same shape as the enclosing chromite crystals (Fig. 3.1.3c,d) in which they are found (Holwell et al., 2011 and McDonald and Holwell, 2011).

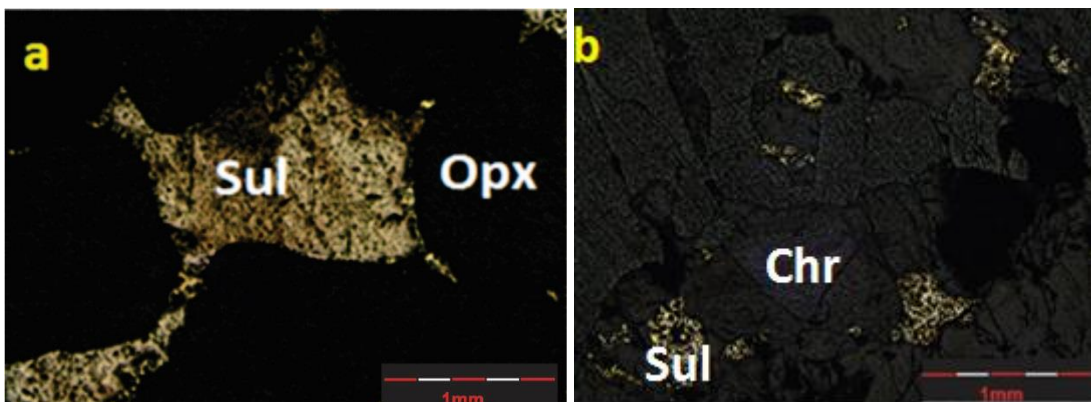


**Figure 3.1.2:** Photomicrographs of the rocks from the chromitite layer of borehole SD14/90. (a) Large sulphide grains that show intergrowth of pyrrhotite and chalcopyrite (photomicrographs under reflected light). (b) Decrease in the sulphide grain size closer to the chromitite contact (photomicrograph under reflected light). Chr, chromite; Opx, orthopyroxene; Sul, sulphide. Scale bars indicate 0.2 mm divisions.

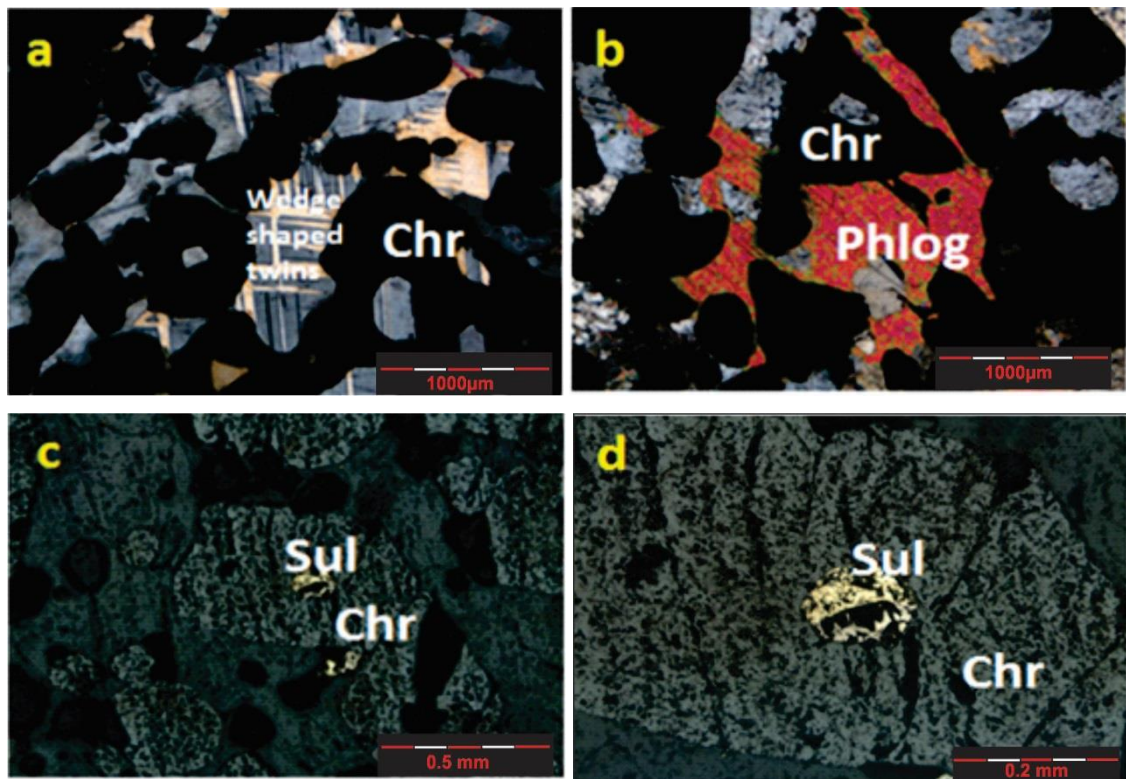


**Figure 3.1.3: Photomicrographs of the rocks from the chromitite layer of borehole SD14/90.**  
**(a)** Intercumulus plagioclase in the chromitite layer showing wedge shaped twins, (photomicrograph under cross-polarized light). **(b)** Phlogopite interspersed between chromite in the chromitite layer (photomicrograph under cross-polarized light). **(c,d)** Sulphide grain visible in a chromite grain that displays a negative crystal shape imposed by the crystal structure of the host chromite (photomicrographs under reflected light). Chr, chromite; Sul, sulphide; Phlog, phlogopite.

The chromitite layer is underlain by a layer of medium grained anorthosite. The plagioclase (~90%) has a cumulus texture of subhedral to lath-shaped crystals (Fig. 3.1.4a). The long axes of the plagioclase define a preferred orientation that is parallel with the contact of the chromitite layer. Most of the plagioclase grains show simple to lamellar twinning and only a few show zoning and spindle-shape twinning. Anhedral phlogopite showing colourless to light brown pleochroism occur interstitial to the plagioclase. Amphibole also occur as patches throughout the section. Anhedral orthopyroxene occur towards the base of the anorthosite layer. Sulphide phases occur between the plagioclase laths and some are poikilitically enclosed by the plagioclase (Fig. 3.1.4b). The observed lithologies in this core compares well with observations presented by Barnes & Maier (2002a) and Kruger & Marsh (1985).

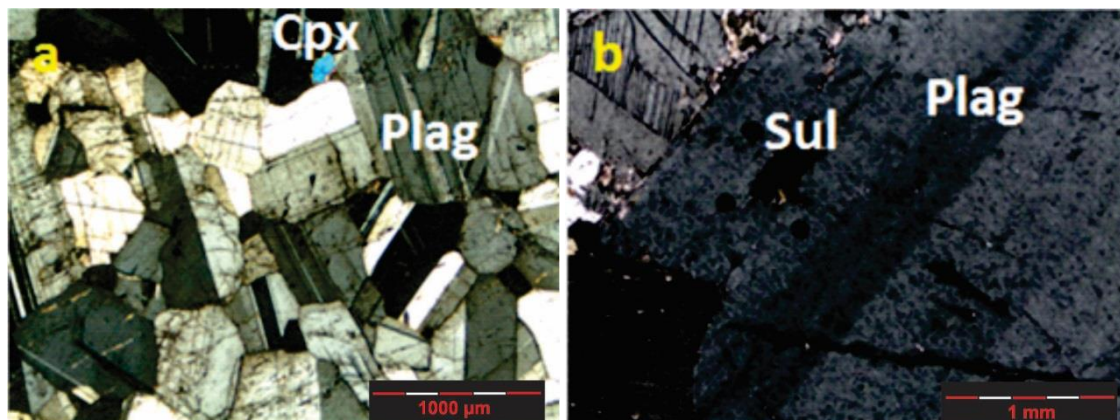


**Figure 3.1.4:** Photomicrographs of the rocks from the footwall (anorthosite) of borehole SD14/90. (a) The plagioclase in the footwall shows subhedral to lath shaped crystals (photomicrograph under cross-polarized light). (b) Some of the sulphide grains are poikilitically enclosed by plagioclase (photomicrograph under cross-polarized light). Cpx, clinopyroxene; Plag, plagioclase; Sul, sulphide. Scale bars indicate 0.2 mm divisions.

The average modal mineral proportions of the hanging wall, chromitite layer and the footwall of borehole SD14/90 are listed in Figure 3.1.5. The modal mineral proportion of each thin section of borehole SD14/90 are listed in Appendix B.

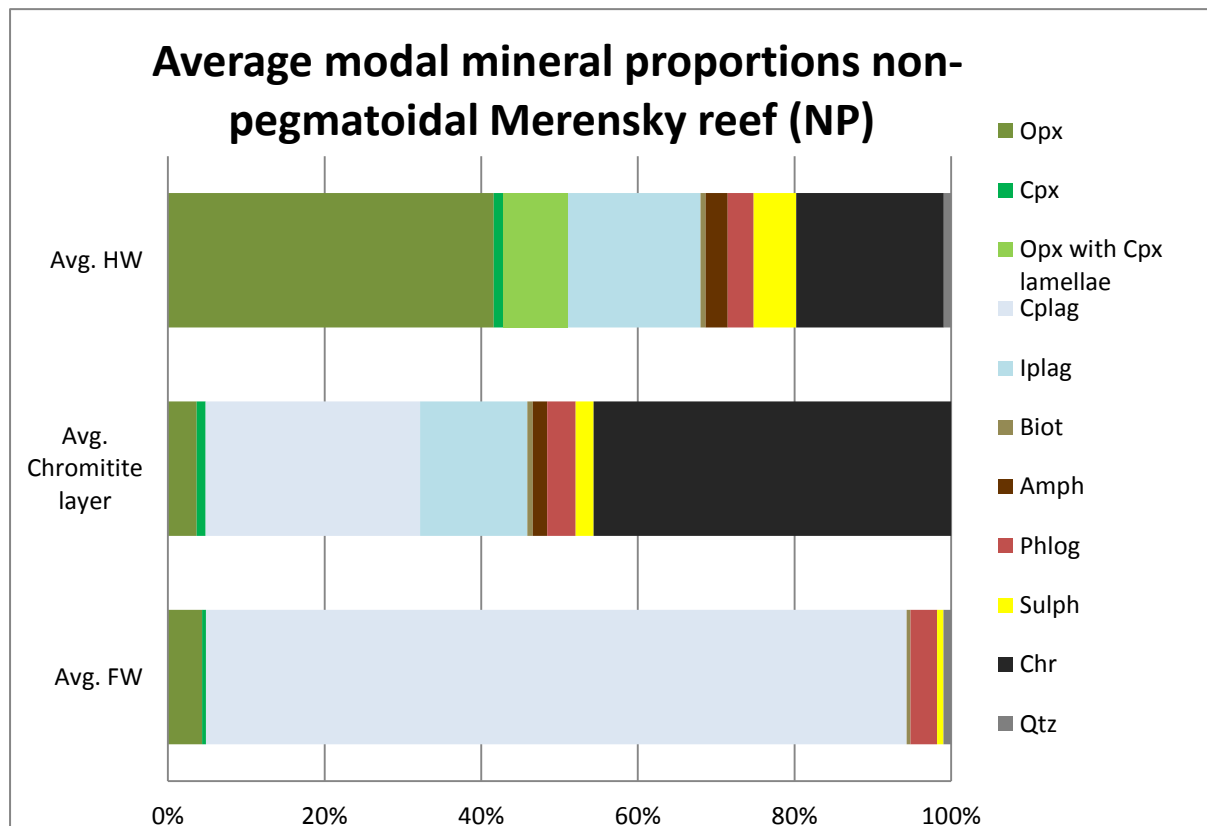


**Figure 3.1.5:** The average modal mineralogical composition of the hangingwall, chromitite layer and the footwall of the non-pegmatoidal Merensky reef (NP) borehole SD14/90. Opx, orthopyroxene; Cpx, clinopyroxene; Cplag, cumulus plagioclase; iplag, intercumulus plagioclase; Biot, biotite; musc, muscovite; amph, amphibole; phlog, phlogopite; sulph, sulphide, Chr, chromite, Qtz, quartz.

### **3.1.2 Borehole BH6259**

The second set of non-pegmatoidal Merensky reef (N) core studied (near shaft 14, borehole: BH6259) also corresponds to the normal Merensky ‘A’ type reef using the nomenclature of Leeb-du Toit, (1986). Reef lithologies observed are feldspathic pyroxenite, chromitite and anorthosite (See figure 2.4 for a detailed core log description of borehole: BH6259).

The top 50 cm of the core consists of medium grained feldspathic pyroxenite. Densely packed anhedral orthopyroxene (70-80%) is the principle phase. Some of the orthopyroxene displays an abundance of narrowly spaced exsolution lamellae of clinopyroxene. Further down in the section the orthopyroxene at some stages tend to be more subhedral than anhedral and closer to the chromitite contact the orthopyroxene tend to be more anhedral. Some subhedral to euhedral orthopyroxene is poikilitically enclosed by plagioclase (Fig. 3.1.6a) and some are poikilitically enclosed by clinopyroxene. Anhedral clinopyroxene (1-5%) is more abundant towards the top of the core. Quartz (2%) in some cases are enclosed in biotite and the biotite occur interstitial to the orthopyroxene (Fig. 3.1.6b). Plagioclase (10-20%) occurs as an intercumulus phase. Wedge-shaped deformation twins and lamellar twinning are visible. Towards the middle of the feldspathic pyroxenite section the plagioclase abundance increases and crystals tend to show cumulus shapes rather than intercumulus shapes. In some cases the plagioclase exhibits undulose extinction and compositional twinning. Towards the lower chromitite contact, a euhedral cumulus plagioclase (showing zoning) occurs within interstitial tridymite (biaxial positive) (Fig. 3.1.6c).

At the top of the feldspathic pyroxenite section fine-grained, mosaic, plagioclase are interspersed between the orthopyroxene (Fig 3.1.6d). Phlogopite (1-3%) showing colourless to light brown-green pleochroism are interstitial to orthopyroxene and plagioclase. Large phlogopite crystals show symplectitic structures at the end with sulphides interspersed between the phlogopite (Fig. 3.1.6e, 3.1.6f). In the middle of the feldspathic pyroxenite section phlogopite occurs as an internetwork (Fig. 3.1.7a). Small amounts of amphibole and biotite, showing light brown to dark brown pleochroism is present. The sulphide phases present consist of intergrowths of pyrrhotite, pentlandite and chalcopyrite. These sulphides occur interstitially to the cumulus phases. Larger sulphide grains ( $\pm 1.49$  mm) occur above the chromitite contact, with a decrease in size closer to the contact.

The contact with the underlying chromitite is sharp. The degree of alteration appears to increase towards the chromitite layer. The chromitite layer consists of  $\pm 55\%$  modal chromite, which ranges in shape from cubic to amoeboidal. In one of the chromite grains, a

sulphide droplet is preserved that have the same shape as the chromites (Fig. 3.1.7 b & c) in which they are found (Holwell et al., 2011). Plagioclase ( $\pm$  35%) in the chromitite layer occurs as an intercumulus phase (Fig. 3.1.7d).

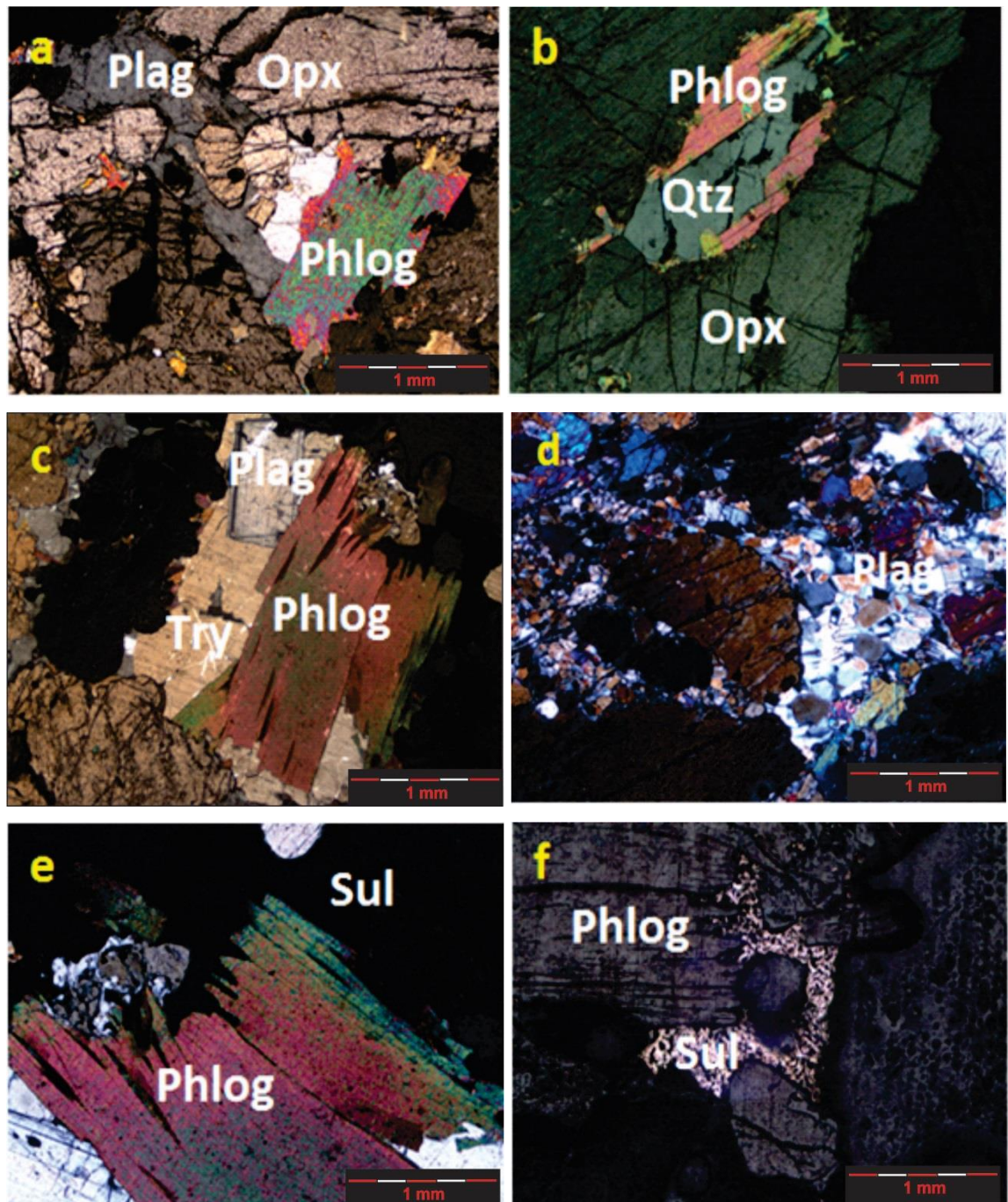


**Figure 3.1.6:** Photomicrographs of the rocks from the hangingwall (Feldspathic pyroxenite) of borehole BH6259 (a) Subhedral to euhedral orthopyroxene are poikilitically enclosed in plagioclase (photomicrograph under cross-polarized light). (b) Quartz enclosed in phlogopite which occurs interspersed between orthopyroxene (photomicrograph under cross-polarised light). (c) Euhedral cumulus plagioclase with interstitial quartz (photomicrograph under cross-polarised light). (d) Fine grained mosaic plagioclase occurs at the top of the melanorite section (photomicrograph under cross-polarised light) (Note the variation in texture of plagioclase through the melanorite section). (e) Phlogopite showing symplectitic structures in contact with sulphide (photomicrograph under cross-polarised light). (f) Phlogopite showing symplectitic structures in contact with sulphide, (photomicrograph under reflected light). Opx, orthopyroxene; Plag, plagioclase; Sul, sulphide; Phlog, phlogopite; Try, tridymite; Qtz, quartz. Scale bars indicate 0.2 mm divisions.

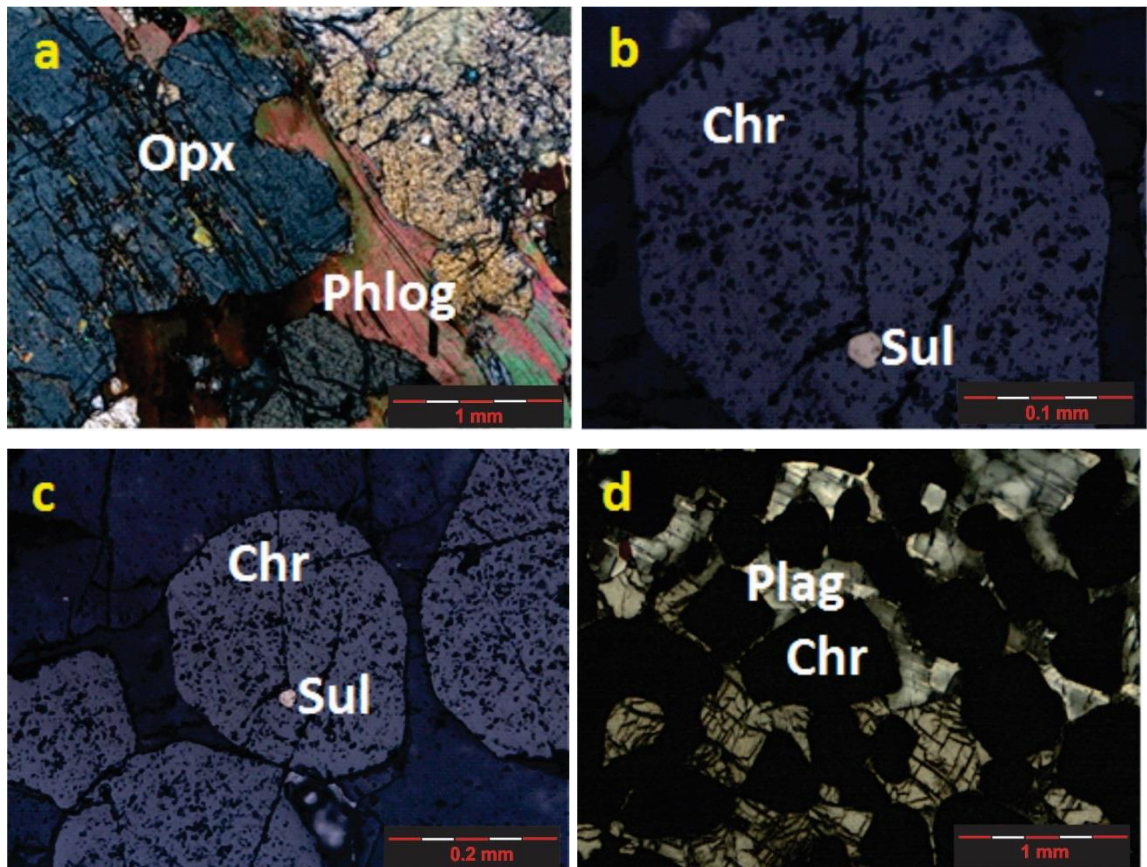


**Figure 3.1.7: Photomicrographs of the rocks from the hangingwall (feldspathic pyroxenite) through the chromitite layer of borehole BH6259.** (a) Phlogopite occurs as an internetwork in the middle of the melanorite section (photomicrograph under cross-polarised light). (b&c) Sulphide grain visible in a chromite grain that displays a negative crystal shape imposed by the crystal structure of the host chromite (photomicrographs under reflected light). (d) Intercumulus plagioclase occurs between the chromite in the chromitite layer (photomicrograph under cross-polarised light). Chr, chromite; Opx, orthopyroxene; Plag, plagioclase; Sul, sulphide; Phlog, phlogopite.

The chromitite is underlain by a layer of fine to medium grained anorthosite. The plagioclase (90-65%) has a cumulus texture of subhedral to anhedral lath shaped crystals (Fig. 3.1.8a). Most of the plagioclase grains show simple to lamellar twinning and only a few show zoning and spindle-shaped twinning. The amount of plagioclase in the anorthosite decreases and then it increases again towards the bottom of the anorthosite section. Orthopyroxene (10-25%) as an intercumulus phase occur in certain parts. Orthopyroxene crystals occur further down in the section, but decreases again towards the bottom. Clinopyroxene occurs interspersed between plagioclase towards the middle of the anorthosite section (Fig. 3.1.8b). Anhedral phlogopite showing colourless to brown-green pleochroism occur interspersed with the plagioclase and orthopyroxene. Fine grained sulphides are present. These sulphides occur interstitial to the plagioclase and orthopyroxene.

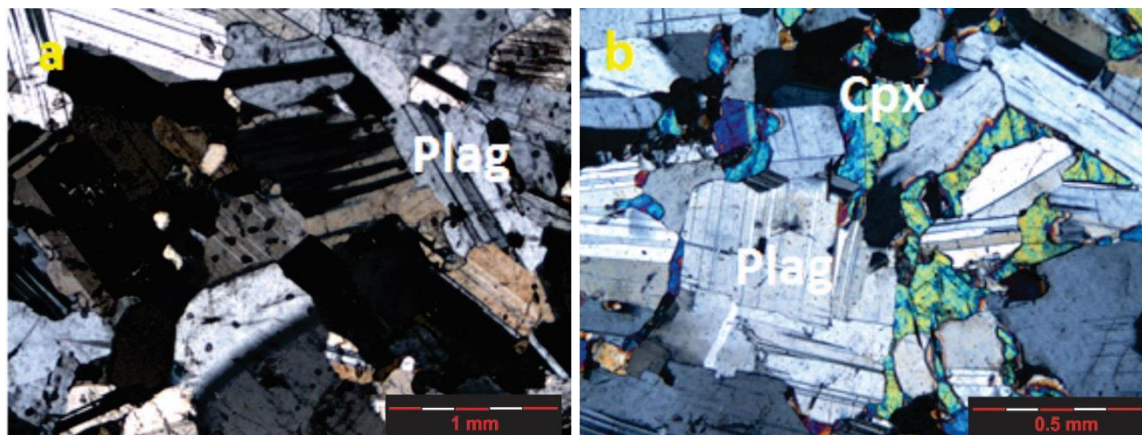


**Figure 3.1.8:** Photomicrographs of the rocks from the footwall (anorthosite) of borehole BH6259. (a) Tabular to lath shaped plagioclase.; (b) Tabular shaped plagioclase with clinopyroxene interspersed between the plagioclase, photomicrograph under cross-polarised light. Cpx, clinopyroxene; Plag, plagioclase.

The average modal mineralogical composition of the hanging wall, chromitite layer and the footwall of borehole BH6259 are listed in Figure 3.1.9. The modal mineralogical composition of each thin section of borehole BH6259 are given in Appendix B.

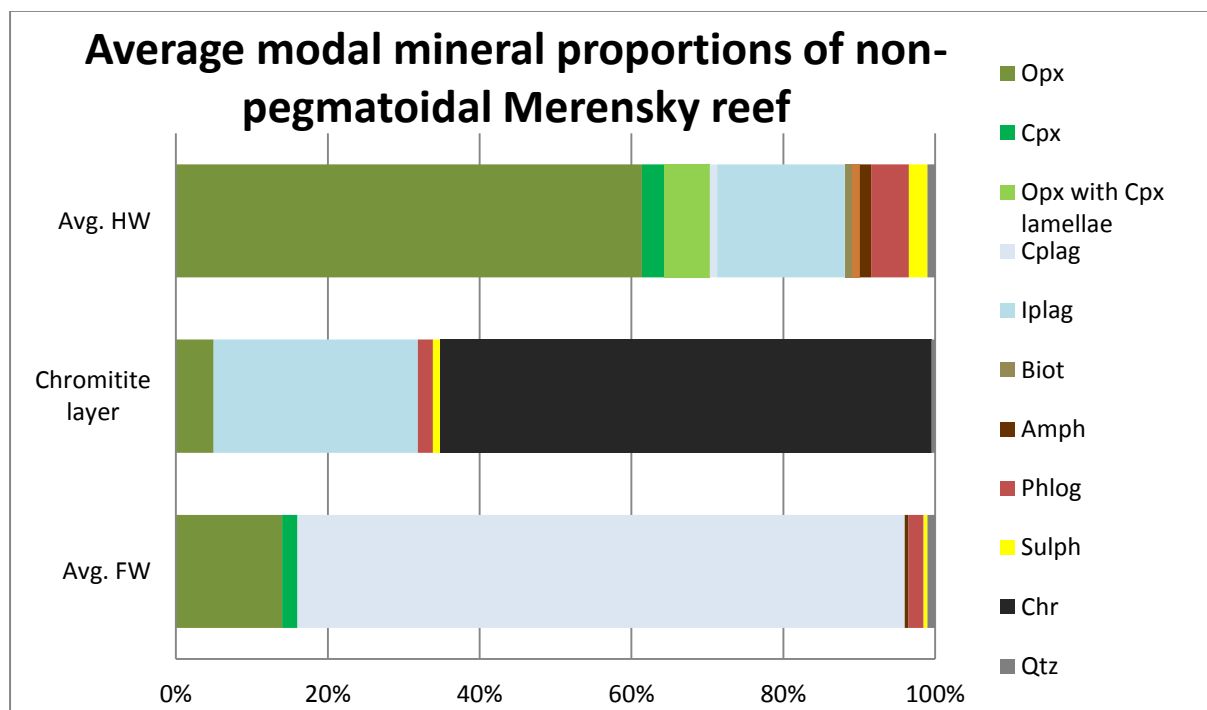


**Figure 3.1.9:** The average modal mineralogical composition of the hangingwall, chromitite layer and the footwall of the non-pegmatoidal Merensky reef (N) borehole BH6259. Opx, orthopyroxene; Cpx, clinopyroxene; Cplag, cumulus plagioclase; iplag, intercumulus plagioclase; Biot, biotite; musc, muscovite; amph, amphibole; phlog, phlogopite; sulph, sulphide; Chr, chromitite, Qtz, quartz.

### **3.1.3 Borehole 20/0252**

The third set of pegmatoidal Merensky reef (P) core studied (shaft 20 borehole 20/0252) also corresponds to the normal Merensky ‘B’ type reef using the nomenclature of Leeb-du Toit, (1986). Reef lithologies observed are feldspathic pyroxenite, pegmatoidal pyroxenite, chromitite and anorthosite (See Appendix A for detailed core log description of borehole 20/0252). The top 22 cm of the core consists of feldspathic pyroxenite. Medium grained (3-4 mm) subhedral orthopyroxene are densely packed and is the principle phase ~55%. Some of the orthopyroxene are interpenetrating on faces oriented at a high angle to the vertical (Fig. 3.1.10a). Orthopyroxene with narrowly spaced exsolution lamellae of clinopyroxene are visible (Fig. 3.1.10b). Veins of serpentine penetrating some of the orthopyroxene occurs throughout the thin sections (Fig. 3.10c). Orthopyroxene in contact with the serpentine veins seem to show alteration (Fig. 3.1.10c). The orthopyroxenes on the rims are altered to amphibole (antophyllite). Finer sulphide grains occur interspersed with the serpentine veins (Fig. 3.1.10d). Other sulphide phases present in the thin sections consists of intergrowths of four phases, chalcopyrite, pyrite, pentlandite and pyrrhotite. Intercumulus plagioclase (30%) are the second most common phase (Fig. 3.1.10a, b). Wedge shaped deformation twins are visible. Clinopyroxene is rare and occur as finer anhedral grains around the edges of orthopyroxene. In one section a large (5-6mm) clinopyroxene grain poikilitically include an orthopyroxene crystal (Fig. 3.1.10e). Small interstitial grains of phlogopite make up ~2% of the rock. Other interstitial to poikilitic minerals include chromite, biotite and talc. The contact with the underlying chromitite layer is gradational.

The thin upper chromitite layer of irregular thickness consists of ~55% chromite. In the thin section the modal mineralogy is different because part of the hangingwall is included in the thin section. Thus the modal mineralogy of chromite in the thin section decreases to 25%. The chromite shape ranges from round to amoeboidal with some grains up to 2 mm in diameter (Fig. 3.1.10f). Orthopyroxene makes up 10-15% of the rock. Orthopyroxene with narrowly spaced exsolution lamellae and a tricuspid shape are visible (Fig. 3.1.11a). Intercumulus plagioclase (3-5%) showing wedge shaped twinning occurs between the chromite (Fig 3.1.10f). Subhedral plagioclase (5%) occurs at the edges of the chromitite stringer. Finer sulphide phases are present in the thin sections. Clinopyroxene (15%) poikilitically include some of the chromite grains (Fig. 3.1.11b). Other interstitial to poikilitic minerals include phlogopite and sulphide.

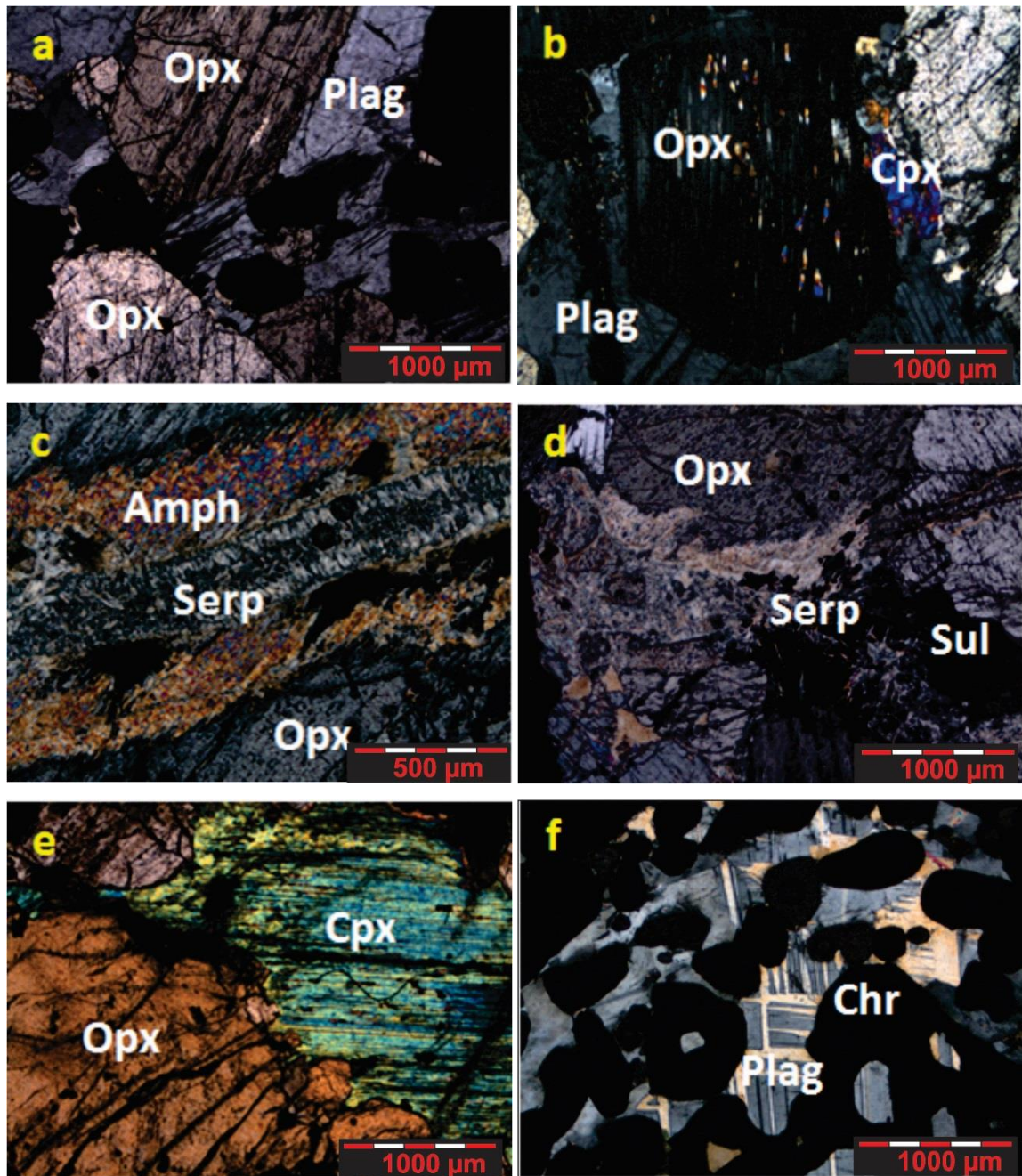
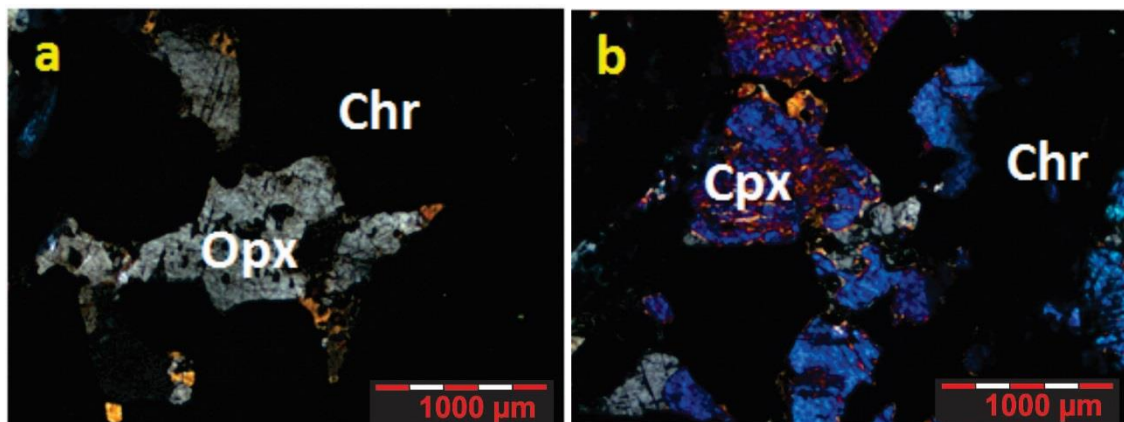


Figure 3.1.10: Photomicrographs of the rocks from the hangingwall (feldspathic pyroxenite) through the chromitite layer of borehole 20/0252. (a) Feldspathic pyroxenite overlying the upper chromitite; orthopyroxene interpenetrating on faces oriented at a high angle to the vertical, (photomicrograph under cross-polarised light). (b) Orthopyroxene with narrowly spaced exsolution lamellae, (photomicrograph under cross- polarized light). (c) Veins of serpentine penetrating orthopyroxene on the side, orthopyroxene showing alteration (photomicrograph under cross- polarized light). (d) Smaller sulphide grains interspersed in the serpentine veins, (photomicrograph under cross- polarized light). (e) A large clinopyroxene grain partially including orthopyroxene, (photomicrograph under cross- polarized light). (f) Chromite shape ranging from round to amoeboidal with intercumulus plagioclase showing wedge shaped twinning, (photomicrograph under cross-polarized light). Chr, chromite; Opx, orthopyroxene; Cpx, clinopyroxene; Plag, plagioclase; Sul, sulphide; Bt, biotite; Serp, serpentine.



**Figure 3.1.11:** Photomicrographs of the rocks from the top chromitite layer of borehole 20/0252. (a) Orthopyroxene with a tricuspid shape in the top chromitite layer, photomicrograph under cross-polarized light. (b) Clinopyroxene interspersed in the chromite layer, (photomicrograph under cross-polarized light). Chr, chromite; Opx, orthopyroxene; Cpx, clinopyroxene.

The top chromitite layer is underlain by a pegmatoidal layer (pegmatoidal pyroxenite). The pegmatoidal layer contains ~55% orthopyroxene, 20% plagioclase, ~10% clinopyroxene, ~5% chromite and ~2-5% sulphide, serpentine and talc. The orthopyroxenes form large phenocrysts (5-10 mm) with narrowly spaced exsolution lamellae of clinopyroxene (Fig. 3.1.12a). Some of the orthopyroxene are altered (Fig. 3.1.12b) to amphibole and poikilitically enclose some clinopyroxene grains. Plagioclase occur as both oikocrysts and intercumulus phases (Fig. 3.1.12c). The plagioclase oikocrysts (10 mm) have wedge shaped deformation twins and exhibit undulose extinction (Fig. 3.1.12c). Some of the orthopyroxene are partially enclosed in the plagioclase oikocrysts. Large veins of serpentine can be seen with smaller sulphides interspersed in the serpentine veins. Talc can be seen around the rims of the orthopyroxene near the contacts of the serpentine veins. Coarse grained clinopyroxene grains are visible (Fig. 3.1.12d). In some patches clinopyroxene grains are altered to amphibole and partially enclose some orthopyroxene. Anhedral phlogopite grains, showing colourless to light brown pleochroism, are interspersed with plagioclase, orthopyroxene and clinopyroxene (Fig. 3.1.12d). Larger sulphide grains consist of intergrowths of, chalcopyrite, pyrite, pentlandite and pyrrhotite. The pegmatoidal layer is underlain by a thin chromitite layer of irregular thickness that consists of 25% chromite (bottom chromitite layer). The chromite shape ranges from round to amoeboidal (Fig. 3.1.12e) with some grains up to 3 mm in diameter. The plagioclase in the chromitite layer takes the form of large oikocrysts up to 10 mm in size. These plagioclase oikocrysts (10-15%) have wedge shaped deformation twins and some are compositionally zoned (Fig. 3.1.12f). Orthopyroxene oikocrysts with narrowly spaced exsolution lamellae of clinopyroxene are visible. Some of the chromite are poikilitically enclosed in the plagioclase and orthopyroxene oikocrysts (Fig. 3.1.13a).

Anhedral sulphide grains occur interspersed between the chromite grains. Phlogopite are interspersed between the chromite grains (Fig. 3.1.12e). Clinopyroxene is rare.

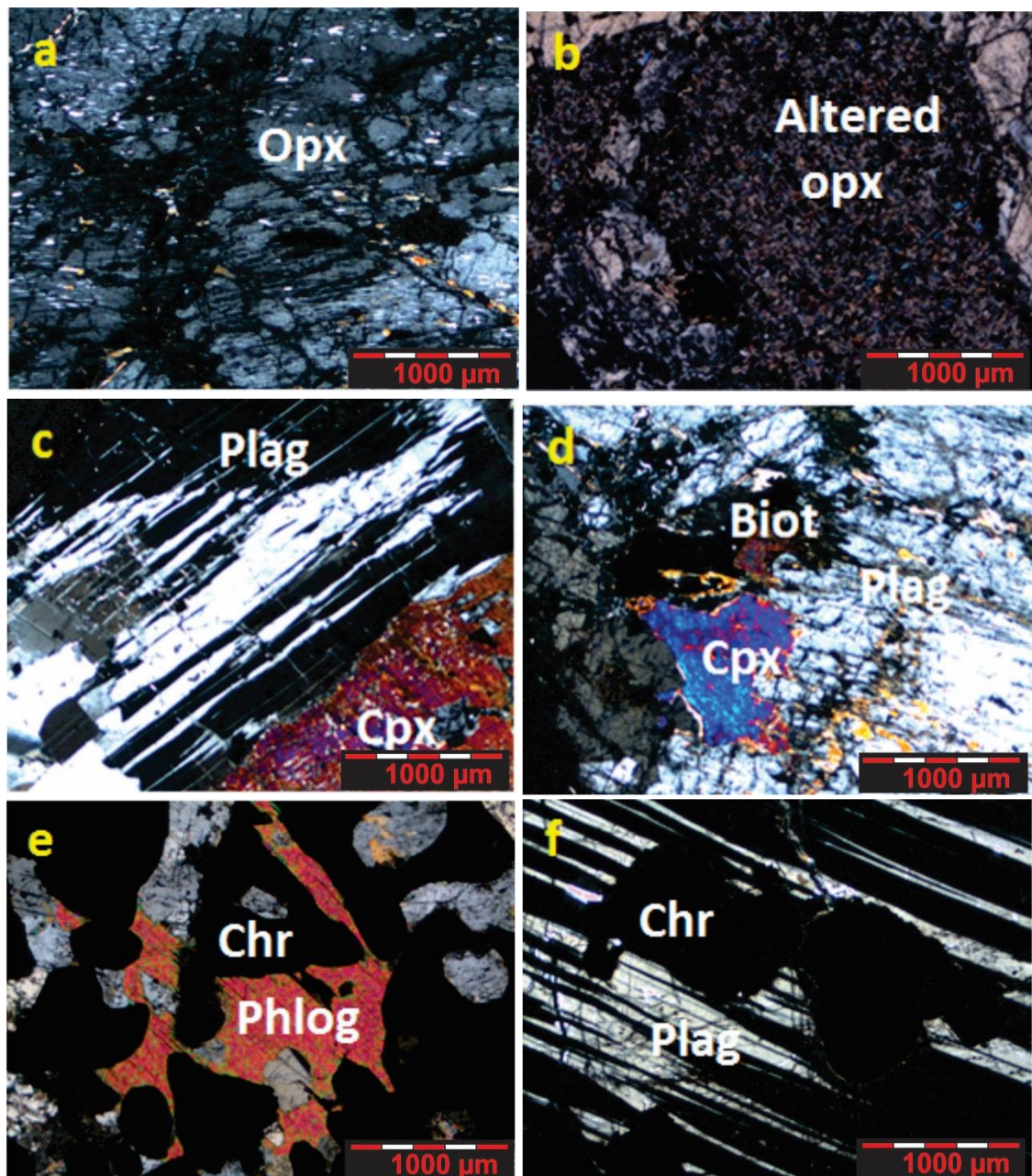
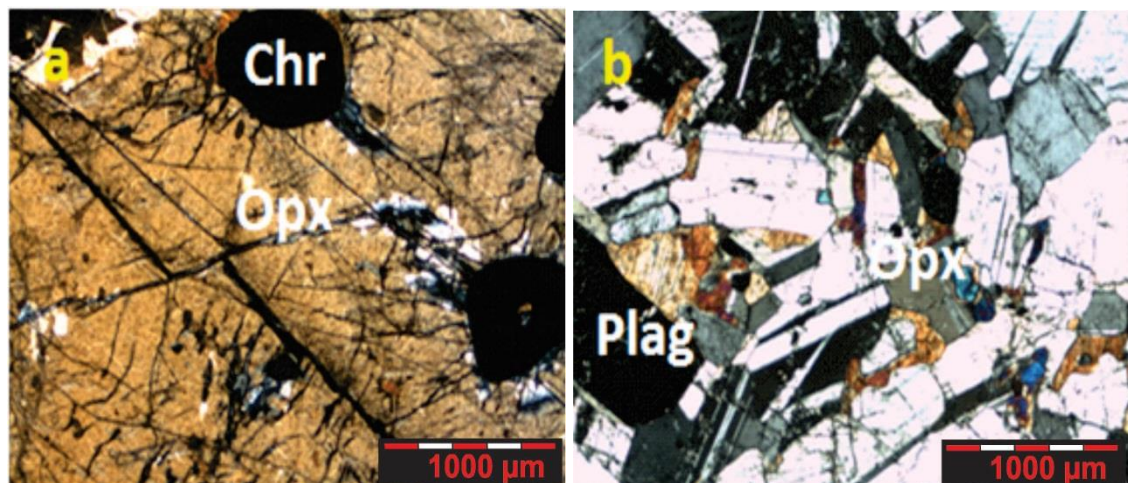


Figure 3.1.12: Photomicrographs of the rocks from the pegmatoidal layer through the bottom chromitite layer of borehole 20/0252. (a) Orthopyroxene forming large oikocrysts some with narrowly spaced exsolution lamellae, (photomicrograph under cross-polarized light). (b) Orthopyroxene altered to amphibole and serpentine, (photomicrograph under cross-polarized light). (c) Plagioclase oikocrysts showing wedge shaped deformation twins, (photomicrograph under cross-polarized light). (d) Biotite is interspersed between orthopyroxene and clinopyroxene, (photomicrograph under cross-polarized light). (e) Bottom chromitite stringer, chromite grains with shapes that ranges from round to amoeboidal and biotite interspersed between the chromite grains. (f) Plagioclase oikocrysts showing wedge shaped deformation twins and poikilitically including chromite, (photomicrograph under cross-polarized light).

The chromitite is underlain by a layer of fine to medium grained anorthosite. The contact between the chromitite and anorthosite is gradational. The plagioclase (90-65%) has a cumulus texture of subhedral to anhedral lath to tabular shaped crystals (Fig. 3.1.13b). Most of the plagioclase grains show simple to lamellar twinning and only a few show zoning and spindle-shaped twinning. Interstitial orthopyroxene (5-10%) and clinopyroxene are visible. The orthopyroxene grains have a tricuspid shape with concave inward boundaries. Sulphides and biotite are rare and typically very fine-grained.



**Figure 3.1.13: Photomicrographs of the rocks from the bottom chromitite layer through the footwall (anorthosite) of borehole 20/0252. (a) Showing orthopyroxene oikocrysts poikilitically including chromite grains, (photomicrograph under cross-polarized light). (b) Lath shaped plagioclase with clinopyroxene and orthopyroxene interspersed between the plagioclase grains, (photomicrograph under cross-polarized light). Chr, chromite; Opx, orthopyroxene; Cpx, clinopyroxene; Plag, plagioclase; Sul, sulphide; Bt, biotite.**

The average modal mineralogical composition of the hanging wall, top chromitite layer, the pegmatoidal layer, the bottom chromitite layer and the footwall of borehole 20/0252 are listed in Figure 3.1.14. In Appendix B the modal mineral proportion of each thin section of borehole 20/0252 is given.

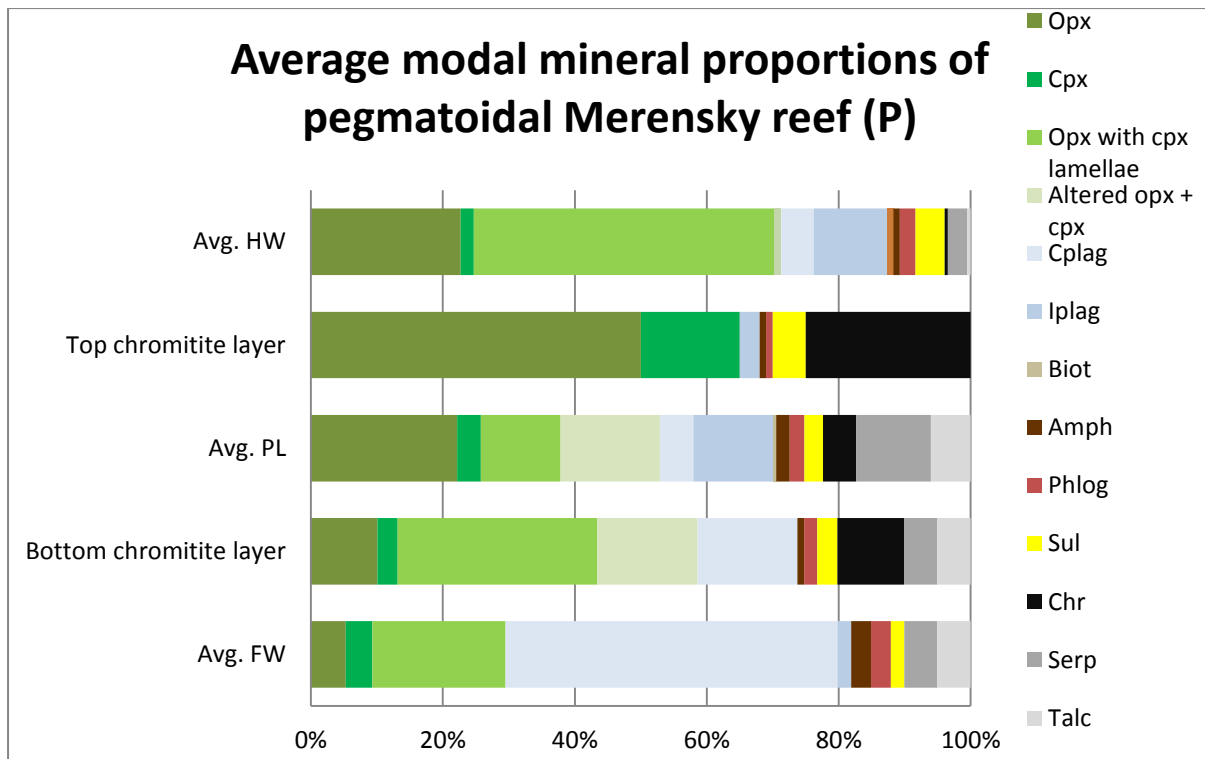


**Figure 3.1.14:** The average modal mineralogical compositions of the hangingwall, top chromitite layer, pegmatoidal layer, the bottom chromitite layer and the footwall of the pegmatoidal Merensky reef (P) borehole 20/0252. Opx, orthopyroxene; Cpx, clinopyroxene; Cplag, cumulus plagioclase; iplag, intercumulus plagioclase; Biot, biotite; musc, muscovite; amph, amphibole; phlog, phlogopite; sul, sulphide; Chr, chromitite. Avg. HW, average hanging wall; Avg. PL, average pegmatoidal layer; Avg. FW, average footwall.

## 3.2 Mineral chemistry

The chemical composition of the most important rock forming minerals was determined with a Jeol JXA 8230 Superprobe at Rhodes University. Representative analyses are given in Table 3.2.1-3.2.5. The remainder of the analytical data are given in Appendix C as well as the characteristic standards used for the analysis of the various oxides. En will be used to denote 100 x cationic ratio of Mg / (Mg + Fe<sup>2+</sup> +Ca) in pyroxene, An to denote 100 x cationic ratio of Ca / (Ca+Na+K) in plagioclase and Mg# to denote cationic ratio of Mg / (Mg +Fe<sup>2+</sup>). The Fe<sub>total</sub> is recalculated into Fe<sup>2+</sup> and Fe<sup>3+</sup> in an 80:20 ratio respectively.

### 3.2.1 Plagioclase

Plagioclase is the main component in anorthosite and is an interstitial mineral in feldspathic pyroxenite, chromitite layers and in the pegmatoidal pyroxenite. The composition of plagioclase in these units covers a range from labradorite to bytownite (Fig. 3.2.1). In

borehole SD14/90 (non-pegmatoidal Merensky reef) the anorthite values increase with depth. In the hangingwall the An% ranges from 56 – 69. In the chromitite layer the An% ranges between 67 – 79, with the highest average An% in the chromitite layer. In the footwall the An% ranges between 71 – 75 (Fig. 3.2.2a). See appendix C table C.5 for An% values. CaO is the highest in the footwall with an average of 15.98 %. Table 3.2.1 contains the average of each unit. Within sample variation expressed as standard deviation is indicated in Appendix C, table C.4.

**Table 3.2.1: Average plagioclase chemistry in the different lithologies of the various boreholes.  
Major element oxides given in wt%**

Sample name	Borehole SD14/90			Borehole BH6259			Borehole 20/0252			
	HW	Chr layer	FW	HW	Chr layer	FW	HW	Top chr layer	Pegmatoidal	FW
SiO <sub>2</sub>	52.84	48.96	50.01	52.76	48.75	49.62	52.75	50.03	50.65	50.10
TiO <sub>2</sub>	0.03	0.02	0.06	0.02	0.01	0.02	0.02	0.03	0.17	0.02
Al <sub>2</sub> O <sub>3</sub>	29.76	32.05	31.34	29.34	32.40	31.88	29.59	31.49	30.97	31.58
FeO	0.13	0.14	0.13	0.15	0.17	0.24	0.12	0.13	0.37	0.26
MnO	n.d.	0.01	0.02	n.d.	n.d.	n.d.	n.d.	n.d.	n.d.	n.d.
MgO	0.03	0.02	0.01	0.02	0.02	0.02	0.01	0.01	0.03	0.02
CaO	13.08	15.98	15.98	12.84	16.26	15.80	13.53	15.34	14.75	15.54
Na <sub>2</sub> O	4.35	2.69	2.73	4.40	2.49	2.74	4.25	3.06	3.31	2.95
K <sub>2</sub> O	0.12	0.06	0.03	0.17	0.03	0.09	0.08	0.11	0.15	0.10
BaO	0.02	0.02	0.03	0.02	0.02	0.02	0.01	0.04	0.01	0.01
SrO	0.01	0.02	0.02	n.d.	n.d.	n.d.	0.01	n.d.	n.d.	n.d.
Total	100.38	99.96	100.38	99.73	100.15	100.43	100.42	100.23	100.40	100.58
An%	62.11	76.42	73.65	61.26	78.21	75.77	62.78	73.06	70.76	74.00

In borehole BH6259 (non-pegmatoidal Merensky reef) the anorthite values increase with depth. In the hangingwall the An% ranges between 51 – 73. In the chromitite layer the An% ranges between 74 – 82, with the highest average An% recorded in the chromitite layer. In the footwall the An% ranges between 70 – 78 (Fig. 3.2.2b). See appendix C table C.7 for An % values. CaO is the highest in the chromitite layer with an average of 16.26%. Table 3.2.1 contains the average of each unit. Within sample variation expressed as standard deviation is indicated in Appendix C, table C.6.

In borehole 20/0252 (pegmatoidal Merensky reef) the anorthite values varies considerably with depth. In the hangingwall the An% ranges between 62 – 63. In the top chromitite layer the An% ranges between 73 – 74. In the pegmatoidal layer the An% ranges between 52 – 79. In the footwall the An% ranges between 71 – 76 (Fig. 3.2.2c). See appendix C table C.9 for An% values. CaO is the highest in the footwall but shows a significant increase in the top chromitite layer. Table 3.2.1 contains the average of each unit. Within sample variation expressed as standard deviation is indicated in Appendix C, table C.8.

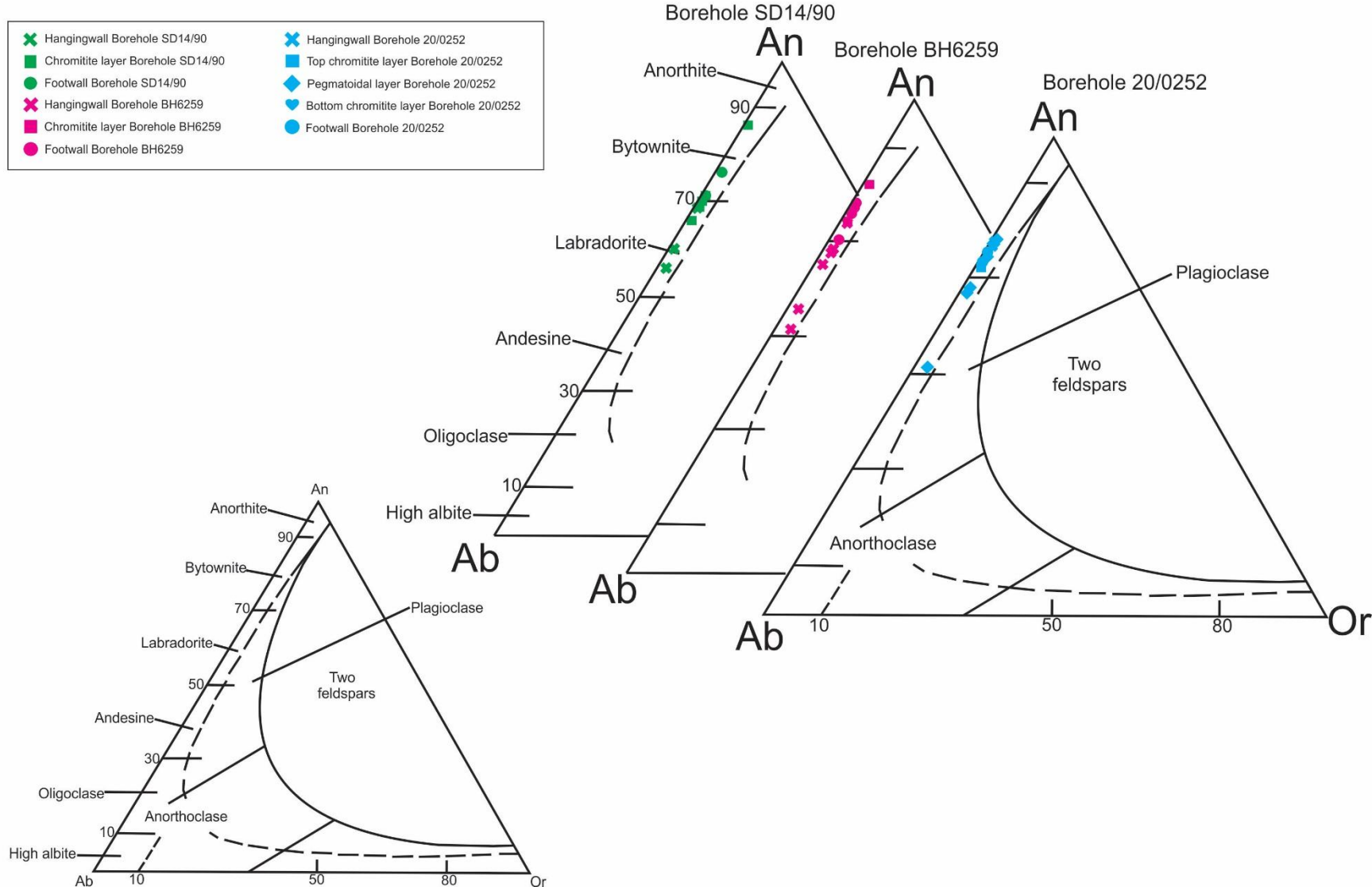
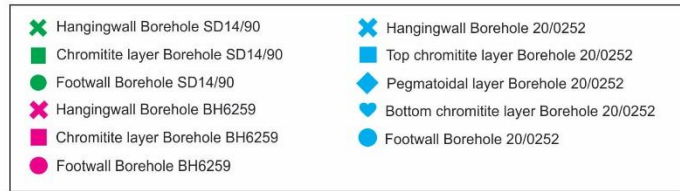


**Figure 3.2.1: Composition of plagioclase in the ternary  $\text{CaAl}_2\text{Si}_2\text{O}_8$ ;  $\text{NaAlSi}_3\text{O}_8$  and  $\text{KAISi}_3\text{O}_8$ . 14 analyses of samples from borehole SD14/90, 16 analyses of samples from borehole BH6259 and 13 analyses of samples from borehole 20/0252 are shown.**

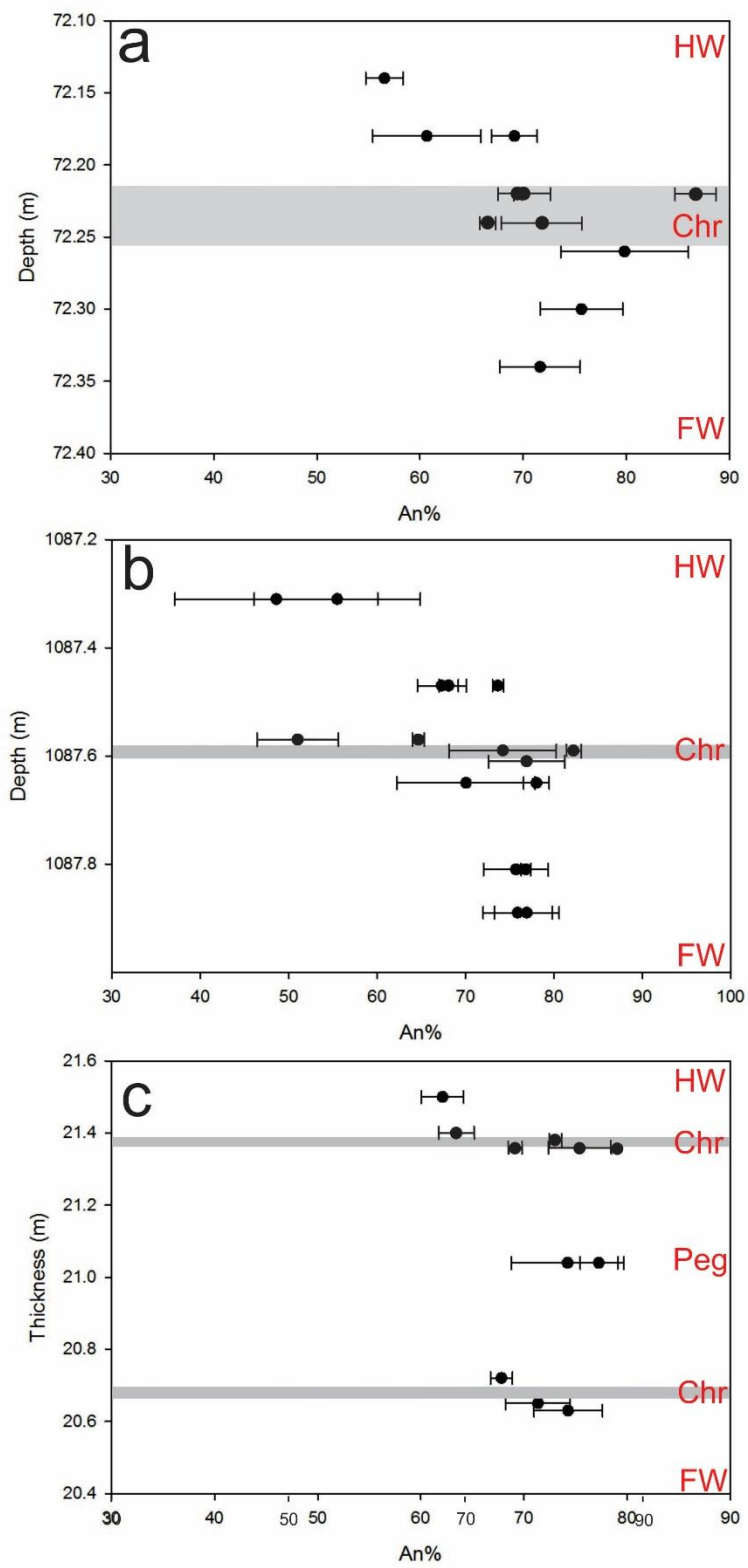


**Figure 3.2.2: Plot of depth/thickness versus An% (with error bars indicating the RSD) in plagioclase of boreholes a) SD14/90; b) BH6259; c) 20/0252.**

### 3.2.2 Orthopyroxene

Orthopyroxene is the most common mineral in the hangingwalls investigated. The composition of orthopyroxene mostly falls within the enstatite field, see figure 3.2.3. In borehole SD14/90 (non-pegmatoidal Merensky reef) the composition of orthopyroxene is generally enstatitic ( $\text{En}_{73-86}$ ) with a wollastonite component of up to 4.82 mol% (Appendix C table C.11). The Mg# varies between 74.36 and 87.02 (Fig. 3.2.4) (similar results were found by Cawthorn, 1996). Table 3.2.2 contains the average of each lithology. Within sample variation expressed as standard deviation is indicated in Appendix C, table C.10.

In borehole BH6259 (non-pegmatoidal Merensky reef) the composition of orthopyroxene is generally enstatitic ( $\text{En}_{75-84}$ ) with a wollastonite component of up to 11.5 mol% (Appendix C table C.13). The Mg# varies between 75.94 and 85.31 (Fig. 3.2.4). Table 3.2.2. contains the average of each lithology. Within sample variation expressed as standard deviation is indicated in Appendix C, table C.12.

In borehole 20/0252 (pegmatoidal Merensky reef) the composition of orthopyroxene is generally enstatitic ( $\text{En}_{76-80}$ ) with a wollastonite component of up to 4.49 mol% (Appendix C table C.15). The Mg# varies between 77.7 and 80.76 (Fig. 3.2.4). Table 3.2.2 contains the average of each lithology. Appendix C table C10 – 15 contains the remainder of the analytical data. The chromitite layer of all three boreholes show the most primitive Mg#.

**Table 3.2.2: Average orthopyroxene chemistry in the different lithologies of the different boreholes. Major element oxides given in wt%.**

Sample name	Borehole SD14/90			Borehole BH6259			Borehole 20/0252			
	Hangingwall	Chromitite layer	Footwall	Hangingwall	Chromitite layer	Footwall	Hangingwall	Pegmatoidal layer	Bottom chr layer	Footwall
$\text{SiO}_2$	55.65	56.17	54.96	55.78	55.93	54.82	55.25	54.65	55.20	55.83
$\text{CaO}$	1.11	0.85	0.79	1.31	0.85	0.66	0.96	0.81	1.75	0.72
$\text{TiO}_2$	0.23	0.15	0.22	0.18	0.15	0.20	0.19	0.28	0.13	0.13
$\text{Al}_2\text{O}_3$	1.08	1.24	0.88	1.25	1.54	0.89	1.19	1.07	1.55	1.36
$\text{FeO}$	12.14	10.41	16.20	11.94	9.77	14.32	13.71	14.52	12.33	12.63
$\text{K}_2\text{O}$	0.02	0.02	0.04	0.05	0.01	0.01	0.02	n.d.	0.01	0.01
$\text{MnO}$	0.25	0.21	0.32	0.25	0.20	0.30	0.28	0.33	0.24	0.27
$\text{NiO}$	0.08	0.07	0.08	0.08	0.09	0.11	0.10	0.06	0.10	0.08
$\text{Na}_2\text{O}$	0.06	0.06	0.06	0.08	0.01	0.02	0.04	n.d.	0.04	0.03
$\text{MgO}$	29.29	30.74	26.76	29.14	31.83	28.51	27.94	28.20	28.57	29.21
$\text{Cr}_2\text{O}_3$	0.38	0.41	0.14	0.40	0.46	0.25	0.37	0.29	0.50	0.42
Total	100.29	100.34	100.45	100.45	100.84	100.09	100.04	100.22	100.42	100.68
Mg#	81.14	84.01	74.65	81.08	85.31	78.02	78.42	77.59	80.52	80.47

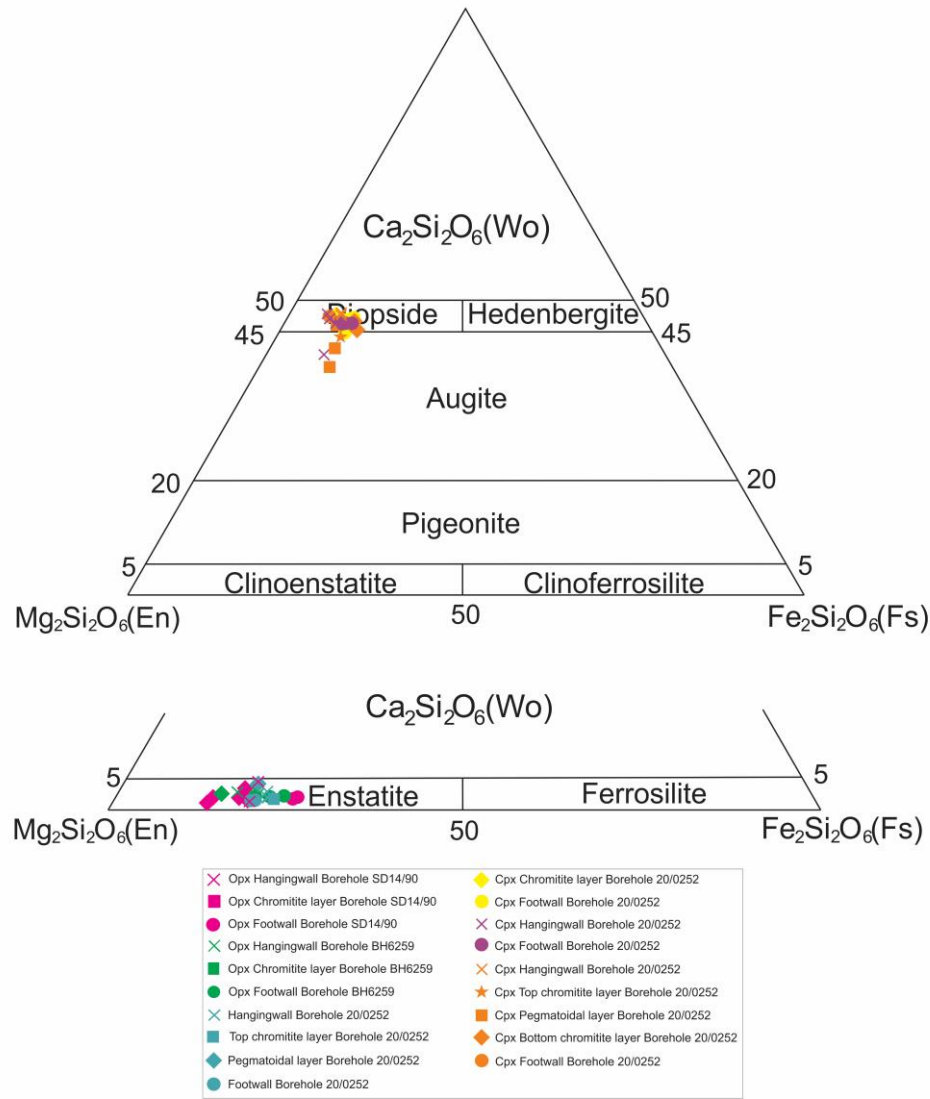


**Figure 3.2.3: Composition of orthopyroxene and clinopyroxene in the ternary  $\text{Ca}_2\text{Si}_2\text{O}_6$ ,  $\text{Mg}_2\text{Si}_2\text{O}_6$  and  $\text{Fe}_2\text{Si}_2\text{O}_6$  system after Morimoto (1988). 15 analyses of samples from borehole SD14/90, 20 analyses of samples from borehole BH6259 and 19 analyses of samples from borehole 20/0252 are shown.**

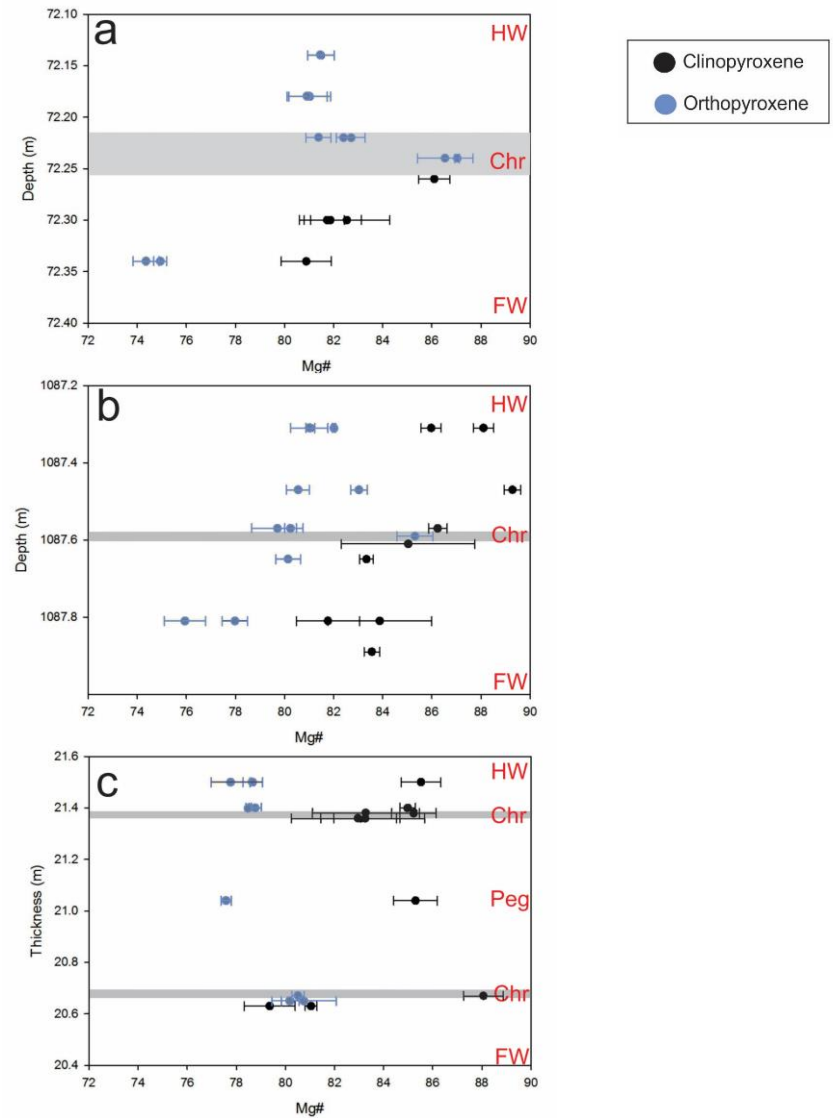


**Figure 3.2.4: Plot of depth/thickness versus Mg# (with error bars indicating the RSD) in orthopyroxene and clinopyroxene of borehole a) SD14/90; b) BH6259; c) 20/0252.**

### 3.2.3 Clinopyroxene

Clinopyroxene is a minor component in the feldspathic pyroxenite and an accessory mineral in the other units. Clinopyroxene occurs as inclusions or as lenses in orthopyroxene or as oikocrysts. The composition of clinopyroxene in these units covers a range from diopside to augite, see figure 3.2.3. In borehole SD14/90 the wollastonite component ranges between 44.35 mol% and 47.36 mol% and an enstatite component between 43.06 - 45.61 mol% (Appendix C table C.17). The Mg# varies between 81.74 and 86.10 (Fig. 3.2.4). Table 3.2.3 contains the average of each lithology. Within sample variation expressed as standard deviation is indicated in Appendix C, table C.16.

In borehole BH 6259 the wollastonite component ranges between 40.91 mol% and 47.82 mol% and an enstatite component between 43.85 - 50.64 mol% (Appendix C table C.19). The Mg# varies between 81.77 and 89.28 (Fig. 3.2.4). Table 3.2.3 contains the average of each lithology. Within sample variation expressed as standard deviation is indicated in Appendix C, table C.18.

In borehole 20/0252 the wollastonite component ranges between 38.56 mol% and 47.73 mol% and an enstatite component between 43.51 - 50.96 mol% (Appendix C table C.21). The Mg# varies between 79.36 and 88.07 (Fig. 3.2.4). Table 3.2.3 contains the average of each lithology. Within sample variation expressed as standard deviation is indicated in Appendix C, table C.20. The chromitite layer show the most primitive value for Mg#.

**Table 3.2.3: Average clinopyroxene chemistry in the different lithologies of the different boreholes. Major element oxides given in wt%.**

Sample name	Borehole SD14/90		Borehole BH6259		Borehole 20/0252				
	Chromitite layer	Footwall	Hangingwall	Footwall	Hangingwall	Top chr layer	Pegmatoidal layer	Bottom chr layer	Footwall
SiO <sub>2</sub>	53.90	53.34	53.74	52.45	53.54	52.65	53.42	52.40	52.42
CaO	23.62	22.53	21.99	22.91	23.23	21.97	20.66	22.70	22.39
TiO <sub>2</sub>	0.56	0.52	0.47	0.46	0.25	0.41	0.41	0.37	0.36
Al <sub>2</sub> O <sub>3</sub>	1.55	1.88	1.97	1.63	1.54	2.03	1.81	2.88	1.31
FeO	4.66	6.15	4.31	5.54	4.81	5.38	5.81	3.86	6.75
K <sub>2</sub> O	0.02	0.02	0.08	0.01	0.02	0.01	0.01	0.01	0.01
MnO	0.16	0.16	0.14	0.13	0.13	0.15	0.12	0.08	0.20
NiO	0.06	0.05	0.07	0.05	0.05	0.05	0.04	0.07	0.04
Na <sub>2</sub> O	0.31	0.36	0.44	0.33	0.39	0.36	0.36	0.44	0.28
MgO	16.17	15.42	16.44	15.72	15.59	16.03	16.57	15.96	15.32
Cr <sub>2</sub> O <sub>3</sub>	0.10	0.53	0.76	0.43	0.66	0.72	0.59	1.09	0.23
Total	101.11	100.95	100.40	99.66	100.20	99.75	99.80	99.86	99.31
Mg#	86.10	81.76	87.40	83.51	85.25	84.26	83.64	88.07	80.20

### 3.2.4 Chromite

Disseminated chromite occurs in either the hanging wall, pegmatoidal or footwall layer in contact with the chromitite layer. Compact chromite (about 55 vol%) occurs in the chromitite stringers (lower and upper chromitite stringers). In borehole SD14/90 (non-pegmatoidal Merensky reef) the chromitite stringer shows  $\text{Cr}_2\text{O}_3$  concentrations ranging from 41.35 wt% to 45.22 wt%. In borehole BH6259 (non-pegmatoidal Merensky reef) the chromitite stringer show  $\text{Cr}_2\text{O}_3$  concentrations ranging from 41.60 wt% to 41.74 wt%. In borehole 20/0252 the disseminated chromite in the hangingwall shows  $\text{Cr}_2\text{O}_3$  concentration that ranges from 40.2 wt% to 50.21 wt%. Compact chromite in the top chromitite layer shows  $\text{Cr}_2\text{O}_3$  concentrations of 41.45 wt%. The disseminated chromite in the pegmatoidal layer shows  $\text{Cr}_2\text{O}_3$  of 38.71 wt%. Compact chromite in the top chromitite layer shows  $\text{Cr}_2\text{O}_3$  concentrations of 44.26 wt%. See Table 3.2.4 for averages of chromite chemistry in the different lithologies. Appendix C table C 22-24 contains the remainder of the analytical data.

**Table 3.2.4: Average chromite chemistry in the different lithologies of the different boreholes.  
Major element oxides given in wt%.**

	Borehole SD14/90	Borehole BH6259		Borehole 20/0252			
	Chromitite layer	Chromitite layer		HW	Top chr layer	Pegmatoidal layer	Bottom chr layer
$\text{SiO}_2$	0.08	0.04		0.06	0.12	0.08	0.12
$\text{CaO}$	0.04	n.d.		0.04	0.01	0.01	0.02
$\text{TiO}_2$	0.88	0.99		1.91	2.74	3.29	1.02
$\text{Al}_2\text{O}_3$	18.51	19.52		9.18	12.38	9.94	16.61
$\text{FeO}$	23.82	23.45		33.41	29.30	33.99	24.16
$\text{Fe}_2\text{O}_3$	6.62	6.52		9.28	8.14	9.44	6.71
$\text{ZnO}$	0.14	0.17		0.24	0.19	0.11	0.05
$\text{MnO}$	0.30	0.27		0.39	0.28	0.33	0.27
$\text{NiO}$	0.15	0.16		0.21	0.25	0.30	0.18
$\text{V}_2\text{O}_3$	0.25	0.29		0.74	0.65	0.69	0.33
$\text{MgO}$	7.74	8.09		2.88	5.68	4.35	7.17
$\text{Cr}_2\text{O}_3$	42.46	41.66		43.99	41.45	38.71	44.26
<b>Total</b>	100.32	100.52		101.38	100.38	100.29	100.23
<b>Mg#</b>	69.75	71.11		39.04	58.07	47.76	67.92

### 3.2.5 Mica (phlogopite)

Phlogopite occur as accessory minerals (less than 4 vol%) in almost all the units investigated. The subhedral phlogopite is commonly interstitial but in some sections euhedral crystals can be observed. In borehole SD14/90 FeO and MgO vary between 2.01 wt% and 5.5 wt% and 20.21 wt% and 23.92 wt% respectively. Phlogopite contains significant amounts of  $\text{TiO}_2$  which ranges between 3.14 wt% and 4.03 wt%. Table 3.2.5 shows the average phlogopite chemistry in the different lithologies for the various boreholes.

In borehole BH6259 FeO and MgO vary between 3.33 wt% and 9.5 wt% and 16.42 wt% and 22.30 wt% respectively. Phlogopite contains significant amounts of TiO<sub>2</sub> which ranges between 0.48 wt% and 4.91 wt%. Table 3.2.5 shows the average phlogopite chemistry in the different lithologies for the various boreholes.

In borehole 20/0252 FeO and MgO vary between 5.65 wt% and 7.91 wt% and 18.22 wt% and 19.80 wt% respectively. Phlogopite contains significant amounts of TiO<sub>2</sub> which ranges between 3.09 wt% and 4.09 wt%. Table 3.2.5 shows the average phlogopite chemistry in the different lithologies for the various boreholes. Appendix C tables C25-27, contain the remainder of the analytical results.

**Table 3.2.5: Average phlogopite chemistry in the different lithologies of the different boreholes. Major element oxides given in wt%.**

	Borehole SD14/90		Borehole BH6259		Borehole 20/0252	
	Chr layer	FW	HW	FW	HW	Pegmatoidal layer
SiO <sub>2</sub>	39.71	38.90	39.09	39.30	39.09	38.88
CaO	0.02	0.01	0.02	0.14	0.08	0.03
Al <sub>2</sub> O <sub>3</sub>	15.31	14.74	14.53	15.20	14.60	14.36
F	0.30	0.26	0.25	0.21	0.02	0.09
MgO	23.19	20.21	19.46	19.73	19.49	18.22
FeO	2.50	5.51	6.15	6.88	5.92	7.91
Fe <sub>2</sub> O <sub>3</sub>	0.70	1.53	1.71	1.91	1.64	2.20
K <sub>2</sub> O	9.10	9.66	9.60	9.24	9.56	9.52
MnO	0.02	0.03	0.04	0.05	0.01	0.06
BaO	0.42	0.83	0.38	0.31	0.22	0.30
Na <sub>2</sub> O	0.53	0.21	0.22	0.24	0.32	0.15
Cl	0.16	0.20	0.35	0.26	0.36	0.31
TiO <sub>2</sub>	3.19	3.73	3.44	2.86	3.26	4.09
Cr <sub>2</sub> O <sub>3</sub>	1.38	1.18	1.07	0.60	1.35	0.40
Total	96.38	96.99	96.32	96.92	95.92	96.52

### 3.2.6 Base metal sulphides

Base metal sulphides mostly occur in the units of feldspathic pyroxenite, chromitite stringers and in the pegmatoidal pyroxenite layer. They are rare in the basal anorthosite layer. The sulphide phase in most of the units consist of intergrowths of three phases namely pentlandite, pyrrhotite and chalcopyrite. Pyrite is very rare. Table 3.2.6 contains the average mineral chemistry of the different lithologies in the various boreholes. In Appendix C Tables C28-37 the remainder of the analytical results are listed.

### **3.2.6.1 Chalcopyrite ( $\text{CuFeS}_2$ )**

Chalcopyrite occurs frequently as single grains but occur mostly as intergrowths with pentlandite and pyrrhotite. The composition of the chalcopyrite show a limited variation, because chalcopyrite is always near stoichiometry. S content in chalcopyrite ranges between 32.11-35.16 wt% for borehole SD14/90, 34.37-35.95 wt% for borehole BH6259, and 33.88-34.70 wt% for borehole 20/0252 (Table 3.2.6a). Fe and Cu content ranges between 28.29-31.46 wt% and 31.58-32.18 wt% respectively for borehole SD14/90. For borehole BH6259 the Fe and Cu varies between 30.15-31.14 wt% and 31.50-33.41 wt% respectively. The Fe and Cu content for borehole 20/0252 ranges between 30.11-30.94 wt% and 32.62-34.22 wt% respectively (Table 3.2.6a and figure 3.2.6.1).

### **3.2.6.2 Pyrrhotite ( $\text{FeS} - \text{Fe}_{1-x}\text{S}$ )**

Pyrrhotite occurs mostly as intergrowths with pentlandite and chalcopyrite and rarely occurs as single grains. The Fe concentration of pyrrhotite in borehole SD14/90; BH6259 and 20/0252 ranges between 61.14-63.93 wt%; 59.45-62.55 wt% and 58.61-60.93 wt% respectively. S content in pyrrhotite, from borehole SD14/90 ranges between 37.13 wt% and 37.91 wt%. In borehole BH6259 and 20/0252, S content ranges between 36.45-38.27 wt% and 38.30-39.22 wt% respectively (Table 3.2.6b).

### **3.2.6.3 Pentlandite ( $\text{Ni, Fe})_9\text{S}_8$**

Two types of pentlandite occur in these units. The main type occur as coarse grained pentlandite, which is intergrown with pyrrhotite and chalcopyrite. The second type is where pentlandite is intergrown with pyrrhotite and chalcopyrite is absent. The composition of pentlandite does not vary considerably between the different boreholes. The S content of pentlandite for borehole SD14/90; BH6259 and 20/0252 ranges between 29.25 - 32.61 wt% ; 32.12 - 33.22 wt% and 32.65 - 33.13 wt% respectively (Table 3.2.6c).

### **3.2.6.4 Pyrite ( $\text{FeS}_2$ )**

Pyrite is usually an accessory mineral. It usually occurs as an intergrowth with pentlandite, pyrrhotite and chalcopyrite. The composition of pyrite in borehole BH6259 doesn't vary considerably. Fe concentrations range between 45.47 wt% and 47.05 wt% and S content ranges between 52.84 wt% and 53.57 wt% (Table 3.2.6d).

**Table 3.2.6a: Average chalcopyrite chemistry in the different lithologies of the different boreholes. Given in wt%.**

	Borehole SD14/90			Borehole BH6259			Borehole 20/0252			
	FW	Chr layer	HW	FW	Chr layer	HW	FW	Top chr layer	Pegmatoidal	FW
Fe	29.44	30.45	29.94	30.73	30.40	30.64	30.53	30.87	30.28	30.35
Ni	0.03	0.13	0.08	0.03	0.06	0.13	0.03	0.01	0.21	0.06
Cu	31.75	31.54	31.64	31.80	31.50	33.01	33.94	33.12	32.62	33.20
Co	0.04	0.03	0.04	0.02	0.02	0.04	0.04	0.04	0.05	0.04
S	33.20	33.95	33.58	34.67	34.37	35.40	34.56	34.13	33.95	34.08
Total	94.44	96.11	95.27	97.24	96.35	99.16	99.09	98.17	97.12	97.73

**Table 3.2.6b: Average pyrrhotite chemistry in the different lithologies of the different boreholes. Given in wt%.**

	Borehole SD14/90			Borehole BH6259			Borehole 20/0252		
	HW	Chr layer	FW	HW	Chr layer	FW	Top Chr layer	Pegmatoidal	
Fe	63.62	61.68	61.55	60.13	62.55		59.93	60.39	58.61
Ni	0.24	0.17	0.17	0.27	0.09		0.38	0.19	0.39
Cu	0.01	0.02	0.03	0.01	n.d.		0.03	0.06	n.d.
Co	0.08	0.05	0.08	0.06	0.08		0.05	0.09	0.05
S	37.51	37.69	37.13	37.44	37.97		38.60	39.22	38.30
Total	101.45	99.61	98.95	97.92	100.69		99.00	99.94	97.35

**Table 3.2.6c: Average pentlandite chemistry in the different lithologies of the different boreholes. Given in wt%.**

	Borehole SD14/90		Borehole BH6259			Borehole 20/0252		
	HW	Chr layer	HW	Chr layer	FW	HW	Pegmatoidal	
Fe	35.83	33.46		31.94	34.40	31.34	30.51	30.36
Ni	31.67	30.52		31.77	30.37	32.67	34.84	32.23
Cu	0.01	0.49		0.03	0.16	0.03	0.03	0.02
Co	0.63	0.53		0.69	0.47	0.58	0.66	0.67
S	31.59	31.57		32.31	32.29	33.22	33.08	32.65
Total	99.73	96.57		97.13	97.69	99.41	99.13	95.93

**Table 3.2.6d: Average pyrite chemistry in borehole 6259. Given in wt%.**

	HW	FW
Fe	47.05	45.47
Ni	0.12	0.14
Cu	0.02	0.00
Co	0.34	0.59
S	52.84	53.57
Total	100.37	99.77

## Whole rock geochemistry

### 3.3 Major element geochemistry (ICP-MS)

XRF results were not used, because the fusion discs that were prepared couldn't be measured accurately for major elements, especially the ones with high amounts of chromite. From the ICP-MS data an overall estimate of the bulk sample composition can be determined. The following major element oxides were measured: SiO<sub>2</sub>, TiO<sub>2</sub>, Al<sub>2</sub>O<sub>3</sub>, Fe<sub>2</sub>O<sub>3</sub>, MnO, MgO, CaO, Na<sub>2</sub>O, K<sub>2</sub>O, P<sub>2</sub>O<sub>5</sub> and NiO. The percentage of major element oxides can be used to give the relative proportions of silicates to chromite in the samples, because no SiO<sub>2</sub> in chromite. This is most likely to be an overestimate of the silicate since all the iron is assigned to silicate forming major element oxides, although chromite also contains significant concentrations of iron.

Compositional ranges of major element oxides in the different units of the various boreholes are given in Appendix D. The standards (Appendix D, Table D.1) were measured several times throughout a full analytical day, (in between the samples), to determine reproducibility, accuracy and to check for instrumental drift. The accuracy of the data was expressed as % relative standard deviation (%RSD). These were consistently less than 2.0%.

Whole rock Mg# and An% as calculated from the norm are generally consistent with variations in the mineral chemistry. Changing whole rock geochemistry is shown in figure 3.3.1. The Mg# reflects the changes in major mineralogy. In borehole SD14/90 (non-pegmatoidal Merensky reef) Mg# ranges between 73.33–75.91 for the hangingwall; 41.87–52.49 for the chromitite stringer and 68.81–76.96 for the footwall. In borehole BH 6259 (non-pegmatoidal Merensky reef) Mg# ranges between 73.62–81.67 for the hangingwall; 51.43 for the chromitite stringer and between 24.64–79.12 for the footwall. In borehole 20/0252 (pegmatoidal Merensky reef) Mg# ranges between 71.83–79.65 for the hangingwall; 61.60 for the top chromitite stringer; 74.42–82.63 for the pegmatoidal layer; 75.33–78.84 for the bottom chromitite stringer and between 54.22–76.77 for the footwall.

Changing whole rock geochemistry of Cr/Cr+Fe<sup>3+</sup> and Cr/Cr+Al metal ratios are plotted against depth in figure 3.3.1. In borehole SD14/90 a decrease in Cr/Cr+Fe<sup>3+</sup> can be seen from bottom to top in the chromitite layer. In the other chromitite stringers of borehole BH6259 and 20/0252 this is less clear because the chromitite stringers are much thinner. In borehole SD14/90 a decrease in Cr/Cr+Al from top to bottom can be seen.

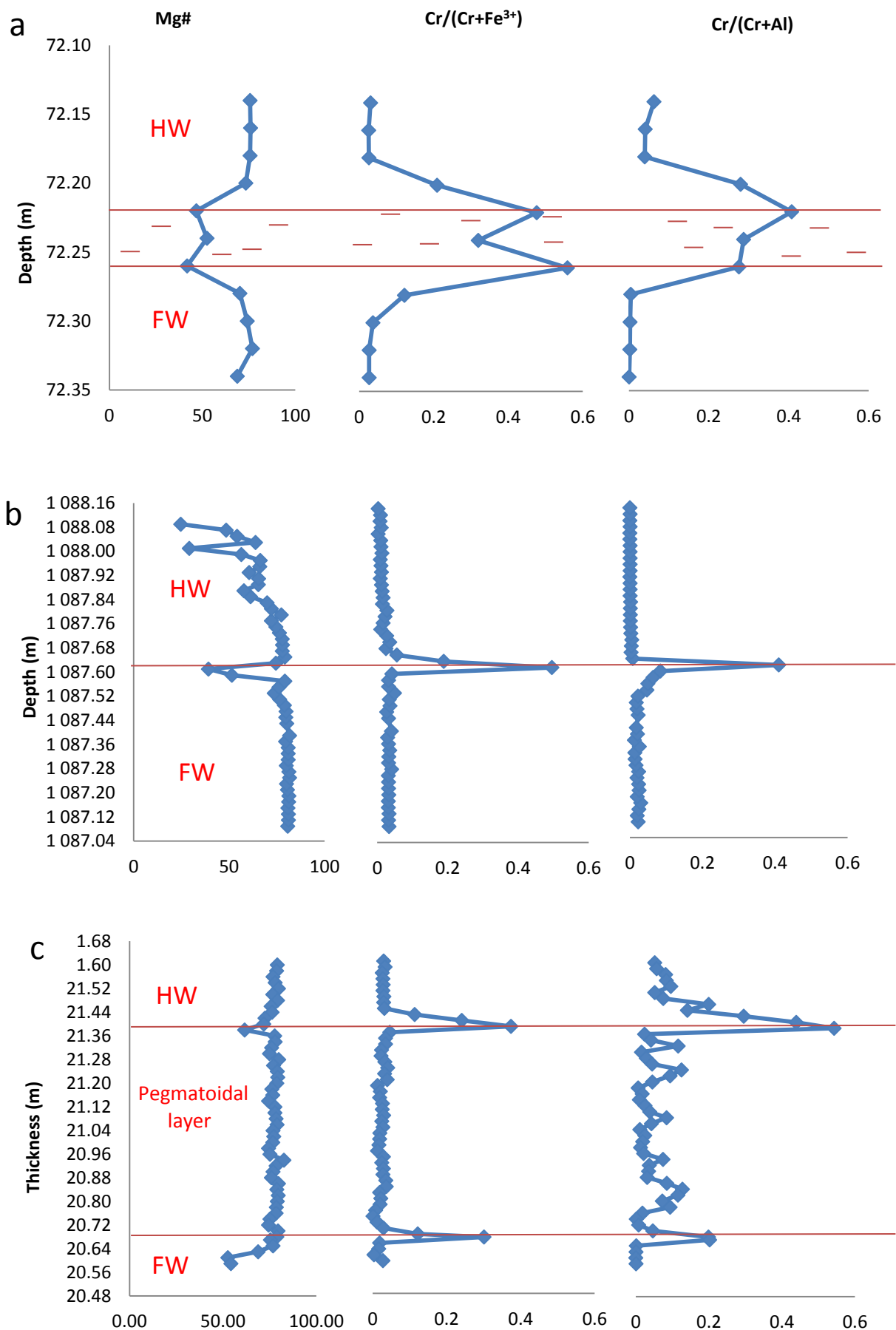


**Figure 3.3.1: Changing whole rock geochemistry, of a) SD14/90;b) BH6259 and c) 20/0252 illustrated by the Mg# and the Cr/(Cr+Fe<sup>3+</sup>) and Cr/(Cr+Al) metal ratios. Data are given in Appendix D. Chromitite stringer indicated by a red line.** 49

In figure 3.3.2 changing whole rock An% is plotted against depth. An% generally decreases from bottom to top which reflects the changes in major mineralogy. An% ranges between 67.92–80.96% for the hangingwall; 81.90–100% for the chromitite stringer and 78.89–84.36% for the footwall of borehole SD14/90. In borehole BH6259 the An% ranges between 60.06–80.02% for the hangingwall 80.38% for the chromitite stringer and between 75.23–84.92% for the footwall. For borehole 20/0252 the An% ranges between 77.05–91.01% for the hangingwall; 91.21% for the top chromitite stringer, 73.49–94.08% for the pegmatoidal layer 82.95–83.34% for the bottom chromitite stringer and 75.49 – 93.30% for the footwall.

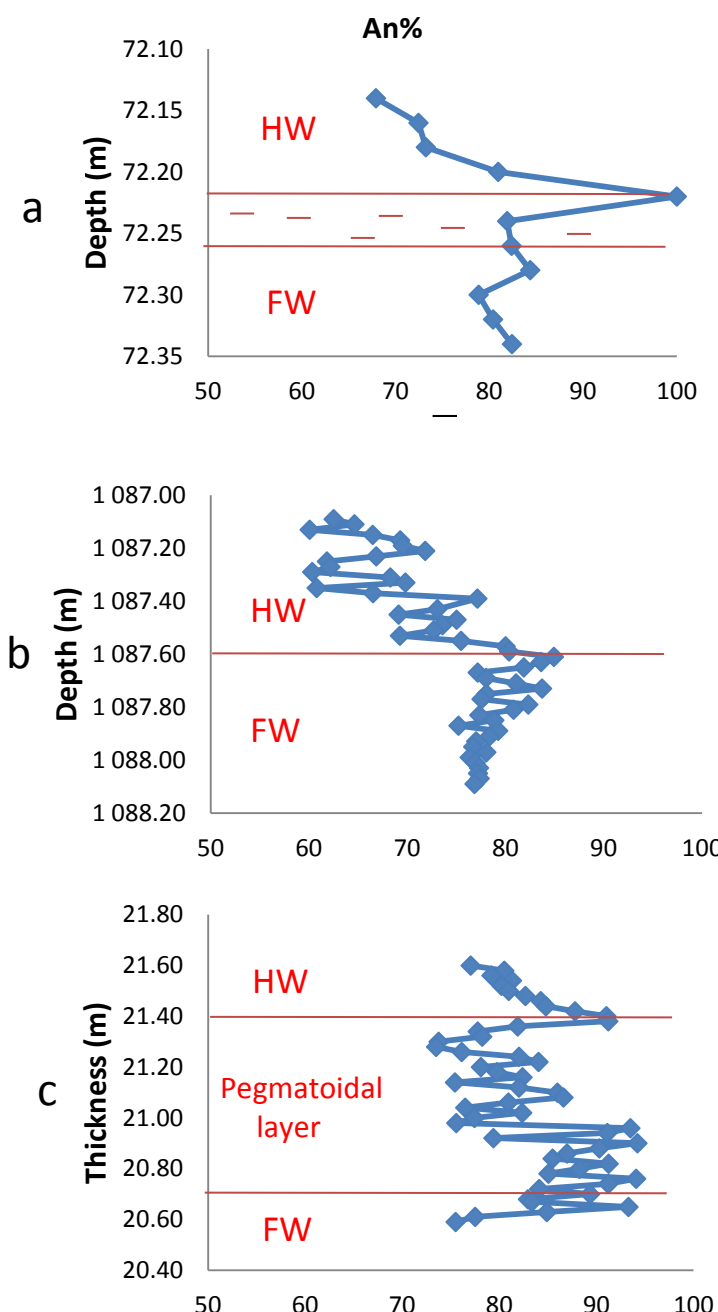


**Figure 3.3.2: Changing whole rock An% of borehole a) SD14/90; b) BH6259 and c) 20/0252. Data are given in appendix D. Chromitite stringer indicated by a red line.**

Comprehensive and detailed descriptions of the whole rock data on the Merensky reef have been given by several authors, for example Barnes and Maier (2002b), Obsahr, et al. (2013), Wilson and Chunnett (2006) and Barnes et al. (2008, 2010). Most of them show similar results, for example a decrease in Mg# from the chromitite stringer to the hangingwall indicating normal melt evolution and a decrease in An% from the chromitite (top) stringer to the hangingwall. See table 3.3.1 for the average whole rock geochemistry of the major element oxides.

**Table 3.3.1: Average whole rock geochemistry (major element oxides and element ratios) of the various boreholes obtained from ICP-MS analysis. Major element oxides in wt%. Cr/(Cr+Al) and Cr/(Cr+Fe<sup>3+</sup>) calculated using molar values.**

	Borehole SD14/90			Borehole BH6259			Borehole 20/0252				
	HW	Chr layer	FW	HW	Chr layer	FW	HW	Top Chr layer	Peg layer	Bottom Chr layer	FW
SiO <sub>2</sub>	49.31	28.74	47.79	51.55	27.73	48.54	49.39	35.08	48.96	45.44	47.95
TiO <sub>2</sub>	0.25	0.56	0.08	0.26	0.62	0.06	0.23	1.08	0.16	0.17	0.04
Al <sub>2</sub> O <sub>3</sub>	5.75	20.21	28.35	5.69	17.87	28.08	3.48	6.53	6.69	8.94	28.19
Fe <sub>2</sub> O <sub>3</sub>	3.01	3.91	0.47	2.41	3.98	0.47	3.07	4.06	2.56	2.54	0.24
FeO	10.85	14.06	1.68	8.69	14.32	1.71	11.04	14.60	9.21	9.15	0.87
MnO	0.22	0.18	0.04	0.20	0.19	0.03	0.26	0.26	0.20	0.21	0.02
MgO	22.98	9.27	3.40	24.09	10.62	3.16	25.61	16.40	22.60	21.85	1.53
CaO	4.30	5.64	15.80	3.82	4.97	14.79	3.54	9.01	4.64	5.79	17.06
Na <sub>2</sub> O	0.51	0.64	1.99	0.61	0.67	2.08	0.20	0.18	0.39	0.49	2.16
K <sub>2</sub> O	0.03	0.11	0.14	0.30	0.11	0.14	0.05	0.08	0.12	0.03	0.38
P <sub>2</sub> O <sub>5</sub>	0.01	0.02	0.03	0.08	0.01	0.02	0.01	n.d.	0.02	0.02	0.02
Cr <sub>2</sub> O <sub>3</sub>	1.31	14.77	0.11	0.40	18.55	0.06	1.04	11.55	0.32	3.36	0.03
NiO	0.66	0.31	0.07	0.37	0.45	0.07	0.64	0.96	0.41	0.11	0.03
LOI	0.49	n.d.	0.31	0.27	n.d.	0.39	0.44	0.03	2.58	1.14	0.97
Total	100.89	99.32	100.43	99.69	100.95	99.78	100.23	101.45	99.89	100.26	99.58
Element ratios											
Mg#	75.15	47.05	72.54	79.88	51.43	63.50	76.76	61.60	77.59	77.09	63.10
An%	73.65	88.10	81.52	68.60	80.38	78.89	82.70	91.21	83.37	83.15	82.80
Cr/(Cr+Fe <sup>3+</sup> )	0.07	0.45	0.05	0.14	0.49	0.02	0.20	0.75	0.12	0.55	0.10
Cr/(Cr+Al)	0.11	0.32	n.d.	0.03	0.41	0.01	0.14	0.54	0.05	0.20	n.d.

Appendix D (Table D.5) contains the calculated CIPW norms that was used to calculate the An%, Ab% and Or % for the ternary diagram. In the ternary diagram, An, Ab and Or, most of the data plot in the labradorite, bytownite and anorthite fields with a few in the 2 feldspar region (Fig 3.3.3). From the ternary diagram it is also evident that the major element trends reflect the changes in major mineralogy. With most of the whole rock compositions in the footwall falling in the anorthite range and the hanging wall falling in the labradorite field. This is also reflected in the An% decreasing from the bottom to the top in the whole rock major element chemistry.

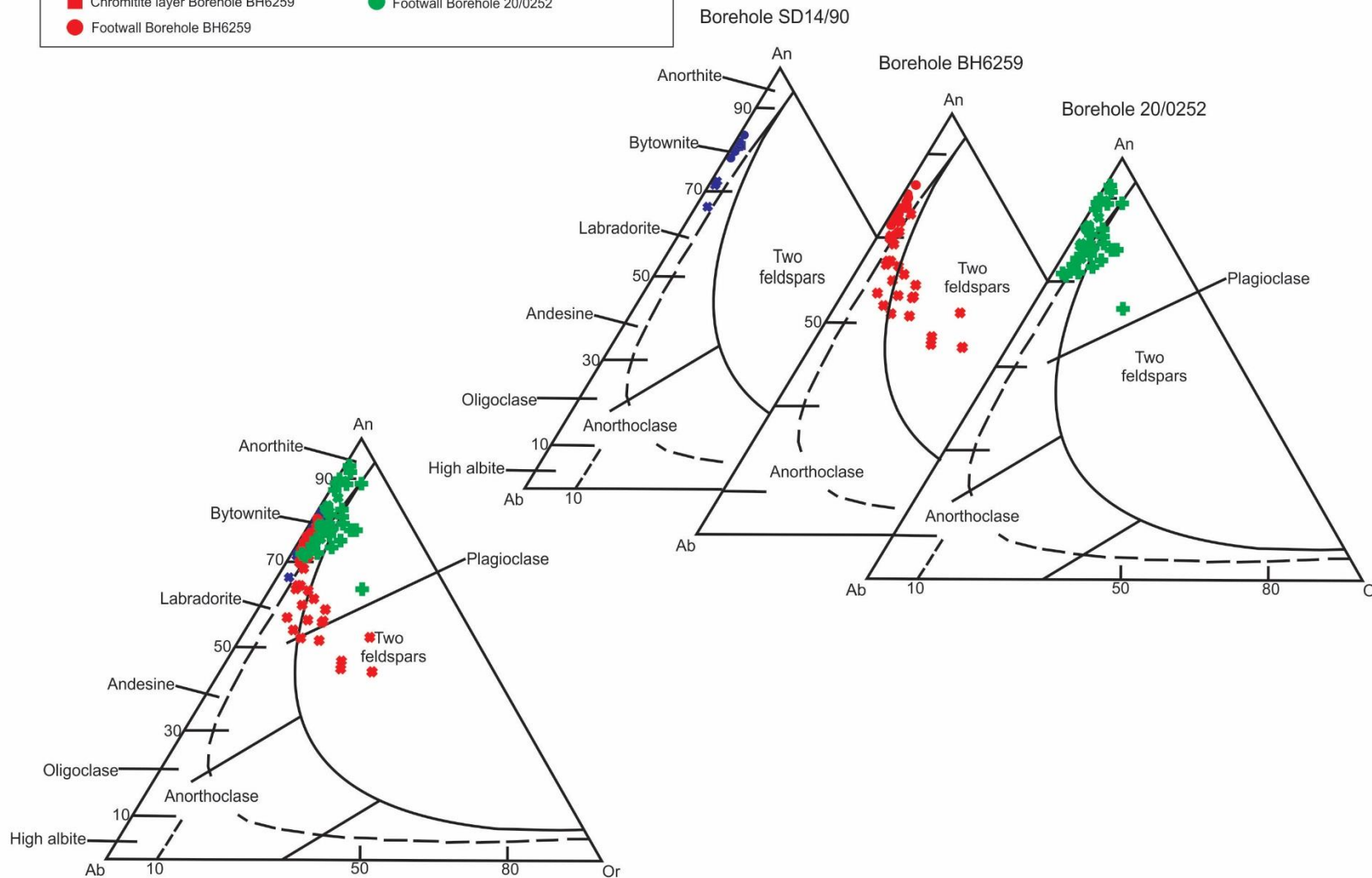


**Figure 3.3.3:** From whole rock data CIPW norms were calculated and plotted in the ternary  $\text{CaAl}_2\text{Si}_2\text{O}_8$ ,  $\text{NaAlSi}_3\text{O}_8$  and  $\text{KAlSi}_3\text{O}_8$ .

### 3.4 Whole rock trace element geochemistry (ICP-MS)

Compositional ranges of trace elements in the different units of the various boreholes are given in Appendix E, Table E.2 – E.4. Table E.5 – E.7 contain REE whole rock geochemistry. The standards (Appendix E, Table E.1) were measured several times throughout a full analytical day, (in between samples), to determine reproducibility, accuracy and to check for instrumental drift. Reproducibility and accuracy was expressed as % RSD. These were all less than 1.1%. See table 3.4.1 for the average whole rock geochemistry of the trace elements.

**Table 3.4.1: Average whole rock geochemistry (trace elements) of the various boreholes obtained from ICP-MS analysis listed in increasing atomic number. Trace element concentrations in ppm.**

	Borehole SD14/90			Borehole BH6259			Borehole 20/0252				
	HW	Chr layer	FW	HW	Chr layer	FW	HW	Top chr layer	Peg layer	Bottom chr layer	FW
V	204	1294	25	127	1265	24	238	1831	109	245	18
Cr	9170	94428	779	2890	119161	408	7311	77992	2213	22782	150
Co	149	157	18	71	180	13	96	199	70	97	6.09
Ni	4897	2471	613	2759	3573	541	4918	7658	3036	854	177
Cu	1693	959	132	656	1246	226	1360	1595	878	150	14
Zn	116	408	23	148	385	60	137	383	96	162	23
Ga	8.44	39	18	7.1	34	16	6.7	25	7.1	13	18
Rb	1.17	2.56	2.06	9.9	1.5	1.7	1.8	3.5	4.4	2.6	7.9
Sr	75	148	423	76	136	416	35	42	76	144	430
Y	5.7	1.3	1.7	6.5	1.2	1.3	5.0	8.8	4.5	2.6	1.0
Zr	14	16	13	134	12	7.4	17	18	48	16	5.6
Nb	0.64	0.94	0.68	1.7	0.43	0.24	0.53	0.47	1.2	0.55	0.35
Sn	2.7	4.8	3.5	1.9	3.9	1.4	2.1	3.3	1.8	3.5	2.1
Cs	0.24	0.26	0.26	0.31	0.28	0.15	0.12	0.21	0.30	0.26	0.34
Ba	31	37	82	65	30	63	11	8.1	34	26	102
Hf	0.31	0.30	0.27	2.2	0.25	0.10	0.31	0.45	0.89	0.35	0.11
Ta	0.04	0.06	0.05	0.11	0.04	0.02	0.04	0.04	0.09	0.04	0.02
Pb	6.7	3.3	1.9	4.6	3.2	1.6	3.9	4.1	4.1	1.4	1.2
Th	0.21	0.16	0.25	0.93	0.09	0.07	0.32	0.15	0.77	0.40	0.13
U	0.05	0.05	0.06	0.26	0.02	0.02	0.08	0.04	0.21	0.11	0.02

Chondrite normalized REE diagrams are plotted for the different units for the various boreholes (Fig. 3.4.1). More elaborate chondrite normalized REE diagrams for each unit of the different boreholes are in Appendix E, figure E.7 – E.12.

In borehole SD14/90 all the lithologies are relatively enriched in LREE with the hangingwall showing an average ( $\text{Ce}/\text{Sm}_N$ ) of 1.58, the chromitite stringer 2.75 and the footwall showing an average of 2.65. The rocks show very little fractionation of the HREE with the hangingwall showing an average ( $\text{Tb}/\text{Yb}_N$ ) of 0.87, the chromitite stringer 1.53 and the footwall showing an average of 1.49 (Fig. 3.4.1a). Both the chromitite layer and the footwall show strong positive Eu anomalies. The hangingwall show a negative Eu anomaly.

In borehole BH6259 all the lithologies are relatively enriched in LREE with the hangingwall showing an average ( $\text{Ce}/\text{Sm}_N$ ) of 2.07, the chromitite stringer 2.43 and the footwall showing an average of 2.83. The rocks show very little fractionation of the HREE with the hangingwall showing an average ( $\text{Tb}/\text{Yb}_N$ ) of 0.93, the chromitite stringer 1.25 and the

footwall showing a little bit more fractionation with an average of 1.75 (Fig. 3.4.1c). Both the chromitite layer and the footwall show strong positive Eu anomalies. The hangingwall show a negative Eu anomaly.

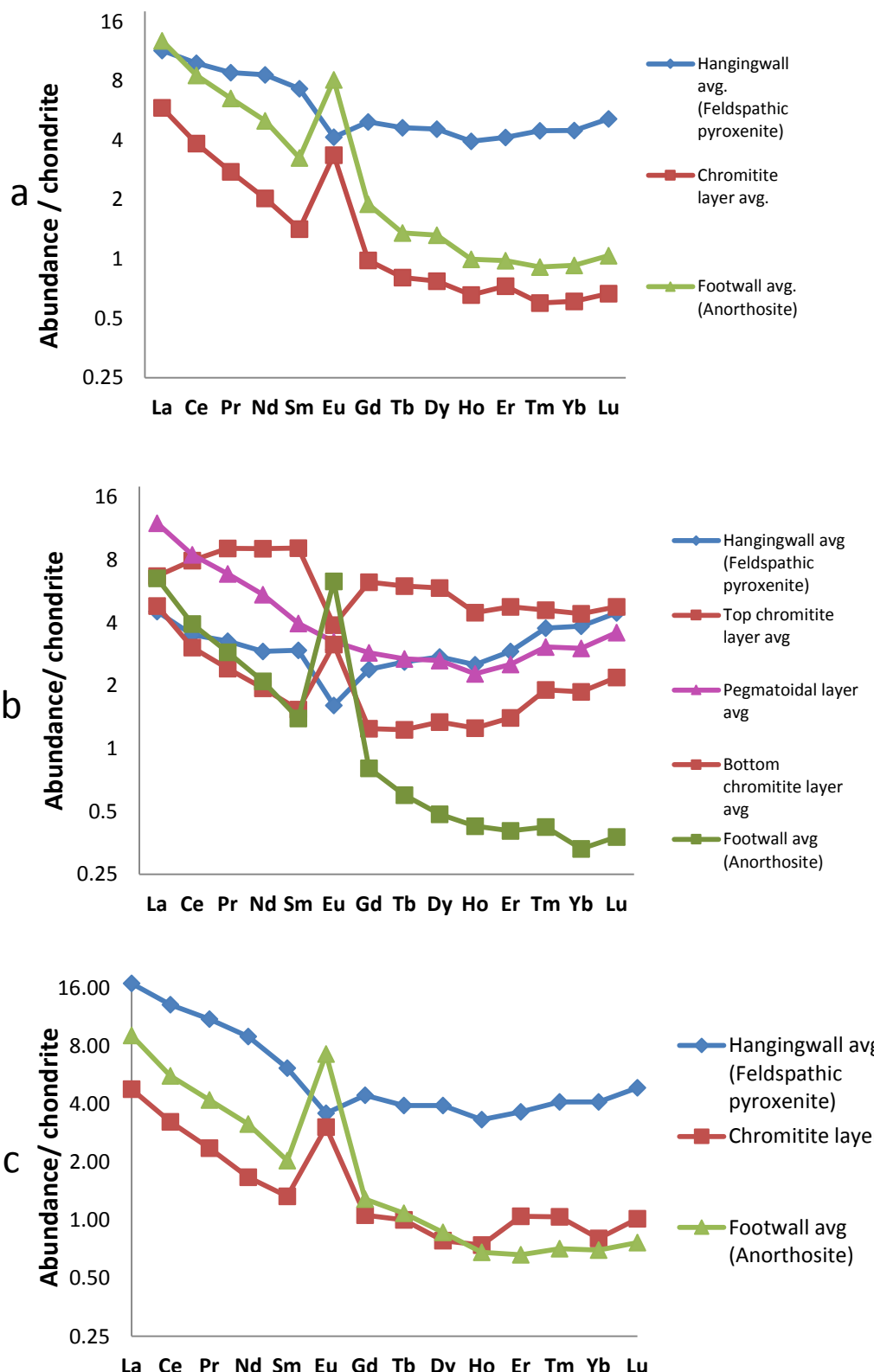


Figure 3.4.1: Chondrite-normalised REE diagrams for a) borehole SD14/90; b) borehole 20/0252 and c) borehole BH6259. C1 chondrite normalised values are from Lodders, 2003.

In borehole 20/0252 the hangingwall and top chromitite stringer are not so enriched in LREE with the hangingwall showing an average ( $\text{Ce}/\text{Sm}_N$ ) of 1.20, the top chromitite stringer showing an average of 0.87. The pegmatoidal layer, bottom chromitite stringer and the footwall are relatively enriched in LREE with the pegmatoidal layer showing an average ( $\text{Ce}/\text{Sm}_N$ ) of 2.21, the bottom chromitite stringer 2.02 and the footwall showing an average of 2.89. The rocks show very little fractionation of the HREE with the hangingwall showing an average ( $\text{Tb}/\text{Yb}_N$ ) of 0.67, the top chromitite stringer 1.35, the pegmatoidal layer 0.86 and the bottom chromitite stringer showing an average of 0.67. The footwall show a little bit more fractionation with an average ( $\text{Tb}/\text{Yb}_N$ ) of 1.86. Eu shows positive anomalies in the footwall, and bottom chromitite layer with negative anomalies in the top chromitite layer and in the hangingwall (Fig. 3.4.1b). Average whole rock geochemistry for the various boreholes are listed in Table 3.4.2.

**Table 3.4.2: Average whole rock geochemistry (REE) of the various boreholes obtained from ICP-MS analysis. REE concentrations in ppm.**

	Borehole SD14/90			Borehole BH6259			Borehole 20/0252				
	HW	Chr layer	FW	HW	Chr layer	FW	HW	Top chr layer	Peg layer	Bottom chr layer	FW
<b>La</b>	2.05	1.36	2.97	3.93	1.11	2.11	1.05	1.56	2.79	1.12	1.52
<b>Ce</b>	4.27	2.39	5.30	8.17	2.01	3.48	2.18	4.94	5.27	1.89	2.46
<b>Pr</b>	0.55	0.26	0.61	1.03	0.22	0.39	0.30	0.85	0.64	0.22	0.27
<b>Nd</b>	2.43	0.93	2.29	4.11	0.76	1.44	1.33	4.14	2.50	0.89	0.96
<b>Sm</b>	0.65	0.21	0.47	0.89	0.19	0.30	0.43	1.32	0.58	0.22	0.20
<b>Eu</b>	0.19	0.18	0.44	0.20	0.17	0.40	0.09	0.21	0.18	0.17	0.35
<b>Gd</b>	0.65	0.20	0.38	0.88	0.21	0.25	0.48	1.24	0.57	0.25	0.16
<b>Tb</b>	0.12	0.03	0.05	0.14	0.04	0.04	0.09	0.21	0.10	0.04	0.02
<b>Dy</b>	0.78	0.18	0.31	0.94	0.19	0.21	0.65	1.40	0.63	0.32	0.12
<b>Ho</b>	0.16	0.04	0.06	0.19	0.04	0.04	0.14	0.25	0.13	0.07	0.02
<b>Er</b>	0.51	0.12	0.16	0.59	0.17	0.11	0.47	0.77	0.41	0.23	0.07
<b>Tm</b>	0.09	0.01	0.02	0.10	0.02	0.02	0.09	0.11	0.07	0.05	0.01
<b>Yb</b>	0.60	0.10	0.15	0.67	0.13	0.11	0.63	0.72	0.49	0.31	0.05
<b>Lu</b>	0.10	0.02	0.02	0.12	0.02	0.02	0.11	0.11	0.09	0.05	0.01

### 3.5 PGE geochemistry (ICP-MS)

Appendix F, table F.2 – F.4 contains the whole rock PGE analysis. The standards (Appendix F table F.1) were measured several times throughout an analytical day to determine the accuracy and the reproducibility of the samples. This was determined and expressed as %RSD, which was 1% for all the samples.

The average results for the three boreholes are:

For borehole **SD14/90**: Pt+Pd+Rh in the hangingwall is 11 ppm, in the chromitite stringer (NP5-6) 66 ppm and in the first 6 cm of the anorthosite footwall (NP7-9) 12 ppm, after which it drops to <0.1 ppm.

For borehole **BH6259**: The average Pt+Pd+Rh in the hangingwall about 8 cm from the chromitite stringer is <1 ppm; the next 8 cm averages at 9 ppm. In the chromitite stringer (N98) the average is 67 ppm and in the anorthosite footwall <1 ppm.

For borehole **20/0252**: The top chromitite stringer (P12) has an average Pt+Pd+Rh of 22 ppm and the bottom chromitite stringer (P47 – P48) 3 ppm. The hangingwall has an average Pt+Pd+Rh of 16 ppm in a zone up to 4 cm above the top chromitite stringer, after which levels drop to < 3 ppm. Mineralisation in the pegmatoidal layer is concentrated in the top 40 cm, just below the top chromitite (average Pt+Pd+Rh 9.34 ppm) with the bottom 28 cm being essentially barren. The footwall shows no PGE (average Pt+Pd+Rh <0.01 ppm) mineralization. In table 3.5.1 it is clear that the top chromitite stringer in the pegmatoidal reef contains the highest concentration of PGE compared to the bottom chromitite stringer and therefore we can say it is top loaded.

The PGE concentrations are very high, with Pt, Pd and Rh reaching a high of 101 g/tonne, in sample NP5 chromitite layer borehole SD14/90, (referred to as ppm, i.e. per million). Table 3.5.1 contains the average whole rock geochemistry of the various boreholes.

**Table 3.5.1: Average whole rock geochemistry (PGE) of the various boreholes obtained from ICP-MS analysis. PGE concentrations in ppm, S and Cr in wt%.**

	Borehole SD14/90			Borehole BH6259			Borehole 20/0252				
	HW	Chr layer	FW	HW	Chr layer	FW	HW	Top chr layer	Peg layer	Bottom chr layer	FW
Os	0.08	0.86	0.01	0.08	1.11	0.01	0.07	0.38	0.10	0.06	n.d.
Ir	0.18	1.42	0.01	0.09	1.67	0.01	0.13	0.60	0.16	0.07	n.d.
Ru	0.91	7.35	0.09	0.53	8.70	0.04	0.66	3.16	0.84	0.47	n.d.
Rh	0.56	4.47	0.05	0.20	5.08	0.02	0.35	1.56	0.39	0.14	n.d.
Pt	6.81	42.99	0.68	2.62	51.40	0.36	5.41	16.54	3.66	1.03	0.01
Pd	2.71	6.58	0.44	1.09	10.35	0.25	1.33	4.11	1.55	0.12	n.d.
Cr	0.77	10.16	0.06	0.34	12.76	0.07	1.09	7.95	0.22	2.31	0.01
S	1.15	0.43	0.02	0.92	0.45	0.06	1.17	0.58	0.40	n.d.	0.01

Figure 3.5.1a – c show PGE, Cr, S, Cu, Pt/Pd and Cu/Pd values plotted vs depth for the various boreholes. In the two non-pegmatoidal Merensky reefs (borehole SD14/90 and borehole BH6259) most of the PGE follow the Cr (the black curve) trend very closely especially in the chromitite stringer. There is a slight indication of PGE following S in the footwall of these two boreholes. In the pegmatoidal Merensky reef (borehole 20/0252) the trend is slightly more irregular with PGE following the Cr trend in the top and bottom chromitite stringers and in the footwall. In the hangingwall and parts of the pegmatoidal layer the PGE follow the S trend. Cu shows a strong correlation with S in all three cases which is suspected. The Cu/Pd ratio shows the exact opposite trend as the Cr trend especially in the non-pegmatoidal Merensky reefs.

In Table 3.5.1 it is evident that the Pt concentration is the lowest in the footwall in all three boreholes. The highest Pt concentration is in the chromitite stringer of borehole SD14/90 and BH6259. In borehole 20/0252 it is clear that the pegmatoidal layer has an effect on the Pt

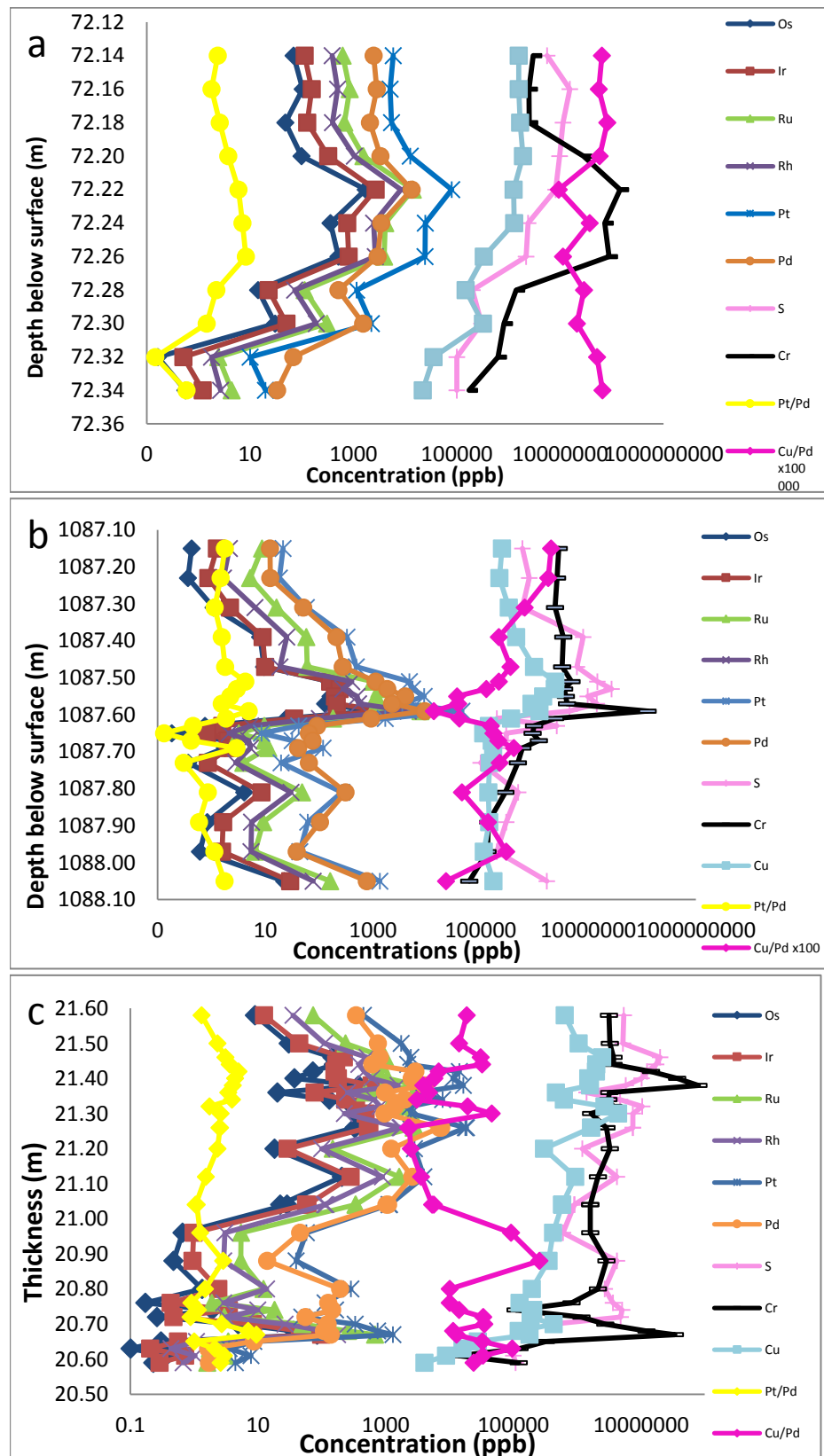


Figure 3.5.1: PGE, Cr, S, Cu, Pt/Pd and Cu/Pd values vs depth for borehole a) SD14/90; b) BH6259 and c) 20/0252.

concentration in the chromitite stringers, with Pt concentration less than half of that in the non-pegmatoidal reef. Os, Ir, Rh, Ru and Pd show a similar trend with concentrations less than half of that in the non-pegmatoidal reef. S concentrations is more or less consistent over the three reefs.

## Chapter 4: Discussion

### 4.1 Petrography

Microscope analysis from the two non-pegmatoidal boreholes (SD14/90 and BH6259) show similar reef lithologies and petrography of the samples and therefore will be discussed together. The Merensky non-pegmatoidal reef composes of 3 different layers, a basal anorthosite, overlain by a chromitite and finally a feldspathic pyroxenite layer. The pegmatoidal reef is composed of 5 different layers, a basal anorthosite, overlain by a chromitite layer, a pegmatoidal layer, a top chromitite layer and then finally by a feldspathic pyroxenite layer.

Main textural differences between the footwall and hangingwall units across the reefs, are the appearance of cumulus plagioclase and intercumulus clino- and orthopyroxene in the footwall versus cumulus clino- and orthopyroxene and interstitial plagioclase in the hangingwall. The plagioclase in the anorthosite shows compositional zoning, igneous lamination and lamellar twinning suggesting that the anorthosite has preserved some of the original igneous textures (Fig. 3.1.4a). Some of the plagioclase in the chromitite layer show wedge shaped twins, low angle grain boundaries and in some cases exhibit undulose extinction. All of these features can indicate post-depositional plastic deformation. These features could also indicate compaction of a cumulate pile (Godel et al., 2007).

Evidence for high temperature strain/deformation is observed in most of the units. Undulose extinction and spindle-shape twins were identified in plagioclase, while indented contacts between grain boundaries were observed in orthopyroxene (Fig. 3.1.1a). This could suggest that both orthopyroxene and plagioclase experienced dislocation creep (Barnes & Maier, 2002a).

Ophitic textures are common in the footwall units of the reefs. Eales et al. (1991) attributed the formation of these ophitic textures to a process of magma mixing in which the textures may develop through the mixing of evolved plagioclase bearing residual magma and primitive magma. Cumulus orthopyroxene grains show exsolution lamellae (Fig. 3.1.7a) of clinopyroxene in all units of the Merensky reef especially in the pyroxenite units.

Rocks that occur in the RLS are mostly cumulates. Cumulate rocks describe the textures of igneous rocks that formed layered intrusions as a result of slow cooling. The term was introduced by Wager & Brown (1968) and was changed or adjusted by him several times. Wager & Brown (1968), describe cumulus minerals as those crystals that precipitate first and accumulate on the magma chamber floor before they undergo any modification. In between the cumulus crystals are interstitial liquids that coexist with the cumulus crystals and are named intercumulus minerals. Accumulation of the cumulus crystals and the cooling of the crystal mush were very slow and this could have led to the modification of the primary textures (Cawthorn & Davies, 1983). Examples of this modification include enlargement of cumulus crystals and a decrease in the pore spaces (Fig. 3.1.4b). In the thin sections, especially the anorthosite layer, enlargement of grain sizes in the cumulate rocks is common and this could be called adcumulus growth. It is described by Wager & Brown. (1960) as the growth of larger grains at the expense of smaller grains.

The relative absence of olivine in these borehole samples may reflect somewhat more passive crystallisation conditions in which the facies formed at lower temperatures, as mentioned by Mitchell & Scoon (2007). It also explains the poorly developed, relatively thin chromitite layers. BMS (pyrrhotite, pyrite, chalcopyrite and pentlandite) occurs as irregular blebs that vary in size. In an article by Wilson and Chunnet (2006) they suggest that the distribution of sulphide in the Merensky reef was influenced by the amount and distribution of trapped interstitial silicate liquid i.e. plagioclase. In the species where interstitial plagioclase did not crystallize, the sulphides tend to concentrate. BMS are typically found in close proximity to biotite and phlogopite, a strong association between BMS and hydrous minerals occur. In the pegmatoidal layer a lot of alteration is observed near the serpentine veins. The serpentine also host an internetwork of smaller sulphide grains (Fig 3.1.10c). The sulphides fill the interstitial spaces and appear to have filtered down into the cumulus pile. Chromite is also closely associated with hydrous silicates.

Inclusions of BMS in chromite grains indicate that the crystallisation of BMS preceded in some instances the crystallisation of chromite. The most interesting previously unreported result is that our microscope analysis showed sulphide inclusions visible in chromite grains (Fig 3.1.2h). These inclusions display negative crystal shapes imposed by the crystal structure of the host chromite. Similar trapped sulphide inclusions have been described from chromite in the Platreef by Holwell et al. (2011). These sulphide droplets can be indicative of early stage sulphide liquid in the system. These sulphide inclusions in the chromite can be used to

reveal the parental composition of sulphide melts within magmatic systems (Holwell & McDonald, 2011). Unlike the interstitial droplets that form when magma cools in an open system, these inclusions cooled and crystallized in a closed system enclosed in chromite. Holwell and McDonald (2011) interpreted their presence as early PGE-rich sulphide liquids with Pt/Pd ratios close to unity that supports the model of sulphide saturation and metal enrichment before intrusion.

Evidence of late hydrous fluid is presented in the form of abundant hydrous minerals and alteration features which occur throughout the Merensky reef. The most common hydrous mineral in the Merensky reef is phlogopite that occurs in all units of the Merensky reef (Fig. 3.1.6e). Other hydrous minerals identified in the Merensky reef is biotite. In addition to the presence of hydrous minerals alteration of primary igneous minerals is abundant. For example serpentinisation of clinopyroxene, which is constrained to the pegmatoidal layer in the pegmatoidal reef unit.

The major mineral chemistry across the Merensky reef, determined by electron microscopy is very variable. Vertical differences caused by the adcumulus/ intercumulus effect can be seen in the mineral chemistry and correlates well with the optical microscopy. Compositional variation in plagioclase, orthopyroxene and chromite between units provides information on the evolution of the Merensky reef. Using ranges and averages in core compositions of plagioclase (Table 3.2.1) as well as figure 3.2.1, various trends are identifiable. In figure 3.2.1 the composition of plagioclase covers a range from labradorite to bytownite.

In borehole SD14/90 and BH6259 the average An% (Table 3.2.1) decreases upward (from the chromitite to the hangingwall) (Fig. 3.2.2) indicating normal melt evolution. In the case of borehole 20/0252 (pegmatoidal reef) the average An% decreases from the top chromitite layer to the hangingwall, indicating normal melt evolution with a decrease from the top chromitite layer towards the pegmatoidal layer which could indicate a more evolved plagioclase. Trends of decreasing An content and CaO from the chromitite layer towards the hangingwall suggest that plagioclase evolves in composition towards this unit, while increase in Na<sub>2</sub>O from the chromitite layer towards the hangingwall reflects the degree of fractional crystallization in plagioclase (Barnes & Maier, 2002a). The footwall is part of a previous melt evolution that's why decreasing in average An% is seen from the chromitite layer to the footwall unit. Most of the plagioclase in the different lithologies covers a range from labradorite to bytownite.

As previously mentioned, plagioclase zoning was identified in the different lithologies of the Merensky reef especially in the footwall. This could explain the fluctuation in An% in Appendix C, Table C4 within samples for example 3NP1 An%-60.66 and 3NP2 An%-69.15. This could indicate reheating and can be evident of possible magma mixing in a chamber, causing a thermal exchange and a chemical interaction between the primitive magma and the resident more evolved magma (Seabrook et al., 2005).

Considering lateral variation there is no significant variance in the two non-pegmatoidal boreholes (Sd14/90 & BH6259). There is a slight decrease in the An% from the chromitite layer of the non-pegmatoidal reef to the top chromitite layer of the pegmatoidal reef.

In addition to a compositional analysis of plagioclase in the different lithologies, pyroxene compositions may elucidate key parameters in the formation of the Merensky reef. From the chemistry of the orthopyroxene in the non-pegmatoidal reefs (borehole SD14/90 & BH6259) one can see that the Mg# increases from the footwall (anorthosite) to the chromitite layer and then decreases from the chromitite layer to the hangingwall (feldspathic pyroxenite) (Fig. 3.2.2). This might seem like it's not a normal melt evolution, since a general decrease should be seen and an increase is observed from the footwall to the chromitite layer. But when looking at a cyclic unit (Merensky cyclic unit in this case) it should start with the chromitite layer then the pyroxenite layer and then the footwall layer. In this study we looked at the footwall (anorthosite layer) of the previous cyclic unit and then the chromitite and hangingwall of the next cyclic unit. In other words it still shows a general decrease in Mg# upwards, thus indicating normal melt evolution. In the pegmatoidal core section (borehole 20/0252) it is difficult to see a trend since not enough data points were obtained in the different lithologies.

The FeO content in both non-pegmatoidal Merensky reefs decrease from bottom to top with a distinctive decrease in the chromitite stringer and a distinctive increase in MgO, which is normal considering that most of the Fe is taken up in the chromite in the chromitite stringer (Table 3.2.2). Upon cooling the chromite becomes more enriched in Fe and exchanges with intercumulus orthopyroxene making the orthopyroxene more Mg rich, which explains the increase in MgO. (Appendix C table C.10 – C.14). En% in the non-pegmatoidal reef show a general decrease from the chromitite layer to the hangingwall of the sections (except for the decrease in the footwall), which could be interpreted as progressive melt evolution (Appendix

C. table C.11 &13). In the pegmatoidal reef a clear pattern can not be seen. (Appendix C. table C.15).

The composition of orthopyroxene in these units falls mostly in the enstatite field. This is evident in figure 3.2.3. The scatter of points from the enstatite to pigeonite field could be the result of the presence of clinopyroxene in orthopyroxene and in some cases it could represent exsolution lamellae corresponding to the optical mineralogy.

Looking at the horizontal difference the two non-pegmatoidal cores correlate with regard to Mg# in the hangingwall, footwall and chromitite layer (Table 3.2.2). There is a significant difference in the Mg# of the footwall from the non-pegmatoidal layer and the footwall of the pegmatoidal layer. The increase in Mg# in the pegmatoidal layer is because of the lower FeO and higher MgO compared to the non-pegmatoidal layer. The reason for this could be the presence of chromite in the section next to the chromite stringer (where only one sample was analysed) and during cooling the chromite becomes more enriched in Fe and exchanges with intercumulus orthopyroxene making the orthopyroxene more Mg rich. The Mg# of the bottom chromitite stringer is also significantly different from the chromitite stringer of the non-pegmatoidal reef, it is difficult to determine what the cause could be without any data from the top chromitite stringer, to see how it correlates with the single chromitite stringer.

The composition of clinopyroxene in these units cover a range from diopside to augite. This is evident in figure 3.2.3. The scatter of points from the diopside to augite field could represent exsolution lamellae corresponding to the optical mineralogy. The chemistry of the two non-pegmatoidal reefs show good correlation (Table 3.2.3). The average Mg# (86.16) of the two chromitite stringers in the pegmatoidal reef correlate with the Mg# (86.10) of the non-pegmatoidal reef. This could indicate that the single chromitite stringer could be a composite. The Mg# in the pegmatoidal reef seems to decrease from the hangingwall to the pegmatoidal layer with an increase in the bottom chromitite layer. The bottom chromitite layer contains much lower FeO and higher CaO.

From the chromite data it is clear that there is a correlation between Cr<sub>2</sub>O<sub>3</sub> of the single chromitite stringer in the non-pegmatoidal reef (borehole BH6259) and the top chromitite stringer in the pegmatoidal reef (Fig. 4.1.1) (borehole 20/0252), but a significant correlation between the rest of the elements of the single chromitite stringer in the non-pegmatoidal reef (borehole BH6259) and the bottom chromitite stringer in the pegmatoidal reef (borehole

20/0252), see table 4.1. There is a significant difference between the top and the bottom chromitite stringer in the pegmatoidal reef. When looking at borehole SD14/90 the chromitite layer is very thick and can be divided into the upper part and the lower part as seen by Hutchinson et al., (2015). The Cr<sub>2</sub>O<sub>3</sub> of the upper part correlates with the upper chromitite layer of the pegmatoidal reef (borehole 20/0252) and the Cr<sub>2</sub>O<sub>3</sub> of the lower part correlates with the lower chromitite layer of the pegmatoidal reef (borehole 20/0252) (see table 4.1 and figure 4.1.1). The rest of the elements in both the upper and lower part of the chromitite layer of the non-pegmatoidal reef, borehole SD14/90 correlates with the bottom chemistry of the pegmatoidal reef, borehole 20/0252, see table 4.1. Data from the chromite in the pegmatoidal layer show no correlation with any of these layers. It is also clear that the chromite from the single chromitite stringer (non-pegmatoidal reef) and the chromite from the bottom chromitite stringer (pegmatoidal reef) are from a more primitive magma (high Mg#, high Cr<sub>2</sub>O<sub>3</sub> and high Al<sub>2</sub>O<sub>3</sub>) and the chromite from the top chromitite stringer are from a more evolved magma (lower Mg# and lower Al<sub>2</sub>O<sub>3</sub>). This is evident in figure 4.1.2 and 4.1.3a-b.

In a recent publication by Cawthorn and Wansbury (2014) they stated that there is a correlation between the chromitite stringer from the non-pegmatoidal reef and the top chromitite stringer from the pegmatoidal reef. From data presented in appendix C, table C.22 – C.24, it is clear that this is not the case in these core sections. Further investigation is needed to investigate these differences. Data indicate that there is a correlation regarding Cr<sub>2</sub>O<sub>3</sub>, but when looking at the rest of the mineral chemistry the correlation changes and further investigation on more samples is necessary to determine whether this is lateral or just a local variation.

The subhedral phlogopite is commonly interstitial but in some sections euhedral crystals are observed. The chemistry of phlogopite shows a significant MgO increase and a FeO and Fe<sub>2</sub>O<sub>3</sub> decrease in the chromitite layer. This may represent subsolidus exchange with chromite (Table 3.2.5).

The mineral chemistry of chalcopyrite, pyrrhotite, pentlandite and pyrite seems fairly constant throughout the different lithologies and no significant differences between the different reefs (pegmatoidal and non-pegmatoidal) are observed (Table 3.2.6a – d).

**Table 4.1: Average chromite chemistry data in the various chromitite layers for the various boreholes. Major element oxides in wt%.(Cr/(Cr+Al) calculated using molar values.**

	SiO <sub>2</sub>	CaO	TiO <sub>2</sub>	Al <sub>2</sub> O <sub>3</sub>	FeO	Fe <sub>2</sub> O <sub>3</sub>	ZnO	MnO	NiO	V <sub>2</sub> O <sub>3</sub>	MgO	Cr <sub>2</sub> O <sub>3</sub>	Total	Mg#	Cr/(Cr+Al)	Cr/(Cr+Fe)
Top Chr layer	0.12	0.01	2.74	12.38	29.30	8.14	0.19	0.28	0.25	0.65	5.68	41.45	100.38	58.07	0.69	0.57
Bottom Chr layer	0.12	0.02	1.02	16.61	24.16	6.71	0.05	0.27	0.18	0.33	7.17	44.26	100.23	67.92	0.64	0.59
Single N 98	0.04	n.d.	0.99	19.52	23.45	6.52	0.17	0.27	0.16	0.29	8.09	41.66	100.52	71.11	0.59	0.57
Top (5-6NP)	0.07	0.01	0.92	18.74	23.98	6.66	0.11	0.29	0.15	0.25	7.87	41.55	99.94	70.08	0.60	0.52
Bottom (7NP)	0.101	0.08	0.82	18.05	23.52	6.53	0.21	0.31	0.15	0.24	7.48	44.27	101.09	69.42	0.62	0.58

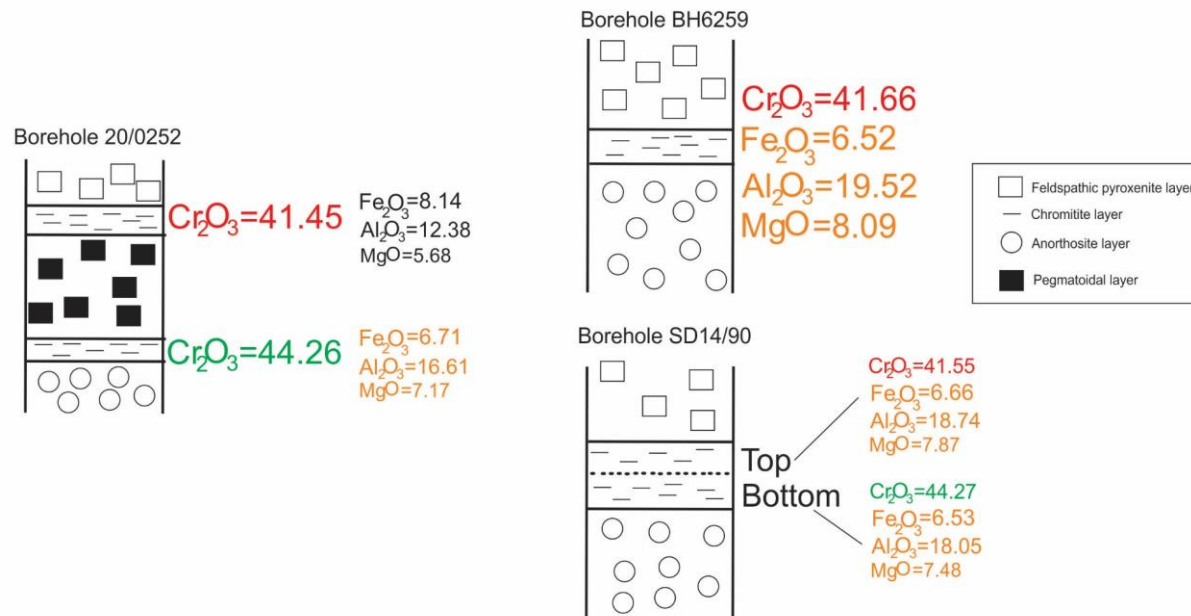


**Figure 4.1.1: Schematic diagram of the pegmatoidal Merensky reef, borehole 20/0252 (with two chromitite stringers); the non-pegmatoidal reef (one chromitite stringer) borehole BH6259 and the non-pegmatoidal reef (one chromitite stringer) borehole SD14/90 with the average chromite chemistry data in the various chromitite layers.**

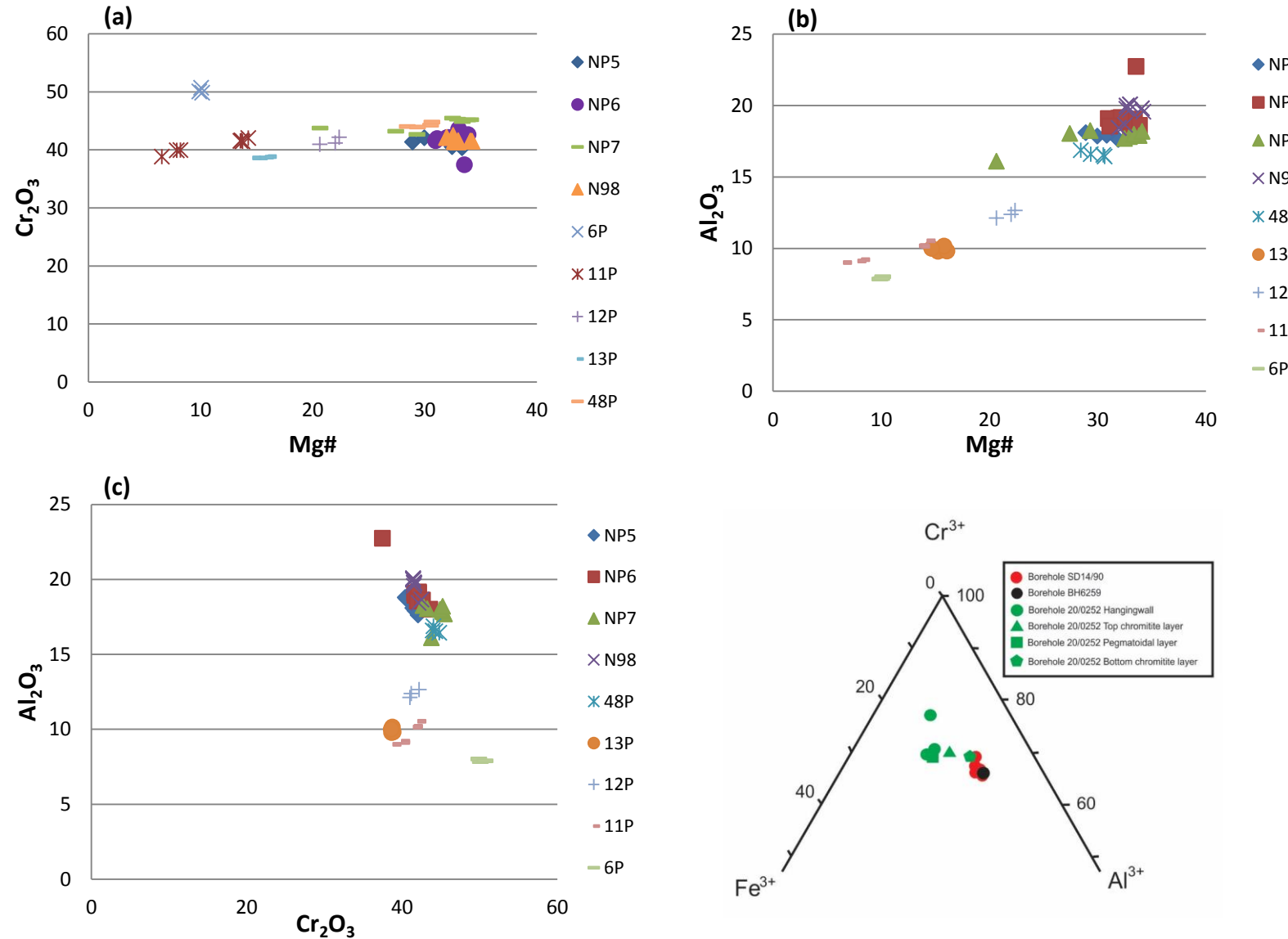


Figure 4.1.2: The various chromitite stringer data plotted. (a)  $\text{Mg}\#$  vs  $\text{Cr}_2\text{O}_3$ , (b)  $\text{Mg}\#$  vs  $\text{Al}_2\text{O}_3$ , (c)  $\text{Cr}_2\text{O}_3$  vs  $\text{Al}_2\text{O}_3$ . NP5 – NP7: borehole SD14/90; N98: borehole BH6259; P11 – P13 and P48: borehole 20/0252.

## 4.2 Whole rock major element data

Whole rock major oxide element profiles (Fig 3.3.1 – 3.3.2) are consistent with control by the dominant rock-forming minerals identified during petrographic investigation. In the non-pegmatoidal reefs, the anorthositic footwall has the highest  $\text{Al}_2\text{O}_3$ ,  $\text{CaO}$  and  $\text{Na}_2\text{O}$  patterns of enrichment, which coincide with the presence of plagioclase rich lithologies in which plagioclase is present as a cumulus phase. The pyroxenitic hangingwall has the highest  $\text{MgO}$  concentrations which coincide with the presence of pyroxenite rich lithologies, in which pyroxene is present as a cumulus phase.  $\text{Cr}_2\text{O}_3$  is the highest in the chromitite stringers. In the pegmatoidal reef the trends are less clear. There is a slight indication of a steady decrease in  $\text{Al}_2\text{O}_3$  and  $\text{CaO}$  from bottom to top of the section, but the trends of the other oxides are irregular. The  $\text{Cr}_2\text{O}_3$  of the two chromitite stringers in the pegmatoidal reef are lower than those of the non-pegmatoidal reefs, indicating that the chromite is more disseminated. The  $\text{SiO}_2$ ,  $\text{TiO}_2$  and  $\text{MnO}$  follow the trends expected from a crystallising magma; i.e. they increase steadily from bottom to top of all three boreholes. There is a good agreement between the modal mineralogy and the norm; however normative plagioclase is somewhat lower than the modal plagioclase.  $\text{NiO}$  show an increase in the hangingwall and chromitite layer of all three boreholes this could be because of the increase in BMS such as pentlandite in these lithologies.

With a decrease in Mg# from the footwall to the chromitite layer and an increase in Mg# from the chromitite layer to the hangingwall. A decrease in Mg# in the chromitite stringer can be attributed to the increase in FeO in the chromitite stringer causing a decrease in the Mg# because of subsolidus exchange (Fig. 3.3.1).

Plots of  $\text{Cr}/(\text{Cr}+\text{Fe}^{3+})$  and  $\text{Cr}/(\text{Cr}+\text{Al})$  metal ratios in figure 3.3.1 show a decrease in  $\text{Cr}/(\text{Cr}+\text{Fe}^{3+})$  from bottom to top in the chromitite layer in borehole SD14/90. In the other chromitite stringers of borehole BH6259 and 20/0252 this is less clear because the chromitite stringers are much thinner. In borehole SD14/90 a decrease in  $\text{Cr}/(\text{Cr}+\text{Al})$  from top to bottom can be seen. The reason for the change in ratio from bottom to top can be explained by normal melt evolution, as the melt gets relatively depleted in  $\text{Cr}^{3+}$  over  $\text{Fe}^{3+}$ , the latter which is slightly less compatible in the chromite lattice. In borehole SD14/90 a decrease in  $\text{Cr}/(\text{Cr}+\text{Al})$  from top to bottom in the chromitite stringers indicate the increase in plagioclase precipitation. The

highest value of Cr/Cr+Al and Cr/Cr+Fe ratio is associated with the highest Mg#, thus they behave mirror-inverted as one decrease the other increase.

In figure 3.3.2 changing whole rock An% show a general decrease from bottom to top which reflects the changes in major mineralogy. TiO<sub>2</sub> is particularly enriched in the chromitite stringer, this could reflect the presence of Ti-bearing phases such as ilmenite and rutile but no ilmenite and rutile was observed during the petrographic analysis of this study, suggesting that the increase in TiO<sub>2</sub> could be accommodated by chromite.

In the ternary diagram, An, Ab and Or, most of the data plot in the labradorite, bytownite and anorthite fields with a few in the 2 feldspar region (figure 3.3.3). This is probably due to mica in the unit, since no orthoclase was observed in the mode. From the ternary diagram it is also evident that the major element trends reflect the changes in major mineralogy. With most of the whole rock compositions in the footwall falling in the anorthite range and the hanging wall falling in the labradorite field. This is also reflected in the An% decreasing from the bottom to the top in the whole rock major element chemistry.

Compositional ranges of the major element oxides in the non-pegmatoidal and pegmatoidal Merensky reef are displayed as bivariate plots with MgO as the differentiation index in figure 4.2.1-4.2.3. It can also be seen in Appendix D (figure D.1-D.3), where the different units are expressed to see the difference with depth. Compositions of plagioclase, orthopyroxene, clinopyroxene and chromite determined by electron microprobe were also plotted on these bivariate plots. This was done to see if the whole rock data correlate with the in-situ mineral data (EMPA data).

In all three boreholes it is notable that there is a positive correlation between MgO vs. SiO<sub>2</sub>; MgO vs MnO; MgO vs FeO and MgO vs TiO<sub>2</sub>. Most of the samples plot inside the compositional fields defined by plagioclase, orthopyroxene, clinopyroxene and chromite. MgO vs Al<sub>2</sub>O<sub>3</sub>; MgO vs CaO; MgO vs Na<sub>2</sub>O and MgO vs Cr<sub>2</sub>O<sub>3</sub> show negative linear correlation between them.

**MgO vs Al<sub>2</sub>O<sub>3</sub>:** Show a negative linear correlation. Al<sub>2</sub>O<sub>3</sub> decreases from chromitite layer to the hangingwall with increasing MgO, which is caused by decreasing amounts of intercumulus plagioclase and chromite precipitating thus consuming less Al<sub>2</sub>O<sub>3</sub>.

**MgO vs Fe<sub>tot</sub>:** The total amount of Fe is influenced by the crystallisation of orthopyroxene, clinopyroxene and chromite. The general trend is a positive linear trend. With increasing MgO the FeO<sub>tot</sub> also increase. This trend implies increasing amounts of chromite, orthopyroxene and clinopyroxene within these layers.

**MgO vs MnO:** The major trend is a positive relation with increasing amounts of MgO and MnO, Fe<sup>2+</sup> and Mg<sup>2+</sup> is often substituted by Mn<sup>2+</sup> due to its valence, which can be in the orthopyroxene and chromite lattice. Thus an increase in orthopyroxene up in the sequence is present. Decreasing MgO and MnO simultaneously is caused by decreasing amounts of orthopyroxene and increasing plagioclase towards the anorthosite layer.

**MgO vs CaO:** CaO is mostly controlled by plagioclase and to a lesser extent by clinopyroxene. The CIPW norms show a decrease in the plagioclase from the bottom to the top and the clinopyroxene doesn't show a definite trend. This could explain the varying CaO concentrations in the different layers. Thus with decreasing MgO the CaO increases, indicating a decrease in pyroxene precipitation and an increase in plagioclase precipitation.

**MgO vs Cr<sub>2</sub>O<sub>3</sub>:** An overall negative correlation can be seen. Within the binary plot three distinct plots can be seen. One show low Cr<sub>2</sub>O<sub>3</sub> and low MgO which are present in the anorthosite layer where both MgO and Cr<sub>2</sub>O<sub>3</sub> concentrations are low. The second group is high in MgO with a low Cr<sub>2</sub>O<sub>3</sub> concentration, which are present in the hanging wall where there is an increase in pyroxene and not so much chromite. The third group show an average amount of MgO and Cr<sub>2</sub>O<sub>3</sub>.

**MgO vs Na<sub>2</sub>O:** Whole rock Na<sub>2</sub>O is mostly controlled by plagioclase and an overall negative trend can be seen. Where Na<sub>2</sub>O increases MgO decrease due to the decrease in pyroxene and the increase in plagioclase, which implies normal fractionation of the melt.

**MgO vs TiO<sub>2</sub>:** TiO<sub>2</sub> in whole rock is mostly controlled by chromite, thus a more or less similar trend can be seen between MgO vs TiO<sub>2</sub> and MgO vs Cr<sub>2</sub>O<sub>3</sub>. Thus indicating a normal fractional crystallization pattern.

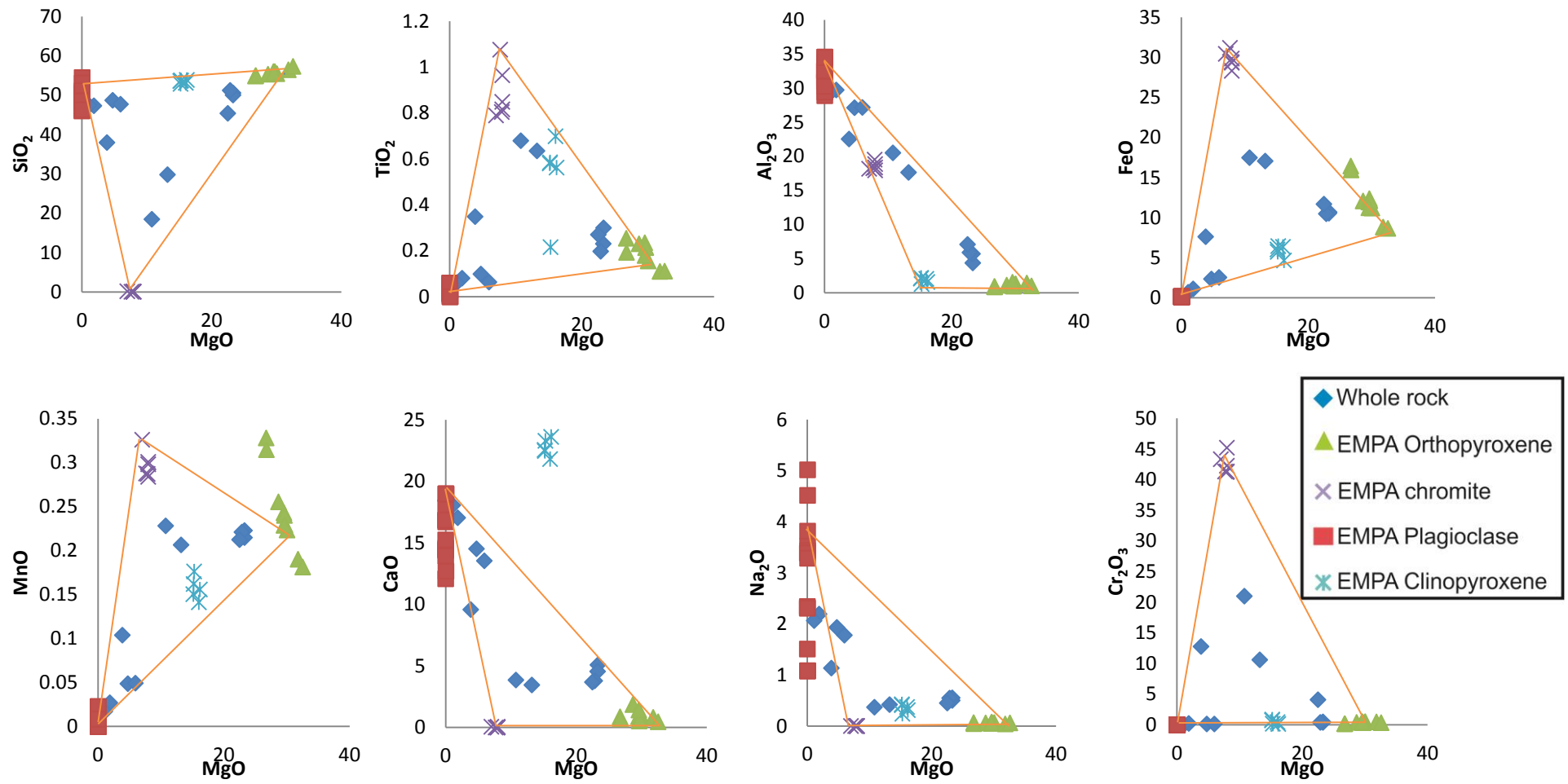
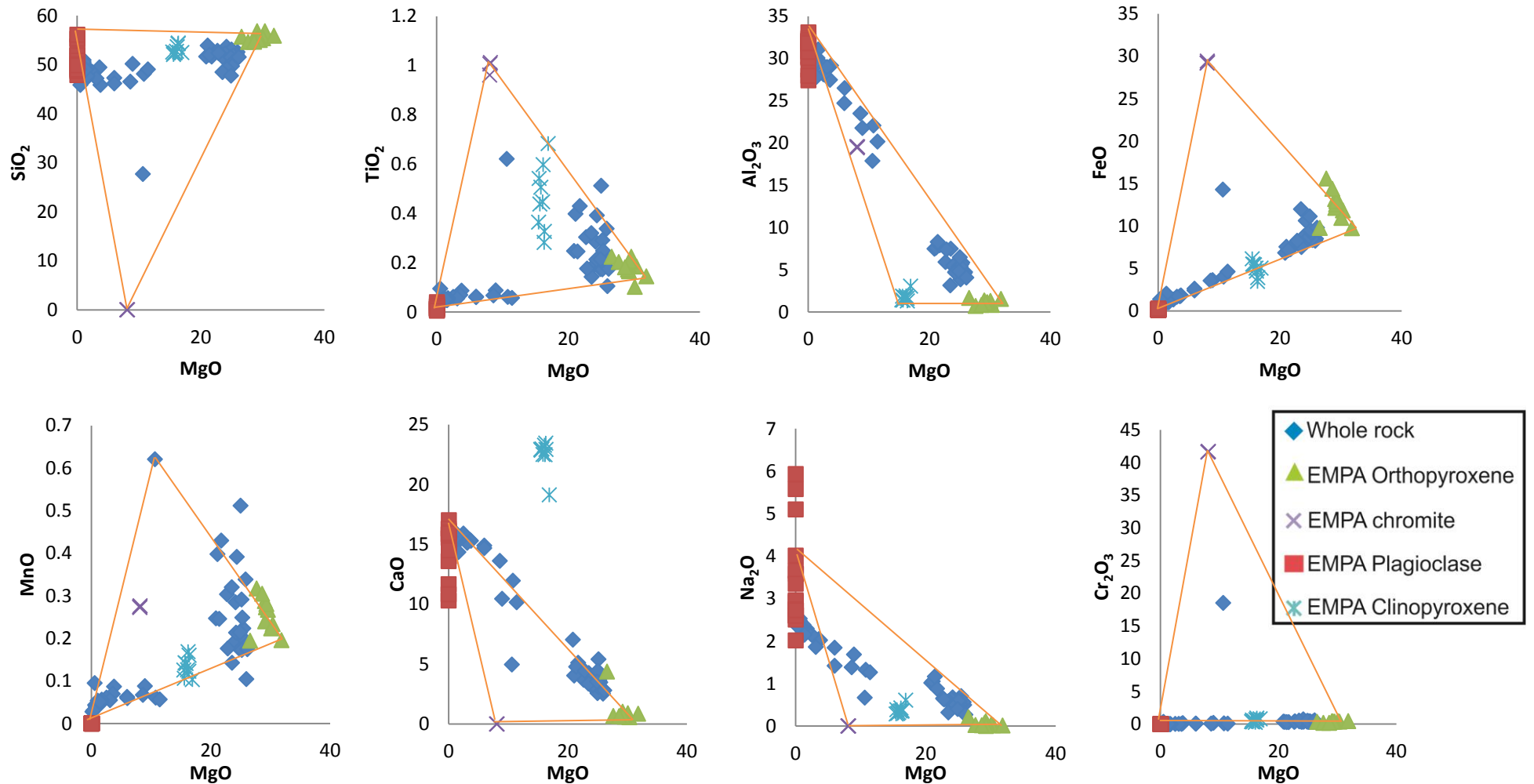


Figure 4.2.1: Major element oxides vs  $\text{MgO}$  for EMPA (orthopyroxene, clinopyroxene, plagioclase and chromite) and whole rock analysis from borehole SD14/90.



**Figure 4.2.2: Major element oxides vs MgO for EMPA (orthopyroxene, clinopyroxene, plagioclase and chromite) and whole rock analysis from borehole BH6259.**

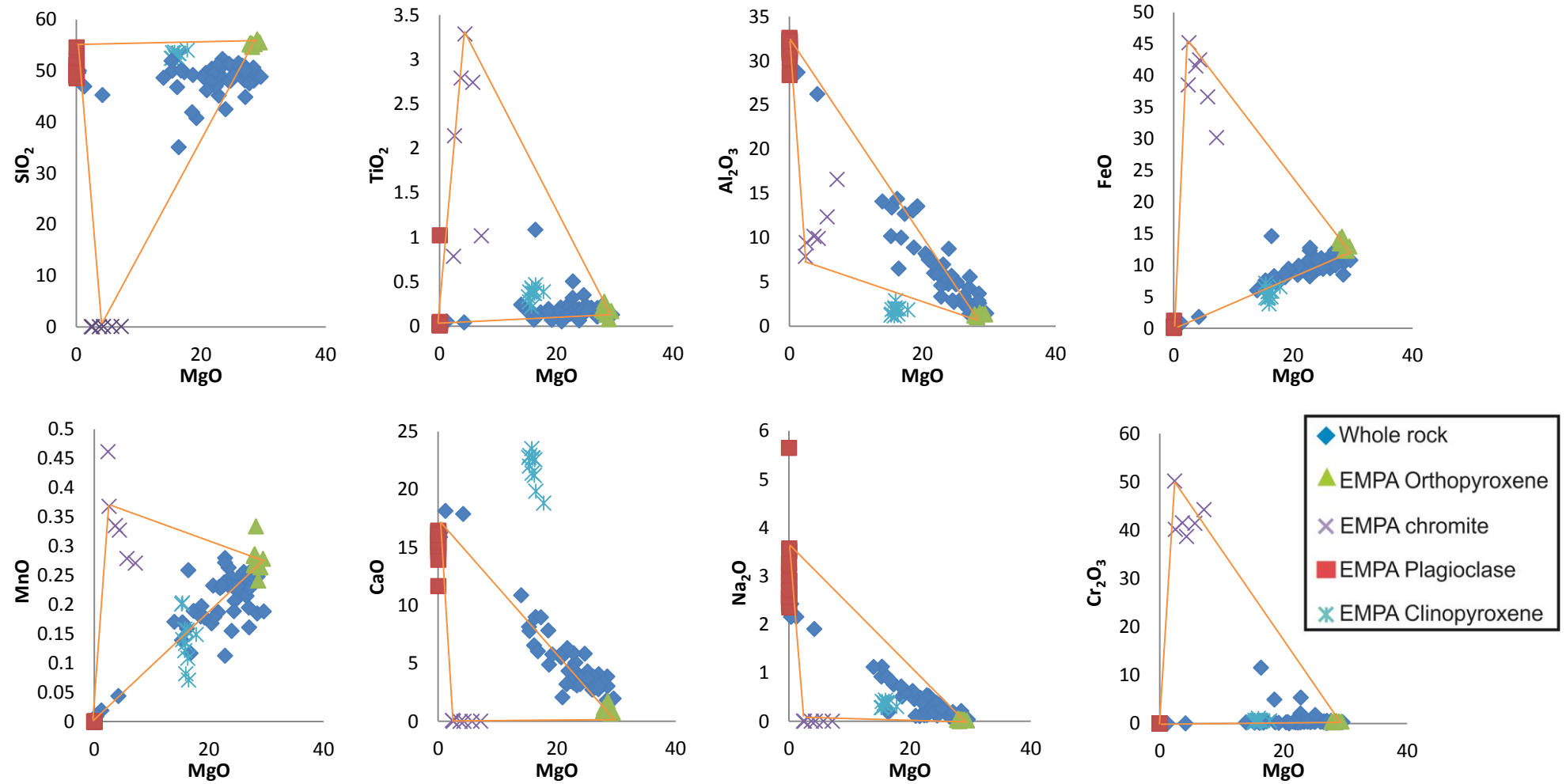


Figure 4.2.3: Major element oxides vs MgO for EMPA (orthopyroxene, clinopyroxene, plagioclase and chromite) and whole rock analysis from borehole 20/0252.

### 4.3 Whole rock trace element data

The REE concentrations of cumulates are largely governed by the relative amount of postcumulus material, which is difficult to determine. REE behave incompatible to chromite, which is the major cumulus phase within the chromitite stringers. REE also behave as incompatible elements towards intercumulus phases like pyroxene and plagioclase. An exception is Eu which is compatible with plagioclase, thus the REE chondrite normalized patterns of the footwall rocks have positive Eu anomalies. The chromitite of the non-pegmatoidal reefs and the bottom chromitite stringer of the pegmatoidal reef also have a positive Eu anomaly, but the top chromitite of the pegmatoidal reef has a negative Eu anomaly (Fig 3.4.1).

REE plots suggest a small amount of local differentiation with respect to La in the top chromitite layer. Whether this is a local or general characteristic can only be determined by analysing more sections from the pegmatoidal Merensky reef. With the exception of Eu which is compatible in plagioclase the REE are incompatible in the major cumulus phases (orthopyroxene and clinopyroxene and chromite). Apart from minor apatite, the minerals that concentrate light REE such as monazite, allanite, sphene or epidote were not observed. In the absence of these phases, we concluded that the concentration of the REE is governed mainly by the amount of trapped liquid and concentration of clinopyroxene (Fig. 3.4.1).

Figure 4.3.1 show average chondrite normalized multi-element diagrams for the different boreholes. More elaborate chondrite normalized multi-element diagrams for each unit of the different boreholes are in Appendix E, figure E.1 – E.6. Normalization values are from Lodders (2003). The positive Sr peaks of the footwall rocks and in some of the chromitite stringers reflect the occurrence of cumulus plagioclase within these layers. The positive TiO<sub>2</sub> anomalies in the hangingwall and chromitite layer is due to the presence of TiO<sub>2</sub> in the chromite lattice. In borehole 20/0252 positive and negative Tb anomalies are evident in the different units.

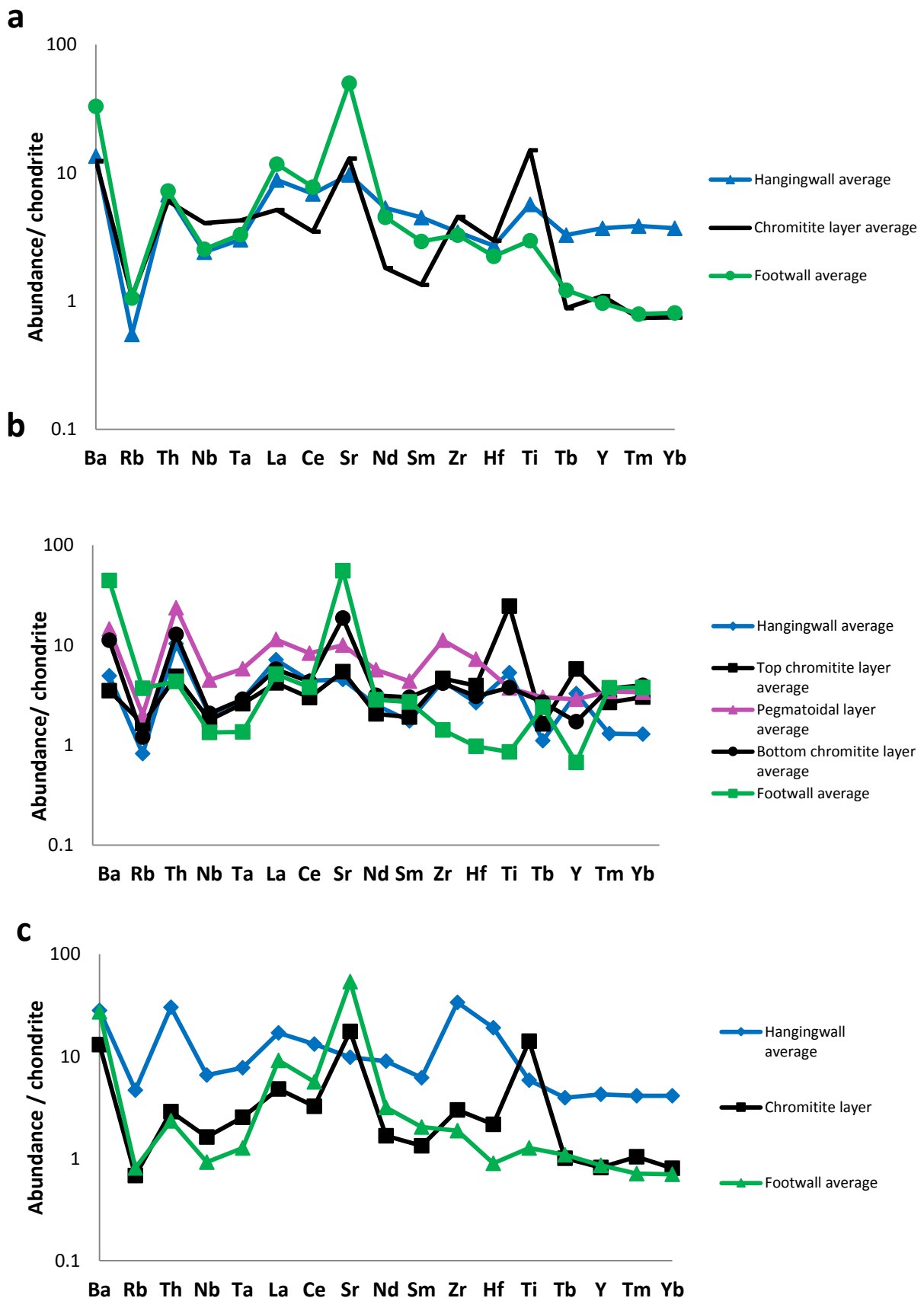


Figure 4.3.1: Chondrite-normalised multi element diagrams for borehole a) SD14/90; b) BH6259 and c) 20/0252. Normalisation values from Lodders (2003).



#### 4.4 PGE data

Three possible processes are considered to explain the observed PGE mineralisation of the Merensky reef. The formation of the Merensky reef could be a result of any one, or the combination of any or all three these processes.

The collection of PGE by an immiscible sulphide liquid. This model is the most popular model. It was shown that  $\pm 95\%$  of PGM in the Merensky reef chromitites are associated with BMS especially at the borders of silicates, chromites and sulphides, because of this numerous authors have favoured this orthomagmatic model (Barnes & Maier, 2002a, 2002b; Campbell et al., 1983 and Naldrett, 1999). Campbell et al. (1983) suggested that magma mixing between resident (evolved magma) and a new injection of primitive magma produces sulphide saturation and ultimately an immiscible sulphide liquid. The PGE will be collected by the immiscible sulphide liquid, due to the high partitioning coefficient of PGE into sulphide liquid. Cawthorn (2002) argued that magma mixing alone will not produce sulphide saturation, he suggested crustal contamination as a source of sulphide oversaturation. It has been suggested by Barnes and Maier (2002b) that the sulphide collection model could be repeated at the start of each cyclic unit within the Lower and Critical Zone. They also suggested that sometimes sulphide liquid may have percolated downwards through the cumulate pile and enriching the underlying mafic rocks in PGE. However observations from this study indicate that the anorthosite footwall is depleted in PGE (Table 3.5.1). The pegmatoidal layer of borehole 20/0252 show enrichment in PGE, therefore, this model could account for the enrichment in the pegmatoidal layer of the pegmatoidal Merneksy reef.

Based on analysis by Lee (1983), he divided metals from the Merensky reef into two groups. 1) Ni, Cu, Au and Pd and 2) Ir, Rh, Pt and Cr. He suggested that Pd and Au were controlled by sulphides (Barnes and Maier, 2002b) and that Pt, Ir and Rh were controlled by PGM or spinel. These assumptions are significant for observations made in this study. For example, figure 3.5.1a – b (borehole SD14/90 and BH6259; non-pegmatoidal Merensky reef) show that most of the PGE follow Cr (the black curve) very closely; especially in the chromitite stringer. There is a slight indication of PGE following S in the footwall of these two boreholes. In figure 3.5.1c (borehole 20/0252; pegmatoidal Merensky reef) the trend is slightly more irregular with PGE following the Cr trend in the top and bottom chromitite stringers

and in the footwall. In the hangingwall and parts of the pegmatoidal layer the PGE follow the S trend. Cu shows a strong correlation with S in all three cases which is suspected. What was also of interest is the Cu/Pd ratio showing the exact opposite trend as the Cr especially in the non-pegmatoidal Merensky reefs. Pd however also seem to follow the Cr trend.

This enrichment is also evident in the chondrite normalized PGE trends. All the elements follow the positive trend on the chondrite normalized plots, typical of mafic igneous rocks. The chondrite normalised patterns showed a relative enrichment in Pd relative to Pt in the footwall and a relative depletion in Pd relative to Pt in the hangingwall.

Figure 4.4.2 – 4.4.4 show binary variation diagrams of the various boreholes. This helps to assess the nature of the different phases controlling the PGE. For borehole SD14/90 and BH6259 (figure 3.5.7 and 3.5.8) Pt shows a relatively good correlation with Pd and Pd shows a good positive correlation with Ir. There is not a good correlation between Pt and Cu and Pd and Cu. Pt and Pd do not show good positive correlations with S, which also supports the evidence in figures 3.5.1a - b. For borehole 20/0252, Pt shows a relatively good correlation with Pd and Pd shows a relatively good positive correlation with Ir. The outliers in these diagrams may be due to the later remobilization of PGE. Pt and Pd show a relatively good correlation with S. The correlation between Pd and Cu is much better than the correlation between Pt and Cu but is still fairly weak. The PGE show a good positive correlation with each other, this could imply that the PGE are essentially controlled by the same phase. The PGE do not show a good correlation with Cu, this could suggest the possibility of remobilisation of Cu.

The correlation between S and PGE is also not good which may suggest that most of the PGE are not hosted by sulphides and that S wasn't the primary metal collector. The lack of correlation between PGE and Cu and PGE and S could suggest that BMS played a subordinale role in PGE fractionation.

Pt/Pd and Cu/Pd ratios are useful geochemical tools for inferring primary magmatic processes. Processes like fractional segregation of sulphides from a magma and scavenging by sulphide liquids (Barnes & Maier, 2002band Wilson & Chunnett, 2006). In this study the pegmatoidal layer (borehole 20/0252) and the hangingwall of all three boreholes is characterised by high Cu/Pd and Pt/Pd ratios relative to the footwall, suggesting that sulphide

underwent fractional segregation and that the hangingwall experienced significant scavenging by sulphide liquids (Wilson & Chunnett, 2006).

This is also reflected in the Pt/Pd ratios (table 4.4) for all the reef types. The chromitite stringers are most depleted in Pd relative to Pt, with the bottom chromite stringer of the pegmatoidal reef being more enriched than the top one. The spatial separation of maximum Pd and Pt concentrations is interpreted as an indication that Pd is controlled more by the sulphide fraction than is the case with Pt.

**Table 4.4: Pt/Pd ratios for the various lithological units in the three boreholes with Merensky reef intersection. NA: not applicable; FW, footwall; HW hanging wall; peg, pegmatoidal.**

Borehole	FW	1 <sup>st</sup> Chr	Peg layer	2 <sup>nd</sup> Chr	HW
<b>SD14/90</b>	1.00	7.12	NA	NA	2.47
<b>BH6259</b>	1.03	4.96	NA	NA	2.08
<b>20/0252</b>	2.16	8.20	1.99	4.02	3.26

Collection and redistribution of PGE by late magmatic/hydrothermal fluid: This has become a popular model to explain for PGE distributions in mineralised reefs (Boudreau & Maier, 1999). Upward migration of Cl-rich intercumulus fluids dissolves local sulphides, this causes the release of PGE and base metals, which can partition into the fluid. The fluid then rises up through the cumulate pile until it encounters a layer in which the intercumulus fluid is water undersaturated. The fluid is then dissolved into the intercumulus silicate liquid and the S, PGM and base metals are then reprecipitated as BMS to form a reef.

Petrographic evidence (for this study) for this model of collection and redistribution is discussed in subsection 3.1. Boudreau & Maier (1999) suggested that hydrous silicates and associated alteration features in the Merensky reef can crystallize in proximity to BMS from volatile-enriched intercumulus melts. This would explain the association often seen in this study between BMS and hydrous silicate/alterations. However this could also be explained by the interaction and replacement of silicates by BMS in which biotite and phlogopite are formed as an alteration and reaction product (Vermaak & Hendriks, 1976).

Godel et al. (2007) stated that there was one major problem with this model and that is, that it has difficulty in accounting for the stratigraphically higher chromitite layer in the Merensky reef. He suggested that the fluid would have been depleted in S and metals by the time it reached the second chromitite layer, although it could account for the first lower chromitite layer. In this study the pegmatoidal Merensky reef contains two chromitite stringers and the

upper chromitite stringer contains higher Pt concentrations than the bottom chromitite stringer (toploaded), for this reason I don't think this model applies for the pegmatoidal reef but can still account for the non pegmatoidal reef with the one chromitite stringer.

Crystallization of PGE and PGM: One of the examples is presented by Tredoux et al. (1995), which suggest that PGE amalgamate together as aggregates or rather as clusters which preconcentrate the PGE. The IPGE, which are heavier than the PPGE, are more likely to form clusters. This model predicts the enrichment of Os, Ir, Ru (and possible Rh). In a sulphur-poor environment, these clusters eventually merge to form PGE alloys, which may act as nucleation sites for early formed oxides. In this study enrichment of the IPGE and the PPGE (Ir, Os, Ru, Rh, Pd and Pt) were recorded in the chromitite unit, especially the top chromitite stringer, thus top loaded. This indicates that the same phase is controlling Ir, Os, Ru, Rh, Pd and Pt. These observations would suggest that chromite is the PGE controlling phase in these sequences.

From the observations from these three models it is suggested that a combination of processes are required to account for the distribution of PGE. The enrichment of Ir, Os, Ru, Rh, Pd and Pt in the upper and lower chromitite stringer or single chromitite stringer can be accounted for by a model involving the crystallization of PGE as PGM and the co-precipitation of chromite. Redistribution of PGE by late magmatic/hydrothermal fluids could account for the non-pegmatoidal reef but not for the pegmatoidal Merensky reef. The fractionation of sulphide liquids has important implications for the observed PGE distribution in the pyroxenite (hangingwall) unit and in the pegmatoidal layer. The collection process of PGE by immiscible sulphide liquid may have been enhanced through the amount of time that the immiscible sulphide liquid spent within the silicate magma. Thereafter the sulphides percolated downwards through the cumulus pile displacing the interstitial liquid and enriching the underlying rocks in S and PGE, which account for the enrichment underlying the upper chromitite stringer.

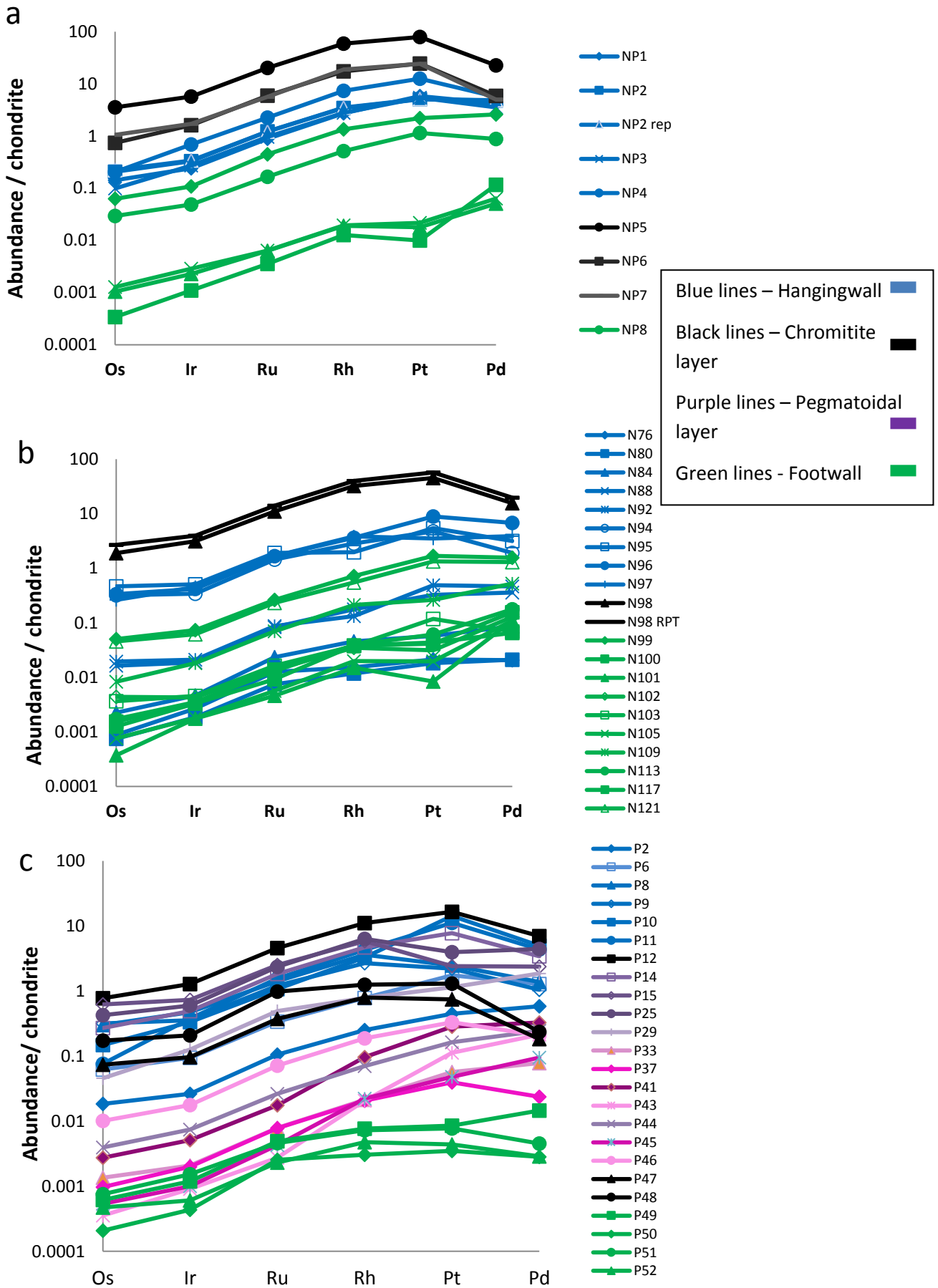


Figure 4.4.1: Chondrite normalized PGE patterns for borehole a) SD14/90; b) BH6259 and c) 20/0252. C1 chondrite normalized values are from Lodders, (2003).

## **4.5 Comparison of whole rock data with mineral chemistry**

In figure 4.4.5a-c mineral chemistry is compared to whole rock major element An%, it is clear that there is an excellent correlation between the An% of the mineral chemistry and that of the whole rock analysis in the non-pegmatoidal Merensky reef. In the case of the pegmatoidal reef it is not so clear, because of the irregular trends of the mineral chemistry, but an overall increase can be seen from top to bottom. Similar results can be seen where the mineral chemistry and whole rock analysis of Mg# is compared (figure 4.4.5d-f).

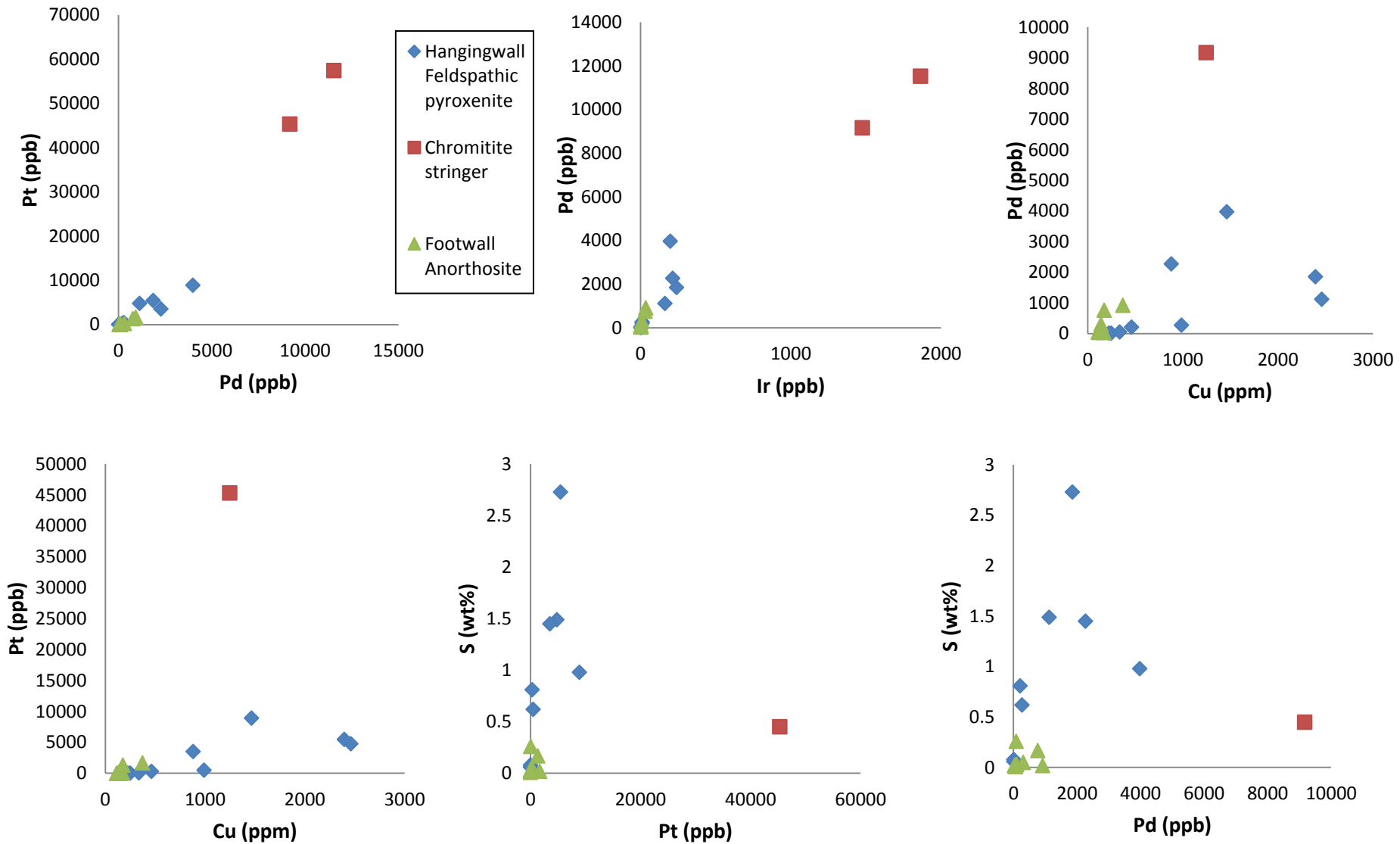


Figure 4.4.2: Binary variation diagrams of Pt, Pd, Ir, Cu and S for the non-pegmatoidal Merensky reef from borehole BH6259.

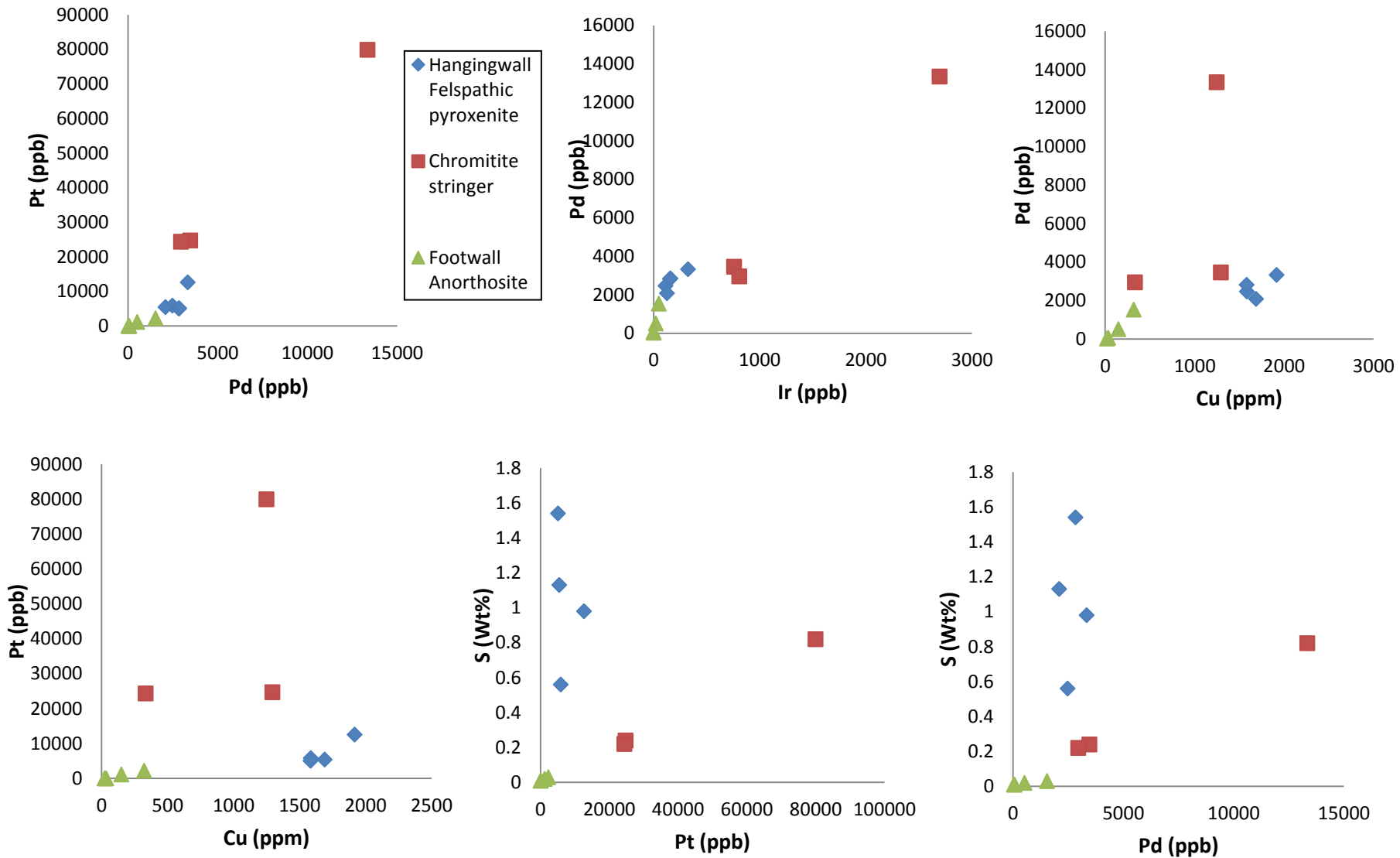


Figure 4.4.3: Binary variation diagrams of Pt, Pd, Ir, Cu and S for the non-pegmatoidal Merensky reef from borehole SD14/90.

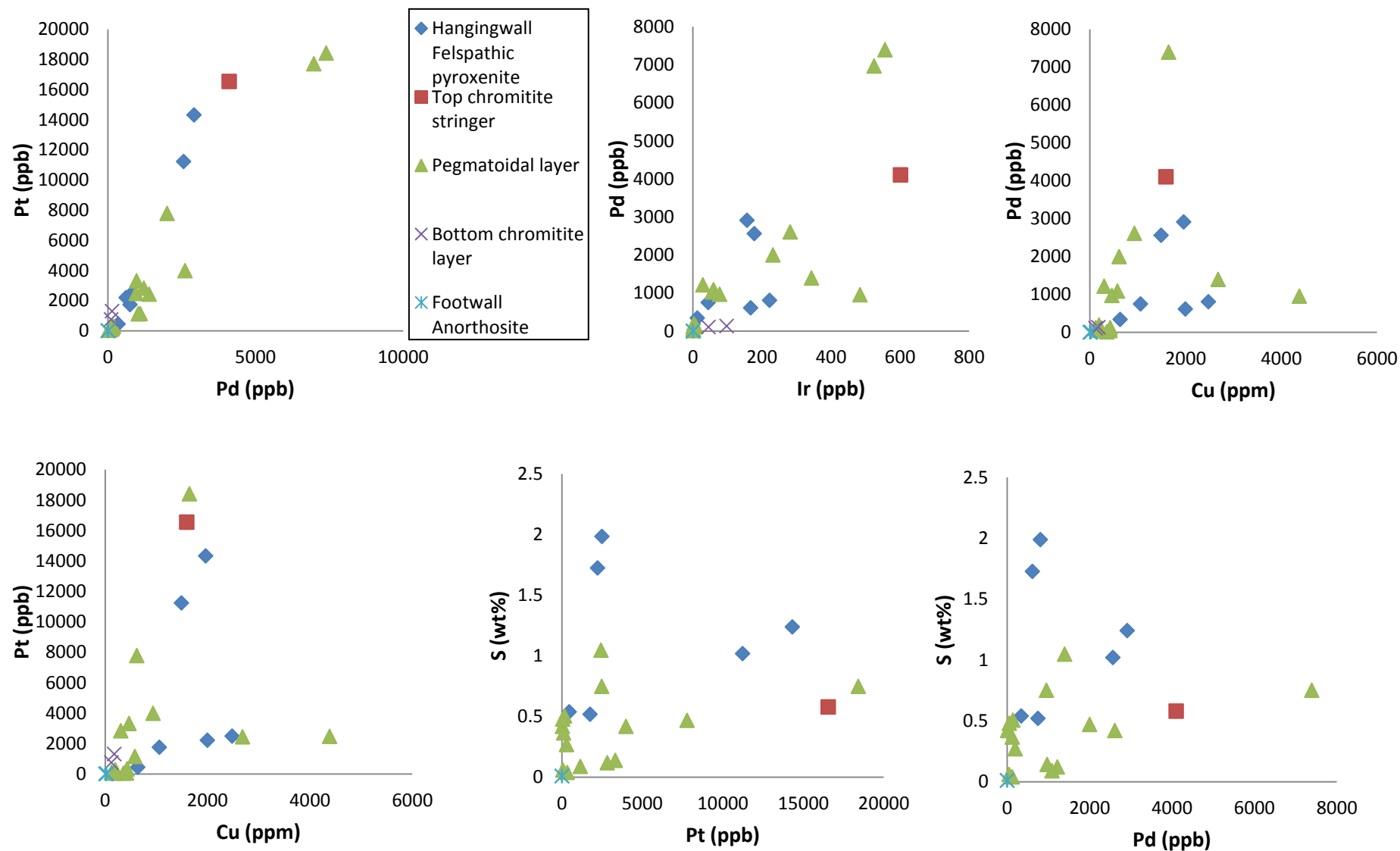


Figure 4.4.4: Binary variation diagrams of Pt, Pd, Ir, Cu and S for the pegmatoidal Merensky reef from borehole 20/0252.

#### 4.5 Comparison between mineral chemistry and whole rock major element analysis

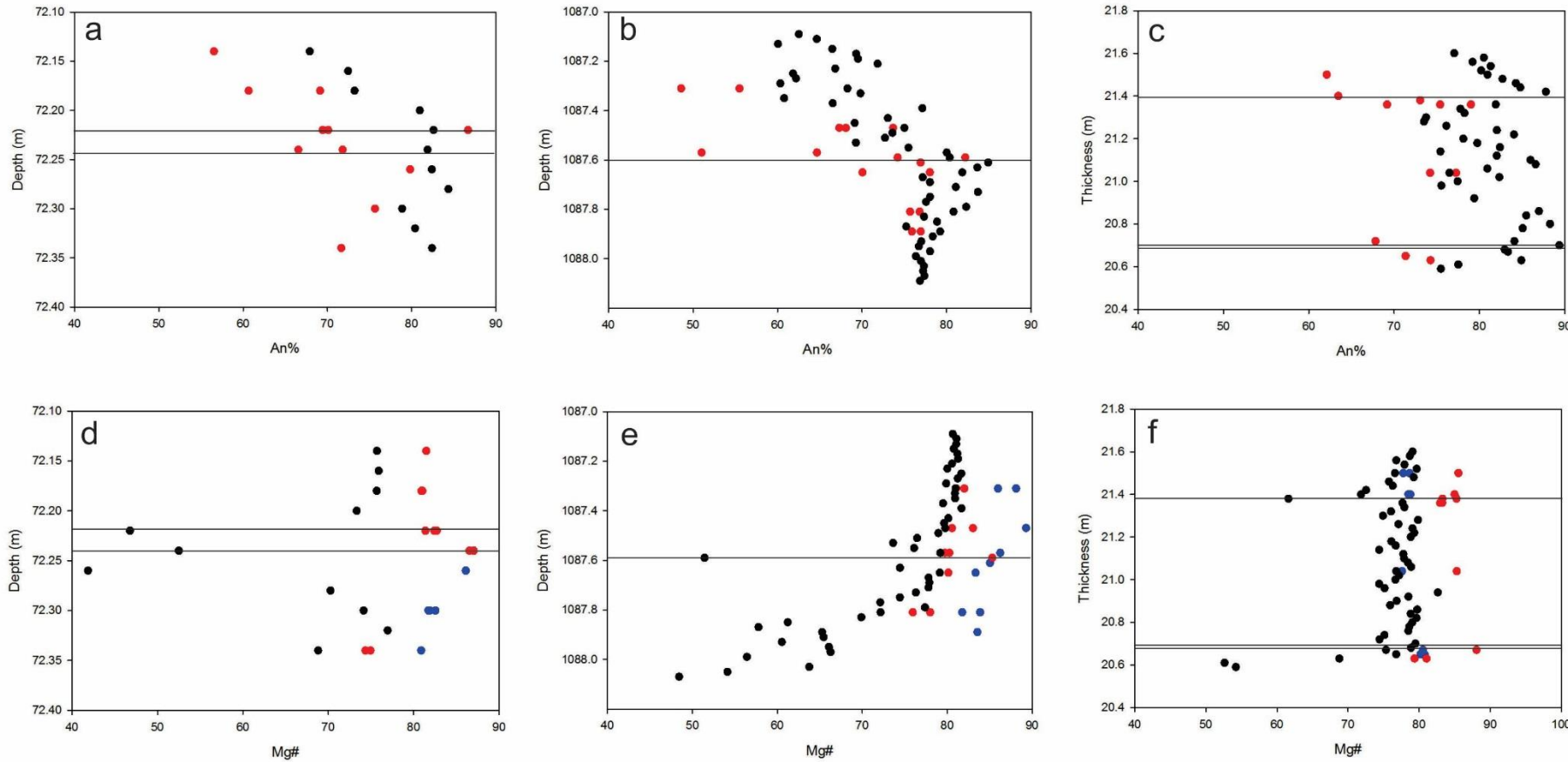


Figure 4.5.1: a-c) Comparing depth versus An% for EMPA of plagioclase and whole rock analysis. The red dots represents the EMPA of plagioclase and the black dots represents the whole rock data. a) Borehole SD14/90; b) Borehole BH6259 and c) Borehole 20/0252.

Figure 4.5.1: d-f) Comparing depth versus Mg# for EMPA of orthopyroxene and clinopyroxene and whole rock analysis. The blue dots represents the EMPA of clinopyroxene, the red dots the orthopyroxene and the black dots the whole rock data. d) Borehole SD14/90; e) Borehole BH6259 and f) Borehole 20/0252. Chromitite stringers indicated by black line. In Borehole SD14/90 the two stringers represents the thickness of the chromitite layer.

## Chapter 5: Conclusions

Consideration of the data that were gathered during this study, as discussed in the previous chapters, has led this candidate to the following conclusions:

1. a) Many similarities occur between the two non-pegmatoidal reefs: for example the modal mineralogy and the textures observed by optical microscopy seem to correlate. The major and trace element data of both whole rock and EMPA data also correlate and show especially strong correlation in the chromitite layers (Fig. 4.1.1). Thus it seems that there is no significant lateral variation within the non-pegmatoidal reefs of the study area around the Impala mine, which could indicate that conditions of deposition in that area remained constant for distances of tens of kilometres. Further investigation is needed to see if this phenomena is a general feature of the Merensky reef.  
b) When comparing the non-pegmatoidal reef with the pegmatoidal reef a lot of variation can be seen not just on a macroscopic scale but also looking at the mineral chemistry (Fig. 4.1.1) and the whole rock data.
2. The observations by optical microscopy included at least one previously unreported association in the Western Bushveld: a sulphide inclusion visible in a chromite grain. Similar results were observed by Hutchinson et al. (2015) for the Platreef. According to Hutchinson et al. (2015), this could indicate the presence of sulphide liquid in the system at a very early stage. Thus formation of sulphide with elevated PGE in a deep staging chamber, prior to intrusion could have occurred. From the data of Holwell et al. (2011) it is clear that these droplets are enriched in PGE. The study of these droplets is important, because it can give an idea of the composition of early-stage sulphide melts in magmatic systems.
3. a) The mineral chemistry of the non-pegmatoidal reef record normal melt evolution with a decrease in Mg# from the chromitite layer to the hangingwall pyroxenite layer of the sections; and a decrease in An% from the chromitite layer to the hangingwall pyroxenite layer. Mg# of orthopyroxene and An% of plagioclase within the chromitite layer is the highest compared to the footwall and the hangingwall; this could be due to a subsolidus exchange in the following way: the chromite in the chromitite layer

becomes more enriched in Fe during cooling by exchanging chemistry with intercumulus orthopyroxene. The result is orthopyroxene which is more Mg-rich and thus have a high Mg#. The decrease in An% in plagioclase from the chromitite layer to the hangingwall indicate a more evolved plagioclase.

- (b) The footwall (anorthosite layer) indicate a normal melt evolution within the layer, however it is important to mention that this anorthosite layer is the top layer of a previous cyclic unit and not part of the Merensky reef cyclic unit discussed above. The zoning identified in the footwall with different compositions in the rim and core of the plagioclase, could indicate that the unit cooled relatively slowly and interstitial plagioclase present within the unit equilibrated with a more evolved trapped liquid. In the case of the pegmatoidal reef very irregular patterns occurred that could indicate in some cases reverse melt evolution or new magma pulses from a deeper staging chamber.
4. The chemistry of the chromite in the chromitite layers show that there is a close correlation, as far as Cr<sub>2</sub>O<sub>3</sub> is concerned, between the single chromitite stringer in the non-pegmatoidal reef and the top chromitite stringer in the pegmatoidal one. For the rest of the major element chemistry there is a better correlation between the single chromitite stringer in the non-pegmatoidal reef and the bottom chromitite stringer in the pegmatoidal reef. The two chromitite stringers of the pegmatoidal reef are significantly different for all major elements. Further investigation is needed to see if this is a local or lateral variation/correlation and what the cause could be.
  5. Whole rock major element data correlate with the results in the mineral chemistry data. In borehole SD14/90 and BH6259, MgO and TiO<sub>2</sub> increase with height and Al<sub>2</sub>O<sub>3</sub> decrease which correlates with the mineral chemistry. In the case of borehole 20/0252 irregular trends could suggest a new magma pulse which caused a change in the normal differentiation trend. Whole rock major element geochemistry in the Merensky reef (particularly in the silicate layers) was attributed to a control by the mutual influence of co-precipitating minerals competing for major elements. Whole rock Mg# is the lowest in the chromitite layer, which is in contrast with what is seen in the mineral chemistry where Mg# is more primitive in the chromitite layer. This could be due to the subsolidus effect where the orthopyroxene within the chromitite

layer is more enriched in Mg, due to the exchange with the chromite as discussed in point two. When looking at the whole rock data the Mg# will be low due to the presence of intercumulus orthopyroxene. Similar results can be seen for An%.

6. The variability in Eu anomalies may be attributed to a control by plagioclase. Where Eu anomalies are strongly negative, one would expect the fractionation of plagioclase from residual liquids within the cumulus pile (Wilson and Chunnet, 2006). Such negative Eu anomalies are observed within the pyroxene unit. Positive Eu anomalies (as seen in footwall and chromitite layer) occur where plagioclase accumulate as cumulus phase. The variability in Sr anomalies is also subjected to the change in plagioclase abundance. REE data suggest a small amount of local differentiation with respect to La, seen in the top chromitite layer. This could be explained by the fact that La is associated with hydrous phase minerals (biotite, amphibole etc.). Since the pegmatoidal layer is just beneath the top chromitite layer it could indicate that the chromitite layer was “dehydrated” of hydrous phase minerals and concentrated in the pegmatoidal layer, causing the negative anomaly in the top chromitite layer.
7. In the non-pegmatoidal Merensky reef the highest whole rock PGE content is associated with the chromitite stringer. In the case of the pegmatoidal reef, the highest PGE content are associated with the upper chromitite stringer and the pegmatoidal layer and thus called top loaded. This could indicate that PGEs are associated with an increase in chromium rather than an increase in sulphur and that it is not controlled by a chalcophile process. The Merensky reef is Pt and Pd dominant and a positive Pt/Pd ratio is always observed. Very high Pt/Pd ratios (1 – 8.2) were observed in this study. These high Pt/Pd ratios could be an artefact of the small sample sizes used. Similar results were found by Hutchinson et al., (2015), from a Merensky reef sample near Impala Platinum Mine, with Pt/Pd ranging from 1.36 – 11.06. They explained the high Pt/Pd results in the chromitite stringers as density driven concentration of PGM transported by magmas that were displaced from a staging chamber, it is possible that the variations observed in this study is caused by similar processes.

From the models proposed it is clear that a combination of geochemical processes and multiple replenishments of magma are required to account for the formation of the Merensky reef. This include processes like crystallization of PGE as PGM (Tredoux

et al., 1995), collection of PGE by an immiscible sulphide liquid (Campbell et al., 1983 and Barnes and Maier, 2002b) and perhaps redistribution of PGE by late magmatic/hydrothermal fluids (Boudreau and Meurer, 1999). Trends of a deeper staging chamber as suggested by Hutchinson and McDonald is supported by several of the observations made in this study.

It is clear from the study that the vertical distribution of PGE are influenced by the presence of a second chromitite stringer (pegmatoidal reef). The vertical distribution of minerals especially chromite and the composition of the chromite, is also influenced by the presence of a second chromitite stringer, whether this was just a local or lateral variation/correlation still need further investigation.

Suggestions for further work:

- a) A study of the PGM will help to clarify some of the associations made.
- b) A study of more pegmatoidal and non-pegmatoidal Merensky reef will help to clarify whether the observations made above was just a local or lateral variation/correlation.

## References

- Barnes, S.J. and Maier, W.D., 2002a. Platinum-group elements and microstructures from Impala Platinum Mines, Bushveld complex. *Journal of Petrology*, **43**, 171-198.
- Barnes, S.J. and Maier, W.D., 2002b. Platinum-group element distributions in the Rustenburg Layered Suite of the Bushveld complex, South Africa. In: *The Geology, Geochemistry, Mineralogy and Mineral Beneficiation of Platinum Group Elements*. Edited by L.J. Cabri. Canadian Institute of Mining, Metallurgy and Petroleum, Special Volume **54**, 431-455.
- Barnes, S.J., Maier, W.D. and Curl, E.A., 2010. Composition of the marginal rocks and sills of the Rustenburg Layered Suite, Bushveld complex, South Africa: implication for the formation of the platinum –group element deposits. *Economic Geology*, **105**, 1491-1511.
- Barnes, S.J., Prichard, H.M., Cox, R.A., Fisher, P.C. and Godel, B., 2008. The location of the chalcophile and siderophile elements in platinum-group element ore deposits (a textural, microbeam and whole rock geochemical study): implications for the formation of the deposits. *Chemical Geology*, **248**(3-4), 295-317.
- Barnes, S.J., Savard, D., Bèdard, L.P. and Maier, W.D., 2009. Selenium and sulphur concentrations in the Bushveld complex South Africa and implications for formation of the platinum-group element deposits. *Mineralium Deposita*, **44**, 647-663.
- Bernstein, F., 1961. Application of x-ray fluorescence analysis to process. *Advance x-ray analysis*, **5**, 486-499.
- Bernstein, F., 1962. Particle size and mineralogical effects in mining applications.In Advances in X-ray analysis (Denver University, Denver Research Institution, Application of X-ray analysis, 11<sup>th</sup> Annual Conference). New York, Plenum Press, **6**, 436-446.
- Boudreau. A.E. and Meurer, W.P., 1999. Chromatographic separation of the platinum-group elements, gold, base metals and sulfur during degassing of a compacting and solidifying crystal pile. *Contribution to Mineralogy and Petrology*, **134**, 174-185.

Brynard, H.J., De Villiers, J.P.R. and Viljoen, E.A. 1976. A mineralogical investigation of the Merensky reef at the Western Platinum Mine, near Marikana, South Africa. *Economic Geology*, **71**, 1299-1307.

Cameron, E.N., 1980. Evolution of the lower critical zone, central sector, Eastern Bushveld Complex. *Economic Geology*, **77**(6), 1307-1327.

Campbell, I.H., Naldrett, A.J. and Barnes, S.J., 1983. A model for the origin of the platinum-rich sulphide horizons in the Bushveld and Stillwater Complexes. *Journal of Petrology*, **24**, 133-165.

Cawthorn, R.G., 1999. The platinum and palladium resources of the Bushveld complex. *South African Journal of Science*, **95**, 481-489.

Cawthorn, R.G., 2005. Stratiform PGE deposits in layered intrusions. *Canadian Mineralogist*, **35**, 57-73.

Cawthorn, R.G., 2010a. Geological interpretations from the PGE distribution in the Bushveld Merensky and UG2 chromitite reefs. *Jornal of the Southern African Institute of Mining and Metallurgy*, **107**, 57-70.

Cawthorn, RG., 2010b. The platinum group element deposits of the Bushveld complex in South Africa. *Platinum metals review*, **54**(4), 205-215.

Cawthorn, R.G., Barnes, S.J., Ballhaus, C. and Malitch, K.N., 2005. Platinum-group element, chromium and vanadium deposits in mafic and ultramafic rocks. *Economic Geology*, **100<sup>th</sup> anniversary volume**, 215-249.

Cawthorn, R.G. and Boerst, K., 2006a. Origin of the Pegmatitic Pyroxenite in the Merensky Unit, Bushveld Complex, South Africa. *Journal of Petrology*, **47**(8), 1509-1530.

Cawthorn, R.G. and Davies, G., 1983. Experimental data at 3 k bars pressure on parental magma to the Bushveld Complex. *Contribution to Mineralogy and Petrology*, **83**, 128-135.

Cawthorn, R.G., Eales, H.V., Walraven, F., Uken, R. and Watkeys, M.K., 2006b. The Bushveld Complex. In: *Geology of South Africa*. Edited by M.R. Johnson, C.R. Anhaeusser and R.J. Thomas. Geological Society of South Africa. 261-281.

Cawthorn, R.G., Lee, C.A., Schouwstra, R. and Mellowship, P., 2002b. Relations between PGE and PGM in the Bushveld complex. *Canadian Mineralogist*, **40**, 311-328.

Cawthorn , R.G., Merkle, R.K.W. and Viljoen, M.J., 2002a. Platinum-group element deposits in the Bushveld Complex, South Africa. In: *The Geology, Geochemistry, Mineralogy and Mineral Beneficiation of Platinum Group Elements*. Edited by L.J. Cabri. Canadian Institute of Mining, Metallurgy and Petroleum, Special Volume **54**, 389-425.

Cawthorn, R.G., and Wansbury N., 2014. Formation of the chromitite layers of the Merensky Unit, Bushveld Complex. Abstract volume – 21<sup>st</sup> General meeting of IMA South Africa 2014. Available online at: [www.ima2014.co.za/.../IMA2014%20ABSTRACT%20VOLUME\\_2.pdf](http://www.ima2014.co.za/.../IMA2014%20ABSTRACT%20VOLUME_2.pdf). Downloaded December 2014.

Cawthorn, R.G., and Webb, S.J., 2013. Cooling of the Bushveld Complex, South Africa: Implications for paleomagnetic reversals. *Geology*, **41**(6), 687-690.

Cheney, E.S. and Twist, S.O., 1991. The conformable emplacement of the Bushveld mafic rocks along a regional unconformity in the Transvall succession of South Africa. *Precambrian Research*, **52**, 115-132.

Clarke, B., Uken, R. and Reinhardt, J., 2009. Structural and compositional constraints on the emplacement of the Bushveld complex, South Africa. *Lithos*, **111**, 21-36.

Davey, S.R., 1992. Lateral variation within the upper Critical Zone of the Bushveld complex on the farm Rooikoppies 297 JQ, Marikana , South Africa. *South African Journal of Geology*, **95**(3/4), 141-149.

Eales, H.V., 2000. Implications of the chromium budget of the Western limb of the Bushveld Complex. *South African Journal of Geology*, **103**(2), 141-150.

Eales, H.V. and Cawthorn R.G., 1996. The Bushveld Complex. In *Layered Intrusions*. Edited by R.G. Cawthorn. Developments in Petrology. 15, Elsevier, 531.

Eales, H.V., Maier, W.D. and Teigler, B., 1991. Corroded plagioclase feldspar inclusions in orthopyroxene and olivine of the Lower and Critical Zones, Western Bushveld Complex. *Mineralogical Magazine*, **55**, 479-486.

Godel, B., Barnes, S.J. and Maier, W.D., 2007. Platinum-group elements in sulphide minerals, platinum-group minerals, and whole-rocks of the Merensky reef (Bushveld complex, South Africa): implications for the formation of the reef. *Journal of Petrology*, **48**(8), 1569-1604.

Gross, J.H., 2011. *Mass spectrometry*, 2<sup>nd</sup> edition., Springer Heidelberg, London New York, p.779.

Gunn, E.L., 1960. The effect of particles and surface irregularities on the x-ray fluorescent intensity of selected substances In *Advances in X-ray analysis* (Denver University, Denver Research Institution, Application of X-ray analysis, 11<sup>th</sup> Annual Conference). New York, Plenum Press, **4**, 382-400.

Huber, H., Koeberl, C., McDonald, I. and Reimold, W.U., 2001. Geochemistry and petrology of Witwatersrand and Dwyka diamictites from South Africa: Search for an extraterrestrial component. *Geochemica et Cosmochimica Acta*, **65**(12), 2007-2016.

Holwell, D.A., McDonald, I. and Butler, I.B., 2011. Precious metal enrichment in the Platreef, Bushveld complex, South Africa: evidence from homogenized magmatic sulfide melt inclusions. *Contribution to Mineralogy and Petrology*, **161**, 1011-1026.

Hutchinson, D., Foster, J., Prichard, H. and Gilbert, S., 2015. Concentration of particulate platinum-group minerals during magma emplacement; a case study from the Merensky reef, Bushveld Complex. *Journal of Petrology*, **56**(1), 113-159.

Irvine, T.N., 1975. Crystallisation sequences in the Muskox intrusion and other layered intrusions-II. Origin of chromitite layers and similar deposits of other magmatic ores. *Geochemica et Cosmochimica Acta*, **39**(6), 991-1020.

Irvine, T.N., 1977. Origin of chromitite layers in the Muskox intusion and other stratiform intrusions: a new interpretation. *Geology*, **5**(5), 273-277.

Jordaan, L.J. and Maritz, H., 2010. Analytical methods 2009, Council for Geoscience Analytical Laboratory. Council for Geoscience. Pretoria South Africa. *Confidential Report*, 2010-0088.

Kinnaird, J.A., Kruger, F.J., Nex, P.A.M. and Cawthorn R.G., 2002. Chromites of the Bushveld complex- processes of formation and PGE enrichment. *Department of Geology, School of Geosciences, university of the Witwatersrand*, information circular No. 369.

Kleemann, G.J. and Twist, D., 1989. The compositionally-zone Sheet-like Granite Pluton of the Bushveld Complex: evidence bearing on the nature of A-type magmatism. *Journal of Petrology*, **30**, 1383-1414.

Kruger, F.J., 1994. The Sr-isotopic stratigraphy of the Western Bushveld Complex. *South African Journal of Geology*, **97**, 393-398.

Kruger, F.J., 2005. Filling the Bushveld Complex magma chamber: lateral expansion, roof and floor interaction, magmatic unconformities, and the formation of giant chromitite, PGE and Ti-V-magnetitite deposits. *Mineralium Deposita*, **40**, 451-472.

Kruger, F.J. and Marsh, J.S., 1982. Significance of  $^{87}\text{Sr}/^{86}\text{Sr}$  ratios in the Merensky Cyclic Unit of the Bushveld Complex. *Nature*, **298**, 53-55.

Kruger, F.J. and Marsh, J.S., 1985. The mineralogy petrology and origin of the Merensky cyclic unit in the Western Bushveld Complex. *Economic Geology*, **80**, 954-974.

Latypov, R., O'Driscoll, B. and Lavrenchuk A., 2013. Towards a model for the in situ origin of PGE reefs in layered intrusions: insights from chromitite seams of the Rum Eastern Layered Intrusions, Scotland. *Contributions to Mineralogy and Petrology*, **166**(1), 309-327.

Lee, C.A., 1983. Trace and platinum-group element geochemistry and the development of the Merensky Unit of the Western Bushveld Complex. *Mineralium Deposita*, **18**(2), 173-190.

Lee, C.A. and Tredoux, M., 1986. Platinum-group element abundances in the lower and the lower Critical zones of the Eastern Bushveld complex. *Economic Geology*, **81**, 1087-1095.

Leeb-du Toit, A., 1986. The Impala Platinum Mines. In Anhaeusser, C.R., & Maske, S. (eds) *Mineral deposits of Southern Africa*. **2**, Johannesburg: Geological Society of South Africa, 1091-1106.

LeHouillier, R. and Turmel, S., 1974. Bead homogeneity in fusion. *Analytical Chemistry*, **46**, 734-736.

Lipin, B.R., 1993. Pressure increases, the formation of chromite seams and the development of the ultramafic series in the Stilwater Complex, Montana. *Journal of Petrology*, **34**, 955-976.

Lodders, K., 2003. Solar system abundances and condensation temperatures of the elements. *Astrophysical Journal*, **591**, 1220-1247.

Maier, W.D., Barnes, S.-J. and Groves, D.I., 2013. The Bushveld Complex, South Africa: formation of platinum, palladium, chrome- and vanadium rich layers via hydrodynamic sorting of a mobilized cumulate slurry in a large, relatively slowly cooling, subsiding magma chamber. *Mineralium Deposita*, **48**, 51-56

Maier, W.D. and Bowen, M.P., 1996. The UG2-Merensky reef interval of the Bushveld complex northwest of Pretoria. *Mineralium Deposita*, **31**, 386-393.

McDonald, I. and Holwell, D.A., 2011. Geology of the Northern Bushveld complex and the setting and genesis of the Platreef Ni-Cu-PGE deposit. *Economic Geology*, **17**, 297-327.

McDonald, I. and Viljoen, K.S., 2006. Platinum-group element geochemistry of mantle eclogites: reconnaissance study of xenoliths from the Orapa kimberlite, Botswana. *Applied Earth Sciences (Trans. Inst. Min. Metall. B)*, **115** (3), 81-93.

Moodley, P., 2008. Facies variation in the Merensky reef at Bafokeng Rasimone Platinum mine. The *Southern African Institute of Mining and Metallurgy*, **108** 87-9.

Morimoto, N., 1988. Nomenclature of pyroxenes. *Mineralogical Magazine*, **52**, 535-550.

Mostert, A.B., Hofmeyer, P.K. and Potgieter, G.A., 1982. The platinum-group mineralogy of the Merensky reef at the Impala Platinum Mines, Bophuthatswana. *Economic Geology*, **77**, 1385-1394.

Naldrett, A.J. 1999. World-class Ni-Cu-PGE deposits: key factors in their genesis. *Mineralium Deposita*, **34**(3), 227-240.

Naldrett, A., Kinnaird, J., Wilson, A., Yudovskaya, M. and Chunnett, G., 2011. Genesis of the PGE-enriched Merensky reef and chromites seams of the Bushveld complex. *Economic Geology*, **107**, 235-296.

Naldrett, A., Wilson, A., Kinnaird, J. and Chunnett, Gordon, 2009. PGE tenor and metal ratios within and below the Merensky reef, Bushveld complex: implications for its genesis. *Journal of Petrology*, **50**, 625-659.

Naldrett, A. Wilson, A., Kinnaird, J., Yudovskaya, M and Chunnett, G., 2012. The origin of chromites and related PGE mineralization in the Bushveld complex: new mineralogical and petrological constraints. *Mineralium Deposita*, **47**(3), 204-232.

Nesse, W.D., 2004. *Introduction to optical mineralogy*, 3<sup>rd</sup> edn., Oxford University Press, New York, p. 348.

Osbahr, I., Klemd, R., Oberthür, T., Brätz, H. and Schouwstra R., 2013. Platinum-group element distribution in base –metal sulfides of the Merensky reef from the eastern and western Bushveld complex, South Africa. *Mineralium Deposita*, **48**, 211-232.

Reed. S.J.B., 2005. *Electron microprobe analysis and scanning electron microscopy in geology*, 2<sup>nd</sup> edn., Cambridge University Press, New York, 189.

Roelofse, F. and Ashwal, L.D., 2012. The Lower Main Zone in the Northern Limb of the Bushveld Complex – a > 1.3 km thick sequence of intruded and variably contaminated crystal mushes. *Journal of Petrology*, **53**(7) 1449-1476.

SACS, 1980. Bushveld Complex. In: K.L.E. (Editor), The stratigraphy of South Africa , Part I, Lithostratigraphy of the Republic of South Africa, South 221 West Africa/Namibia and the Republics of Bophuthatswana, Transkei and Venda. Geological Survey of South Africa, 223-231.

Scoon, R.N. and Mitchell, A.A., 2009. Discovery and Geology of the platinum group element deposits of the Bushveld Complex, South Africa. *SEG Newsletter*, **78**, 13-19.

Seabrook, A.L., Cawthorn, R.G. and Kruger, F.J, 2005. The Merensky reef, Bushveld complex: mining of minerals not mixing of magmas. *Economic Geology*, **100**, 1191-1206.

Tredoux, M., Lindsay, N.M., Davies, G., and McDonald I., 1995. The fractionation of platinum-group elements in magmatic systems, with the suggestion of a novel causal mechanism. *South African Journal of Geology*, **98**(2), 157-167.

Vermaak, C.F. 1976. The Merensky reef; thoughts on its environment and genesis. *Economic Geology*, **71**, 1270-1298.

Vermaak, C.F. and Hendriks, L.P., 1976. A review of the mineralogy of the Merensky reef, with specific refrence to new data on the precious metal mineralogy. *Economic Geology*, **71**(7), 1244-1269.

Verwoerd, W.J., 2006. The Pilanesberg Alkaline Province. In: The Geology of South Africa, Eddited by: Johnson, M.R., Anhaeusser, C.R., Thomas, R.J. Geological Society of South Africa., Johannesburg and Council for Geoscience, Pretoria, 381-393.

Vrebos, B.A.R. and Helsen, J.A., 1983. Ab initio calculations of XRF intensities in non-homogeneous matrices. *Spectrochimica Acta*, **38B**(5-6), 835-842.

Viljoen, M.J. and Hieber, R., 1986. The Rustenburg section of Rustenburg Platinum Mines Limited, with reference to the Merensky reef. In Anhaeusser, C.R. and Maske, S.(eds.), *Mineral deposits of Southern Africa*, **2**, Geological Society of South Africa, 1107-1134.

Wager, L.R. and Brown G.M. 1968. Layered Igneous rocks. Oliver and Boyd, Edinburgh, 588.

Walraven, F., 1997. Geochronology of the Rooiberg Group, Transvaal Supergroup, South Africa. *Information circular*, **316**, Economic Geology Research Unit, University of Witwatersrand, Johannesburg, South Africa, 21.

Walraven, F., Armstrong, R.A. and Kruger, F.J., 1990. A chronostratigraphic framework for the north-central Kaapvaal craton, the Bushveld complex and the Vredefort structure. *Tectonophysics*, **171**, 23-48.

Willis, J., Turner, K. and Pritchard, G., 2011. XRF in the workplace: *A guide to practical XRF spectrometry*, Milla Litho (Pty) Ltd, South Africa.

Willmore, C.C., Boudreau, A.E. and Kruger, F.J., 2000. The halogen geochemistry of the Bushveld Complex Republic of South Africa: implications for chalcophile element distribution in the lower and critical zones. *Journal of Petrology*, **41**, 1517-1539.

Wilson, A., and Chunnett, G., 2006. Trace element and Platinum group element distributions and the genesis of the Merensky reef, Western Bushveld complex, South Africa. *Journal of Petrology*, **47**(12), 2369-2403.

Wilson, A.H., Lee, C.A. and Brown, R.T., 1999. Geochemistry of the Merensky reef, Rustenburg Section, Bushveld Complex: controls on the silicate framework and distribution of trace elements. *Mineralium Deposita*, **34**, 657-672.

## Appendix – Table of contents

### Appendix A

- Table A.1:** Description of each core set, the length, the amount of samples used and the names of each section used for analysis. Samples are spread across the core sections.
- Table A.2:** List of certified reference materials used for calibration. X-ray fluorescence spectrometry was used to determine whole rock major element data.
- Table A.3:** Characteristic standards for oxides in chromitite layers with EMPA.
- Table A.4:** Characteristic standards for oxides in pyroxenes and plagioclases with EMPA.
- Table A.5:** Characteristic standards for oxides in sulphides with EMPA.
- Table A.6:** List of the various crystals used in the wavelength dispersive X-ray spectrometry (WDS-EMPA) analysis.
- Table A.7:** List of the various crystals used in X-ray fluorescence spectrometer (XRF) at the University of the Free State.
- Table A.8:** List of standards used for calibration of the Eltra analyser for determination of sulphur.

### Appendix B

- Figure B.1** Modal mineral proportions of non-pegmatoidal Merensky reef from borehole SD14/90.
- Figure B.2** Modal mineral proportions of non-pegmatoidal Merensky reef from borehole BH6259.
- Figure B.3** Modal mineral proportions of pegmatoidal Merensky reef from borehole 20/0252.

### Appendix C

- Table C.1** Average plagioclase chemistry data in the hangingwall, chromitite layer and in the footwall from borehole SD14/90. Major element oxides in wt%.
- Table C.2** An%, Ab% and Or% for plagioclase in the hangingwall, chromitite layer and in the footwall of borehole SD14/90.
- Table C.3** Average plagioclase chemistry data in the hangingwall, chromitite layer and in the footwall from borehole BH6259. Major element oxides in wt%.
- Table C.4** An%, Ab% and Or% for plagioclase in the hangingwall, chromitite layer

and in the footwall of borehole BH6259.

**Table C.5**

Average plagioclase chemistry data in the hangingwall, top chromitite layer, pegmatoidal layer, bottom chromitite layer and in the footwall from borehole 20/0252. Major element oxides in wt%.

**Table C.6**

An%, Ab% and Or% for plagioclase in the hangingwall, top chromitite layer, in the pegmatoidal layer and in the footwall of borehole 20/0252.

**Table C.7**

Average orthopyroxene chemistry data in the hangingwall, chromitite layer and in the footwall from borehole SD14/90. Major element oxides in wt%.

**Table C.8**

En%, Fs% and Wo% for orthopyroxene in the hangingwall, chromitite layer, and in the footwall of borehole SD14/90.

**Table C.9**

Average orthopyroxene chemistry data in the hangingwall, chromitite layer and in the footwall from borehole BH6259. Major element oxides in wt%.

**Table C.10**

En%, Fs% and Wo% for orthopyroxene in the hangingwall, chromitite layer, and in the footwall of borehole BH6259.

**Table C.11**

Average orthopyroxene chemistry data in the hangingwall, pegmatoidal layer, bottom chromitite layer and in the footwall from borehole 20/0252. Major element oxides in wt%.

**Table C.12**

En%, Fs% and Wo% for orthopyroxene in the hangingwall, pegmatoidal layer, bottom chromitite layer and in the footwall of borehole 20/0252.

**Table C.13**

Average clinopyroxene chemistry data in the chromitite layer and in the footwall from borehole SD14/90. Major element oxides in

**Table C.14**

En%, Fs% and Wo% for clinopyroxene in the chromitite layer, and in the footwall of borehole SD14/90.

**Table C.15**

Average clinopyroxene chemistry data in the hangingwall, and in the footwall from borehole BH6259. Major element oxides in wt%.

**Table C.16**

En%, Fs% and Wo% for clinopyroxene in the hangingwall and in the footwall of borehole BH6259.

**Table C.17**

Average clinopyroxene chemistry data in the hangingwall, top chromitite layer, pegmatoidal layer, bottom chromitite layer and in the footwall from borehole 20/0252. Major element oxides in wt%.

**Table C.18**

En%, Fs% and Wo% for clinopyroxene in the hangingwall, top chromitite layer, pegmatoidal layer, bottom chromitite layer and in the footwall of borehole 20/0252.

**Table C.19**

Average chromitite chemistry data in the chromitite layer from borehole SD14/90. Major element oxides in wt%.

**Table C.20**

Average chromitite chemistry data in the chromitite layer from borehole BH6259. Major element oxides in wt%.

<b>Table C.21</b>	Average chromitite chemistry data in the hangingwall, top chromitite layer, pegmatoidal layer and the bottom chromitite layer from borehole 20/0252. Major element oxides in wt%.
<b>Table C.22</b>	Average mica chemistry data in the footwall from borehole SD14/90. Major element oxides in wt%.
<b>Table C.23</b>	Average mica chemistry data in the hangingwall, chromitite layer and in the footwall from borehole BH6259. Major element oxides in wt%.
<b>Table C.24</b>	Average mica chemistry data the hangingwall and in the pegmatoidal layer from borehole 20/0252. Major element oxides in wt%.
<b>Table C.25</b>	Average chalcopyrite chemistry data in the hangingwall, chromitite layer and in the footwall from borehole SD14/90. Major element oxides in wt%.
<b>Table C.26</b>	Average chalcopyrite chemistry data in the hangingwall, chromitite layer and in the footwall from borehole BH6259. Major element oxides in wt%.
<b>Table C.27</b>	Average chalcopyrite chemistry data in the hangingwall, top chromitite layer, pegmatoidal layer and in the footwall from borehole 20/0252. Major element oxides in wt%.
<b>Table C.28</b>	Average pyrrhotite chemistry data in the hangingwall, chromitite layer and in the footwall from borehole SD14/90. Major element oxides in wt%.
<b>Table C.29</b>	Average pyrrhotite chemistry data in the hangingwall, chromitite layer and in the footwall from borehole BH6259. Major element oxides in wt%.
<b>Table C.30</b>	Average pyrrhotite chemistry data in the hangingwall, top chromitite layer and in the pegmatoidal layer from borehole 20/0252. Major element oxides in wt%.
<b>Table C.31</b>	Average pentlandite chemistry data in the hangingwall, chromitite layer and in the footwall from borehole SD14/90. Major element oxides in wt%.
<b>Table C.32</b>	Average pentlandite chemistry data in the hangingwall, chromitite layer and in the footwall from borehole BH6259. Major element oxides in wt%.
<b>Table C.33</b>	Average pentlandite chemistry data in the hangingwall and in the pegmatoidal layer from borehole 20/0252. Major element oxides in wt%.
<b>Table C.34</b>	Average pyrite chemistry data in the hangingwall, chromitite layer and in the footwall from borehole BH6259. Major element oxides in wt%.

## Appendix D

<b>Table D.1</b>	Whole rock geochemistry of standards analyzed and the certified
------------------	---

reference material values.

**Table D.2**

Whole rock geochemistry of borehole SD14/90 obtained from ICP-MS analysis (major element oxides) and element ratios. Major element oxides in wt%. (Cr/(Cr+Al) and (Cr/(Cr+Al) calculated using molar values.

**Table D.3**

Whole rock geochemistry of borehole BH6259 obtained from ICP-MS analysis (major element oxides) and element ratios. Major element oxides in wt%. (Cr/(Cr+Al) and (Cr/(Cr+Al) calculated using molar values.

**Table D.4**

Whole rock geochemistry of borehole 20/0252 obtained from ICP-MS analysis, (major element oxides) and element ratios. Major element oxides in wt%. (Cr/(Cr+Al) and (Cr/(Cr+Al) calculated using molar values.

**Table D.5**

Normative mineralogy of the major element oxides in borehole SD14/90.

**Table D.6**

Normative mineralogy of the major element oxides in borehole 20/0252.

**Table D.7**

Normative mineralogy of the major element oxides in borehole BH6259.

**Figure D.1**

Modified MgO-Harker plots of the major element oxides, related to the different lithologies with depth (see Appendix A), of borehole SD14/90.

**Figure D.2**

Modified MgO-Harker plots of the major element oxides, related to the different lithologies with depth (see Appendix A), of borehole 20/0252.

**Figure D.3**

Modified MgO-Harker plots of the major element oxides, related to the different lithologies with depth (see Appendix A), of borehole BH6259.

## Appendix E

**Table E.1**

Trace element whole rock geochemistry of standards analyzed and the certified reference material values.

**Table E.2**

Whole rock geochemistry of borehole SD14/90 obtained from ICP-MS analysis. Trace element concentrations in ppm.

**Table E.3**

Whole rock geochemistry of borehole 20/0252 obtained from ICP-MS analysis. Trace element concentrations in ppm.

**Table E.4**

Whole rock geochemistry of borehole BH6259 obtained from ICP-MS analysis. Trace element concentrations in ppm.

<b>Table E.5</b>	Whole rock geochemistry of borehole SD14/90 obtained from ICP-MS analysis. Rare earth element concentrations in ppm.
<b>Table E.6</b>	Whole rock geochemistry of borehole 20/0252 obtained from ICP-MS analysis. Rare earth element concentrations in ppm.
<b>Table E.7</b>	Whole rock geochemistry of borehole BH6259 obtained from ICP-MS analysis. Rare earth element concentrations in ppm.
<b>Figure E1</b>	Chondrite normalised multi element diagram for borehole SD14/90. Normalised values from Lodders, 2003.
<b>Figure E.2</b>	Chondrite normalised multi element diagram from borehole 20/0252. Normalised values from Lodders, 2003.
<b>Figure E.3</b>	Chondrite normalised multi element diagram from borehole 20/0252. Normalised values from Lodders, 2003.
<b>Figure E.4</b>	Chondrite normalised multi element diagram from borehole 20/0252. Normalised values from Lodders, 2003.
<b>Figure E.5</b>	Chondrite normalised multi element diagram from borehole BH6259. Normalised values from Lodders, 2003.
<b>Figure E.6</b>	Chondrite normalised multi element diagram from borehole BH6259. Normalised values from Lodders, 2003.
<b>Figure E.7</b>	Chondrite normalised REE diagrams for borehole SD14/90. C1 chondrite values from Lodders, 2003.
<b>Figure E.8</b>	Chondrite normalised REE diagrams for the hangingwall and the top chromitite stringer, from borehole 20/0252. C1 chondrite values from Lodders, 2003.
<b>Figure E.9</b>	Chondrite normalised REE diagrams for the top and bottom chromitite stringer and the pegmatoidal layer, from borehole 20/0252.
<b>Figure E.10</b>	Chondrite normalised REE diagrams for the bottom chromitite stringer and the footwall, from borehole 20/0252.
<b>Figure E.11</b>	Chondrite normalised REE diagrams for the chromitite stringer and the hangingwall, from borehole BH6259.
<b>Figure E.12</b>	Chondrite normalised REE diagrams for the chromitite stringer and the footwall, from borehole BH6259.

## Appendix F

<b>Table F.1</b>	PGE whole rock geochemistry of standards analyzed.
------------------	--

**Table F.2** Whole rock PGE analysis of the non-pegmatoidal reef, from borehole SD14/90. PGE values in ppm, Cr and S in wt%.

**Table F.3** Whole rock PGE analysis of the pegmatoidal reef, from borehole 20/0252. PGE values in ppm, Cr and S in wt%.

**Table F.4** Whole rock PGE analysis of the non-pegmatoidal reef, from borehole BH6259. PGE values in ppm, Cr and S in wt%.

## Appendix G

**Table G.1** Sulphur analysis for non-pegmatoidal Merensky reef, from borehole SD14/90. Sulphur values in %.

**Table G.2** Sulphur analysis for non-pegmatoidal Merensky reef, from borehole BH6259. Sulphur values in %.

**Table G.3** Sulphur analysis for pegmatoidal Merensky reef, from borehole 20/0252. Sulphur values in %.

## Appendix H

**Appendix H.1** Mineralogical and geochemical interpretations on the pegmatoidal and non-pegmatoidal Merensky reef (24<sup>th</sup> Colloquium of African Geology; CAG24).

**Appendix H.2** Platinum group elements within the Merensky reef: Preliminary results of a high resolution mineralogical and geochemical study (6<sup>th</sup> IMSG abstract).

**Appendix H.3** Platinum-group elements within the Merensky reef, Western Limb, Bushveld complex: results of a high resolution mineralogical and geochemical study (12<sup>th</sup> International Platinum Symposium).

**Appendix H.4** Platinum group elements within the Merensky reef: preliminary results of a high resolution mineralogical and geochemical study (IMA,2014).

## Appendix A

**Table A.1: Description of each core set, the length, the amount of samples used and the names of each section used for analysis. Samples are spread across the core sections. (See appendix A)**

	Non-pegmatoidal core set (NP)	Non-pegmatoidal core set BH6259	Pegmatoidal core set (P)
Length of core	± 22 cm	± 338 cm	± 104 cm
Length <u>above</u> chromitite stringer	± 8 cm	± 50 cm	Length above top chromitite stringer ± 22 cm
Thickness of chromitite stringer	± 4 cm	± 2 cm	Thickness of top chromitite stringer ± 2 cm, thickness of bottom chromite stringer ± 4 cm
Length <u>below</u> chromitite stringer	± 10 cm	± 50 cm	Length below bottom chromitite stringer ± 8 cm
Length between two chromitite stringers	NA	NA	± 68 cm
Amount of samples analysed for PGE	11	15	20
Amount of samples analysed for major and traces elements	11	50	52
Samples analysed for PGE	1NP, 2NP, 3NP, 4NP, 5NP, 6NP, 7NP, 8NP, 9NP, 10NP, 11NP	76N, 80N, 84N, 88N, 92N, 96N, 97N, 98N, 99N, 100N, 101N, 105N, 109N, 113N, 117N	3P, 4P, 5P, 6P, 7P, 8P, 12P, 16P, 19P, 24P, 28P, 32P, 35P, 39P, 40P, 41P, 42P, 43P, 47P, 51P

**Table A.2: List of certified reference materials used for calibration. X-ray fluorescence spectrometry was used to determine whole rock major element data.**

Certified reference materials used	Type
SARM 8	Chromium ore
SARM 9	Chromium ore
SARM 76	Merensky ore (platinum ore)
BCS 370	Chrome magnesite
NIM-P	Pyroxenite
NIM-N	Norite

**Table A.3: Characteristic standards for oxides in chromitite layers with EMPA.**

Oxides	Standard name
SiO <sub>2</sub>	Olivine_SPI
CaO	Cr_Diopside_SPI
TiO <sub>2</sub>	Rutile_SPI
Al <sub>2</sub> O <sub>3</sub>	Spinel_SPI
FeO	Hematite_SPI
ZnO	Willemite_SPI
MnO	Rhodonite_SPI
NiO	Nickel_Silicide_SPI
V <sub>2</sub> O <sub>3</sub>	V_SPI
MgO	Spinel_SPI
Cr <sub>2</sub> O <sub>3</sub>	Chromium_oxide_SPI

**Table A.4: Characteristic standards for oxides in pyroxenes and plagioclases with EMPA.**

Oxides	Standard name
SiO <sub>2</sub>	Plag-An65_SPI
CaO	Cr_Diopside_SPI
TiO <sub>2</sub>	Rutile_SPI
Al <sub>2</sub> O <sub>3</sub>	Almandine_SPI
FeO	Almandine_SPI
K <sub>2</sub> O	Orthoclase_SPI
MnO	Rhodonite_SPI
NiO	Pentlandite_SPI
Na <sub>2</sub> O	Albite
MgO	Periclase_SPI
Cr <sub>2</sub> O <sub>3</sub>	Chromium_oxide_SPI

**Table A.5: Characteristic standards for oxides in sulphides with EMPA.**

Oxides	Standard name
Fe	Chalcopyrite_SPI
Ni	Pentlandite_SPI
Cu	Chalcopyrite_SPI
Co	Co_SPI
S	Chalcopyrite_SPI

**Table A.6: List of the various crystals used in the wavelength dispersive X-ray spectrometry (WDS-EMPA) analysis.**

Element	Crystal
Si, Al	TAP
Fe, Zn, Mn, Ni, V, Mg, Cu, Co	LIF
Ca, Ti	PETJ
Mg, Na,	TAPL
Cr, K, S	PETL

**Table A.7: List of the various crystals used in X-ray fluorescence spectrometer (XRF) at the University of the Free State.**

Element	Crystal	Element	Crystal
Al	PE 002	Ti	LiF 200
Ca	LiF 200	Cr	LiF 200
Fe	LiF 200	P	Ge 111
Mg	PX 1	Na	PX 1
Mn	LiF 200	K	LiF 200
Si	PE 002		

**Table A.8: List of standards used for calibration of the Eltra analyser for determination of sulphur.**

Standards	Type
Euronorm-CRM 484-1	White heart malleable iron
Euronorm-CRM 058-2	Sulphur steel
Euronorm-CRM 086-1	Carbon steel

## Appendix B

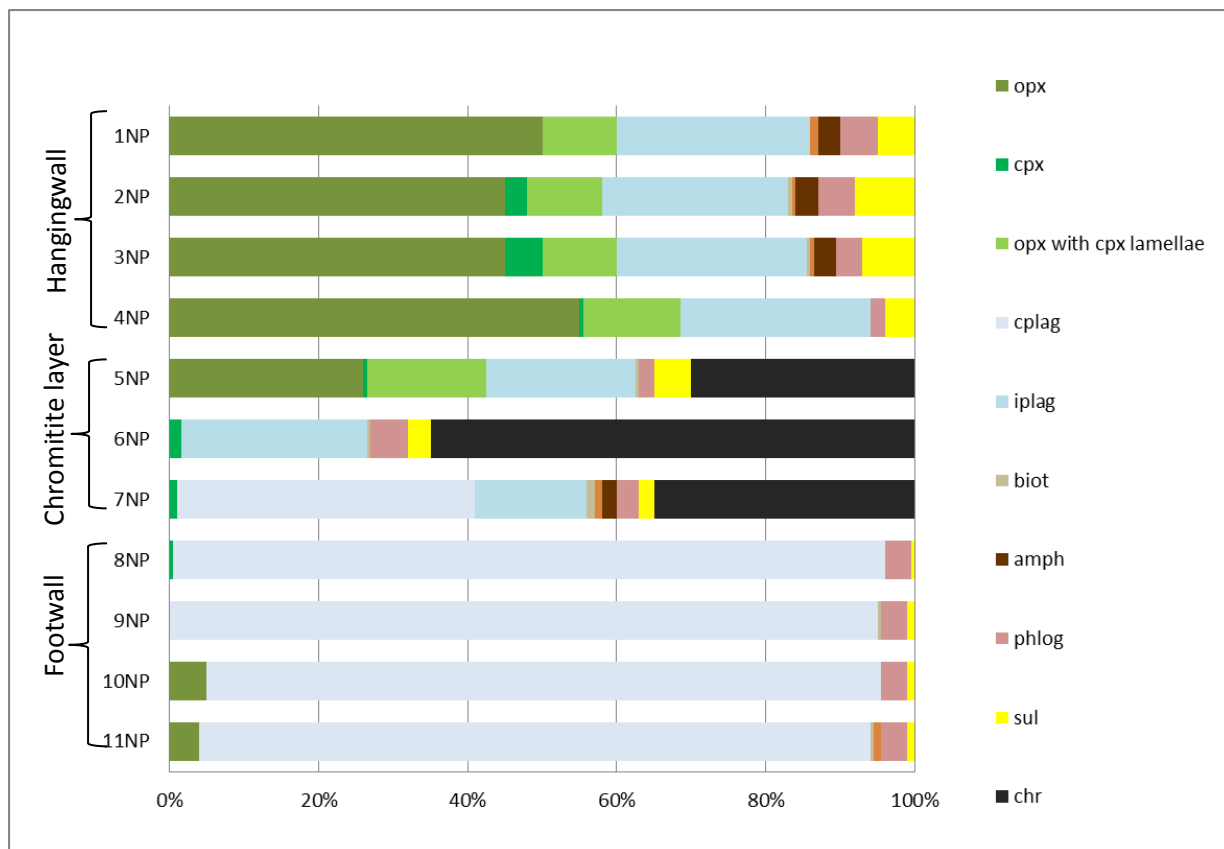


**Figure B.1: Modal mineral proportions of non-pegmatoidal Merensky reef from borehole SD14/90.**

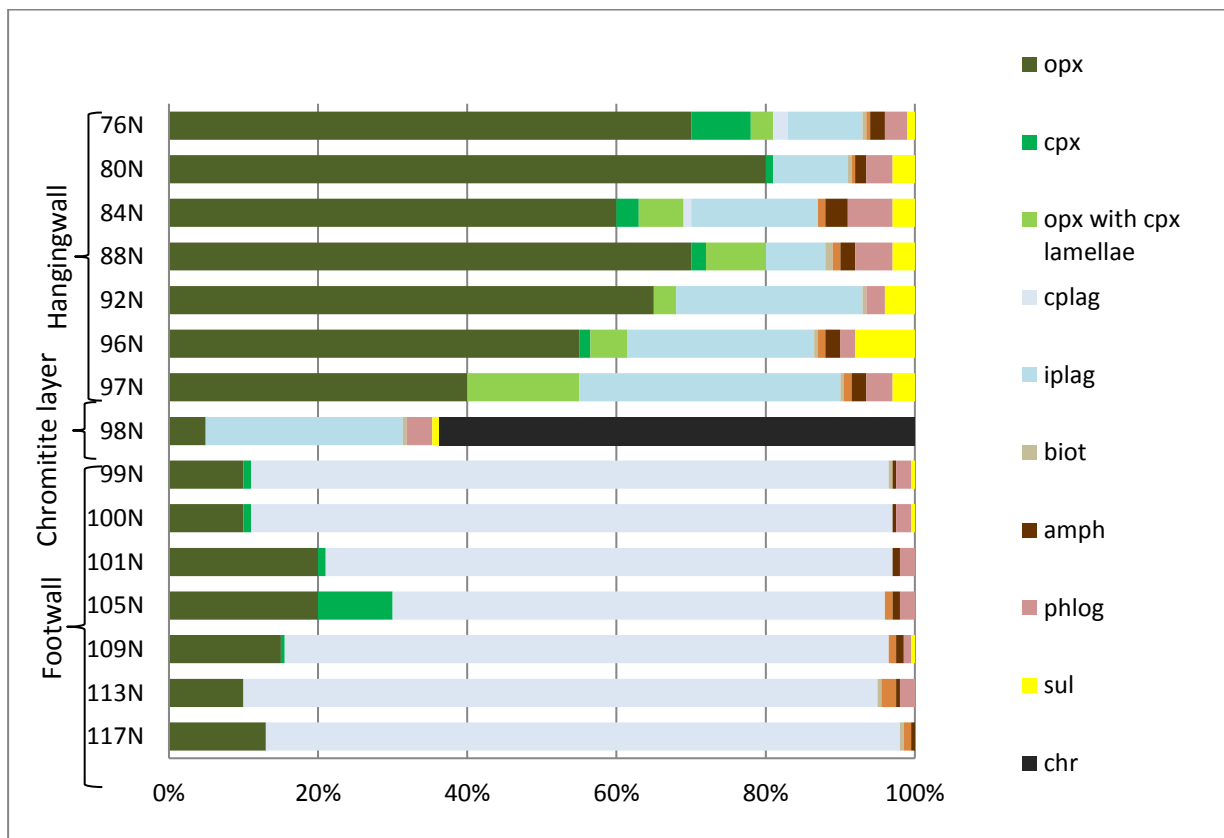


**Figure B.2: Modal mineral proportions of non-pegmatoidal Merensky reef from borehole BH6259.**

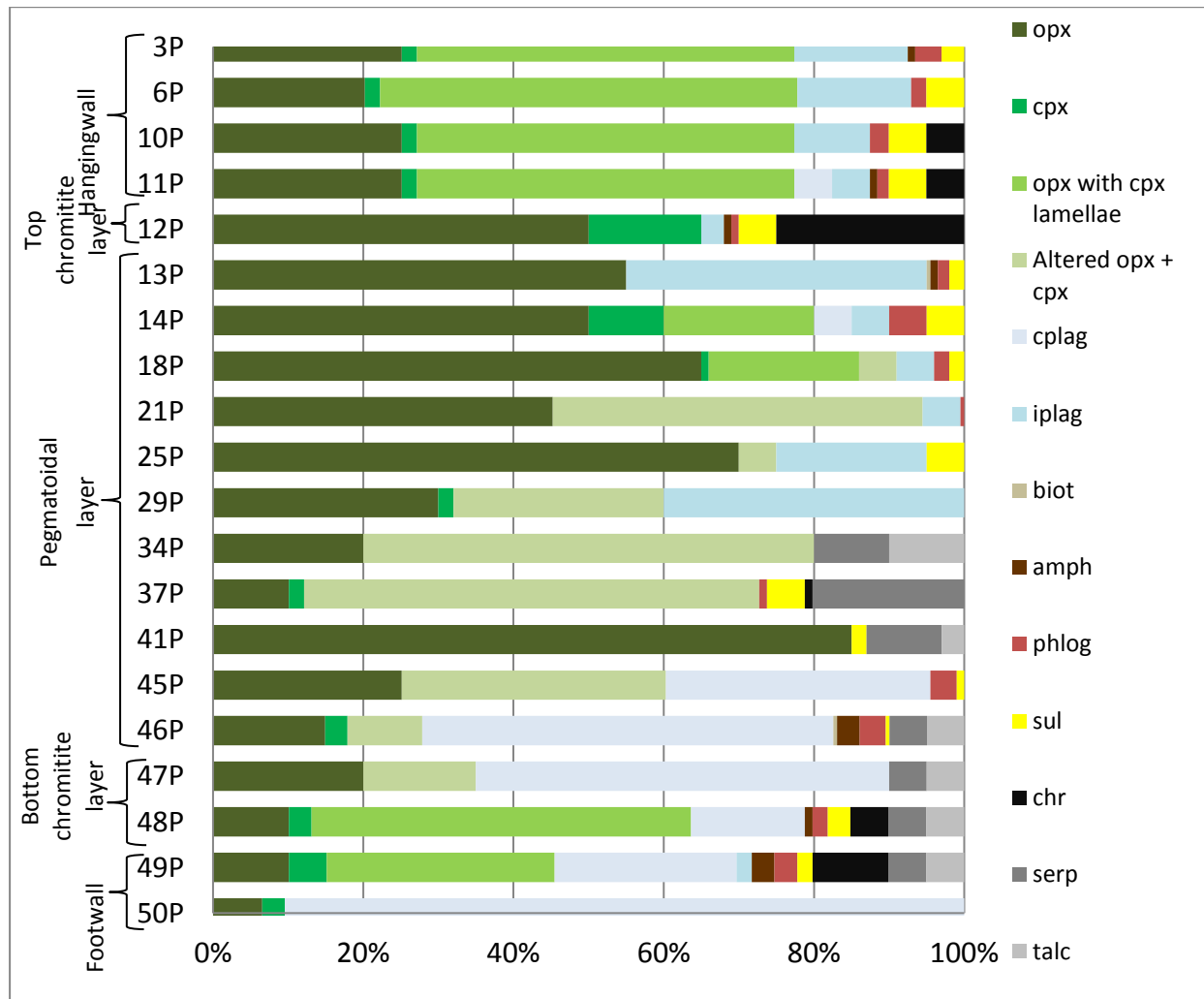


Figure B.3: Modal mineral proportions of pegmatoidal Merensky reef from borehole 20/0252.

## Appendix C

### Plagioclase

**Table C.1: Average plagioclase chemistry data in the hangingwall, chromitite layer and in the footwall from borehole SD14/90. Major element oxides in wt%. (Where the number in front of NP represent the sample number and the 1 or 2 at the end represent the various plagioclase minerals analysed within the sample)(n= number of spots within each mineral analysed)**

Depth (m)	72.14	n=3	72.18	n=4	72.18	n=5	72.22	n=4	72.22	n=4	72.22	n=4	72.24	n=2	72.24	n=3	72.26	n=4	72.26	n=2	72.30	n=4	72.34	n=4
Sample name	1NP	RSD	3NP 1	RSD	3NP 2	RSD	5NP 1	RSD	5NP 2	RSD	5NP 3	RSD	6NP 1	RSD	6NP 2	RSD	7NP 1	RSD	7NP 2	RSD	9NP 1	Sdev	11NP 1	RSD
SiO <sub>2</sub>	54.45	0.64	53.11	1.34	50.97	0.61	50.30	0.42	50.40	0.71	45.99	0.62	50.11	0.86	51.15	0.63	48.50	1.48	46.27	0.11	49.89	1.49	50.13	1.48
TiO <sub>2</sub>	0.01	0.01	0.03	0.02	0.05	0.07	0.02	0.00	0.01	0.02	0.01	0.01	0.02	0.02	0.02	0.06	0.06	n.d.	n.d.	0.06	0.06	0.06	0.06	
Al <sub>2</sub> O <sub>3</sub>	28.85	0.54	29.40	0.69	31.02	0.54	30.88	0.12	30.94	0.42	33.76	0.26	31.47	0.41	30.24	0.13	32.55	1.13	34.54	0.05	31.59	1.08	31.09	1.15
FeO	0.10	0.05	0.14	0.04	0.15	0.06	0.13	0.05	0.11	0.07	0.16	0.05	0.18	n.d.	0.15	0.03	0.13	0.09	0.10	0.08	0.13	0.09	0.13	0.09
MnO	n.d.	n.d.	n.d.	n.d.	n.d.	n.d.	n.d.	n.d.	n.d.	n.d.	n.d.	n.d.	n.d.	n.d.	n.d.	n.d.	n.d.	n.d.	n.d.	n.d.	n.d.	n.d.	n.d.	n.d.
MgO	0.03	0.03	0.05	0.06	0.02	0.02	0.02	0.01	0.01	n.d.	0.01	0.01	0.02	0.02	0.03	0.05	0.01	0.01	0.04	0.04	0.01	0.01	0.01	0.01
CaO	12.09	0.36	12.71	1.07	14.44	0.41	14.40	0.14	14.57	0.54	17.88	0.47	15.24	0.76	13.94	0.17	16.84	1.26	18.97	0.10	16.54	1.16	15.42	1.24
Na <sub>2</sub> O	5.01	0.22	4.51	0.63	3.52	0.27	3.43	0.05	3.38	0.29	1.51	0.23	3.28	0.46	3.82	0.11	2.34	0.72	1.08	0.04	2.31	0.71	3.15	0.71
K <sub>2</sub> O	0.20	0.02	0.08	0.02	0.08	0.02	0.12	0.02	0.08	0.01	0.02	0.00	0.05	0.01	0.09	0.02	0.03	0.02	0.03	0.01	0.03	0.01	0.02	0.02
BaO	0.04	0.03	0.03	0.01	0.01	0.03	0.01	0.02	0.01	n.d.	n.d.	0.04	0.04	0.04	0.03	0.03	0.02	n.d.	n.d.	0.03	0.02	0.03	0.02	0.02
SrO	0.02	0.03	n.d.	n.d.	0.01	0.01	n.d.	n.d.	n.d.	n.d.	n.d.	0.05	0.07	0.02	0.02	0.04	0.05	n.d.	n.d.	0.04	0.05	0.04	0.05	0.05
Total	100.81		100.06		100.26		99.33		99.53		99.34		100.47		99.50		100.54		101.05		100.64		100.10	
An%	56.54		60.66		69.15		69.45		70.11		86.71		71.81		66.57		79.83		90.50		75.65		71.65	

NP1 – NP4: Hangingwall  
NP5 – NP7: Chromitite layer  
NP8 – NP11: Footwall

Depth (m)	Sample name	An%	Ab%	Or%
72.14	1NP	56.54	42.32	1.14
72.18	3NP 1	60.65	38.89	0.47
72.18	3NP 2	69.14	30.41	0.45
72.22	5NP 1	69.45	29.89	0.67
72.22	5NP 2	70.11	29.42	0.47
72.22	5NP 3	86.71	13.19	0.10
72.24	6NP 1	71.80	27.94	0.25
72.24	6NP 2	66.57	32.91	0.52
72.26	7NP 1	79.82	20.03	0.15
72.26	7NP 2	90.50	9.35	0.15
72.30	9NP 1	75.65	24.17	0.18
72.34	11NP 1	71.65	28.11	0.24

**Table C.2: An%, Ab% and Or% for plagioclase in the hangingwall, chromitite layer and in the footwall of borehole SD14/90.**

**Table C.3: Average plagioclase chemistry data in the hangingwall, chromitite layer and in the footwall from borehole BH6259. Major element oxides in wt%. (Where the number in front of N represent the sample number and the 1 or 2 at the end represent the various plagioclase minerals analysed within the sample)(n= number of spots within each mineral analysed)**

Depth (m)	1087.31	n=4	1087.31	n=5	1087.47	n=3	1087.47	n=4	1087.47	n=4	1087.57	n=3	1087.57	n=4	1087.59	n=4	1087.59	n=4	1087.61	n=6	1087.65	n=4	1087.65	n=4	1087.81	n=8	1087.81	n=4	1087.89	n=4	1087.89	n=4		
Sample name	84N 1	RSD	84N 2	RSD	92N 1	RSD	92N 2	RSD	92N 3	RSD	97N 1	RSD	97N 2	RSD	98N 1	RSD	98N 2	RSD	99N	RSD	101N 1	RSD	101N 2	RSD	109N 1	RSD	109N 2	RSD	113N 1	RSD	113N 2	RSD		
SiO <sub>2</sub>	53.76	2.13	55.33	2.90	50.69	0.40	49.67	0.17	51.84	0.34	56.15	1.40	51.91	0.43	47.92	0.25	49.58	1.59	49.21	1.08	48.73	0.27	50.87	1.86	50.08	0.90	49.56	0.33	49.00	0.78	49.90	0.9073		
CaO	11.67	1.82	10.30	2.29	14.25	0.10	15.25	0.13	13.99	0.66	10.82	0.86	13.60	0.17	17.01	0.24	15.52	1.30	16.13	0.83	16.29	0.36	14.51	1.53	15.84	0.69	15.98	0.08	15.94	0.76	15.91	0.7592		
MgO	0.01	0.01	0.01	n.d.	0.04	0.03	0.02	0.01	0.02	0.01	0.01	0.02	0.01	n.d.	0.02	0.01	0.01	n.d.	0.02	0.02	0.01	0.02	0.01	0.01	0.01	0.03	n.d.	0.02	0.02	0.04	0.0062			
Al <sub>2</sub> O <sub>3</sub>	28.67	1.48	27.40	1.91	30.28	0.35	30.88	0.19	30.15	0.82	27.93	0.77	30.05	0.34	33.09	0.28	31.71	0.82	32.07	0.60	32.41	0.36	30.79	1.40	32.03	0.74	32.15	0.25	31.94	0.80	31.80	0.7701		
FeO	0.15	0.05	0.15	0.08	0.14	0.04	0.16	0.02	0.16	0.04	0.10	0.01	0.16	0.08	0.17	0.13	0.17	0.08	0.26	0.06	0.19	0.02	0.21	0.04	0.23	0.08	0.17	0.07	0.32	0.10	0.27	0.0299		
K <sub>2</sub> O	0.15	0.03	0.20	0.04	0.17	0.02	0.13	0.01	0.15	0.02	0.28	0.05	0.15	0.04	0.03	0.02	0.03	0.01	0.11	0.03	0.05	0.01	0.13	0.06	0.10	0.02	0.09	0.02	0.07	0.02	0.11	0.0245		
MnO	n.d.	n.d.																																
BaO	0.02	0.02	0.02	0.02	0.04	0.03	0.02	0.02	0.02	0.01	0.02	0.02	0.02	0.02	0.02	0.02	0.02	0.02	0.02	0.02	0.02	0.02	0.01	0.00	0.01	0.01	0.02	0.01	0.01	0.03	0.02	0.03	0.0234	
Na <sub>2</sub> O	5.10	1.14	5.93	1.40	3.58	0.15	2.93	0.08	3.66	0.29	5.58	0.59	4.01	0.07	2.02	0.10	2.96	0.69	2.61	0.49	2.51	0.16	3.35	0.88	2.75	0.43	2.61	0.09	2.60	0.41	2.73	0.4506		
TiO <sub>2</sub>	0.02	0.02	0.01	0.02	0.01	0.01	0.01	0.03	0.02	0.01	0.01	0.04	0.01	0.01	0.01	0.01	0.01	0.01	0.03	0.02	0.01	0.01	0.01	0.01	0.02	0.01	0.01	0.01	0.01	0.01	0.01	0.01	0.01	0.0067
SrO	n.d.	n.d.	n.d.	n.d.	0.01	0.02	n.d.	n.d.																										
Total	99.57		99.36		99.22		99.07		100.00		100.90		99.96		100.28		100.02		100.47		100.22		99.89		101.08		100.65		99.92		100.79			
An%	55.49		48.59		68.10		73.68		67.31		51.02		64.67		82.22		74.21		76.93		78.03		70.06		75.70		76.81		76.94		75.91			

Depth(m)	Sample name	An%	Ab%	Or%
1087.31	84N 1	55.40	43.76	0.84
1087.31	84N 2	48.48	50.43	1.10
1087.47	92N 1	68.09	30.94	0.97
1087.47	92N 2	73.68	25.55	0.77
1087.47	92N 3	67.32	31.83	0.85
1087.57	97N 1	50.99	47.47	1.54
1087.57	97N 2	64.67	34.47	0.86
1087.59	98N 1	82.21	17.60	0.18
1087.59	98N 2	74.22	25.59	0.19
1087.61	99N	76.91	22.47	0.62
1087.65	101N 1	78.03	21.69	0.28
1087.65	101N 2	70.02	29.20	0.77
1087.81	109N 1	75.68	23.75	0.57
1087.81	109N 2	76.81	22.67	0.52
1087.89	113N 1	76.94	22.64	0.42
1087.89	113N 2	75.89	23.49	0.61

**Table C.4: An%, Ab% and Or% for plagioclase in the hangingwall, chromitite layer and in the footwall of borehole BH6259.**

N73 – N97: Hangingwall  
N98: Chromitite layer  
N99 – N121: Footwall

**Table C.5.: Average plagioclase chemistry data in the hangingwall, top chromitite layer, pegmatoidal layer, bottom chromitite layer and in the footwall from borehole 20/0252. Major element oxides in wt%. (Where the number in front of P represent the sample number and the 1 or 2 at the end represent the various plagioclase minerals analysed within the sample)(n= number of spots within each mineral analysed)**

Thickness (m)	21.50		n= 4		21.40		n= 3		21.38		n= 4		21.36		n= 3		21.36		n= 2		21.36		n= 2		21.04		n= 2		21.04		n= 4		20.72		n= 3		20.70		n= 2		20.65		n= 3		20.63		n= 4		20.63		n= 4	
	Sample name	6P	RSD	11P	RSD	12P	RSD	13P 1	RSD	13P 2	RSD	13P 3	RSD	29P 1	RSD	29P 2	RSD	45P	RSD	46P	RSD	49P	RSD	50P 1	RSD	50P 2	RSD																									
SiO <sub>2</sub>	52.84	0.43	52.67	0.63	50.03	0.27	51.98	0.65	48.82	0.02	48.52	0.59	49.61	0.30	49.98	1.34	51.12	0.14	54.52	0.00	51.18	0.83	49.73	1.11	49.39	1.13																										
CaO	13.08	0.46	13.99	0.29	15.34	0.27	14.61	0.12	16.39	0.18	14.94	1.50	16.19	0.53	15.51	1.13	13.95	0.21	11.66	0.30	15.07	0.83	15.47	0.51	16.06	1.06																										
MgO	0.02	0.01	0.02	0.02	0.03	0.00	0.01	0.01	0.03	0.02	1.02	1.42	0.03	0.02	0.05	0.02	0.02	0.01	0.03	0.01	0.04	0.01	0.02	0.01	0.01	0.01	0.01	0.01	0.01	0.01	0.01	0.01	0.01	0.01	0.01																	
Al <sub>2</sub> O <sub>3</sub>	29.66	0.25	29.54	0.44	31.49	0.18	30.85	0.18	32.30	0.17	30.92	1.54	32.28	0.40	31.83	0.86	30.19	0.13	28.39	0.02	31.21	0.91	31.35	0.57	32.18	0.97																										
FeO	0.13	0.03	0.13	0.02	0.13	0.06	0.11	0.05	0.18	0.03	1.20	1.30	0.28	0.10	0.28	0.02	0.26	0.01	0.27	n.d.	0.30	0.04	0.25	0.11	0.22	0.05																										
K <sub>2</sub> O	0.13	0.01	0.07	0.01	0.11	0.01	0.14	0.01	0.09	0.01	0.10	0.02	0.11	0.01	0.13	0.04	0.15	0.01	0.32	n.d.	0.14	0.04	0.10	0.02	0.07	0.02																										
MnO	0.01	n.d.	n.d.	n.d.	n.d.	n.d.	n.d.	n.d.	n.d.	n.d.	n.d.	n.d.	n.d.	n.d.	n.d.	n.d.	n.d.	n.d.	n.d.	n.d.	n.d.	n.d.	n.d.	n.d.	n.d.	n.d.	n.d.	n.d.	n.d.	n.d.	n.d.	n.d.	n.d.	n.d.																		
BaO	0.02	0.02	n.d.	0.01	0.04	0.01	0.04	0.01	0.02	0.02	n.d.	n.d.	n.d.	n.d.	n.d.	n.d.	n.d.	n.d.	n.d.	n.d.	n.d.	0.01	n.d.	0.01	0.02	0.01	0.01	0.01	0.01	0.01	0.01	0.01	0.01	n.d.																		
Na <sub>2</sub> O	4.45	0.23	4.05	0.21	3.06	0.06	3.51	0.07	2.35	0.04	2.62	0.16	2.57	0.18	2.90	0.62	3.57	0.14	5.65	0.03	3.25	0.31	2.91	0.40	2.70	0.55																										
TiO <sub>2</sub>	0.01	0.01	0.01	0.01	0.01	0.01	0.02	n.d.	0.02	n.d.	0.04	0.02	0.02	0.02	0.04	0.01	0.02	0.01	0.02	n.d.	0.02	0.01	0.02	0.02	0.02	0.02	0.02	0.02	0.02	0.02	0.02	0.02	0.02	0.02	0.02	0.02	0.02	0.02														
SrO	n.d.	0.01	0.02	0.04	n.d.	n.d.	n.d.	n.d.	n.d.	n.d.	n.d.	n.d.	n.d.	n.d.	n.d.	n.d.	n.d.	n.d.	n.d.	n.d.	n.d.	n.d.	n.d.	n.d.	n.d.	n.d.	n.d.	n.d.	n.d.	n.d.	n.d.	n.d.	n.d.	n.d.	n.d.																	
Total	100.34		100.50		100.23		101.28		100.20		99.37		101.09		100.73		99.29		100.87		101.22		99.86		100.66																											
An%	62.11		63.45		73.06		69.19		79.01		75.39		77.25		74.22		67.82		52.44		71.35		74.27		76.38																											

Thickness (m)	Sample name	An%	Ab%	Or%
21.50	6P	77.63	21.87	0.50
21.40	11P	78.60	21.03	0.38
21.38	12P 1	73.06	26.33	0.61
21.36	13P 1	69.19	30.02	0.80
21.36	13P 3	79.01	20.48	0.51
21.36	13P 4	75.49	23.89	0.63
21.04	29P 1	77.26	22.13	0.61
21.04	29P 2	74.22	25.07	0.71
20.72	45P	67.82	31.34	0.84
20.70	46P	52.44	45.87	1.69
20.65	49P	71.38	27.84	0.79
20.63	50P 1	74.25	25.18	0.58
20.63	50P 2	76.38	23.21	0.41

P1 – P11: Hangingwall  
P12: Top chromitite layer  
P13 – P46: Pegmatoidal layer  
P47 – P48: Bottom chromitite layer  
P49 – P52: Footwall

**Table C.6: An%, Ab% and Or% for plagioclase in the hangingwall, top chromitite layer, in the pegmatoidal layer and in the footwall of borehole 20/0252.**

## Orthopyroxene

**Table C.7: Average orthopyroxene chemistry data in the hangingwall, chromitite layer and in the footwall from borehole SD14/90. Major element oxides in wt%. (Where the number in front of NP represent the sample number and the 1 or 2 at the end represent the various orthopyroxene minerals analysed within the sample)(n= number of spots within each mineral analysed)**

Depth (m) Sample name	72.14 1NP	n=7 RSD	72.18 3NP 1	n=5 RSD	72.18 3NP 2	n=3 RSD	72.22 SNP 1	n=4 RSD	72.22 SNP 2	n=4 RSD	72.22 SNP 3	n=4 RSD	72.24 6NP 1	n=8 RSD	72.24 6NP 2	n=2 RSD	72.34 11NP 1	n=3 RSD	72.34 11NP 2	n=3 RSD
SiO <sub>2</sub>	55.97	0.59	55.36	0.38	55.62	0.88	55.44	0.40	55.99	0.14	55.64	0.47	56.43	0.45	57.34	0.10	54.90	0.53	55.02	0.32
CaO	0.91	0.49	1.88	2.17	0.53	0.14	0.82	0.16	0.68	0.09	1.44	0.91	0.84	0.55	0.47	0.02	0.87	0.09	0.71	0.07
TiO <sub>2</sub>	0.24	0.07	0.23	0.06	0.21	0.05	0.16	0.02	0.22	0.02	0.18	0.06	0.11	0.03	0.11	0.00	0.26	0.04	0.19	0.03
Al <sub>2</sub> O <sub>3</sub>	1.14	0.23	1.10	0.24	1.00	0.17	1.30	0.13	0.95	0.14	1.54	0.11	1.39	0.19	0.98	0.05	0.93	0.06	0.84	0.02
FeO	11.97	0.31	12.08	1.16	12.38	0.55	11.20	0.50	12.13	0.45	11.25	0.33	8.83	0.72	8.66	0.04	16.44	0.49	15.96	0.04
K <sub>2</sub> O	0.02	0.01	0.02	0.01	0.03	0.01	0.03	0.01	0.03	0.02	0.03	0.01	0.02	0.01	0.02	0.01	0.06	0.03	0.03	0.01
MnO	0.24	0.01	0.26	0.04	0.24	0.02	0.22	0.01	0.23	0.02	0.23	0.05	0.19	0.03	0.18	0.01	0.33	0.03	0.32	0.04
NiO	0.08	0.02	0.10	0.03	0.08	0.04	0.09	0.04	0.07	0.03	0.05	0.01	0.08	0.03	0.06	0.02	0.09	0.02	0.07	0.05
Na <sub>2</sub> O	0.05	0.02	0.06	0.03	0.08	0.02	0.07	0.03	0.06	0.02	0.06	0.03	0.04	0.02	0.06	0.02	0.07	0.05	0.05	0.01
MgO	29.54	0.58	28.67	1.35	29.64	0.33	30.04	0.74	29.71	0.19	29.58	0.69	31.81	0.87	32.56	0.14	26.74	0.11	26.77	0.43
Cr <sub>2</sub> O <sub>3</sub>	0.39	0.13	0.38	0.10	0.36	0.03	0.49	0.02	0.34	0.09	0.49	0.05	0.43	0.08	0.33	0.01	0.13	0.02	0.15	0.11
Total	100.55		100.14		100.17		99.85		100.40		100.49		100.18		100.77		100.80		100.10	
Mg#	81.48		80.92		81.03		82.70		81.37		82.42		86.53		87.02		74.36		74.94	

NP1 – NP4: Hangingwall  
NP5 – NP7: Chromitite layer  
NP8 – NP11: Footwall

Depth (m)	Sample name	En%	Fs%	Wo%
72.14	1NP	79.72	17.95	2.33
72.18	3NP 1	77.12	18.05	4.82
72.18	3NP 2	80.06	18.57	1.37
72.22	5NP 1	81.09	16.80	2.11
72.22	5NP 2	80.10	18.17	1.74
72.22	5NP 3	79.51	16.80	3.68
72.24	6NP 1	84.80	13.07	2.13
72.24	6NP 2	86.10	12.72	1.18
72.34	11NP 1	72.85	24.89	2.26
72.34	11NP 2	73.72	24.42	1.86

**Table C.8: En%, Fs% and Wo% for orthopyroxene in the hangingwall, chromitite layer, and in the footwall of borehole SD14/90.**

**Table C.9: Average orthopyroxene chemistry data in the hangingwall, chromitite layer and in the footwall from borehole BH6259. Major element oxides in wt%. (Where the number in front of N represent the sample number and the 1 or 2 at the end represent the various orthopyroxene minerals analysed within the sample)(n= number of spots within each mineral analysed)**

Depth (m) Sample name	1087.31 84N 1	n=2 RSD	1087.31 84N 2	n=4 RSD	1087.31 84N 3	n=3 RSD	1087.47 92N	n=4 RSD	1087.47 92N 2	n=4 RSD	1087.57 97N	n=4 RSD	1087.57 97N 2	n=3 RSD	1087.59 98N	n=4 RSD	1087.65 101N	n=4 RSD	1087.81 109N	n=4 RSD	1087.81 109N 2	n=3 RSD
SiO <sub>2</sub>	56.87	0.17	56.83	0.99	55.74	0.38	55.43	0.08	55.36	0.18	55.23	0.34	55.04	0.39	55.93	0.51	55.12	0.42	54.63	0.12	54.72	0.05
CaO	0.58	0.01	0.81	0.17	4.37	6.58	0.91	0.32	1.03	0.90	0.85	0.39	0.61	0.13	0.85	0.32	0.68	0.21	0.66	0.18	0.65	0.15
TiO <sub>2</sub>	0.19	0.00	0.19	0.06	0.22	0.19	0.10	0.01	0.17	0.07	0.17	0.03	0.22	0.09	0.15	0.02	0.21	0.06	0.20	0.03	0.18	0.03
Al <sub>2</sub> O <sub>3</sub>	0.85	0.03	1.35	0.24	1.67	1.23	1.31	0.08	1.05	0.30	1.36	0.46	1.17	0.23	1.54	0.21	1.08	0.09	0.73	0.17	0.84	0.17
FeO	11.87	0.05	12.17	0.34	9.80	4.40	10.97	0.29	12.58	0.13	13.19	0.73	12.98	0.33	9.77	0.36	12.95	0.41	15.62	0.60	14.40	0.35
K <sub>2</sub> O	0.01	n.d.	0.04	0.04	0.12	0.16	0.02	0.01	0.06	0.07	0.08	0.02	n.d.	0.01	0.01	0.01	n.d.	0.01	0.01	0.02	0.01	0.01
MnO	0.23	0.03	0.24	0.01	0.19	0.11	0.22	0.02	0.27	0.04	0.29	0.06	0.27	0.03	0.20	0.03	0.28	0.05	0.32	0.03	0.31	0.03
NiO	0.12	n.d.	0.08	0.03	0.06	0.03	0.08	0.01	0.07	0.04	0.08	0.02	0.11	0.01	0.09	0.02	0.10	0.04	0.10	0.03	0.13	0.01
Na <sub>2</sub> O	0.02	0.01	0.05	0.02	0.21	0.27	0.04	0.01	0.11	0.06	0.07	0.04	0.02	0.01	0.01	0.01	0.01	0.01	0.01	0.03	0.02	0.01
MgO	30.35	0.02	29.11	0.69	26.57	5.24	30.09	0.20	29.22	0.67	29.06	0.45	29.55	0.41	31.83	0.75	29.29	0.35	27.65	0.20	28.60	0.29
Cr <sub>2</sub> O <sub>3</sub>	0.39	0.04	0.41	0.08	0.34	0.27	0.47	0.03	0.39	0.15	0.43	0.13	0.39	0.04	0.46	0.06	0.38	0.09	0.18	0.02	0.18	0.13
Total	101.47		101.28		99.28		99.65		100.31		100.79		100.37		100.84		100.09		100.13		100.05	
Mg#	82.01		81.00		81.05		83.03		80.55		79.71		80.24		85.31		80.14		75.94		77.98	

N73 – N97: Hangingwall  
N98: Chromitite layer  
N99 – N121: Footwall

Depth (m)	Sample name	En%	Fs%	Wo%
1087.31	84N	80.95	17.59	1.46
1087.31	84N 2	79.45	18.45	2.10
1087.31	84N 3	73.45	15.05	11.50
1087.47	92N	81.22	16.45	2.33
1087.47	92N 2	78.59	18.79	2.63
1087.57	97N	78.11	19.70	2.18
1087.57	97N 2	79.13	19.30	1.57
1087.59	98N	83.61	14.26	2.14
1087.65	101N	78.89	19.37	1.74
1087.81	109N	74.81	23.48	1.71
1087.81	109N 2	76.85	21.49	1.66

**Table C.10:** En%, Fs% and Wo% for orthopyroxene in the hangingwall, chromitite layer, and in the footwall of borehole BH6259.

**Table C.11:** Average orthopyroxene chemistry data in the hangingwall, pegmatoidal layer, bottom chromitite layer and in the footwall from borehole 20/0252. Major element oxides in wt%. (Where the number in front of P represent the sample number and the 1 or 2 at the end represent the various orthopyroxene minerals analysed within the sample)(n= number of spots within each mineral analysed)

Thickness (m)	21.50	n=2	21.50	n=4	21.40	n=3	21.40	n=2	21.04	n=2	20.67	n=2	20.65	n=4	20.65	n=5
	6P 1	RSD	6P 2	RSD	11P 1	RSD	11P 2	RSD	29P	RSD	48P	RSD	49P 1	RSD	49P 2	RSD
SiO <sub>2</sub>	55.28	0.20	55.08	0.19	55.40	0.28	55.25	1.28	54.65	0.04	55.20	0.29	56.14	0.26	55.53	1.35
CaO	0.84	0.19	0.92	0.21	1.22	0.18	0.88	0.78	0.81	0.04	1.75	0.02	0.68	0.31	0.77	0.15
TiO <sub>2</sub>	0.20	0.05	0.18	0.06	0.21	0.02	0.16	0.01	0.28	0.01	0.13	0.02	0.08	0.02	0.17	0.03
Al <sub>2</sub> O <sub>3</sub>	1.35	0.24	1.21	0.20	1.20	0.08	1.01	0.24	1.07	0.02	1.55	0.08	1.38	0.14	1.34	0.61
FeO	14.17	0.29	13.44	0.38	13.43	0.14	13.78	0.13	14.52	0.01	12.33	0.11	12.29	0.29	12.96	0.39
K <sub>2</sub> O	0.01	0.01	0.02	0.01	0.02	0.01	0.04	0.02	0.01	n.d.	0.01	0.01	0.02	n.d.	0.01	0.01
MnO	0.27	0.01	0.28	0.04	0.29	0.04	0.27	0.03	0.33	0.03	0.24	0.03	0.26	0.02	0.28	0.05
NiO	0.11	0.05	0.09	0.01	0.10	0.01	0.09	0.03	0.06	n.d.	0.10	0.02	0.07	0.02	0.09	0.02
Na <sub>2</sub> O	0.03	0.01	0.03	n.d.	0.06	0.03	0.05	0.02	0.01	n.d.	0.04	n.d.	0.04	0.02	0.02	0.03
MgO	27.81	0.09	27.80	0.54	27.94	0.09	28.20	0.39	28.20	0.01	28.57	0.18	28.99	0.26	29.42	1.63
Cr <sub>2</sub> O <sub>3</sub>	0.41	0.03	0.41	0.08	0.37	0.02	0.27	0.06	0.29	0.01	0.50	0.03	0.43	0.07	0.40	0.16
Total	100.48		99.46		100.24		100.00		100.22		100.42		100.37		100.99	
Mg#	77.77		78.66		78.77		78.50		77.59		80.52		80.76		80.19	

P1 – P11: Hangingwall  
 P12: Top chromitite layer  
 P13 – P46: Pegmatoidal layer  
 P47 – P48: Bottom chromitite layer  
 P49 – P52: Footwall

Thickness (m)	Sample name	En%	Fs%	Wo%
21.50	6P 1	76.22	21.58	2.20
21.50	6P 2	76.91	20.67	2.42
21.40	11P 1	76.43	20.40	3.17
21.40	11P 2	76.86	20.86	2.28
21.04	29P	76.13	21.79	2.08
20.67	48P	77.05	18.47	4.49
20.65	49P 1	79.51	18.72	1.77
20.65	49P 2	78.76	19.27	1.97

**Table C.12:** En%, Fs% and Wo% for orthopyroxene in the hangingwall, pegmatoidal layer, bottom chromitite layer and in the footwall of borehole 20/0252.

## Clinopyroxene

**Table C.13: Average clinopyroxene chemistry data in the chromitite layer and in the footwall from borehole SD14/90. Major element oxides in wt%. (Where the number in front of NP represent the sample number and the 1 or 2 at the end represent the various clinopyroxene minerals analysed within the sample)(n= number of spots within each mineral analysed)**

Depth (m)	72.26	n=3	72.3	n=4	72.3	n=2	72.3	n=5	72.34	n=3
Sample name	7NP	RSD	9NP 1	RSD	9NP 2	RSD	9NP 3	RSD	11NP 1	RSD
SiO <sub>2</sub>	53.90	0.48	53.60	0.64	52.89	0.20	53.14	0.35	53.75	0.68
CaO	23.62	0.24	22.55	0.37	22.46	0.20	21.81	1.42	23.29	0.44
TiO <sub>2</sub>	0.56	0.06	0.58	0.06	0.59	0.03	0.70	0.06	0.22	0.20
Al <sub>2</sub> O <sub>3</sub>	1.55	0.12	2.07	0.10	2.18	0.10	2.01	0.20	1.27	0.49
FeO	4.66	0.23	6.04	0.31	5.75	0.78	6.34	0.71	6.45	0.39
K <sub>2</sub> O	0.02	n.d.	0.01	n.d.	0.02	0.01	0.02	0.01	0.01	n.d.
MnO	0.16	0.04	0.15	0.02	0.16	0.03	0.14	0.03	0.18	0.05
NiO	0.06	0.02	0.04	0.01	0.05	0.02	0.05	0.03	0.05	0.01
Na <sub>2</sub> O	0.31	0.02	0.41	0.02	0.42	n.d.	0.37	0.01	0.24	0.05
MgO	16.17	0.12	15.17	0.42	15.20	0.23	16.02	0.47	15.29	0.08
Cr <sub>2</sub> O <sub>3</sub>	0.10	0.06	0.71	0.09	0.85	0.03	0.39	0.20	0.16	0.05
Total	101.11		101.34		100.56		100.99		100.91	
Mg#	86.10		81.74		82.54		81.87		80.88	

Depth (m)	Sample name	En%	Fs%	Wo%
72.26	7NP	45.38	7.26	47.36
72.30	9NP 1	43.80	9.70	46.51
72.30	9NP 2	44.15	9.27	46.58
72.30	9NP 3	45.61	10.04	44.35
72.34	11NP 1	43.06	10.08	46.86

**Table C.14: En%, Fs% and Wo% for clinopyroxene in the chromitite layer, and in the footwall of borehole SD14/90.**

NP1 – NP4: Hangingwall  
NP5 – NP7: Chromitite layer  
NP8 – NP11: Footwall

**Table C.15: Average clinopyroxene chemistry data in the hangingwall, and in the footwall from borehole BH6259. Major element oxides in wt%. (Where the number in front of N represent the sample number and the 1 or 2 at the end represent the various clinopyroxene minerals analysed within the sample)(n= number of spots within each mineral analysed)**

Depth (m)	1087.31	n=3	1087.31	n=2	1087.47	n=3	1087.57	n=3	1087.61	n=6	1087.65	n=3	1087.81	n=3	1087.81	n=2	1087.89	n=4
Sample name	84N 1	RSD	84N 2	RSD	92N	RSD	97N	RSD	99N	RSD	101N	RSD	109N 1	RSD	109N 2	RSD	113N	RSD
SiO <sub>2</sub>	53.69	0.06	54.46	0.64	54.30	0.08	52.51	1.58	52.76	0.60	52.11	0.34	52.59	0.29	52.47	0.49	52.34	0.11
CaO	22.48	0.40	22.93	0.07	23.44	0.49	19.13	6.02	23.29	0.47	22.87	0.28	22.93	0.65	22.49	0.19	22.95	0.34
TiO <sub>2</sub>	0.60	0.05	0.33	0.05	0.28	0.03	0.68	0.29	0.45	0.09	0.54	0.15	0.36	0.05	0.51	0.07	0.44	0.06
Al <sub>2</sub> O <sub>3</sub>	1.90	0.19	1.30	0.02	1.60	0.15	3.06	2.41	1.71	0.28	1.88	0.43	1.42	0.20	1.74	0.02	1.39	0.14
FeO	4.71	0.23	3.94	0.22	3.50	0.18	5.08	0.91	5.06	1.01	5.55	0.16	6.15	0.50	5.44	0.86	5.50	0.11
K <sub>2</sub> O	0.04	0.01	0.02	n.d.	0.01	n.d.	0.25	0.35	0.03	0.01	0.01	0.01	0.01	n.d.	0.01	0.01	0.01	0.01
MnO	0.17	0.04	0.16	0.03	0.12	n.d.	0.10	0.04	0.13	0.04	0.11	0.10	0.13	0.11	0.14	0.03	0.14	0.03
NiO	0.02	0.03	0.07	0.07	0.08	0.02	0.09	0.05	0.04	0.03	0.05	0.05	0.06	0.05	0.04	0.01	0.08	0.03
Na <sub>2</sub> O	0.43	0.01	0.37	0.03	0.35	0.03	0.61	0.26	0.36	0.04	0.39	0.03	0.29	0.04	0.32	0.03	0.30	0.03
MgO	16.18	0.37	16.35	0.24	16.33	0.38	16.91	1.57	16.08	0.56	15.56	0.14	15.46	0.45	15.83	0.03	15.67	0.05
Cr <sub>2</sub> O <sub>3</sub>	0.70	0.01	0.63	0.04	0.91	0.13	0.79	0.31	0.26	0.27	0.63	0.07	0.37	0.01	0.52	0.20	0.36	0.02
Total	100.91		100.57		100.92		99.22		100.16		99.69		99.77		99.49		99.19	
Mg#	85.97		88.10		89.28		86.24		85.03		83.34		81.77		83.88		83.55	

N73 – N97: Hangingwall  
N98: Chromitite layer  
N99 – N121: Footwall

Depth (m)	Sample name	En%	Fs%	Wo%
1087.31	84N	46.42	7.51	46.07
1087.31	84N 2	46.83	6.27	46.90
1087.47	92N	46.63	5.55	47.82
1087.57	97N	50.64	8.45	40.91
1087.61	99N	45.27	7.91	46.82
1087.65	101N	44.49	8.81	46.70
1087.81	109N 1	43.85	9.69	46.46
1087.81	109N 2	45.33	8.65	46.02
1087.89	113N	44.62	8.70	46.68

**Table C.16:** En%, Fs% and Wo% for clinopyroxene in the hangingwall and in the footwall of borehole BH6259.

**Table C.17:** Average clinopyroxene chemistry data in the hangingwall, top chromitite layer, pegmatoidal layer, bottom chromitite layer and in the footwall from borehole 20/0252. Major element oxides in wt%. (Where the number in front of P represent the sample number and the 1 or 2 at the end represent the various clinopyroxene minerals analysed within the sample)(n= number of spots within each mineral analysed).

Thickness (m)	21.50	n=3	21.40	n=4	21.38	n=4	21.38	n=3	21.36	n=2	21.36	n=3	21.36	n=3	21.04	n=4	20.67	n=2	20.63	n=3	20.63	n=3
Sample name	6P	RSD	11P	RSD	12P 1	RSD	12P 2	RSD	13P 1	RSD	13P 2	RSD	13P 3	RSD	29P	RSD	48P	RSD	50P 1	RSD	50P 2	RSD
SiO <sub>2</sub>	53.59	0.61	53.49	1.09	52.60	0.20	52.69	0.39	53.99	1.28	52.94	0.13	53.35	0.56	53.39	0.48	52.40	0.01	52.41	0.36	52.44	0.14
CaO	23.53	0.35	22.94	0.26	21.21	0.83	22.73	2.22	18.83	2.22	21.40	2.25	19.87	3.74	22.56	1.12	22.70	0.13	22.02	0.12	22.76	0.22
TiO <sub>2</sub>	0.22	0.21	0.27	0.05	0.40	0.03	0.42	0.09	0.39	0.11	0.43	0.03	0.47	0.13	0.37	0.08	0.37	0.01	0.39	0.02	0.33	0.05
Al <sub>2</sub> O <sub>3</sub>	1.18	0.80	1.90	0.42	1.95	0.11	2.10	0.33	1.87	0.17	1.99	0.15	2.01	0.22	1.36	0.18	2.88	0.06	1.36	0.13	1.25	0.04
FeO	4.76	0.18	4.86	0.26	5.85	0.44	4.91	1.39	6.58	0.15	5.77	0.99	5.89	1.61	5.00	0.20	3.86	0.01	7.14	0.12	6.36	0.44
K <sub>2</sub> O	0.02	0.01	0.02	0.02	0.02	n.d.	n.d.	0.01	0.01	n.d.	0.01	n.d.	0.03	0.01	0.01	0.01	0.01	n.d.	0.01	n.d.	0.01	0.01
MnO	0.12	0.01	0.14	0.01	0.16	0.02	0.13	0.05	0.15	0.10	0.16	0.02	0.07	0.06	0.11	0.08	0.08	n.d.	0.20	0.02	0.20	0.02
NiO	0.05	0.03	0.04	0.01	0.04	0.03	0.07	0.04	0.06	0.01	0.04	0.02	0.01	0.02	0.05	0.03	0.07	0.01	0.03	0.02	0.06	0.03
Na <sub>2</sub> O	0.37	0.02	0.41	0.05	0.39	0.02	0.33	0.10	0.31	0.01	0.37	0.04	0.38	0.08	0.37	0.02	0.44	n.d.	0.28	0.00	0.28	0.04
MgO	15.76	0.45	15.42	0.60	16.17	0.35	15.89	1.21	17.78	1.07	15.79	0.98	16.44	1.98	16.28	0.59	15.96	0.02	15.39	0.11	15.24	0.02
Cr <sub>2</sub> O <sub>3</sub>	0.64	0.14	0.68	0.18	0.73	0.12	0.71	0.02	0.58	0.07	0.68	0.09	0.64	0.10	0.45	0.03	1.09	0.01	0.25	0.05	0.20	0.03
Total	100.24		100.17		99.53		99.97		100.53		99.57		99.14		99.96		99.86		99.49		99.12	
Mg#	85.52		84.98		83.28		85.24		82.95		83.06		83.25		85.30		88.07		79.36		81.04	

Thickness (m)	Sample name	En%	Fs%	Wo%
21.50	6P	44.77	7.50	47.73
21.40	11P	44.69	7.83	47.49
21.38	12P 1	46.79	9.40	43.81
21.38	12P 2	45.58	7.83	46.58
21.36	13P 1	50.96	10.48	38.56
21.36	13P 2	46.06	9.36	44.59
21.36	13P 3	48.50	9.65	41.86
21.04	29P	46.29	7.90	45.81
20.67	48P	46.51	6.24	47.25
20.63	50P 1	43.86	11.31	44.83
20.63	50P 2	43.51	10.08	46.41

**Table C.18:** En%, Fs% and Wo% for clinopyroxene in the hangingwall, top chromitite layer, pegmatoidal layer, bottom chromitite layer and in the footwall of borehole 20/0252.

P1 – P11: Hangingwall  
 P12: Top chromitite layer  
 P13 – P46: Pegmatoidal layer  
 P47 – P48: Bottom chromitite layer  
 P49 – P52: Footwall

## Chromitite

**Table C.19: Average chromite chemistry data in the chromitite layer from borehole SD14/90. Major element oxides in wt%. (Where the number in front of NP represent the sample number and the 1 or 2 at the end represent the various chromite minerals analysed within the sample)(n= number of spots within each mineral analysed).**

Depth (m)	72.22	n=3	72.22	n=4	72.24	n=5	72.24	n=6	72.26	n=5	72.26	n=3
Sample name	5NP 1	RSD	5NP 2	RSD	6NP 1	RSD	6NP 2	RSD	7NP 1	RSD	7NP 2	RSD
SiO <sub>2</sub>	0.02	0.01	0.13	0.07	0.06	0.02	0.08	0.03	0.06	0.02	0.14	0.35
CaO	n.d.	n.d.	0.02	0.01	0.02	0.02	0.02	0.02	0.07	0.06	0.08	0.15
TiO <sub>2</sub>	1.08	0.12	0.96	0.05	0.82	0.08	0.81	0.06	0.85	0.06	0.79	0.10
Al <sub>2</sub> O <sub>3</sub>	18.22	0.44	18.36	0.70	18.86	0.47	19.51	1.60	17.92	0.19	18.17	1.18
FeO	24.96	0.74	23.91	0.62	23.49	0.54	23.56	0.74	22.68	0.61	24.35	1.96
Fe <sub>2</sub> O <sub>3</sub>	6.93	0.74	6.64	0.62	6.53	0.54	6.55	0.74	6.30	0.61	6.77	1.96
ZnO	0.10	0.13	0.13	0.12	0.03	0.04	0.19	0.20	0.21	0.28	0.20	0.09
MnO	0.29	0.01	0.30	0.01	0.30	0.05	0.29	0.05	0.28	0.03	0.33	0.04
NiO	0.15	0.02	0.18	0.06	0.13	0.02	0.13	0.04	0.16	0.02	0.15	0.05
V <sub>2</sub> O <sub>3</sub>	0.31	0.01	0.31	0.03	0.18	0.03	0.21	0.04	0.25	0.02	0.22	0.01
MgO	7.65	0.50	7.97	0.31	7.95	0.09	7.90	0.39	7.95	0.10	7.01	1.09
Cr <sub>2</sub> O <sub>3</sub>	41.35	0.76	41.35	0.70	42.28	0.74	41.24	1.89	45.22	0.21	43.32	0.54
Total	100.36		99.59		100.64		99.81		101.32		100.86	

NP1 – NP4: Hangingwall

NP5 – NP7: Chromitite layer

NP8 – NP11: Footwall

**Table C.20: Average chromite data in the chromitite layer from borehole BH6259. Major element oxides in wt%. (Where the number in front of N represent the sample number and the 1 or 2 at the end represent the various chromite minerals analysed within the sample)(n= number of spots within each mineral analysed).**

Depth (m)	1087.59	n=4	1087.59	n=4	1087.59	n=4
Sample name	98N 1	RSD	98N 2	RSD	98N 3	RSD
SiO <sub>2</sub>	0.04	0.02	0.05	0.02	0.04	0.02
CaO	n.d.	n.d.	n.d.	n.d.	n.d.	n.d.
TiO <sub>2</sub>	1.01	0.57	1.01	0.57	0.96	0.60
Al <sub>2</sub> O <sub>3</sub>	19.55	0.62	19.44	0.69	19.57	0.77
FeO	23.43	0.55	23.55	0.65	23.37	0.53
Fe <sub>2</sub> O <sub>3</sub>	6.51	0.55	6.54	0.65	6.49	0.53
ZnO	0.16	0.12	0.17	0.09	0.18	0.12
MnO	0.28	0.03	0.27	0.04	0.27	0.04
NiO	0.18	0.05	0.17	0.06	0.15	0.02
V <sub>2</sub> O <sub>3</sub>	0.30	0.03	0.29	0.02	0.29	0.02
MgO	8.14	0.25	8.08	0.24	8.04	0.24
Cr <sub>2</sub> O <sub>3</sub>	41.74	0.50	41.64	0.32	41.60	0.35
Total	100.68		100.55		100.32	

N73 – N97: Hangingwall

N98: Chromitite layer

N99 – N121: Footwall

**Table C.21: Average chromite chemistry data in the hangingwall, top chromitite layer, pegmatoidal layer and the bottom chromitite layer from borehole 20/0252. Major element oxides in wt%. (Where the number in front of P represent the sample number and the 1 or 2 at the end represent the various chromite minerals analysed within the sample)(n= number of spots within each mineral analysed).**

Thickness (m)	21.50	n=3	21.40	n=4	21.40	n=3	21.38	n=3	21.36	n=4	20.67	n=4
Sample name	6P	RSD	11P 1	RSD	11P 2	RSD	12P	RSD	13P	RSD	48P	RSD
SiO <sub>2</sub>	0.05	0.02	0.06	0.01	0.07	0.03	0.12	0.07	0.08	0.02	0.12	0.04
CaO	0.11	0.08	n.d.	n.d.	0.01	0.01	0.01	0.02	0.01	0.01	0.02	n.d.
TiO <sub>2</sub>	0.78	0.05	2.79	0.05	2.14	0.27	2.74	0.12	3.29	0.10	1.02	0.10
Al <sub>2</sub> O <sub>3</sub>	7.91	0.09	10.17	0.03	9.46	0.72	12.38	0.27	9.94	0.17	16.61	0.19
FeO	30.82	0.29	33.24	0.09	36.16	3.28	29.30	0.32	33.99	0.66	24.16	0.80
Fe <sub>2</sub> O <sub>3</sub>	8.56	0.29	9.24	0.09	10.05	3.28	8.14	0.32	9.44	0.66	6.71	0.80
ZnO	0.14	0.15	0.32	0.22	0.25	0.30	0.19	0.19	0.11	0.12	0.05	0.05
MnO	0.46	0.02	0.34	0.04	0.37	0.04	0.28	0.02	0.33	0.05	0.27	0.04
NiO	0.10	0.02	0.31	0.01	0.22	0.07	0.25	0.02	0.30	0.02	0.18	0.02
V <sub>2</sub> O <sub>3</sub>	0.80	0.04	0.72	0.05	0.71	0.02	0.65	0.02	0.69	0.05	0.33	0.03
MgO	2.41	0.03	3.68	0.03	2.55	0.83	5.68	0.34	4.35	0.17	7.17	0.26
Cr <sub>2</sub> O <sub>3</sub>	50.21	0.44	41.55	0.08	40.20	1.33	41.45	0.64	38.71	0.10	44.26	0.38
Total	101.49		101.49		101.16		100.38		100.29		100.23	

P1 – P11: Hangingwall  
 P12: Top chromitite layer  
 P13 – P46: Pegmatoidal layer  
 P47 – P48: Bottom chromitite layer  
 P49 – P52: Footwall

## Mica

**Table C.22: Average mica chemistry data in the footwall from borehole SD14/90. Major element oxides in wt%. (Where the number in front of NP represent the sample number and the 1 or 2 at the end represent the various mica minerals analysed within the sample)(n= number of spots within each mineral analysed).**

Depth (m)	72.22	n=2	72.26	n=3	72.30	n=3
Sample name	5NP	RSD	7NP	RSD	9NP	RSD
SiO <sub>2</sub>	39.81	0.88	39.61	0.25	38.90	0.64
CaO	0.03	n.d.	0.02	0.01	0.01	0.01
Al <sub>2</sub> O <sub>3</sub>	15.15	0.18	15.48	0.10	14.74	0.09
F	0.28	0.01	0.33	0.14	0.26	0.16
MgO	23.08	0.35	23.30	0.18	20.21	0.04
FeO	2.48	0.09	2.52	0.05	5.51	0.19
Fe <sub>2</sub> O <sub>3</sub>	0.69	0.03	0.70	0.01	1.53	0.05
K <sub>2</sub> O	9.14	0.18	9.06	0.05	9.66	0.09
MnO	n.d.	n.d.	0.03	0.01	0.03	0.01
BaO	0.41	n.d.	0.43	0.03	0.83	0.25
Na <sub>2</sub> O	0.38	0.02	0.68	0.01	0.21	0.03
Cl	0.17	0.01	0.15	0.01	0.20	0.03
TiO <sub>2</sub>	3.14	0.65	3.24	0.06	3.73	0.28
Cr <sub>2</sub> O <sub>3</sub>	1.46	0.17	1.29	0.04	1.18	0.21
Total	96.23		96.83		96.99	

NP1 – NP4: Hangingwall  
 NP5 – NP7: Chromitite layer  
 NP8 – NP11: Footwall

**Table C.23: Average mica chemistry data in the hangingwall, chromitite layer and in the footwall from borehole BH6259. Major element oxides in wt%. (Where the number in front of N represent the sample number and the 1 or 2 at the end represent the various mica minerals analysed within the sample)(n= number of spots within each mineral analysed).**

Depth (m)	1087.31	n=3	1087.31	n=5	1087.31	n=3	1087.47	n=5	1087.57	n=4	1087.59	n=2	1087.61	n=5	1087.61	n=4	1087.65	n=4	1087.81	n=2	1087.89	n=4
Sample name	84N	RSD	84N 2	RSD	84N 3	RSD	92N	RSD	97N	RSD	98N	RSD	99N	RSD	99N 2	RSD	101N	RSD	109N	RSD	113N	RSD
SiO <sub>2</sub>	38.67	0.16	38.26	0.55	38.59	0.36	39.21	0.21	40.75	0.09	46.29	0.16	39.32	1.30	37.91	1.56	40.33	0.54	40.28	0.06	38.66	0.31
CaO	0.03	0.01	0.01	0.01	0.01	0.01	0.03	0.02	0.01	0.01	11.58	0.02	0.39	0.48	0.14	0.19	n.d.	0.00	0.04	n.d.	0.11	0.02
Al <sub>2</sub> O <sub>3</sub>	14.56	0.19	14.18	0.21	14.21	0.44	14.62	0.43	15.07	0.17	11.06	0.10	15.67	0.32	15.45	0.74	15.41	0.60	15.01	0.01	14.45	0.57
F	0.36	0.10	0.12	0.14	0.18	0.16	0.30	0.14	0.31	0.07	0.09	0.04	0.31	0.12	0.22	0.19	0.28	0.13	0.13	n.d.	0.09	0.07
MgO	19.27	0.39	18.45	0.56	18.89	0.37	19.15	0.50	21.55	0.13	18.07	0.08	22.30	1.15	19.37	1.82	20.92	1.87	19.62	0.09	16.42	2.17
FeO	6.01	0.28	6.38	0.19	6.03	0.28	6.24	0.27	6.09	0.47	3.59	0.32	3.33	1.01	7.40	3.32	5.75	1.23	8.44	0.07	9.50	2.37
Fe <sub>2</sub> O <sub>3</sub>	1.67	0.08	1.77	0.05	1.67	0.08	1.73	0.07	1.69	0.13	1.00	0.09	0.93	0.28	2.06	0.92	1.60	0.34	2.35	0.05	2.64	0.66
K2O	9.75	0.18	9.57	0.05	9.37	0.16	9.63	0.20	9.68	0.39	0.28	0.14	9.36	0.95	8.90	1.99	9.01	0.66	9.22	0.01	9.71	0.28
MnO	0.05	0.03	0.03	0.03	0.02	0.01	0.04	0.04	0.05	0.02	0.09	n.d.	0.03	0.02	0.04	0.05	0.03	0.02	0.09	0.01	0.05	0.07
BaO	0.45	0.04	0.55	0.24	0.40	0.10	0.46	0.52	0.05	0.02	0.05	0.05	0.34	0.07	0.58	0.67	0.20	0.04	0.10	n.d.	0.35	0.08
Na <sub>2</sub> O	0.21	0.07	0.19	0.04	0.25	0.02	0.19	0.09	0.26	0.06	1.94	0.05	0.30	0.23	0.13	0.08	0.35	0.06	0.25	0.06	0.17	0.05
Cl	0.30	0.01	0.30	0.02	0.32	0.03	0.36	0.07	0.46	0.02	0.17	0.08	0.22	0.06	0.31	0.11	0.19	0.04	0.21	n.d.	0.35	0.16
TiO <sub>2</sub>	3.61	0.32	4.85	0.63	4.91	0.22	3.35	0.86	0.48	0.32	2.11	0.05	3.92	1.13	4.25	0.53	1.63	0.29	0.89	0.01	3.61	0.12
Cr <sub>2</sub> O <sub>3</sub>	0.90	0.06	1.12	0.20	1.47	0.14	1.60	0.15	0.27	0.24	2.26	0.04	1.05	0.07	0.56	0.61	0.89	0.46	0.09	n.d.	0.41	0.04
Total	95.83		95.79		96.32		96.93		96.71		98.58		97.46		97.31		96.59		96.71		96.52	

**Table C.24: Average mica chemistry data in the hangingwall and in the pegmatoidal layer from borehole 20/0252. Major element oxides in wt%. (Where the number in front of P represent the sample number and the 1 or 2 at the end represent the various mica minerals analysed within the sample)(n= number of spots within each mineral analysed).**

Thickness (m)	21.50	n=3	21.40	n=2	21.36	n=2
Sample name	6P	RSD	11P	RSD	13P	RSD
SiO <sub>2</sub>	39.37	0.02	38.81	0.01	38.88	0.28
CaO	0.05	0.03	0.10	0.01	0.03	0.01
Al <sub>2</sub> O <sub>3</sub>	14.39	0.20	14.80	0.04	14.36	0.23
F	0.03	0.04	0.01	n.d.	0.09	0.07
MgO	19.19	0.13	19.80	0.05	18.22	0.43
FeO	5.65	0.27	6.19	0.03	7.91	0.42
Fe <sub>2</sub> O <sub>3</sub>	1.57	0.07	1.72	0.01	2.20	0.12
K2O	9.56	0.04	9.55	0.04	9.52	0.30
MnO	n.d.	n.d.	0.02	n.d.	0.06	0.01
BaO	0.11	0.03	0.34	0.01	0.30	0.03
Na <sub>2</sub> O	0.26	0.01	0.38	0.02	0.15	0.04
Cl	0.39	0.01	0.34	0.03	0.31	0.02
TiO <sub>2</sub>	3.09	0.07	3.42	n.d.	4.09	0.12
Cr <sub>2</sub> O <sub>3</sub>	1.75	0.01	0.95	0.07	0.40	0.09
Total	95.42		96.42		96.52	

P1 – P11: Hangingwall  
 P12: Top chromitite layer  
 P13 – P46: Pegmatoidal layer  
 P47 – P48: Bottom chromitite layer  
 P49 – P52: Footwall

## Sulphides

### Chalcopyrite

**Table C.25: Average chalcopyrite chemistry data in the hangingwall, chromitite layer and in the footwall from borehole SD14/90. Major element oxides in wt%. (Where the number in front of NP represent the sample number and the 1 or 2 at the end represent the various chalcopyrite minerals analysed within the sample)(n= number of spots within each mineral analysed).**

Depth (m)	72.14	n=3	72.18	n=2	72.22	n=2	72.22	n=2	72.24	n=3	72.24	n=3	72.24	n=2	72.26	n=2	72.30	n=4	72.30	n=3
Sample name	1NP	RSD	3NP	RSD	5NP 1	RSD	5NP 2	RSD	6NP 1	RSD	6NP 2	RSD	6NP 3	RSD	7NP	RSD	9NP 1	RSD	9NP 2	RSD
Fe	30.58	0.33	28.29	0.06	30.44	0.65	30.27	1.33	30.77	0.06	30.02	0.49	29.76	0.10	31.46	0.95	31.16	0.59	30.18	0.82
Ni	0.03	0.03	n.d.	n.d.	0.04	0.06	0.58	0.46	0.03	0.06	0.02	0.02	0.08	0.12	0.03	0.04	0.02	0.02	0.06	0.10
Cu	31.90	0.17	31.59	0.01	31.52	0.08	31.38	1.09	31.77	0.23	31.59	0.34	31.06	0.16	31.91	0.31	32.18	0.66	31.09	1.12
Co	0.04	n.d.	0.05	n.d.	0.01	0.02	0.04	n.d.	0.03	0.01	0.01	0.01	0.04	0.03	0.06	0.01	0.05	0.01	0.06	0.02
S	33.26	0.17	33.13	0.01	34.34	0.41	33.65	0.26	35.16	0.26	33.71	0.13	32.11	0.35	34.76	0.19	33.37	2.03	33.42	1.71
Total	95.82		93.06		96.35		95.92		97.77		95.35		93.05		98.21		96.77		94.80	

**Table C.26: Average chalcopyrite chemistry data in the hangingwall, chromitite layer and in the footwall from borehole BH6259. Major element oxides in wt%. (Where the number in front of N represent the sample number and the 1 or 2 at the end represent the various chalcopyrite minerals analysed within the sample)(n= number of spots within each mineral analysed).**

Depth (m)	1087.47	n=2	1087.59	n=3	1087.65	n=2	1087.81	n=2
Sample name	92N	RSD	98N	RSD	101N	RSD	109N	RSD
Fe	30.73	0.81	30.40	0.15	30.15	0.56	31.14	0.22
Ni	0.03	0.04	0.06	0.06	n.d.	n.d.	0.13	0.08
Cu	31.80	0.24	31.50	0.40	32.61	0.48	33.41	0.30
Co	0.02	0.02	0.02	0.04	0.04	0.01	0.05	0.01
S	34.67	0.52	34.37	0.27	35.95	1.04	34.86	0.70
Total	97.24	1.52	96.35	0.56	98.74	2.07	99.59	0.71

N73 – N97: Hangingwall  
N98: Chromitite layer  
N99 – N121: Footwall

**Table C.27: Average chalcopyrite chemistry data in the hangingwall, top chromitite layer, pegmatoidal layer and in the footwall from borehole 20/0252. Major element oxides in wt%. (Where the number in front of P represent the sample number and the 1 or 2 at the end represent the various chalcopyrite minerals analysed within the sample)(n= number of spots within each mineral analysed).**

Thickness (m)	21.50	n=2	21.40	n=2	21.38	n=3	21.36	n=3	20.65	n=2	20.65	n=4
Sample name	6P	RSD	11P	RSD	12P	RSD	13P	RSD	49P 1	RSD	49P 2	RSD
Fe	30.94	0.88	30.12	1.04	30.87	0.48	30.28	0.67	30.11	0.20	30.59	0.59
Ni	0.03	0.04	0.02	0.03	0.01	0.02	0.21	0.28	0.09	0.03	0.02	0.10
Cu	33.66	0.13	34.22	0.05	33.12	0.34	32.62	0.08	33.14	0.13	33.25	0.47
Co	0.03	0.02	0.05	0.04	0.04	0.03	0.05	0.01	0.04	0.02	0.05	0.02
S	34.41	0.15	34.70	0.01	34.13	0.07	33.95	0.07	34.28	0.49	33.88	0.51
Total	99.07		99.11		98.17		97.12		97.66		97.80	

## Pyrrhotite

**Table C.28: Average pyrrhotite chemistry data in the hangingwall, chromitite layer and in the footwall from borehole SD14/90. Major element oxides in wt%. (Where the number in front of NP represent the sample number and the 1 or 2 at the end represent the various pyrrhotite minerals analysed within the sample)(n= number of spots within each mineral analysed).**

Depth (m)	72.18 3NP 1	n=2 RSD	72.18 3NP 2	n=2 RSD	72.22 5NP	n=3 RSD	72.24 6NP	n=3 RSD	72.26 7NP	n=2 RSD	72.30 9NP	n=3 RSD
Fe	63.96	0.61	63.27	0.44	61.14	1.13	61.60	0.94	62.30	0.39	61.55	0.94
Ni	0.32	0.13	0.16	0.22	0.09	0.08	0.20	0.13	0.22	0.14	0.17	0.03
Cu	0.02	0.03	n.d.	n.d.	n.d.	0.01	0.03	0.02	0.02	0.02	0.03	0.02
Co	0.07	0.02	0.09	0.03	0.06	0.02	0.05	0.04	0.04	0.02	0.08	0.05
S	37.46	0.12	37.56	0.34	37.27	0.22	37.91	0.14	37.91	0.48	37.13	0.76
Total	101.82		101.08		98.56		99.78		100.49		98.95	

NP1 – NP4: Hangingwall  
NP5 – NP7: Chromitite layer  
NP8 – NP11: Footwall

**Table C.29: Average pyrrhotite chemistry data in the hangingwall, chromitite layer and in the footwall from borehole BH6259. Major element oxides in wt%. (Where the number in front of N represent the sample number and the 1 or 2 at the end represent the various pyrrhotite minerals analysed within the sample)(n= number of spots within each mineral analysed).**

Depth (m)	1087.31 84N	n=1 RSD	1087.47 92N	n=2 RSD	1087.57 97N	n=2 RSD	1087.59 98N	n=1 RSD
Fe	59.45	N.A.	59.93	1.57	61.03	0.49	62.55	N.A.
Ni	0.20		0.21	0.03	0.41	0.04	0.09	
Cu	0.03		n.d.	n.d.	n.d.	n.d.	n.d.	
Co	0.06		0.07	0.03	0.06	n.d.	0.08	
S	36.45		37.60	0.17	38.27	0.19	37.97	
Total	96.19		97.81		99.76		100.69	

N73 – N97: Hangingwall  
N98: Chromitite layer  
N99 – N121: Footwall

**Table C.30: Average pyrrhotite chemistry data in the hangingwall, top chromitite layer and in the pegmatoidal layer from borehole 20/0252. Major element oxides in wt%. (Where the number in front of P represent the sample number and the 1 or 2 at the end represent the various pyrrhotite minerals analysed within the sample)(n= number of spots within each mineral analysed).**

Thickness (m)	21.50 6P	n=2 RSD	21.40 11P	n=2 RSD	21.38 12P	n=2 RSD	20.72 45P	n=4 RSD
Fe	60.93	0.26	58.94	0.51	60.39	1.98	58.61	0.41
Ni	0.35	0.02	0.41	0.02	0.19	0.06	0.39	0.25
Cu	0.02	n.d.	0.03	n.d.	0.06	0.03	n.d.	0.03
Co	0.08	0.01	0.03	0.01	0.09	0.03	0.05	0.02
S	38.55	0.21	38.66	0.13	39.22	0.38	38.30	0.90
Total	99.92		98.07		99.94		97.35	

P1 – P11: Hangingwall  
P12: Top chromitite layer  
P13 – P46: Pegmatoidal layer  
P47 – P48: Bottom chromitite layer  
P49 – P52: Footwall

## Pentlandite

**Table C.31: Average pentlandite chemistry data in the hangingwall, chromitite layer and in the footwall from borehole SD14/90. Major element oxides in wt%. (Where the number in front of NP represent the sample number and the 1 or 2 at the end represent the various pentlandite minerals analysed within the sample)(n= number of spots within each mineral analysed).**

Depth (m)	72.14	n=3	72.18	n=3	72.24	n=6	72.26	n=2	72.26	n=2
Sample name	1NP	RSD	3NP	RSD	6NP	RSD	7NP	RSD	7NP 2	RSD
Fe	36.54	0.57	35.13	0.73	33.54	1.17	34.21	0.82	32.62	0.33
Ni	31.11	0.36	32.22	0.57	31.03	0.37	31.47	1.50	29.06	0.61
Cu	0.02	0.02	n.d.	n.d.	0.03	0.04	1.39	1.72	0.05	0.03
Co	0.59	0.01	0.67	0.07	0.57	0.02	0.53	0.03	0.51	0.04
S	31.01	2.56	32.16	0.47	32.61	0.06	32.84	0.10	29.25	0.89
Total	99.27		100.18		97.78		100.45		91.49	

NP1 – NP4: Hangingwall  
NP5 – NP7: Chromitite layer  
NP8 – NP11: Footwall

**Table C.32: Average pentlandite chemistry data in the hangingwall, chromitite layer and in the footwall from borehole BH6259. Major element oxides in wt%. (Where the number in front of N represent the sample number and the 1 or 2 at the end represent the various pentlandite minerals analysed within the sample)(n= number of spots within each mineral analysed).**

Depth (m)	1087.31	n=1	1087.47	n=1	1087.59	n=1	1087.89	n=1
Sample name	84N	RSD	92N	RSD	98N	RSD	113N	RSD
Fe	31.74	N.A.	32.14	N.A.	34.40	N.A.	31.34	N.A.
Ni	30.58		32.96		30.37		32.67	
Cu	0.02		0.03		0.16		0.03	
Co	0.75		0.62		0.47		0.58	
S	32.12		32.51		32.29		33.22	
Total	95.20		98.26		97.69		97.84	

N73 – N97: Hangingwall  
N98: Chromitite layer  
N99 – N121: Footwall

**Table C.33: Average pentlandite chemistry data in the hangingwall and in the pegmatoidal layer from borehole 20/0252. Major element oxides in wt%. (Where the number in front of P represent the sample number and the 1 or 2 at the end represent the various pentlandite minerals analysed within the sample)(n= number of spots within each mineral analysed).**

Thickness (m)	21.5	n=1	21.4	n=1	20.72	n=1
Sample name	6P	RSD	11P	RSD	45P	RSD
Fe	29.73	N.A.	31.30	N.A.	30.36	N.A.
Ni	35.37		34.32		32.23	
Cu	n.d.		0.05		0.02	
Co	0.73		0.60		0.67	
S	33.03		33.13		32.65	
Total	98.85		99.41		95.93	

P1 – P11: Hangingwall  
P12: Top chromitite layer  
P13 – P46: Pegmatoidal layer  
P47 – P48: Bottom chromitite layer  
P49 – P52: Footwall

## Pyrite

**Table C.34: Average pyrite chemistry data in the hangingwall, chromitite layer and in the footwall from borehole BH6259. Major element oxides in wt%.**  
(Where the number in front of N represent the sample number and the 1 or 2 at the end represent the various pyrite minerals analysed within the sample)(n= number of spots within each mineral analysed).

Depth (m)	1087.57	n=3	1087.89	n=1
Sample name	97N	RSD	113N	RSD
Fe	47.05	1.52	45.47	N.A.
Ni	0.12	0.13	0.14	
Cu	0.02	0.03	n.d.	
Co	0.34	0.52	0.59	
S	52.84	0.23	53.57	
Total	100.37		99.77	

N73 – N97: Hangingwall

N98: Chromitite layer

N99 – N121: Footwall

## Appendix D

	Standards analysed		
	JB1a	MRG1	NIM-P
<b>SiO<sub>2</sub></b>	52.40	38.28	50.53
<b>TiO<sub>2</sub></b>	1.29	3.71	0.20
<b>Al<sub>2</sub>O<sub>3</sub></b>	14.38	8.38	3.94
<b>Fe<sub>2</sub>O<sub>3</sub></b>	9.16	17.98	12.51
<b>MnO</b>	0.16	0.18	0.23
<b>MgO</b>	7.78	13.70	25.61
<b>CaO</b>	9.35	14.88	2.67
<b>Na<sub>2</sub>O</b>	2.65	0.77	0.39
<b>K<sub>2</sub>O</b>	1.40	0.18	0.08
<b>P<sub>2</sub>O<sub>5</sub></b>	0.25	0.08	0.03
<b>Cr<sub>2</sub>O<sub>3</sub></b>	0.06	0.06	3.78
<b>NiO</b>	0.02	0.03	0.08
<b>LOI</b>	0.78	1.02	0.56
<b>Total</b>	99.66	99.24	100.60

	Certified/ Preferred values		
	JB1a	MRG1	NIM-P
<b>SiO<sub>2</sub></b>	52.16	39.12	51.10
<b>TiO<sub>2</sub></b>	1.30	3.74	0.20
<b>Al<sub>2</sub>O<sub>3</sub></b>	14.51	8.47	4.18
<b>Fe<sub>2</sub>O<sub>3</sub></b>	9.10	17.94	12.76
<b>MnO</b>	0.15	0.17	0.22
<b>MgO</b>	7.75	13.55	25.33
<b>CaO</b>	9.23	14.70	2.66
<b>Na<sub>2</sub>O</b>	2.74	0.74	0.37
<b>K<sub>2</sub>O</b>	1.42	0.18	0.09
<b>P<sub>2</sub>O<sub>5</sub></b>	0.27	0.08	0.02
<b>Cr<sub>2</sub>O<sub>3</sub></b>	0.06	0.05	3.80
<b>NiO</b>	0.02	0.03	0.07
<b>LOI</b>	0.78	1.02	0.56
<b>Total</b>	99.48	99.79	101.36

**Table D.1: Whole rock geochemistry of standards analyzed and the certified reference material values.**

**Table D.2: Whole rock geochemistry of borehole SD14/90 obtained from ICP-MS analysis (major element oxides) and element ratios. Major element oxides in wt%. (Cr/(Cr+Fe<sup>3+</sup>) and (Cr/(Cr+Al) calculated using molar values.**

Depth(m)	72.14	72.16	72.18	72.20	72.22	72.24	72.26	72.28	72.30	72.32	72.34
Sample name	NP1	NP2	NP3	NP4	NP5	NP6	NP7	NP8	NP9	NP10	NP11
<b>SiO<sub>2</sub></b>	50.53	50.05	51.24	45.41	18.48	29.81	37.94	47.28	48.68	47.71	47.48
<b>TiO<sub>2</sub></b>	0.30	0.23	0.20	0.27	0.68	0.64	0.35	0.08	0.10	0.06	0.06
<b>Al<sub>2</sub>O<sub>3</sub></b>	4.36	5.70	5.89	7.06	20.50	17.62	22.50	29.70	27.09	27.16	29.45
<b>Fe<sub>2</sub>O<sub>3</sub></b>	2.97	2.93	2.91	3.25	4.86	4.74	2.12	0.31	0.65	0.71	0.19
<b>FeO</b>	10.68	10.54	10.49	11.68	17.48	17.07	7.62	1.13	2.36	2.54	0.70
<b>MnO</b>	0.22	0.22	0.22	0.21	0.23	0.21	0.10	0.03	0.05	0.05	0.02
<b>MgO</b>	23.30	23.27	22.85	22.49	10.76	13.21	3.85	1.86	4.73	5.94	1.08
<b>CaO</b>	5.09	4.57	3.81	3.71	3.87	3.46	9.58	17.05	14.53	13.55	18.07
<b>Na<sub>2</sub>O</b>	0.50	0.55	0.55	0.45	0.37	0.42	1.13	2.19	1.93	1.78	2.06
<b>K<sub>2</sub>O</b>	0.05	0.03	0.03	0.02	0.10	0.05	0.17	0.16	0.17	0.17	0.05
<b>P<sub>2</sub>O<sub>5</sub></b>	0.01	0.01	0.00	0.01	0.02	0.02	0.02	0.03	0.03	0.03	0.02
<b>Cr<sub>2</sub>O<sub>3</sub></b>	0.44	0.36	0.36	4.08	20.98	10.57	12.75	0.20	0.12	0.09	0.02
<b>NiO</b>	0.72	0.80	0.62	0.49	0.44	0.35	0.14	0.02	0.14	0.10	0.00
<b>LOI</b>	0.53	0.76	0.47	0.21	n.d.	n.d.	0.17	0.30	0.38	0.25	0.31
<b>Total</b>	100.91	101.21	100.82	100.63	99.46	99.20	99.30	100.48	101.23	100.42	99.60
<b>Element ratios</b>											
<b>Mg#</b>	75.7	75.91	75.67	73.33	46.78	52.49	41.87	70.26	74.14	76.96	68.81
<b>An%</b>	67.92	72.46	73.24	80.96	100.00	81.90	82.39	84.36	78.89	80.41	82.43
<b>Cr/(Cr+Fe<sup>3+</sup>)</b>	0.03	0.03	0.03	0.21	0.48	0.32	0.56	0.12	0.04	0.03	0.03
<b>Cr/(Cr+Al)</b>	0.06	0.04	0.04	0.28	0.41	0.29	0.28	n.d.	n.d.	n.d.	

NP1-NP4: Hangingwall  
 NP5-NP7: Chromitite layer  
 NP8-NP11: Footwall

**Table D.3: Whole rock geochemistry of borehole BH6259 obtained from ICP-MS analysis (major element oxides) and element ratios. Major element oxides in wt%. ( $\text{Cr}/(\text{Cr}+\text{Fe}^{3+})$ ) and ( $\text{Cr}/(\text{Cr}+\text{Al})$ ) calculated using molar values.**

Depth(m)	1087.1	1087.11	1087.13	1087.15	1087.17	1087.19	1087.21	1087.23	1087.25	1087.27	1087.29	1087.31	1087.33	1087.35	1087.37	1087.39	1087.43	1087.45	1087.47	1087.49	1087.51	1087.53	
Sample name	N73	N74	N75	N76	N77	N78	N79	N80	N81	N82	N83	N84	N85	N86	N87	N88	N89	N90	N91	N92	N93	N94	N95
$\text{SiO}_2$	53.66	50.88	52.29	52.30	50.82	52.60	53.14	52.87	52.16	51.66	53.91	51.66	51.90	52.05	52.27	51.60	51.53	50.52	52.42	49.75	49.21	48.52	
$\text{TiO}_2$	0.28	0.22	0.39	0.29	0.20	0.10	0.51	0.30	0.34	0.25	0.40	0.43	0.25	0.25	0.19	0.14	0.17	0.17	0.18	0.21	0.21	0.32	
$\text{Al}_2\text{O}_3$	5.32	5.84	4.79	3.86	5.69	4.73	4.94	5.91	4.61	7.50	7.62	7.91	5.04	8.31	5.51	7.50	5.36	5.38	7.40	6.47	4.69	3.16	
$\text{Fe}_2\text{O}_3$	2.30	2.35	2.25	2.38	2.33	2.37	2.39	2.25	2.30	1.91	2.11	2.03	2.37	2.00	2.45	2.10	2.44	2.55	2.30	2.65	2.96	3.34	
$\text{FeO}$	8.27	8.47	8.11	8.55	8.38	8.53	8.60	8.09	8.29	6.88	7.58	7.29	8.52	7.20	8.81	7.54	8.80	9.19	8.27	9.52	10.66	12.01	
$\text{MnO}$	0.21	0.20	0.20	0.18	0.19	0.12	0.21	0.22	0.20	0.18	0.19	0.20	0.22	0.19	0.19	0.21	0.20	0.18	0.22	0.22	0.22	0.22	
$\text{MgO}$	24.13	25.45	24.33	25.15	25.35	25.92	24.97	22.68	25.83	20.86	21.09	21.74	25.27	21.40	23.94	23.53	24.84	25.17	22.83	25.03	24.23	23.48	
$\text{CaO}$	3.30	3.48	3.54	5.41	3.54	2.54	2.59	3.69	2.93	7.03	4.04	5.11	3.68	4.77	3.20	4.25	3.64	3.08	4.44	4.44	3.25	3.37	
$\text{Na}_2\text{O}$	0.67	0.71	0.61	0.43	0.59	0.50	0.41	0.65	0.56	1.02	1.06	0.88	0.52	1.16	0.64	0.58	0.50	0.58	0.63	0.59	0.44	0.32	
$\text{K}_2\text{O}$	0.50	0.37	0.71	0.32	0.31	0.14	0.76	0.49	0.65	0.28	0.53	0.21	0.21	0.45	0.25	0.10	0.07	0.14	0.13	0.08	0.10	0.24	
$\text{P}_2\text{O}_5$	0.03	0.01	0.01	0.15	0.11	n.d.	0.01	0.24	n.d.	n.d.	0.01	0.58	n.d.	0.13	n.d.	0.02	0.01	0.05	0.02	n.d.	0.01	0.01	
$\text{Cr}_2\text{O}_3$	0.37	0.37	0.37	0.37	0.36	0.38	0.38	0.36	0.35	0.39	0.33	0.32	0.41	0.31	0.35	0.41	0.38	0.33	0.41	0.45	0.72	0.52	
$\text{NiO}$	0.12	0.22	0.13	0.12	0.10	0.08	0.12	0.12	0.16	0.09	0.10	0.12	0.12	0.09	0.10	0.20	0.30	0.43	0.44	0.48	1.20	1.94	
$\text{LOI}$	0.01	-0.07	0.07	0.21	0.05	0.07	0.39	0.30	0.24	0.11	0.22	0.27	0.03	0.17	0.05	0.17	0.16	0.19	0.17	0.24	0.70	1.01	
<b>Total</b>	100.10	99.45	98.70	100.66	98.97	99.04	100.36	99.08	99.55	98.94	100.02	99.56	99.48	99.30	98.94	99.18	99.40	98.98	100.79	101.20	99.80	99.80	
<b>Element ratios</b>																							
$\text{Mg}\#$	80.64	81.09	81.06	80.77	81.19	81.27	80.57	80.01	81.65	81.23	79.88	80.97	80.90	80.92	79.50	81.67	80.12	79.63	79.76	78.96	76.45	73.62	
An%	62.51	64.64	60.06	66.48	69.31	69.54	71.85	66.84	61.83	62.18	60.32	68.29	69.81	60.78	66.53	77.13	73.06	69.13	75.01	73.60	72.71	69.27	
$\text{Cr}/(\text{Cr}+\text{Fe}^{3+})$	0.15	0.14	0.15	0.14	0.14	0.14	0.14	0.14	0.14	0.17	0.14	0.14	0.15	0.14	0.13	0.17	0.14	0.12	0.16	0.15	0.20	0.14	
$\text{Cr}/(\text{Cr}+\text{Al})$	0.02	0.02	0.02	0.03	0.02	0.03	0.02	0.02	0.02	0.02	0.01	0.01	0.03	0.01	0.02	0.02	0.02	0.02	0.02	0.02	0.05	0.05	

Depth(m)	1087.6	1087.57	1087.59	1087.61	1087.63	1087.65	1087.67	1087.69	1087.71	1087.73	1087.75	1087.77	1087.79	1087.81	1087.83	1087.85	1087.87	1087.89	1087.91	1087.93	1087.95	1087.97	
Sample name	N96	N97	N98	N99	N100	N101	N102	N103	N104	N105	N106	N107	N108	N109	N110	N111	N112	N113	N114	N115	N116	N117	
$\text{SiO}_2$	47.81	51.60	27.73	45.89	45.88	48.14	50.21	47.33	49.09	46.18	49.50	48.46	46.58	47.23	49.42	48.14	49.00	47.27	50.99	49.56	49.60	47.75	
$\text{TiO}_2$	0.21	0.17	0.62	0.10	0.09	0.06	0.09	0.06	0.06	0.06	0.07	0.06	0.07	0.05	0.06	0.05	0.04	0.05	0.04	0.05	0.05	0.05	
$\text{Al}_2\text{O}_3$	4.81	4.09	17.87	31.46	29.16	22.08	21.76	24.72	20.17	26.50	27.48	28.13	23.48	29.00	29.72	30.54	29.64	30.07	29.02	30.06	29.86	31.06	
$\text{Fe}_2\text{O}_3$	3.10	2.73	3.98	0.32	0.51	1.13	1.01	0.67	1.29	0.74	0.49	0.38	1.00	0.47	0.29	0.21	0.18	0.32	0.22	0.27	0.25	0.33	
$\text{FeO}$	11.16	9.81	14.32	1.15	1.85	4.06	3.65	2.42	4.65	2.65	1.75	1.38	3.60	1.71	1.05	0.74	0.66	1.17	0.78	0.96	0.89	1.20	
$\text{MnO}$	0.23	0.25	0.19	0.01	0.04	0.09	0.08	0.05	0.09	0.06	0.04	0.03	0.07	0.04	0.02	0.01	0.01	0.02	0.01	0.02	0.02	0.03	
$\text{MgO}$	24.89	26.13	10.62	0.52	3.76	10.77	8.96	5.97	11.42	5.98	3.58	2.49	8.61	3.10	1.70	0.82	0.64	1.54	1.03	1.04	1.21	1.65	
$\text{CaO}$	3.54	2.82	4.97	16.20	15.29	11.97	10.45	14.91	10.16	14.69	15.36	15.90	13.61	15.12	15.31	16.13	15.90	15.49	15.43	15.22	15.68	14.35	
$\text{Na}_2\text{O}$	0.40	0.27	0.67	2.35	2.02	1.33	1.69	1.84	1.27	1.42	2.05	2.15	1.38	1.86	2.30	2.41	2.53	2.28	2.13	2.36	2.38	2.23	
$\text{K}_2\text{O}$	0.09	0.08	0.11	0.20	0.16	0.12	0.16	0.17	0.14	0.14	0.12	0.12	0.07	0.13	0.11	0.14	0.18	0.17	0.12	0.15	0.12	0.18	
$\text{P}_2\text{O}_5$	0.01	0.02	0.01	0.02	0.03	0.02	0.01	n.d.	n.d.	0.02	n.d.	n.d.	0.02	n.d.	n.d.	n.d.	n.d.	0.03	0.01	n.d.	n.d.	0.02	
$\text{Cr}_2\text{O}_3$	0.49	0.56	18.55	0.35	0.14	0.13	0.18	0.09	0.06	0.06	0.05	0.05	0.07	0.04	0.02	0.01	0.01	0.02	0.01	0.01	0.02	0.02	
$\text{NiO}$	1.42	0.58	0.45	0.10	0.03	0.12	0.07	0.05	0.11	0.06	0.04	0.03	0.08	0.04	0.02	0.02	0.01	0.02	0.01	0.05	0.01	0.02	
$\text{LOI}$	1.01	0.68	-0.74	0.26	0.36	0.50	0.49	0.33	0.49	0.44	0.29	0.35	0.33	0.34	0.37	0.41	0.37	0.30	0.20	-0.07	0.31	0.36	
<b>Total</b>	100.40	100.86	100.95	99.05	99.53	100.96	99.21	98.89	99.53	99.30	101.00	99.68	99.35	99.34	100.50	99.71	99.26	98.88	100.09	99.79	100.50	99.38	
<b>Element ratios</b>																							
$\text{Mg}\#$	76.11	79.17	51.43	39.11	74.43	79.12	77.81	77.89	77.8	76.3	74.42	72.11	77.37	72.16	69.89	61.22	57.77	65.27	65.46	60.53	66.08	66.27	
An%	75.49	80.02	80.38	84.92	83.64	81.87	77.18	78.03	81.10	83.71	78.04	77.57	82.31	80.83	77.33	78.87	75.23	79.24	78.36	77.01	76.72	78.05	
$\text{Cr}/(\text{Cr}+\text{Fe}^{3+})$	0.03	0.04	0.49	0.19	0.06	0.02	0.04	0.03	0.01	0.02	0.02	0.03	0.01	0.02	0.01	0.01	0.01	0.01	0.01	0.01	0.01	0.01	
$\text{Cr}/(\text{Cr}+\text{Al})$	0.06	0.08	0.41	0.01	n.d.	n.d.	0.01	n.d.															

Depth(m)	1088	1088.01	1088.03	1088.05	1088.07	1088.09
Sample name	N118	N119	N120	N121	N122	N123
SiO <sub>2</sub>	49.21	49.64	50.55	49.69	49.00	49.09
TiO <sub>2</sub>	0.04	0.03	0.04	0.04	0.05	0.03
Al <sub>2</sub> O <sub>3</sub>	30.65	30.27	29.47	30.21	27.84	29.74
Fe <sub>2</sub> O <sub>3</sub>	0.19	0.13	0.23	0.25	0.57	0.39
FeO	0.69	0.48	0.83	0.89	2.06	1.41
MnO	0.01	0.01	0.02	0.01	0.03	0.01
MgO	0.62	0.14	1.03	0.74	1.36	0.32
CaO	15.08	15.28	15.31	15.59	15.65	15.64
Na <sub>2</sub> O	2.48	2.38	2.28	2.35	2.15	2.35
K <sub>2</sub> O	0.19	0.18	0.13	0.12	0.10	0.18
P <sub>2</sub> O <sub>5</sub>	n.d.	n.d.	n.d.	0.01	n.d.	n.d.
Cr <sub>2</sub> O <sub>3</sub>	0.01	0.01	0.01	0.01	0.03	0.01
NiO	0.01	n.d.	0.01	0.08	0.45	0.32
LOI	0.40	0.47	0.50	0.49	0.80	0.71
Total	99.67	99.07	100.50	100.57	100.31	100.36
Element ratios						
Mg#	56.42	29.14	63.76	54.12	48.44	24.64
An%	76.36	76.96	77.32	77.22	77.38	76.86
Cr/(Cr+Fe <sup>3+</sup> )	0.01	0.01	0.01	0.01	0.01	n.d.
Cr/(Cr+Al)	n.d.	n.d.	n.d.	n.d.	n.d.	n.d.

N73 – N97: Hangingwall

N98: Chromitite layer

N99 – N121: Footwall

**Table D.4: Whole rock geochemistry of borehole 20/0252 obtained from ICP-MS analysis (major element oxides) and element ratios. Major element oxides in wt%. (Cr/(Cr+Fe<sup>3+</sup>) and (Cr/(Cr+Al) calculated using molar values.**

Thickness(m)	21.60	21.58	21.56	21.54	21.52	21.50	21.48	21.46	21.44	21.42	21.40	21.38	21.36	21.34	21.32	21.30	21.28	21.26	21.24	21.22	21.20	21.18
Sample name	P1	P2	P3	P4	P5	P6	P7	P8	P9	P10	P11	P12	P13	P14	P15	P16	P17	P18	P19	P20	P21	P22
SiO <sub>2</sub>	50.77	51.62	49.75	50.85	49.64	52.29	48.09	48.14	47.52	49.48	45.17	35.08	49.68	50.54	48.01	51.94	51.16	50.38	51.48	50.99	51.10	46.78
TiO <sub>2</sub>	0.16	0.19	0.20	0.21	0.18	0.19	0.17	0.21	0.23	0.32	0.50	1.08	0.16	0.21	0.35	0.19	0.19	0.22	0.20	0.16	0.16	0.07
Al <sub>2</sub> O <sub>3</sub>	4.75	4.79	3.05	2.96	2.60	4.91	3.68	1.37	2.22	3.34	4.60	6.53	12.70	6.99	2.74	10.20	5.89	6.01	2.63	2.90	6.69	14.39
Fe <sub>2</sub> O <sub>3</sub>	2.62	2.56	3.13	2.92	2.89	2.84	2.96	3.43	3.42	3.42	3.55	4.06	1.97	2.60	3.09	2.03	2.28	2.56	2.73	2.75	2.42	2.01
FeO	9.45	9.23	11.25	10.50	10.40	10.21	10.65	12.34	12.32	12.31	12.77	14.60	7.10	9.34	11.11	7.31	8.22	9.22	9.83	9.91	8.70	7.25
MnO	0.24	0.25	0.26	0.25	0.25	0.26	0.26	0.25	0.26	0.28	0.27	0.26	0.19	0.24	0.23	0.14	0.11	0.23	0.23	0.24	0.24	0.16
MgO	24.99	23.87	26.07	25.97	28.52	23.42	28.48	27.02	27.75	22.78	22.82	16.40	17.30	23.10	24.70	15.28	22.79	21.74	26.01	26.60	22.69	16.16
CaO	3.66	3.87	2.94	2.74	3.05	4.13	3.88	4.08	3.43	3.82	3.34	9.01	8.98	5.08	5.84	8.15	5.88	6.33	3.23	2.99	4.48	6.57
Na <sub>2</sub> O	0.37	0.31	0.21	0.18	0.17	0.31	0.21	0.07	0.11	0.13	0.13	0.18	0.76	0.52	0.18	0.92	0.54	0.48	0.15	0.15	0.49	0.92
K <sub>2</sub> O	0.05	0.06	0.07	0.08	0.05	0.06	0.03	0.02	0.02	0.05	0.05	0.08	0.12	0.14	0.29	0.17	0.07	0.17	0.12	0.05	0.12	0.10
P <sub>2</sub> O <sub>5</sub>	n.d.	0.02	0.01	n.d.	0.01	0.01	n.d.	0.01	n.d.	n.d.	0.02	0.04	0.02	0.01	n.d.	0.02	0.01	0.01	0.02	0.02	0.02	0.02
Cr <sub>2</sub> O <sub>3</sub>	0.39	0.43	0.40	0.40	0.41	0.40	0.45	0.51	0.54	2.09	5.37	11.55	0.46	0.45	0.54	0.24	0.26	0.42	0.56	0.45	0.47	0.13
NiO	0.10	0.42	0.56	0.36	0.40	0.55	0.45	1.40	1.16	0.99	0.69	0.96	0.21	0.31	1.48	0.63	0.19	0.68	0.31	0.38	0.20	0.17
LOI	0.15	0.38	0.44	0.22	0.27	0.50	0.34	0.87	0.56	0.65	0.52	0.03	0.89	0.79	1.12	1.27	0.49	0.73	0.63	0.29	0.83	5.41
Total	98.75	99.03	99.58	98.82	99.99	101.21	100.84	101.08	100.95	101.04	101.20	101.45	101.33	101.39	100.93	99.27	99.00	100.21	99.22	98.98	99.58	100.94
Element ratios																						
Mg#	79.07	78.69	76.79	77.94	79.65	76.61	79.24	75.76	76.28	72.54	71.83	61.6	77.66	77.92	76.04	74.91	79.83	77.09	79.07	79.31	78.83	76.09
An%	77.05	80.52	79.19	81.31	80.20	80.95	82.69	84.26	84.79	87.78	91.01	91.21	81.91	77.76	78.24	73.74	73.49	76.13	82.03	84.04	78.11	79.74
Cr/(Cr+Fe <sup>3+</sup> )	0.13	0.15	0.12	0.13	0.13	0.13	0.14	0.14	0.14	0.39	0.61	0.75	0.20	0.15	0.15	0.11	0.11	0.15	0.18	0.15	0.17	0.06
Cr/(Cr+Al)	0.05	0.06	0.08	0.08	0.10	0.05	0.08	0.20	0.14	0.30	0.44	0.54	0.02	0.04	0.12	0.02	0.03	0.04	0.13	0.09	0.05	0.01

Thickness(m)	21.16	21.14	21.12	21.10	21.08	21.06	21.04	21.02	21.00	20.98	20.96	20.94	20.92	20.90	20.88	20.86	20.84	20.82	20.80	20.78	20.76	20.74
Sample name	P23	P24	P25	P26	P27	P28	P29	P30	P31	P32	P33	P34	P35	P36	P37	P38	P39	P40	P41	P42	P43	P44
<b>SiO<sub>2</sub></b>	49.17	50.02	49.54	48.44	51.32	49.03	48.64	49.41	48.72	50.04	46.96	50.58	48.13	47.92	42.47	50.79	50.77	48.81	50.01	49.86	50.15	46.21
<b>TiO<sub>2</sub></b>	0.19	0.15	0.21	0.17	0.20	0.23	0.24	0.20	0.16	0.12	0.14	0.13	0.18	0.12	0.06	0.18	0.19	0.13	0.16	0.15	0.11	0.06
<b>Al<sub>2</sub>O<sub>3</sub></b>	8.90	13.42	7.90	5.65	2.92	5.00	14.10	6.83	8.20	10.03	5.94	2.88	5.69	7.07	8.75	3.40	2.44	1.46	2.66	1.91	4.35	7.53
<b>Fe<sub>2</sub>O<sub>3</sub></b>	2.25	2.10	2.35	2.63	2.67	2.67	1.68	2.58	2.47	2.30	2.93	2.37	2.65	2.59	3.01	2.64	2.88	3.00	2.79	2.91	2.93	2.75
<b>FeO</b>	8.10	7.57	8.45	9.48	9.62	9.62	6.04	9.28	8.88	8.26	10.56	8.52	9.53	9.31	10.83	9.50	10.37	10.80	10.05	10.47	10.56	9.90
<b>MnO</b>	0.20	0.17	0.23	0.23	0.21	0.24	0.17	0.23	0.17	0.12	0.23	0.19	0.19	0.16	0.22	0.24	0.19	0.22	0.20	0.16	0.18	
<b>MgO</b>	18.67	15.37	20.73	23.35	24.49	25.17	13.97	21.96	20.44	16.79	22.36	28.40	24.36	21.62	23.92	26.20	27.02	29.56	26.55	26.96	26.99	20.92
<b>CaO</b>	4.90	7.81	5.54	3.11	3.58	4.30	10.88	4.34	5.68	6.07	3.48	1.85	3.73	3.23	3.21	3.84	2.92	1.98	2.94	3.11	2.78	2.09
<b>Na<sub>2</sub>O</b>	0.51	1.13	0.46	0.25	0.12	0.31	1.12	0.39	0.62	0.84	0.12	0.08	0.38	0.11	0.19	0.14	0.11	0.04	0.10	0.09	0.08	0.11
<b>K<sub>2</sub>O</b>	0.19	0.14	0.22	0.18	0.16	0.15	0.25	0.19	0.16	0.10	0.07	0.04	0.23	0.19	0.03	0.09	0.12	0.02	0.02	0.07	0.03	0.06
<b>P<sub>2</sub>O<sub>5</sub></b>	0.02	0.01	0.03	0.10	n.d.	0.02	0.03	n.d.	n.d.	0.01	0.04	0.01	0.01	n.d.	0.02	0.01	0.01	0.01	0.02	0.01	0.01	0.02
<b>Cr<sub>2</sub>O<sub>3</sub></b>	0.24	0.20	0.31	0.34	0.40	0.33	0.23	0.25	0.23	0.19	0.19	0.35	0.32	0.38	0.42	0.47	0.53	0.28	0.31	0.29	0.12	0.02
<b>NiO</b>	0.22	0.71	0.52	0.18	0.31	0.38	0.14	0.19	1.76	1.32	0.25	0.12	1.26	0.43	0.26	0.15	0.15	0.11	0.18	0.13	0.18	0.30
<b>LOI</b>	4.55	1.56	1.63	4.63	1.70	1.69	2.01	2.72	2.38	2.14	4.52	3.74	2.82	5.86	6.47	2.61	1.39	1.54	2.06	2.02	n.d.	7.71
<b>Total</b>	99.01	101.20	99.06	99.79	98.75	100.20	100.18	99.61	100.87	99.26	98.97	100.20	100.54	100.05	101.02	101.30	100.30	99.14	99.17	99.35	99.28	98.95
<b>Element ratios</b>																						
<b>Mg#</b>	76.7	74.37	77.79	77.86	78.42	78.89	76.77	77.16	76.67	74.36	75.14	82.63	78.49	76.83	75.92	79.74	78.81	79.63	79.05	78.62	78.49	75.11
<b>An%</b>	82.40	75.42	82.02	85.98	86.59	80.93	76.48	82.34	77.45	75.55	93.49	91.13	79.39	94.21	90.28	86.96	85.47	91.25	88.26	85.06	94.08	91.22
<b>Cr/(Cr+Fe<sup>3+</sup>)</b>	0.10	0.09	0.12	0.12	0.14	0.12	0.13	0.09	0.08	0.06	0.13	0.11	0.13	0.13	0.16	0.16	0.09	0.10	0.10	0.04	0.01	n.d.
<b>Cr/(Cr+Al)</b>	0.02	0.01	0.03	0.04	0.08	0.04	0.01	0.02	0.02	0.01	0.02	0.07	0.04	0.03	0.03	0.09	0.13	0.12	0.07	0.09	0.02	n.d.
Thickness(m)	20.72	20.70	20.68	20.67	20.65	20.63	20.61	20.59														
Sample name	P45	P46	P47	P48	P49	P50	P51	P52														
<b>SiO<sub>2</sub></b>	40.76	44.85	48.99	41.89	45.28	46.93	49.59	50.01														
<b>TiO<sub>2</sub></b>	0.07	0.11	0.17	0.16	0.04	0.05	0.03	0.03														
<b>Al<sub>2</sub>O<sub>3</sub></b>	13.57	5.58	4.81	13.07	26.24	28.70	28.69	29.13														
<b>Fe<sub>2</sub>O<sub>3</sub></b>	2.62	2.78	2.68	2.41	0.50	0.22	0.11	0.13														
<b>FeO</b>	9.44	10.00	9.63	8.67	1.81	0.80	0.41	0.46														
<b>MnO</b>	0.18	0.23	0.23	0.18	0.04	0.02	0.01	0.01														
<b>MgO</b>	19.24	27.09	25.15	18.55	4.19	1.23	0.32	0.38														
<b>CaO</b>	5.77	3.06	3.73	7.85	17.90	18.16	15.90	16.28														
<b>Na<sub>2</sub>O</b>	0.60	0.19	0.27	0.72	1.91	2.16	2.16	2.42														
<b>K<sub>2</sub>O</b>	0.05	0.02	0.04	0.03	0.02	0.03	0.01	0.01														
<b>P<sub>2</sub>O<sub>5</sub></b>	0.03	0.02	0.02	0.03	0.02	0.03	0.01	0.01														
<b>Cr<sub>2</sub>O<sub>3</sub></b>	0.16	0.40	1.78	4.94	0.05	0.02	n.d.	0.02														
<b>NiO</b>	0.08	0.17	0.13	0.08	0.01	n.d.	n.d.	0.08														
<b>LOI</b>	5.45	4.58	0.91	1.38	0.79	0.78	1.16	1.16														
<b>Total</b>	99.05	100.20	99.60	100.92	99.07	99.48	99.01	100.75														
<b>Element ratios</b>																						
<b>Mg#</b>	74.42	79.46	78.84	75.33	76.77	68.78	52.62	54.22														
<b>An%</b>	84.09	89.35	82.95	83.34	93.30	84.91	77.52	75.49														
<b>Cr/(Cr+Fe<sup>3+</sup>)</b>	0.06	0.13	0.41	0.68	0.09	0.08	n.d.	0.13														
<b>Cr/(Cr+Al)</b>	0.01	0.05	0.20	0.20	n.d.	n.d.	n.d.	n.d.														

P1-P11: Hangingwall

P12: Top chromitite layer

P13-P46: Pegmatoidal layer

P47-P48: Bottom chromitite layer

P49-P52: Footwall

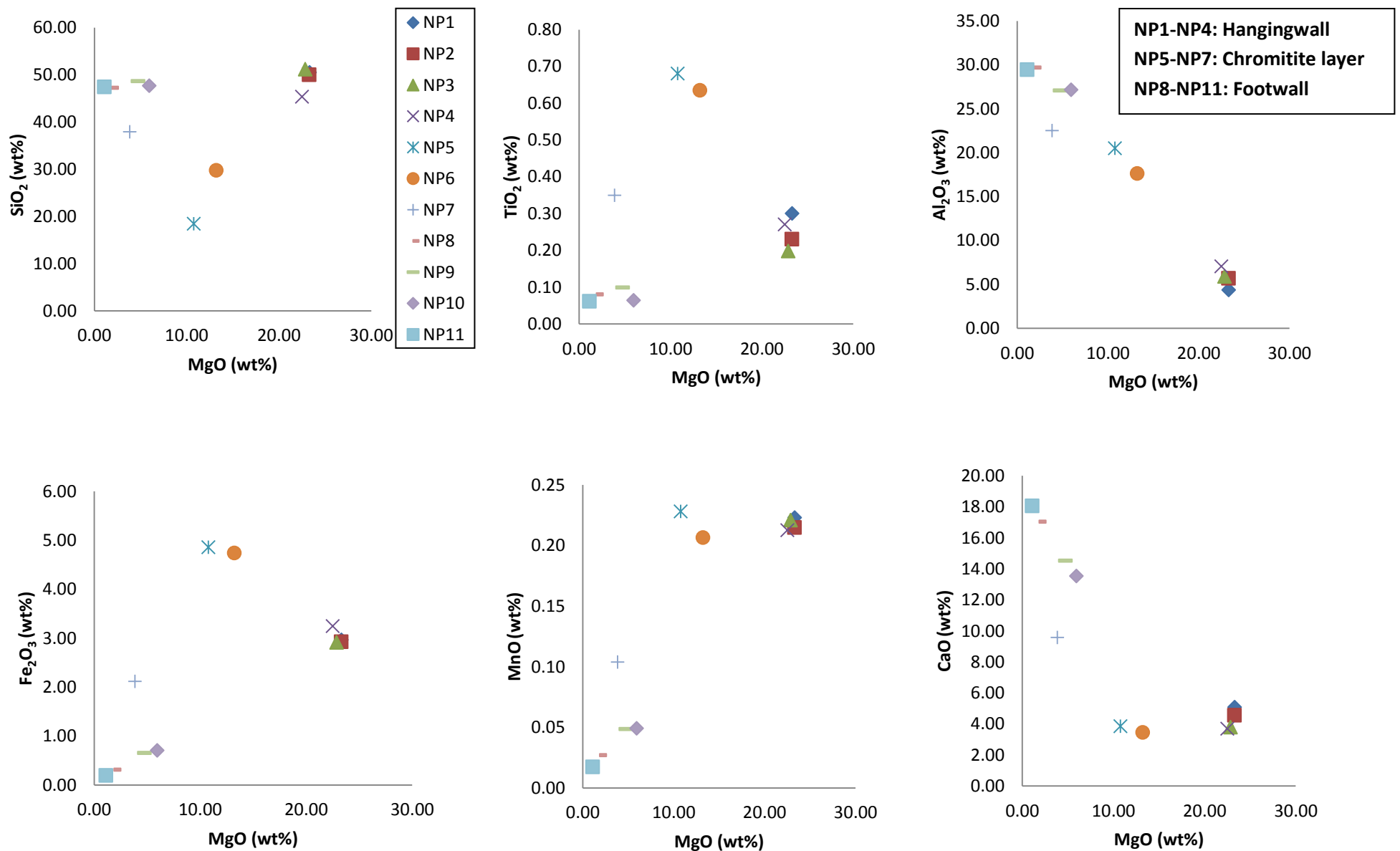


Figure D.1: Modified MgO-Harker plots of the major element oxides, related to the different lithologies with depth (see Appendix A), of borehole SD14/90.

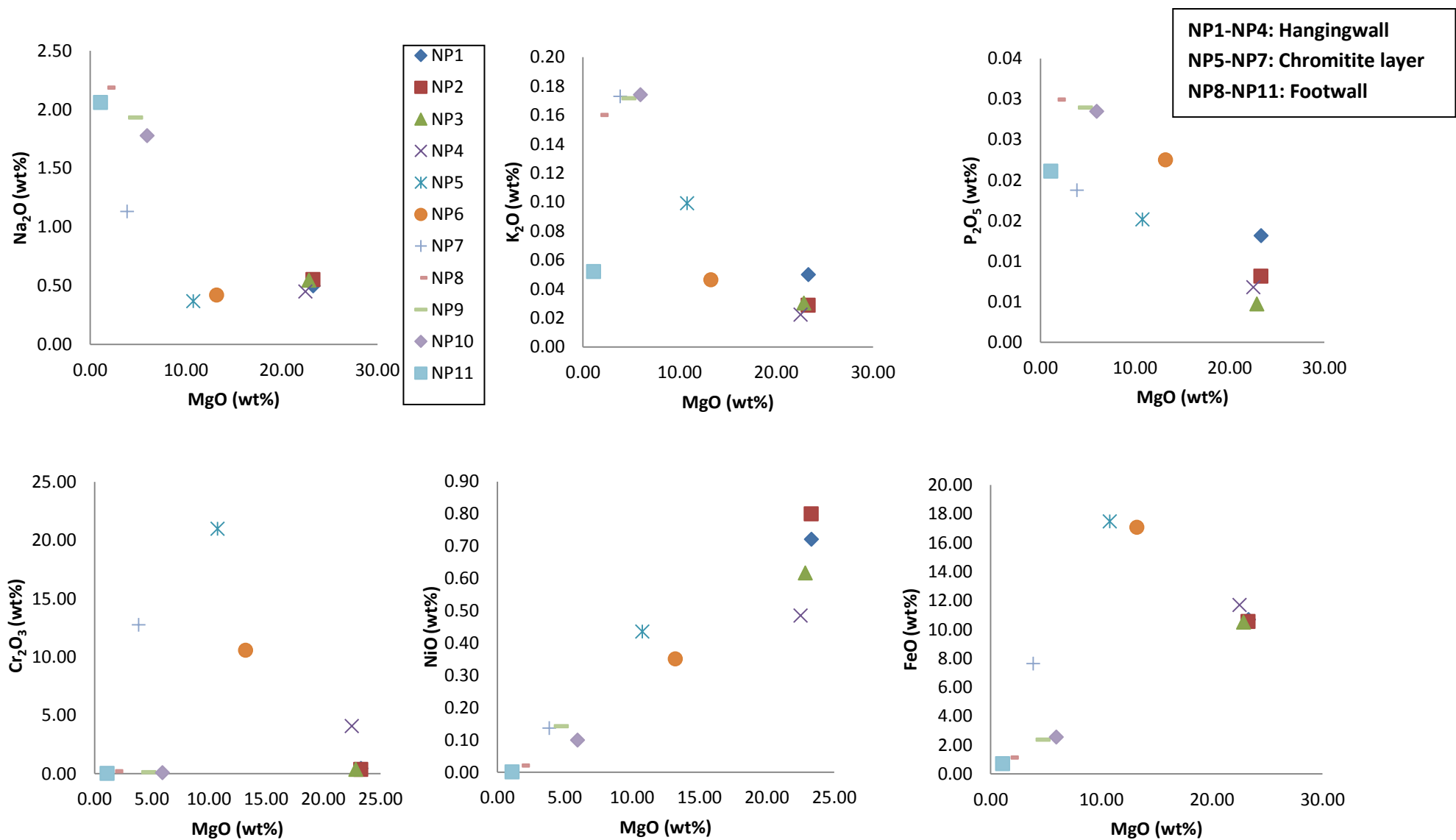


Figure D.1: Modified MgO-Harker plots of the major element oxides, related to the different lithologies with depth (see Appendix A), of borehole SD14/90.

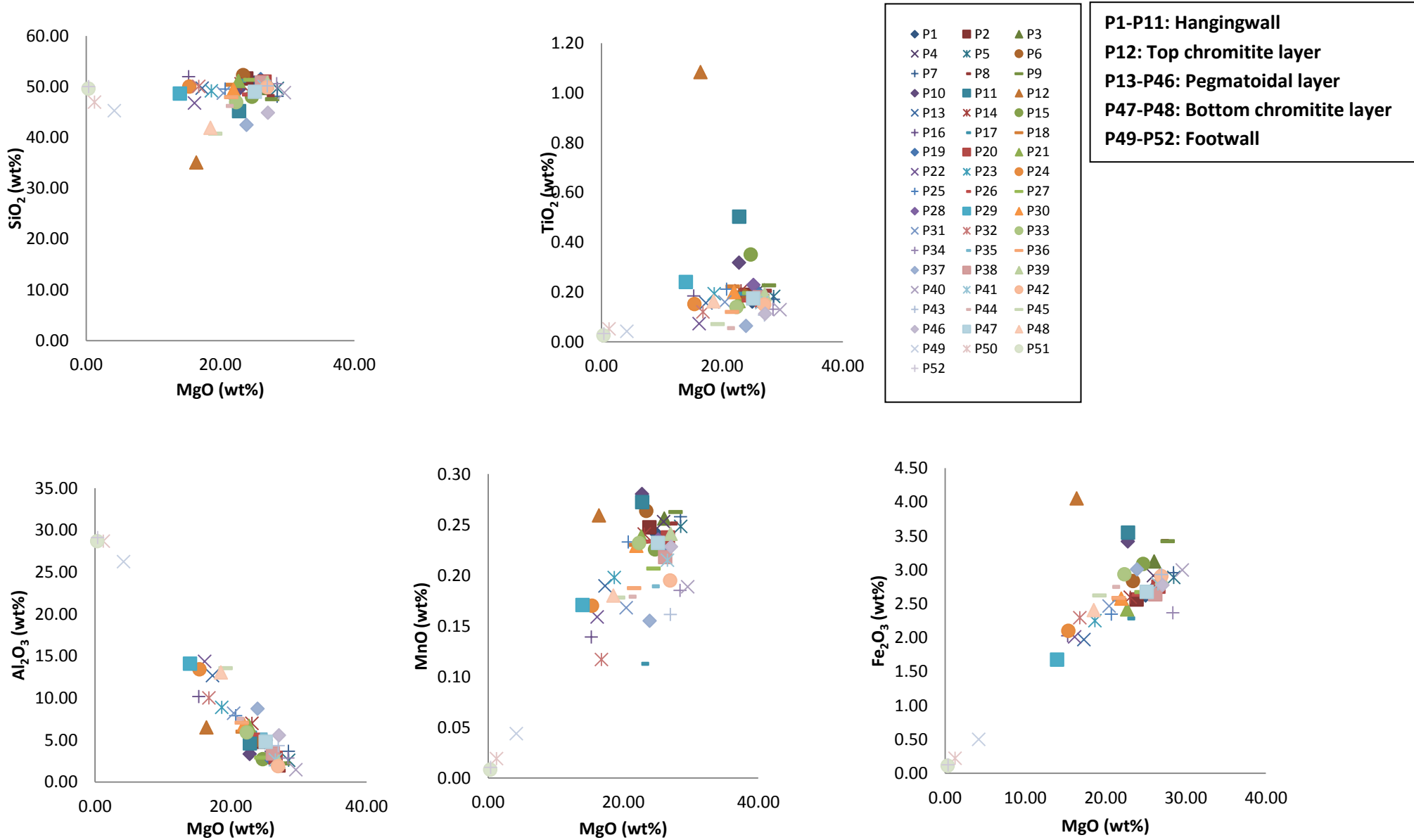


Figure D.2: Modified MgO-Harker plots of the major element oxides, related to the different lithologies with depth (see Appendix A), of borehole 20/0252.

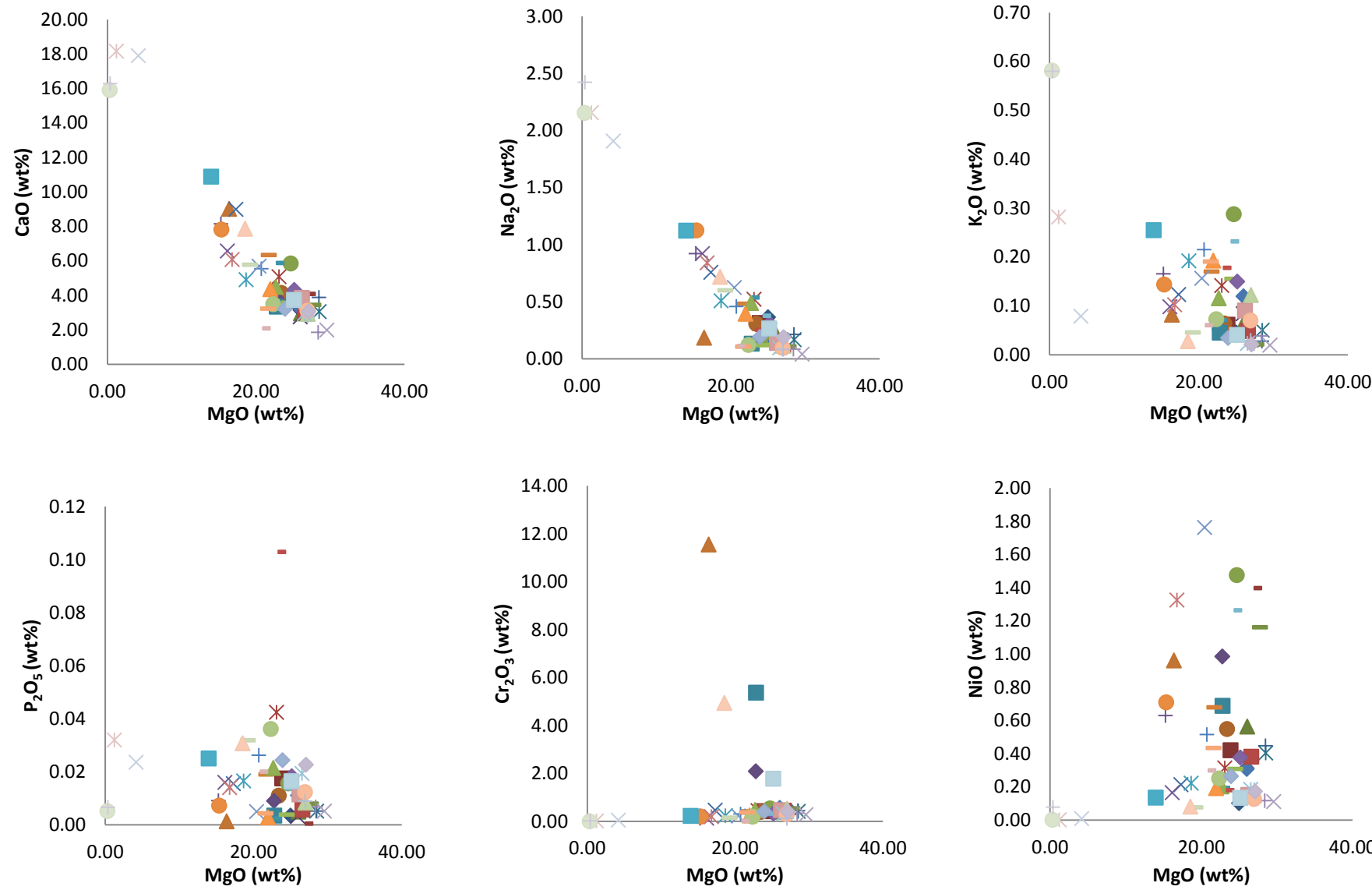


Figure D.2: Modified MgO-Harker plots of the major element oxides, related to the different lithologies with depth see Appendix A), of borehole 20/0252.

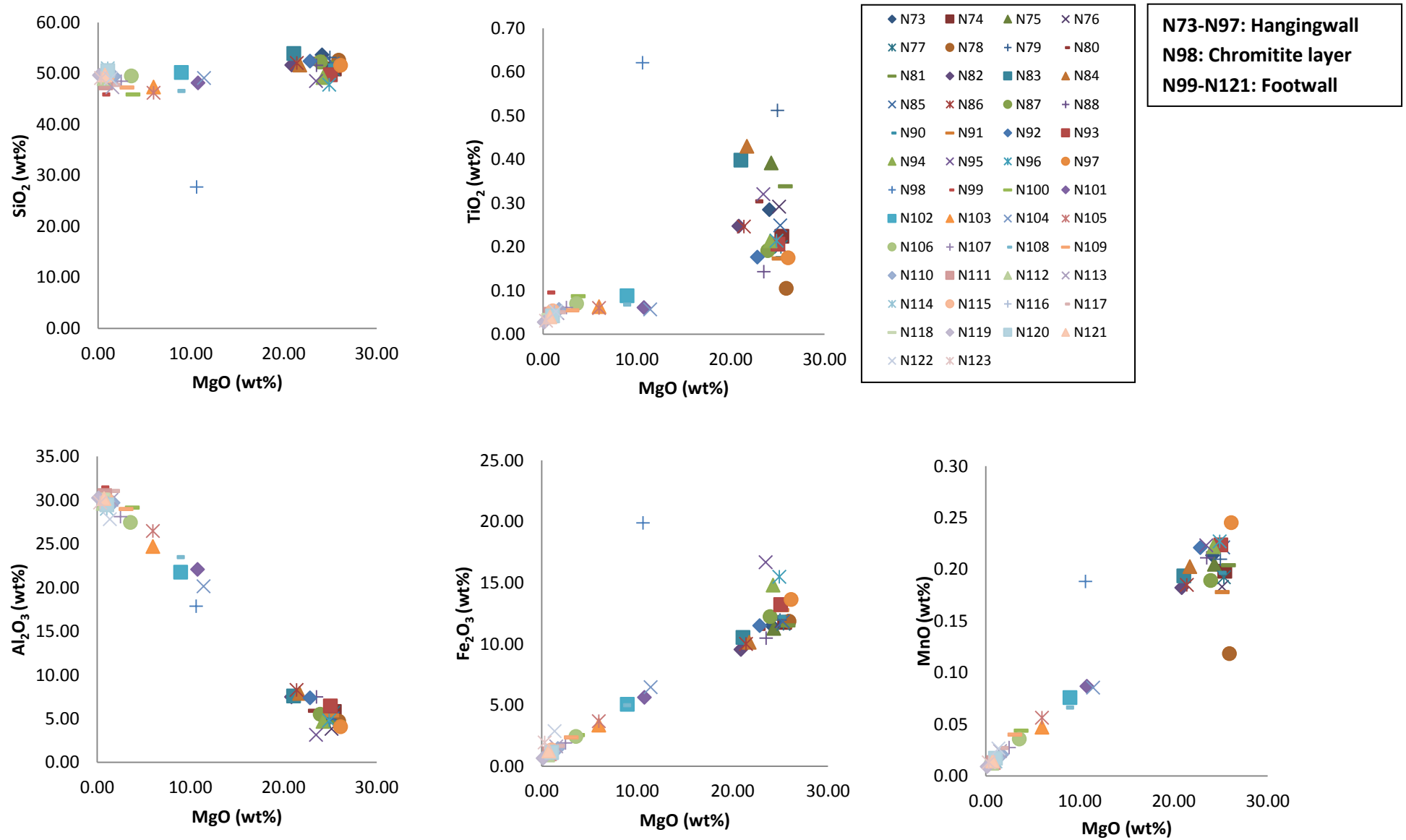


Figure D.3: Modified MgO-Harker plots of the major element oxides, related to the different lithologies with depth (see Appendix A), of borehole BH6259.

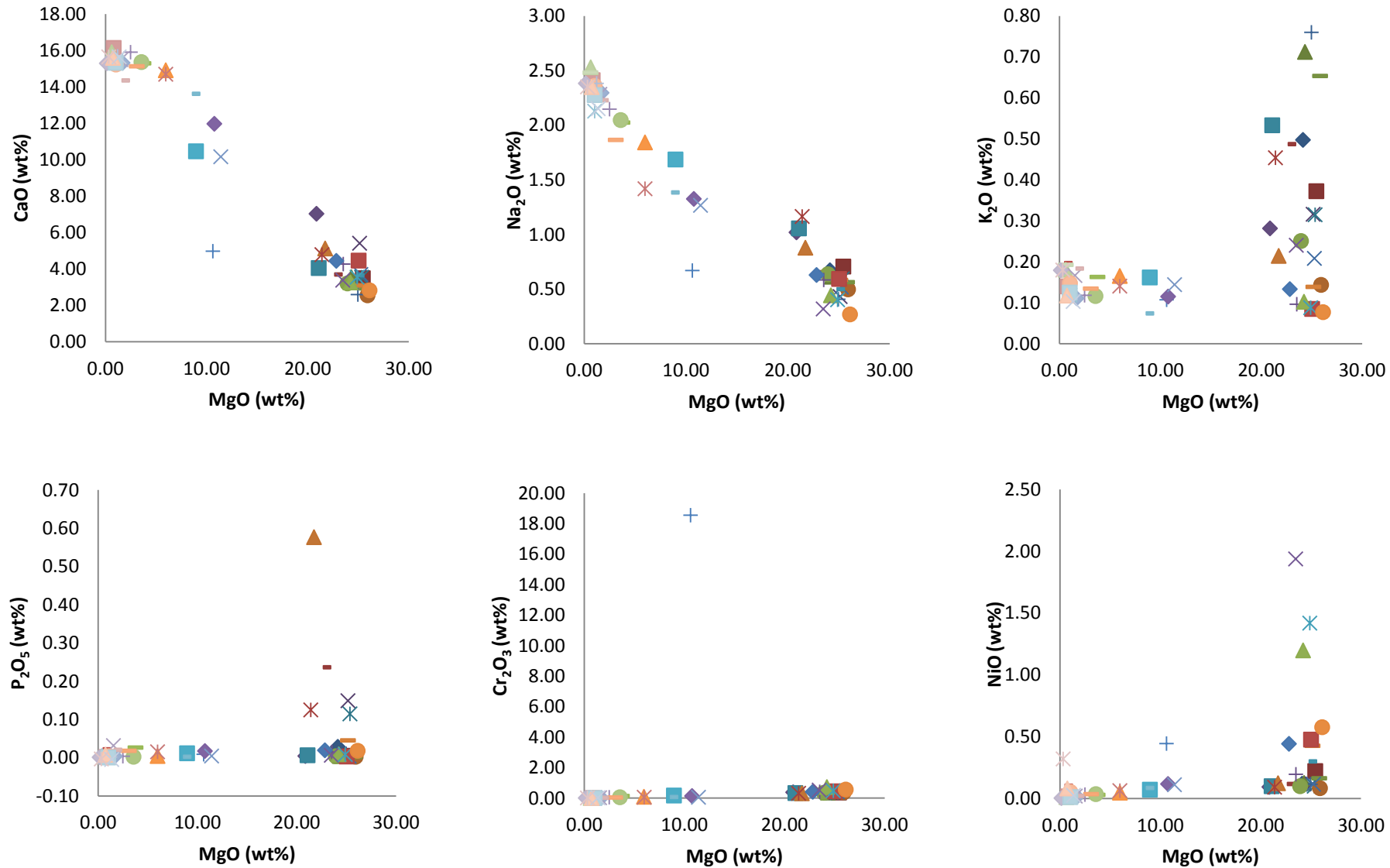


Figure D.3: Modified MgO-Harker plots of the major element oxides, related to the different lithologies with depth (see Appendix A), of borehole BH6259.

Norm calculations was done using the “CIPW norm calculations-Whitman College”

<https://www.whitman.edu/geology/winter/Petrology/CIPW%20Norm%20Hollacher.xls>

**Table D.5: Normative mineralogy of the major element oxides in borehole SD14/90.**

	NP1	NP2	NP3	NP4	NP5	NP6	NP7	NP8	NP9	NP10	NP11
Normative Minerals	Weight % Norm										
Quartz	0	0	0	0	0	0	4.03	0	0	0	0
Plagioclase	13.74	17.65	18.17	20.99	19.1	20.62	57.04	83.09	81.08	80.68	85.22
Orthoclase	0.3	0.18	0.18	0.12	0	0.3	1	0.95	1	1	0.3
Nepheline	0	0	0	0	1.7	0	0	3.34	0	0	1.72
Kalsilite	0	0	0	0	0.34	0	0	0	0	0	0
Corundum	0	0	0	0	12.78	10.62	3.06	0	0	0	0
Diopside	12.55	7.68	4.27	0.94	0	0	0	11.05	5.82	1.23	7.72
Hypersthene	60.19	60.74	69.81	52.57	0	21.39	10.55	0	7.36	8.79	0
Wollastonite	0	0	0	0	0	0	0	0	0	0	3.79
Olivine	6.19	5.95	0.29	12.08	26.61	21.42	0	0.64	3.96	6.86	0
Ilmenite	0.57	0.44	0.38	0.51	1.29	1.22	0.66	0.15	0.19	0.11	0.11
Magnetite	4.31	4.25	4.22	4.71	7.05	6.87	3.07	0.45	0.94	1.03	0.28
Apatite	0.02	0.02	0.02	0.02	0.05	0.05	0.05	0.07	0.07	0.07	0.05
Chromite	0.66	0.53	0.57	6.13	27.72	15.14	18.13	0.32	0.18	0.13	0.04
Pyrite	1.19	3.27	2.4	2.08	1.74	0.51	0.47	0.04	0.06	0.02	0.02
Total	99.72	100.71	100.31	100.15	98.38	98.14	98.06	100.1	100.66	99.92	99.25

NP1-NP4: Hangingwall

NP5-NP7: Chromitite layer

NP8-NP11: Footwall

P1-P11: Hangingwall

P12: Top chromitite layer

P13-P46: Pegmatoidal layer

P47-P48: Bottom chromitite layer

P49-P52: Footwall

**Table D.6: Normative mineralogy of the major element oxides in borehole 20/0252.**

	P1	P2	P3	P4	P5	P6	P7	P8	P9	P10	P11	P12	P13	P14	P15	P16	P17	P18	P19	P20	P21	P22
Normative Minerals	Weight % Norm																					
Quartz	0.00	0.92	0.00	0.00	0.00	1.08	0.00	0.00	0.00	1.05	0.00	0.00	0.00	0.00	4.39	0.00	0.00	0.00	0.00	0.00	0.00	0
Plagioclase	14.28	14.12	8.95	8.56	7.62	14.45	10.79	3.96	6.44	9.48	12.92	18.30	37.32	20.73	7.33	30.98	18.01	17.80	7.42	8.36	19.85	40.3
Orthoclase	0.30	0.35	0.41	0.47	0.30	0.35	0.18	0.12	0.12	0.30	0.30	0.47	0.71	0.83	1.71	1.00	0.41	1.00	0.71	0.30	0.71	0.59
Corundum	0.00	0.00	0.00	0.00	0.00	0.00	0.00	0.00	0.00	0.00	0.00	0.00	0.00	0.00	0.00	0.00	0.00	0.00	0.00	0.00	0.00	0.85
Diopside	5.60	6.04	5.86	5.23	7.06	6.88	8.11	13.46	9.12	8.39	3.79	22.34	10.83	6.88	18.39	13.76	12.52	14.00	7.81	6.11	5.11	0
Hypersthene	67.53	70.79	68.53	74.76	63.05	71.08	50.95	58.17	56.09	69.50	60.54	8.30	40.84	58.44	47.51	42.53	59.35	55.87	75.01	73.48	66.15	43.32
Olivine	5.12	0.00	7.55	2.55	14.63	0.00	23.36	14.71	19.01	0.00	6.56	24.72	5.91	7.22	16.37	0.00	2.89	4.11	1.06	3.94	1.27	6.29
Ilmenite	0.30	0.36	0.38	0.40	0.34	0.36	0.32	0.40	0.44	0.61	0.95	2.05	0.30	0.40	0.66	0.36	0.36	0.42	0.38	0.30	0.30	0.13
Magnetite	3.80	3.71	4.54	4.23	4.19	4.12	4.29	4.97	4.96	4.96	5.15	5.89	2.86	3.77	4.48	2.94	3.31	3.71	3.96	3.99	3.51	2.91
Apatite	0.00	0.05	0.02	0.00	0.02	0.02	0.02	0.00	0.02	0.02	0.00	0.00	0.05	0.09	0.05	0.02	0.00	0.05	0.02	0.02	0.05	0.05
Chromite	0.57	0.69	0.59	0.59	0.60	0.71	0.66	0.75	0.80	3.55	7.79	16.79	0.68	0.65	0.80	0.35	0.38	0.63	0.82	0.66	0.69	0.19
Sphene	0.00	0.00	0.00	0.00	0.00	0.00	0.00	0.00	0.00	0.00	0.00	0.00	0.00	0.00	0.00	0.00	0.00	0.00	0.00	0.00	0.00	0
Pyrite	0.11	1.15	1.97	1.17	1.42	1.10	1.17	4.22	3.67	2.63	2.16	1.23	0.30	1.00	2.23	1.59	0.66	1.59	0.53	0.74	0.25	0.17
Total	97.61	98.18	98.80	97.96	99.23	100.15	99.85	100.76	100.67	100.49	100.16	100.09	99.8	100.01	99.53	97.92	97.89	99.18	97.72	97.9	97.89	94.8

**Table D.6: Normative mineralogy of the major element oxides in borehole 20/0252.**

	P23	P24	P25	P26	P27	P28	P29	P30	P31	P32	P33	P34	P35	P36	P37	P38	P39	P40	P41	P42	P43	P44
Normative	Weight %																					
Minerals	Norm																					
Quartz	1.86	0	0	0	1.18	0	0	0	0	2.95	0	0	0	1.01	0	0	0	0	0	0	0	2.53
Plagioclase	25.75	40.69	22.73	15.88	7.97	14.43	42.18	19.62	24.36	30.41	16.48	8.06	16.36	17.01	17.46	9.57	6.74	4.08	7.6	5.36	12.1	11.2
Orthoclase	1.12	0.83	1.3	1.06	0.95	0.89	1.48	1.12	0.95	0.59	0.41	0.24	1.36	1.12	0.18	0.53	0.71	0.12	0.12	0.41	0.18	0.35
Corundum	0	0	0	0	0	0	0	0	0	0	0	0	0	0.79	2.6	0	0	0	0	0	0	3.52
Diopsidite	2.21	6.08	6.75	0.81	8.61	7.5	16.86	4.17	7.23	5.43	1.25	1.37	4.24	0	0	8.43	6.86	4.78	6.13	8.57	1.86	0
Hypersthene	58.45	45.57	58.46	67.32	72.24	56.93	26.86	63.22	53.44	50.79	64.48	76.36	56.77	67.83	44.92	68.63	71.85	66.58	71.98	69.11	70.13	67.7
Olivine	0	1.11	2.41	4.09	0	12.58	6.72	2.97	4.58	0	5.67	5.13	11.61	0	22.6	5.5	6.15	15.55	5.04	7.63	9.11	0
Ilmenite	0.36	0.28	0.4	0.32	0.38	0.44	0.46	0.38	0.3	0.23	0.27	0.25	0.34	0.23	0.11	0.34	0.36	0.25	0.3	0.28	0.21	0.11
Magnetite	3.26	3.04	3.41	3.81	3.87	3.87	2.44	3.74	3.58	3.33	4.25	3.44	3.84	3.76	4.36	3.83	4.18	4.35	4.05	4.22	4.25	3.99
Hematite	0	0	0	0	0	0	0	0	0	0	0	0	0	0	0	0	0	0	0	0	0	0
Apatite	0.05	0.02	0.07	0.23	0	0.05	0.07	0	0	0.02	0.09	0.02	0.02	0	0.05	0.02	0.02	0.02	0.05	0.02	0.02	0.05
Chromite	0.35	0.29	0.44	0.5	0.59	0.49	0.35	0.37	0.34	0.28	0.31	0.52	0.47	0.56	0.63	0.69	0.78	0.41	0.43	0.43	0.18	0.03
Pyrite	0.25	1.59	0.89	0.15	0.38	0.51	0.19	0.49	4.94	3.99	0.13	0.25	3.01	1.59	0.89	0.17	0.19	0.4	0.57	0.21	0.78	1.08
Total	93.66	99.5	96.86	94.17	96.17	97.69	97.61	96.08	99.72	98.02	93.34	95.64	98.02	93.9	93.8	97.71	97.84	96.54	96.27	96.24	98.82	90.56

**Table D.6: Normative mineralogy of the major element oxides in borehole 20/0252.**

	P45	P46	P47	P48	P49	P50	P51	P52
Normative	Weight %							
Minerals	Norm							
Quartz	0	0	0	0	0	0	2.56	0.87
Plagioclase	33.56	15.92	14.08	38.43	67.04	79.15	85.15	87.38
Orthoclase	0.3	0.12	0.24	0.18	0.47	1.65	3.43	3.43
Nepheline	0	0	0	0	6.45	3.75	0	0
Diopsidite	0	0.61	5.25	5.15	20.74	8.87	2.87	3.56
Hypersthene	25.32	46.8	63.05	18.95	0	0	0	0
Wollastonite	0	0	0	0	0	4.68	3.58	4.02
Olivine	26.53	26.14	8.14	24.78	2.46	0	0	0
Ilmenite	0.13	0.21	0.32	0.3	0.08	0.09	0.06	0.06
Magnetite	3.8	4.03	3.89	3.49	0.72	0.32	0.16	0.19
Apatite	0.07	0.05	0.05	0.07	0.05	0.07	0.02	0.02
Chromite	0.24	0.59	2.62	7.19	0.07	0.03	0	0.03
Pyrite	1.02	0.08	NA	0	0	0.02	0.02	0.02
Total	93.06	94.55	97.64	98.54	98.08	98.63	97.85	99.58

**Table D.7: Normative mineralogy of the major element oxides in borehole BH6259.**

	N73	N74	N75	N76	N77	N78	N79	N80	N81	N82	N83	N84	N85	N86	N87	N88	N89	N90	N91	N92	N93	N94	N95
Normative Minerals	Weight %																						
	Norm																						
Quartz	0.33	0.00	0.00	0.00	0.00	0.00	0.00	1.51	0.00	0.00	1.51	0.00	0.00	0.00	0.00	0.00	0.00	0.00	0.00	0.16	0.00	0.00	0.00
Plagioclase	15.70	17.66	13.40	11.30	16.95	14.48	12.86	17.26	12.88	23.69	23.44	24.46	15.20	25.95	16.84	22.47	16.40	16.57	22.31	19.76	14.25	9.18	
Orthoclase	2.95	2.19	4.20	1.89	1.83	0.83	4.49	2.90	3.84	1.65	3.13	1.24	1.24	2.66	1.48	0.59	0.41	0.83	0.77	0.47	0.59	1.42	
Diopside	4.90	4.42	7.37	14.48	3.90	1.89	2.71	3.98	5.09	15.75	4.40	3.63	5.94	5.32	3.56	2.70	4.64	2.64	3.93	5.79	4.43	8.12	
Hypersthene	70.70	57.39	64.37	61.35	61.12	75.17	73.52	67.19	64.96	47.85	62.12	63.28	66.63	55.48	70.64	66.63	68.62	64.91	67.44	53.63	64.36	64.88	
Olivine	0.00	12.40	3.74	5.50	9.57	1.42	0.35	0.00	6.89	5.25	0.00	0.21	4.88	4.74	0.90	0.87	3.06	7.40	0.00	14.57	6.76	4.44	
Ilmenite	0.53	0.42	0.74	0.55	0.38	0.19	0.97	0.57	0.65	0.47	0.76	0.82	0.47	0.47	0.36	0.27	0.32	0.32	0.34	0.40	0.40	0.61	
Magnetite	3.33	3.41	3.26	3.45	3.38	3.44	3.47	3.26	3.33	2.77	3.06	2.94	3.44	2.90	3.55	3.04	3.54	3.70	3.33	3.84	4.29	4.84	
Apatite	0.07	0.02	0.02	0.35	0.25	0.00	0.02	0.56	0.00	0.00	0.02	1.34	0.00	0.30	0.00	0.05	0.02	0.12	0.05	0.00	0.02	0.02	
Chromite	0.54	0.54	0.54	0.65	0.53	0.56	0.56	0.60	0.52	0.57	0.49	0.53	0.60	0.46	0.52	0.74	0.56	0.49	0.72	0.66	1.06	0.77	
Pyrite	0.19	0.21	0.15	0.13	0.11	0.08	0.13	0.17	0.42	0.08	0.08	0.13	0.17	0.06	0.11	1.72	1.21	1.48	1.31	1.40	3.16	5.79	
Total	99.24	98.66	97.79	99.65	98.02	98.06	99.08	98	98.58	98.08	99.01	98.58	98.57	98.34	97.96	99.08	98.78	98.46	100.36	100.52	99.32	100.07	

**Table D.7: Normative mineralogy of the major element oxides in borehole BH6259.**

	N96	N97	N98	N99	N100	N101	N102	N103	N104	N105	N106	N107	N108	N109	N110	N111	N112	N113	N114	N115	N116	N117	
Normative Minerals	Weight %																						
	Norm																						
Quartz	0	0	0	0	0	0	1.49	0	0	0	0	0	0	0	0.71	0	0.22	0	4.56	1.44	0.85	0.02	
Plagioclase	14.45	12	30.31	87.2	82.94	65.18	65.62	74.26	59.67	77.54	82.77	84.94	69.34	86.13	89.91	90.3	90.39	88.92	87.29	90.95	90.58	90.06	
Orthoclase	0.53	0.47	0.65	1.18	0.95	0.71	0.95	1	0.83	0.83	0.71	0.71	0.41	0.77	0.65	0.83	1.06	1	0.71	0.89	0.71	1.06	
Nepheline	0	0	0	4	2.27	0	0	0	0	0	0	0	0	0	0	0	1.19	0	0.91	0	0	0	
Corundum	0	0	7.62	0	0	0	0	0	0	0	0	0	0	0	0	0	0	0	0	0	0	1.1	
Diopside	5.16	3.29	0	4.74	4.59	4.33	0.45	12.26	1.27	5.86	8.73	9.83	7.95	3.7	4.54	6.41	5.29	4.42	5.94	3.77	6.04	0	
Hypersthene	55.34	75.44	11.39	0	0	18.8	27.88	1.11	32.62	4.5	7.19	1.26	8.48	3.9	3.66	0	0	0	0.89	2.09	1.42	5.99	
Wollastonite	0	0	0	0	0	0	0	0	0	0	0	0	0	0	0.06	1.49	0	0	0	0	0		
Olivine	15.69	1.07	15.85	0.32	6.76	8.98	0	8.43	2.05	8.52	0.2	1.68	10.74	3.37	0	0	0	2.53	0	0	0		
Ilmenite	0.4	0.32	1.18	0.19	0.17	0.11	0.17	0.11	0.11	0.13	0.11	0.13	0.13	0.09	0.11	0.09	0.08	0.09	0.08	0.09	0.09	0.09	
Magnetite	4.49	3.96	5.77	0.46	0.74	1.64	1.46	0.97	1.87	1.07	0.71	0.55	1.45	0.68	0.42	0.3	0.26	0.46	0.32	0.39	0.36	0.48	
Apatite	0.02	0.05	0.02	0.05	0.07	0.05	0.02	0	0	0.05	0	0	0	0.05	0	0	0	0.07	0.02	0	0	0.05	
Chromite	0.84	0.9	25.65	0.57	0.25	0.21	0.27	0.13	0.09	0.1	0.07	0.07	0.1	0.07	0.03	0.01	0.01	0.03	0.01	0.01	0.03	0.03	
Sphene	0	0	0	0	0	0	0	0	0	0	0	0	0	0	0	0	0	0	0	0	0	0	
Pyrite	2.08	3.07	0.95	0.04	0.55	0.06	0.06	0.04	0.04	0.02	0.06	0.08	0.06	0.11	0.04	0.08	0.04	0.06	0.02	0.25	0.06	0.04	
Total	99	100.57	99.39	98.75	99.29	100.07	98.37	98.31	98.55	98.6	100.57	99.23	98.66	98.87	100.07	99.27	98.84	98.49	99.84	99.88	100.14	98.92	

**Table D.7: Normative mineralogy of the major element oxides in borehole BH6259.**

Normative Minerals	N118	N119	N120	N121	N122	N123
	Weight %					
Norm	Norm	Norm	Norm	Norm	Norm	
Quartz	0.94	2.79	3.17	1.76	2.05	1.5
Plagioclase	92.92	91.52	89.09	91.41	84.21	89.95
Orthoclase	1.12	1.06	0.77	0.71	0.59	1.06
Diopside	2.46	1.96	5.09	4.8	9.58	5.17
Hypersthene	1.37	0	1.37	0.67	0.86	0
Wollastonite	0	0.94	0	0	0	0.66
Ilmenite	0.08	0.06	0.08	0.08	0.09	0.06
Magnetite	0.28	0.19	0.33	0.36	0.83	0.57
Apatite	0	0	0	0.02	0	0
Chromite	0.01	0	0.01	0.01	0.04	0
Pyrite	0.04	0.11	0.04	0.36	1.95	0.98
Total	99.22	98.63	99.95	100.18	100.2	99.95

**N73-N97: Hangingwall****N98: Chromitite layer****N99-N121: Footwall**

## Appendix E

Standard	JB1a	MRG1	NIM-P
V	210	529	218
Cr	418	433	24052
Co	37	84	99
Ni	166	198	579
Cu	56	118	15
Zn	75	189	100
Ga	18	16	7
Rb	42	6.6	2.6
Sr	434	257	27
Y	24	13	2.9
Zr	149	105	20
Nb	29	17	1.58
Sn	2.5	3.3	1.7
Cs	1.21	0.55	0.28
Ba	483	62	28
Hf	3.5	3.7	0.39
Ta	1.7	0.77	0.10
Pb	6.7	8.5	4.0
Th	8.9	0.78	0.41
U	1.6	0.20	0.11

Certified values	JB1a	MRG1	NIM-P
51V	206	526	230
52Cr	415	430	24000
59Co	40	87	110
60Ni	134	193	560
65Cu	55	134	18
66Zn	82	191	100
71Ga	18	17	8.00
85Rb	41	8.5	5.0
88Sr	443	266	32
89Y	24	14	5.00
90Zr	146	108	30
93Nb	27	20	na
118Sn	2.00	3.6	2.00
133Cs	1.20	0.57	na
137Ba	497	61	46
178Hf	3.5	3.8	na
181Ta	2.00	0.80	na
208Pb	7.2	10	6.00
232Th	8.8	0.93	0.50
238U	1.6	0.24	0.20

**Table E.1: Trace element whole rock geochemistry of standards analysed and the certified reference material values.**

**Table E.2: Whole rock geochemistry of borehole SD14/90 obtained from ICP-MS analysis. Trace element concentrations in ppm.**

Depth (m)	72.14	72.16	72.18	72.20	72.22	72.24	72.26	72.28	72.30	72.32	72.34
	NP1	NP2	NP3	NP4	NP5	NP6	NP7	NP8	NP9	NP10	NP11
V	192	139	132	354	1696	1440	746	30	32	24	16
Cr	3072	2486	2639	28482	128741	70317	84226	1472	812	644	189
Co	164	155	140	136	210	160	100	9.9	28	27	5.3
Ni	5609	5676	4713	3590	3436	2883	1094	172	1447	804	29
Cu	1585	1582	1690	1917	1249	1295	334	149	322	36	22
Zn	116	89	81	178	529	370	325	14	30	25	24
Ga	7.1	6.8	7.0	13	45	41	30	19	17	16	18
Rb	1.4	0.8	0.8	1.6	1.8	2.9	3.1	2.0	2.4	2.1	1.7
Sr	66	74	81	78	107	94	245	445	410	383	453
Y	7.6	5.7	5.2	4.1	1.1	2.2	0.6	1.7	2.3	1.6	1.2
Zr	22	13	10	8.7	17	19	12	13	12	13	15
Nb	0.96	0.59	0.52	0.48	1.01	1.14	0.66	0.53	0.78	0.60	0.80
Sn	1.8	4.9	1.6	2.3	8.0	2.0	4.4	3.2	1.9	7.5	1.4
Cs	0.23	0.21	0.26	0.27	0.25	0.24	0.28	0.26	0.28	0.29	0.22
Ba	29.5	35.2	30.9	29.4	23.0	34.3	52.9	88.2	89.1	71.7	79.2
Hf	0.52	0.31	0.24	0.18	0.29	0.39	0.22	0.24	0.28	0.25	0.29
Ta	0.06	0.03	0.05	0.03	0.06	0.06	0.05	0.04	0.05	0.04	0.06
Pb	7.5	6.4	7.2	5.6	3.3	3.9	2.6	1.9	2.2	1.8	1.5
Th	0.30	0.22	0.16	0.16	0.13	0.24	0.11	0.26	0.27	0.21	0.26
U	0.09	0.04	0.03	0.04	0.03	0.06	0.04	0.06	0.07	0.05	0.06

Sample NP1 – NP4 hangingwall pyroxenite; sample NP5 –NP7 chromitite layer; sample NP8 – NP11 footwall anorthositic

**Table E.3: Whole rock geochemistry of borehole 20/0252 obtained from ICP-MS analysis. Trace element concentrations in ppm.**

Thickness (m)	21.60	21.58	21.56	21.54	21.52	21.50	21.48	21.46	21.44	21.42	21.40	21.38	21.36	21.34	21.32	21.30	21.28
Sample name	P1	P2	P3	P4	P5	P6	P7	P8	P9	P10	P11	P12	P13	P14	P15	P16	P17
V	123	157	142	156	151	172	149	175	183	390	815	1831	161	167	196	103	136
Cr	2658	3202	2752	2743	2818	3302	3052	3499	3727	16467	36205	77992	3170	3005	3678	1653	1778
Co	59	97	70	68	62	134	63	71	80	175	174	199	75	107	72	41	29
Ni	782	3274	4330	2743	3110	4192	3443	10745	8931	7325	5223	7658	1609	2348	11350	4844	1489
Cu	104	636	1462	1210	1580	1059	984	2480	1997	1961	1490	1595	463	617	2681	4381	710
Zn	77	139	141	144	109	116	121	137	132	159	239	383	81	99	126	86	50
Ga	6.4	5.6	6.0	5.8	5.5	6.3	6.2	4.6	5.1	7.7	14.0	24.6	10.4	7.6	5.5	8.6	8.4
Rb	1.0	1.5	2.7	3.8	2.4	1.7	1.3	1.0	0.9	1.2	1.9	3.5	1.6	4.2	11.2	3.1	2.6
Sr	60.9	47.2	32.6	26.2	27.9	50.5	43.1	10.2	21.4	30.3	34.5	42.0	175.9	75.8	18.0	139.5	81.0
Y	4.6	4.3	5.2	5.5	4.7	4.5	4.4	6.5	6.2	4.6	4.6	8.8	4.1	4.9	9.8	6.9	5.8
Zr	14	10	23	22	41	13	15	19	9.4	11	13	18	10	15	21	19	14
Nb	0.23	0.67	0.60	0.84	0.61	0.86	0.51	0.64	0.46	0.24	0.19	0.47	0.25	0.75	2.81	1.43	0.99
Sn	0.64	2.85	2.09	1.07	1.22	3.56	1.89	1.24	1.13	3.95	3.42	3.34	2.85	4.89	1.38	1.86	1.49
Cs	0.03	0.23	0.07	0.10	0.07	0.25	0.07	0.03	0.03	0.20	0.22	0.21	0.23	0.27	0.20	0.09	0.07
Ba	12.7	14.9	15.1	17.9	13.0	12.3	14.0	5.4	5.5	6.0	8.5	8.1	31.5	33.4	83.4	44.6	32.4
Hf	0.13	0.24	0.42	0.31	0.55	0.32	0.22	0.42	0.21	0.27	0.27	0.45	0.26	0.34	0.48	0.32	0.44
Ta	0.02	0.07	0.05	0.05	0.06	0.06	0.03	0.06	0.03	0.02	0.01	0.04	0.02	0.06	0.17	0.11	0.08
Pb	1.92	2.94	3.30	4.29	4.34	5.05	4.86	3.08	3.66	5.59	3.85	4.15	4.45	3.30	4.81	7.45	4.35
Th	0.20	0.23	0.49	0.53	0.43	0.51	0.45	0.25	0.19	0.12	0.11	0.15	0.17	0.45	0.60	0.67	0.51
U	0.04	0.06	0.09	0.12	0.11	0.12	0.13	0.07	0.04	0.03	0.02	0.04	0.04	0.12	0.18	0.15	0.14

Sample P1 – P11 hangingwall pyroxenite; sample P12 chromitite layer; sample P13 – P17 pegmatoidal layer

Thickness (m)	21.26	21.24	21.22	21.20	21.18	21.16	21.14	21.12	21.10	21.08	21.06	21.04	21.02	21.00	20.98	20.96	20.94
Sample name	P18	P19	P20	P21	P22	P23	P24	P25	P26	P27	P28	P29	P30	P31	P32	P33	P34
V	182	142	131	149	32	86	79	132	105	138	130	155	101	96	104	98	81
Cr	2939	3840	3059	3184	898	1621	1349	2029	2303	2735	2268	1634	1733	1592	1602	1453	2363
Co	145	66	65	93	47	54	48	143	60	53	61	52	59	56	57	93	45
Ni	5165	2374	2936	1493	1274	1716	5451	3934	1392	2369	2898	1114	1477	13562	4986	1892	899
Cu	1647	607	930	302	137	201	3255	934	227	490	760	581	1148	3526	1527	420	205
Zn	97	83	89	116	76	84	97	117	84	79	87	67	104	119	101	95	72
Ga	7.4	5.4	5.1	6.6	10.6	8.4	10.2	7.1	7.3	5.6	6.2	10.8	6.8	8.6	8.2	7.0	5.2
Rb	7.0	4.8	1.5	1.8	1.9	7.5	2.7	6.7	7.5	7.2	5.6	7.5	7.7	5.4	7.5	4.1	1.8
Sr	66	19	25	70	141	73	176	60	32	15	44	158	52	100	86	69	14
Y	7.7	5.5	4.8	3.6	2.0	3.8	4.3	4.2	6.2	6.0	6.0	7.9	4.9	4.8	5.4	3.6	2.8
Zr	17	26	19	14	6.9	27	21	27	954	13	14	17	19	13	132	21	6.5
Nb	1.40	0.85	0.40	0.66	0.70	3.2	1.1	2.5	3.3	2.4	1.7	1.7	2.3	1.4	2.4	0.81	0.51
Sn	4.2	0.47	0.45	4.43	0.90	1.10	0.73	5.53	1.28	0.81	0.92	3.01	1.54	1.50	1.69	1.33	0.77
Cs	0.29	0.14	0.05	0.26	0.47	0.48	0.14	0.33	0.58	0.23	0.18	0.33	0.30	0.18	0.33	0.51	0.30
Ba	39	27	10	21	38	64	49	51	24	51	42	80	51	48	60	19	8.8
Hf	0.42	0.38	0.27	0.27	0.21	0.60	0.48	0.62	16.29	0.41	0.27	0.46	0.29	0.37	2.36	0.45	0.16
Ta	0.08	0.06	0.02	0.06	0.05	0.17	0.07	0.19	0.31	0.14	0.10	0.15	0.18	0.09	0.18	0.06	0.03
Pb	4.9	3.7	2.4	2.1	7.3	4.0	4.9	2.6	16.9	2.4	2.1	8.4	8.7	13.8	9.6	1.6	0.7
Th	0.76	0.68	0.23	0.27	0.37	1.75	0.62	1.6	4.6	1.1	0.98	0.92	1.6	1.00	1.79	0.58	0.21
U	0.22	0.16	0.06	0.07	0.09	0.26	0.15	0.32	1.47	0.24	0.24	0.21	0.54	0.45	0.55	0.13	0.05

Sample P18 – P34 pegmatoidal layer

Thickness (m)	20.92	20.90	20.88	20.86	20.84	20.82	20.80	20.78	20.76	20.74	20.72	20.70	20.68	20.67	20.65	20.63	20.61	20.59
Sample name	P35	P36	P37	P38	P39	P40	P41	P42	P43	P44	P45	P46	P47	P48	P49	P50	P51	P52
V	100	58	47	106	129	95	135	97	57	14	50	104	209	280	31	27	5.8	9.7
Cr	2209	2589	2945	3225	3644	1949	2009	2012	816	108	1112	2738	12199	33365	320	142	14	122
Co	63	74	95	63	66	39	110	47	51	65	57	117	100	93	13	4.9	3.3	3.3
Ni	9716	3336	2282	1171	1157	860	1467	977	1410	2300	587	1389	1039	670	71	24	14	600
Cu	1747	435	356	122	127	84	195	105	126	204	187	429	122	179	28	16	8.9	4.1
Zn	108	124	143	87	96	62	111	78	60	169	96	116	127	198	39	27	BD	3.1
Ga	6.3	7.9	9.7	4.5	4.1	4.1	4.6	3.3	5.3	7.7	9.9	7.6	8.7	17.2	15.4	17.2	18.4	19.3
Rb	8.5	6.8	2.8	3.1	4.4	1.1	1.7	2.6	1.7	2.1	1.7	2.9	3.0	2.1	0.7	5.4	11.5	13.9
Sr	56	140	199	25	13	11	24	13	78	117	159	55	58	230	380	423	436	479
Y	4.9	2.7	1.4	4.5	4.9	2.2	3.7	3.6	2.7	1.3	2.0	2.9	3.2	2.0	0.7	0.9	1.3	1.3
Zr	32	7.7	11	40	43	8.7	12	4.9	8.5	5.5	12	13	25	8.0	7.5	11	0.5	3.4
Nb	1.8	1.07	0.48	0.77	0.78	0.46	0.34	0.62	0.57	0.72	0.37	0.48	0.73	0.37	0.19	0.83	0.16	0.23
Sn	1.2	1.7	4.05	0.39	0.51	0.46	2.23	1.10	0.81	2.24	0.88	1.7	4.04	3.04	1.3	5.9	0.43	0.67
Cs	0.32	0.52	0.53	0.26	0.22	0.11	0.28	0.15	0.29	0.51	0.43	0.53	0.26	0.27	0.20	0.31	0.37	0.49
Ba	49	33	22	18	17	7	10	17	12	15	24	17	25	26	51	77	140	142
Hf	0.78	0.20	0.24	0.67	0.81	0.20	0.29	0.17	0.23	0.12	0.23	0.26	0.56	0.15	0.15	0.23	0.03	0.04
Ta	0.11	0.08	0.04	0.04	0.06	0.04	0.03	0.04	0.03	0.04	0.03	0.04	0.05	0.03	0.01	0.04	0.01	0.01
Pb	4.2	2.4	2.5	0.71	0.74	0.67	1.7	0.75	0.86	1.40	2.54	1.39	0.96	1.78	1.04	2.40	0.60	0.88
Th	1.07	0.52	0.27	0.60	0.63	0.20	0.24	0.39	0.17	0.25	0.25	0.22	0.63	0.16	0.16	0.13	0.08	
U	0.32	0.15	0.07	0.14	0.14	0.04	0.06	0.09	0.04	0.06	0.08	0.05	0.19	0.04	0.03	0.02	0.02	0.02

Sample P35 – P46 pegmatoidal layer; P47 – P52 footwall anorthosite

**Table E.4: Whole rock geochemistry of borehole BH6259 obtained from ICP-MS analysis. Trace element concentrations in ppm.**

Depth (m)	1087.09	1087.11	1087.13	1087.15	1087.17	1087.19	1087.21	1087.23	1087.25	1087.27	1087.29	1087.31	1087.33	1087.35	1087.37	1087.39	1087.43
Sample name	N73	N74	N75	N76	N77	N78	N79	N80	N81	N82	N83	N84	N85	N86	N87	N88	N90
V	120	119	139	170	110	66	143	156	129	136	121	137	127	114	115	124	109
Cr	2553	2510	2517	2986	2438	2581	2571	2837	2407	2638	2252	2447	2797	2139	2422	3432	2599
Co	57	54	54	68	51	31	59	83	57	45	50	76	56	48	53	94	51
Ni	921	1702	967	900	767	645	889	894	1259	715	773	931	899	710	768	1567	2311
Cu	251	318	320	248.7	303	123	243	224.7	415	232	154	335.4	208	282	197	461.1	1051
Zn	95	107	299	120	140	66	85	130	92	477	116	115	103	90	92	132	207
Ga	7.2	6.7	6.8	5.6	7.7	5.2	6.3	7.4	7.2	9.0	8.6	8.2	7.2	9.5	7.3	6.9	7.5
Rb	16	11	26	13	11	4.3	27	23	26	8.5	16	7.4	6.7	13	7.2	1.1	1.7
Sr	74	82	60	44	79	67	45	73	58	114	113	111	68	127	78	92	77
Y	7.2	6.3	8.4	9.9	5.8	3.1	8.9	7.6	7.3	9.7	6.2	10.8	6.6	7.6	5.9	3.2	4.9
Zr	17	60	130	46	16	7.5	1888	52.3	517	33	54	29	26	117	18	16	20
Nb	1.3	1.1	3.6	1.3	1.0	0.4	4.4	1.7	1.8	0.91	7.06	3.6	2.2	1.2	0.84	0.45	0.59
Sn	0.84	0.90	0.87	3.37	0.88	0.42	1.2	3.6	0.62	1.5	0.65	3.3	0.48	0.72	0.80	3.7	1.5
Cs	0.35	0.34	0.73	0.43	0.39	0.12	0.73	0.61	0.57	0.27	0.40	0.32	0.23	0.39	0.27	0.21	0.05
Ba	96	67	128	76	72	44	154	107	137	65	101	54	45	91	50	23	30
Hf	0.31	0.92	2.4	0.98	0.32	0.12	28	1.07	9.09	0.58	0.93	0.59	0.50	2.08	0.42	0.31	0.35
Ta	0.08	0.09	0.30	0.09	0.07	0.02	0.28	0.11	0.12	0.07	0.37	0.27	0.11	0.07	0.08	0.04	0.03
Pb	2.1	2.1	2.7	1.9	2.3	1.6	2.1	6.5	2.4	4.3	4.0	3.9	2.6	5.9	3.8	2.2	21
Th	1.06	0.82	1.61	1.23	1.17	0.27	2.72	2.12	1.77	1.02	1.05	1.36	0.64	1.36	0.97	0.21	0.35
U	0.28	0.24	0.35	0.25	0.20	0.06	0.61	0.31	0.37	0.38	0.51	0.26	0.28	0.29	0.20	0.06	0.17

Sample N73 – N90 hangingwall pyroxenite

Depth (m) Sample name	1087.45	1087.47	1087.49	1087.51	1087.53	1087.55	1087.57	1087.59	1087.61	1087.63	1087.65	1087.67	1087.69	1087.71	1087.73	1087.75	1087.77
	N91	N92	N93	N94	N95	N96	N97	N98	N99	N100	N101	N102	N103	N104	N105	N106	N107
V	105	132	105	134	152	152	142	1265	56	48	33	37	23	23	33	32	28
Cr	2255	3356	3051	4938	3561	3903	4170	119161	2647	1148	970	1209	598	418	496	350	346
Co	55	111	65	67	82	203	137	180	14	16	50	25	16	31	32	11	8.9
Ni	3279	3268	3665	9221	14903	9821	4436	3573	750	236	860	554	368	856	496	278	245
Cu	1283	988	917	2462	2395	1464	880	1246	371	143	112	161	171	175	148	126	219
Zn	199	166	129	146	147	150	143	385	62	98	109	100	41	74	74	61	60
Ga	7.4	7.0	6.8	7.0	6.0	6.3	5.5	34	17	15	12	13	15	13	14	16	17
Rb	2.9	2.8	1.2	2.1	7.4	1.8	1.5	1.5	1.8	2.0	1.8	1.4	1.3	1.7	1.8	1.4	1.2
Sr	78	91	92	66	39	56	37	136	467	419	334	329	368	314	347	427	434
Y	5.6	4.0	6.0	4.9	8.0	4.5	3.7	1.2	0.9	2.5	1.1	2.2	1.8	1.6	1.5	2.0	1.9
Zr	12	55	8.9	29	21	21	14	12	7.2	8.1	12	20	0.8	8.6	9.8	4.8	6.7
Nb	0.58	3.5	0.95	0.92	0.89	0.92	0.33	0.43	0.32	0.19	0.26	0.25	0.15	0.09	0.39	0.18	0.19
Sn	1.4	5.07	1.05	1.01	1.6	6.9	3.5	3.9	7.7	4.02	3.53	0.79	0.18	0.23	2.68	0.51	0.58
Cs	0.12	0.26	0.05	0.06	0.12	0.21	0.23	0.28	0.22	0.29	0.26	0.22	0.10	0.14	0.28	0.07	0.08
Ba	37	36	24	29	60	21	13	30	73	34	43	60	68	60	25	73	75
Hf	0.28	1.15	0.19	0.35	0.51	0.38	0.29	0.25	0.15	0.18	0.26	0.29	0.07	0.05	0.18	0.11	0.11
Ta	0.04	0.19	0.07	0.05	0.07	0.05	0.02	0.04	0.02	0.02	0.02	0.03	0.01	0.01	0.03	0.02	0.01
Pb	9.9	4.8	5.4	5.3	6.7	3.3	3.5	3.2	2.3	1.5	1.1	1.1	0.74	0.65	0.83	2.49	1.72
Th	0.44	0.40	0.22	0.40	0.56	0.44	0.22	0.09	0.11	0.11	0.08	0.11	0.03	0.03	0.12	0.05	0.08
U	0.22	0.10	0.05	0.34	0.40	0.14	0.05	0.02	0.03	0.02	0.02	0.01	0.01	0.01	0.02	0.03	0.03

Sample N91 – N97 hangingwall pyroxenite; N98 chromitite layer; N99 – N107 footwall anorthosite

Depth (m) Sample name	1087.79	1087.81	1087.83	1087.85	1087.87	1087.89	1087.91	1087.93	1087.95	1087.97	1087.99	1088.01	1088.03	1088.05	1088.07	1088.09
	N108	N109	N110	N111	N112	N113	N114	N115	N116	N117	N118	N119	N120	N121	N122	N123
V	39	26	21	16	12	17	13	16	21	23	12	4.3	16	13	29	5.8
Cr	485	310	132	80	53	146	76	76	108	137	60	10	83	62	174	28
Co	23	14	6.3	4.3	4.3	7.4	4.6	5.8	5.4	7.8	4.4	2.9	4.9	5.2	12.3	7.8
Ni	653	257	122	141	83	145	94	418	111	158	73	32	85	624	3424	2460
Cu	151	139	212	75	88	144	91	180	136	116	70	86	102	174	1339	911
Zn	55	45	33	10	33	36	48	45	36	75	35	17	78	87	103	79
Ga	14.2	13.9	16.4	16.9	17.9	16.1	14.7	15.8	17.1	16.2	19.0	19.5	18.3	18.1	17.1	19.0
Rb	1.4	1.1	1.2	1.5	1.9	1.2	1.2	1.4	1.2	1.1	3.9	2.9	1.5	1.9	1.4	3.7
Sr	343	387	439	451	478	444	408	452	447	454	462	452	439	446	418	453
Y	2.4	1.0	1.1	0.8	0.5	0.8	0.9	1.2	1.5	1.2	0.7	0.6	0.9	0.9	2.1	0.6
Zr	5.5	7.4	0.2	1.9	5.5	13.7	11.0	4.6	5.7	8.4	6.1	1.9	3.3	20.4	10.2	2.1
Nb	0.15	0.19	0.13	0.10	0.14	0.82	0.16	0.20	0.06	0.98	0.32	0.12	0.14	0.16	0.25	0.14
Sn	0.26	1.31	0.28	0.34	1.7	2.7	1.09	0.86	0.34	2.2	0.51	0.34	0.25	1.57	0.66	1.25
Cs	0.09	0.27	0.13	0.05	0.09	0.31	0.07	0.10	0.08	0.23	0.18	0.10	0.10	0.07	0.08	0.15
Ba	62	27	73	75	81	35	63	68	70	40	112	77	70	70	60	79
Hf	0.08	0.15	0.04	0.02	0.04	0.28	0.05	0.03	0.03	0.16	0.05	0.02	0.05	0.04	0.09	0.02
Ta	0.01	0.01	0.01	0.01	0.01	0.05	0.01	0.01	<0.005	0.08	0.03	0.01	0.01	0.01	0.02	0.01
Pb	0.85	0.55	0.49	1.5	1.6	0.82	1.3	2.5	0.80	0.56	1.7	0.88	0.79	2.2	6.9	4.0
Th	0.07	0.08	0.06	0.04	0.05	0.10	0.05	0.07	0.04	0.09	0.09	0.07	0.04	0.07	0.03	0.12
U	<0.005	0.01	0.01	0.01	0.02	0.02	0.01	0.01	0.01	0.02	0.04	0.01	0.01	0.02	0.02	0.02

Sample N108 – N123 footwall anorthosite

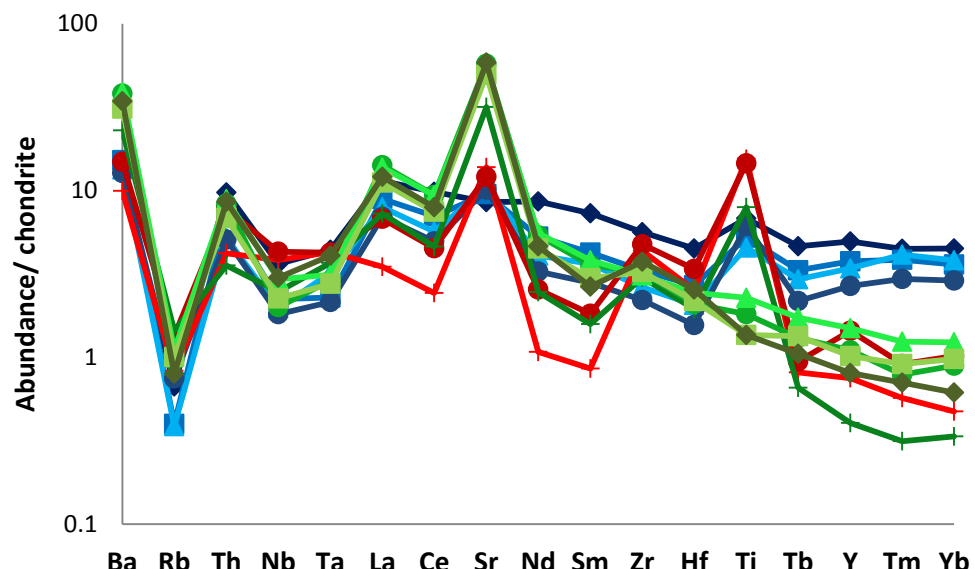


**Figure E.1:** Chondrite normalised multi element diagram for borehole SD14/90. Normalised values from Lodders, 2003.

Sample NP1 – NP4 Hangingwall pyroxenite

Sample NP5 – NP7 Chromitite layer

Sample NP7 – NP11 Footwall anorthosite

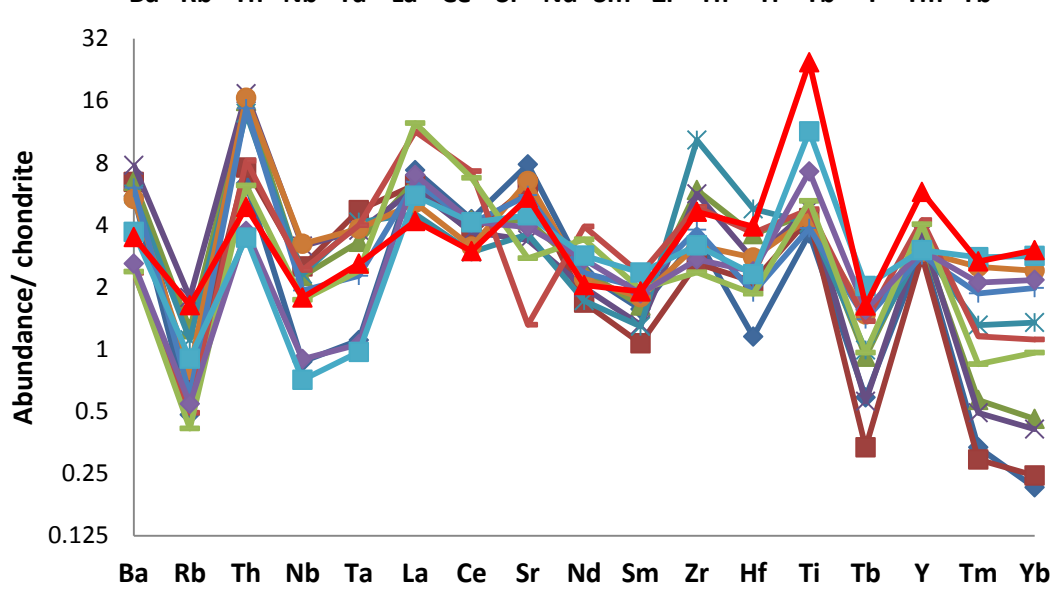


**Figure E.2:** Chondrite normalised multi element diagram from borehole 20/0252. Normalise values from Lodders, 2003.

Sample 1P -11P Hangingwall pyroxenite

Sample 12P Chromitite layer

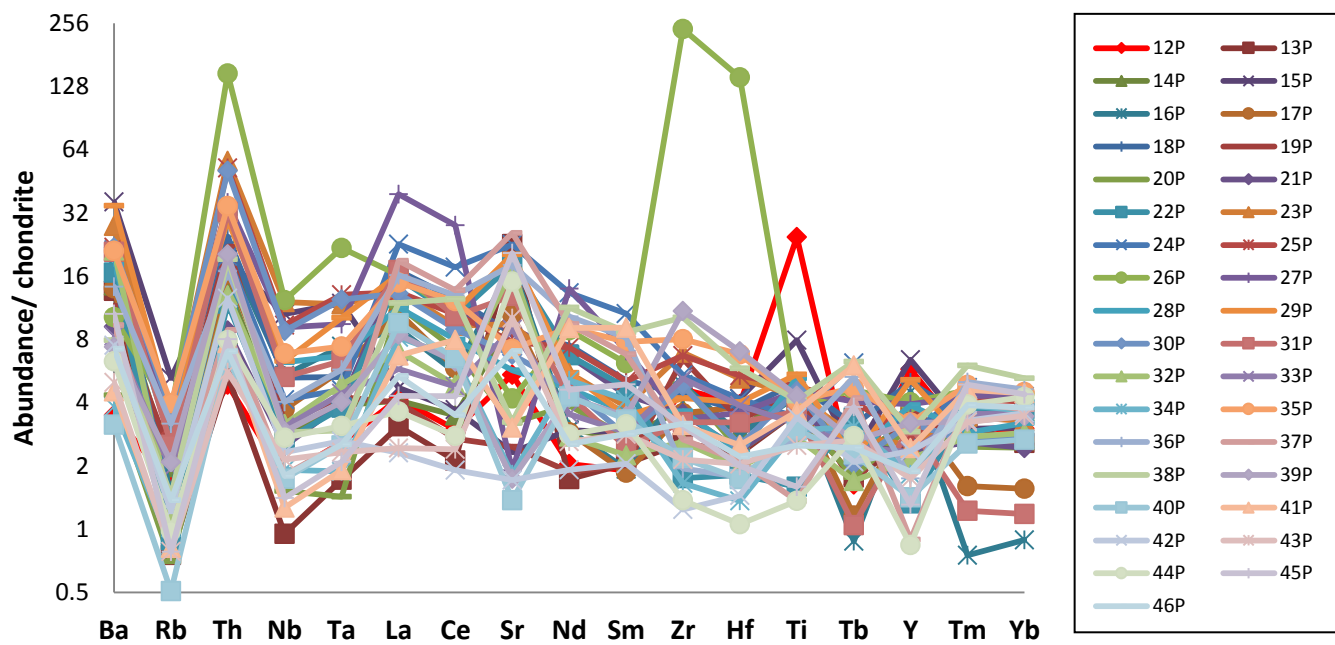


**Figure E.3: Chondrite normalised multi element diagram from borehole 20/0252. Normalise values from Lodders, 2003.**

Sample 12P Chromitite layer  
Sample 13P - 46P Pegmatoidal layer

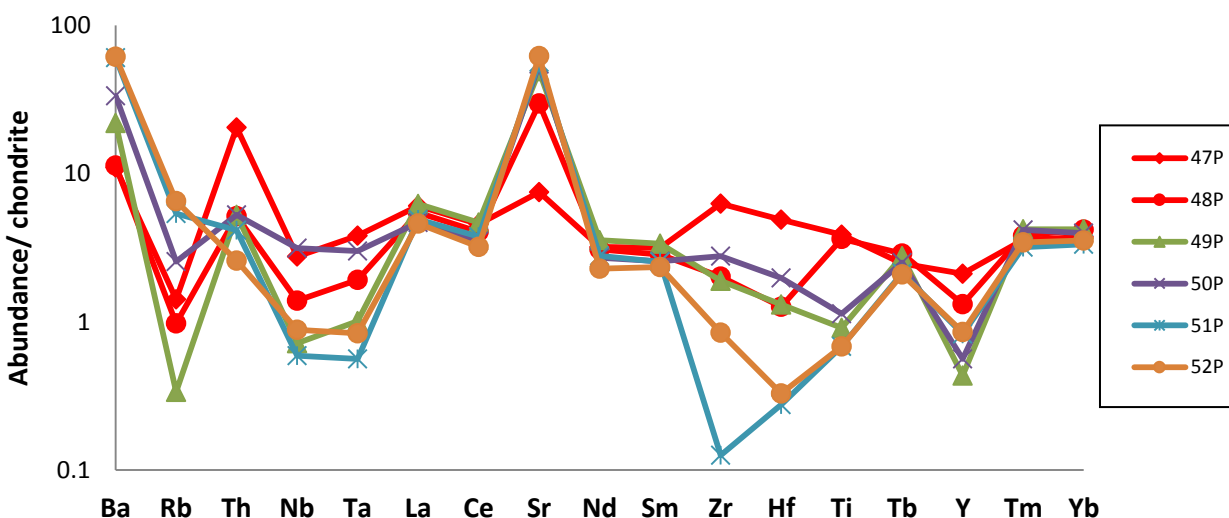


**Figure E.4: Chondrite normalised multi element diagram from borehole 20/0252. Normalised values from Lodders, 2003.**

Sample 47P – 48P Chromitite layer  
Sample 49P - 52P Footwall anorthosite

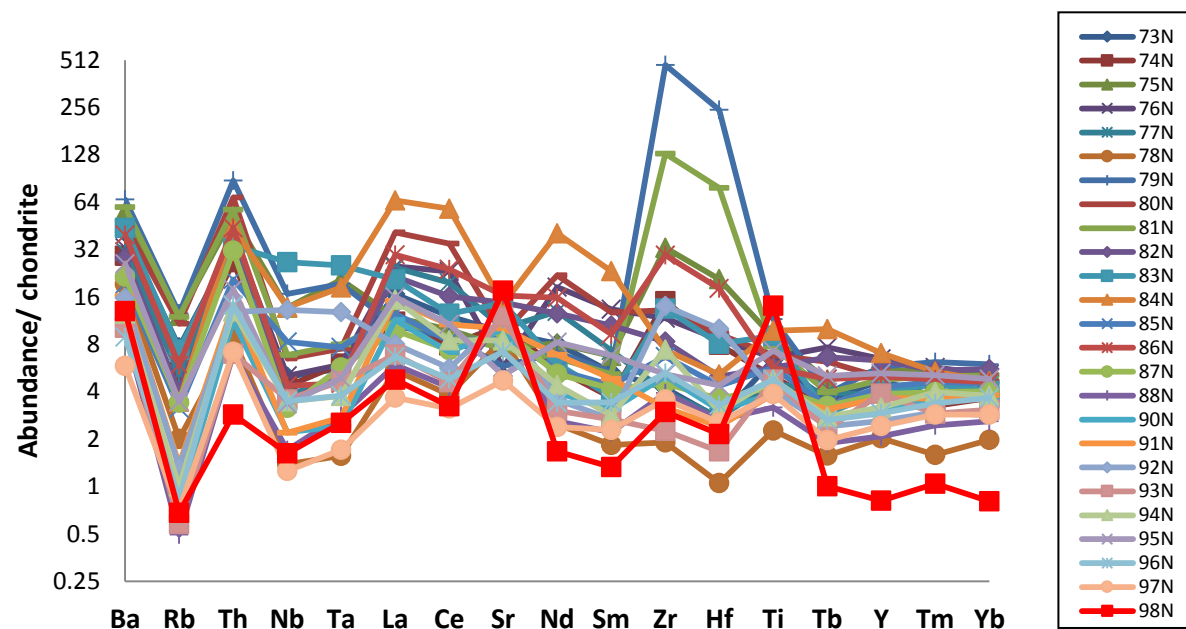


**Figure E.5: Chondrite normalised multi element diagram from borehole BH6259.**  
Normalise values from Lodders, 2003.

Sample 73N – 97N Hangingwall pyroxenite  
Sample 98N Chromitite layer

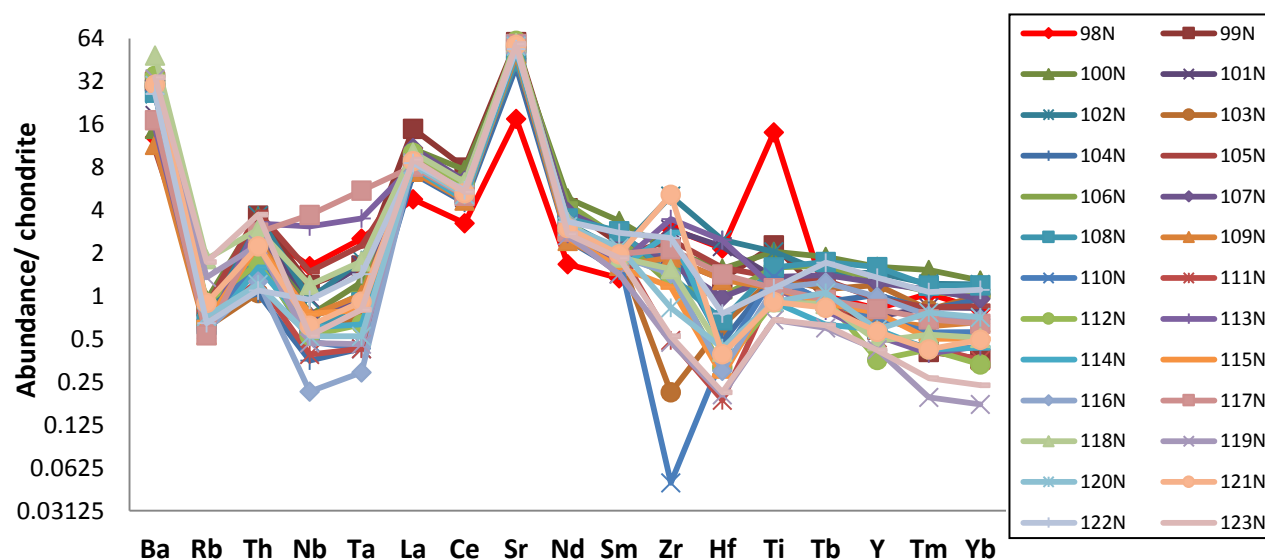


**Figure E.6: Chondrite normalised multi element diagram from borehole BH6259.**  
Normalised values from Lodders, 2003.

Sample 98N Chromitite layer  
Sample 99N – 110N Footwall anorthosite

**Table E.5: Whole rock geochemistry of borehole SD14/90 obtained from ICP-MS analysis. Rare earth element concentrations in ppm.**

Depth(m)	72.14	72.16	72.18	72.20	72.22	72.24	72.26	72.28	72.30	72.32	72.34
Sample	NP1	NP2	NP3	NP4	NP5	NP6	NP7	NP8	NP9	NP10	NP11
La	2.65	2.07	1.85	1.62	0.81	1.57	1.69	3.29	3.19	2.59	2.80
Ce	6.10	4.35	3.53	3.07	1.51	2.81	2.87	5.83	5.80	4.65	4.94
Pr	0.82	0.56	0.43	0.38	0.15	0.31	0.31	0.65	0.66	0.55	0.56
Nd	3.93	2.42	1.86	1.50	0.49	1.17	1.13	2.46	2.54	2.05	2.12
Sm	1.06	0.61	0.53	0.41	0.12	0.26	0.23	0.52	0.55	0.43	0.39
Eu	0.23	0.19	0.19	0.15	0.13	0.16	0.27	0.49	0.46	0.39	0.43
Gd	0.98	0.64	0.54	0.45	0.14	0.26	0.19	0.40	0.47	0.33	0.31
Tb	0.17	0.12	0.10	0.08	0.03	0.03	0.02	0.05	0.06	0.05	0.04
Dy	1.08	0.82	0.72	0.52	0.20	0.23	0.12	0.32	0.41	0.28	0.25
Ho	0.22	0.17	0.15	0.11	0.04	0.05	0.03	0.06	0.07	0.06	0.04
Er	0.67	0.50	0.50	0.37	0.11	0.17	0.07	0.16	0.21	0.14	0.12
Tm	0.11	0.09	0.10	0.07	0.01	0.02	0.01	0.02	0.03	0.02	0.02
Yb	0.73	0.59	0.62	0.47	0.08	0.17	0.05	0.15	0.20	0.16	0.10
Lu	0.12	0.10	0.10	0.08	0.01	0.03	0.01	0.02	0.03	0.03	0.02

**Table E.6: Whole rock geochemistry of borehole 20/0252 obtained from ICP-MS analysis. Rare earth element concentrations in ppm.**

Thickness (m)	21.6	21.58	21.56	21.54	21.52	21.5	21.48	21.46	21.44	21.42	21.4	21.38	21.36	21.34	21.32	21.3	21.28
Sample name	1P	2P	3P	4P	5P	6P	7P	8P	9P	10P	11P	12P	13P	14P	15P	16P	17P
La	1.07	1.14	1.09	1.45	1.26	1.40	1.25	1.00	0.84	0.56	0.54	1.56	2.22	1.95	2.77	4.39	3.76
Ce	1.99	2.33	2.17	2.90	2.51	2.83	2.17	2.67	1.73	1.49	1.19	4.94	4.05	3.89	7.75	8.53	8.07
Pr	0.25	0.30	0.28	0.38	0.34	0.36	0.31	0.44	0.28	0.22	0.18	0.85	0.47	0.48	1.17	1.09	1.09
Nd	1.05	1.27	1.24	1.62	1.41	1.46	1.16	2.11	1.29	1.20	0.88	4.14	1.96	1.93	5.18	4.32	4.71
Sm	0.34	0.37	0.37	0.49	0.41	0.46	0.41	0.71	0.46	0.41	0.30	1.32	0.48	0.50	1.26	0.99	1.19
Eu	0.12	0.10	0.07	0.07	0.08	0.12	0.09	0.08	0.06	0.08	0.09	0.21	0.25	0.16	0.15	0.29	0.29
Gd	0.38	0.39	0.43	0.51	0.46	0.48	0.43	0.74	0.52	0.51	0.38	1.24	0.49	0.52	1.34	1.00	1.30
Tb	0.07	0.08	0.09	0.10	0.10	0.09	0.09	0.14	0.10	0.09	0.07	0.21	0.08	0.09	0.22	0.15	0.19
Dy	0.54	0.55	0.63	0.75	0.62	0.67	0.58	0.92	0.70	0.65	0.57	1.40	0.56	0.66	1.47	0.98	1.33
Ho	0.14	0.12	0.14	0.16	0.13	0.14	0.14	0.19	0.14	0.14	0.12	0.25	0.11	0.13	0.28	0.18	0.22
Er	0.45	0.41	0.51	0.52	0.48	0.46	0.42	0.61	0.46	0.47	0.42	0.77	0.36	0.43	0.85	0.53	0.65
Tm	0.08	0.08	0.10	0.10	0.09	0.08	0.09	0.12	0.09	0.08	0.08	0.11	0.06	0.08	0.14	0.10	0.12
Yb	0.58	0.54	0.65	0.69	0.68	0.61	0.62	0.72	0.69	0.57	0.58	0.72	0.43	0.56	0.85	0.61	0.75
Lu	0.09	0.09	0.12	0.12	0.11	0.11	0.12	0.13	0.10	0.10	0.09	0.11	0.08	0.10	0.16	0.09	0.11

**Table E.6: Whole rock geochemistry of borehole 20/0252 obtained from ICP-MS analysis. Rare earth element concentrations in ppm.**

Thickness (m)	21.26	21.24	21.22	21.2	21.18	21.16	21.14	21.12	21.1	21.08	21.06	21.04	21.02	21	20.98	20.96	20.94
Sample name	18P	19P	20P	21P	22P	23P	24P	25P	26P	27P	28P	29P	30P	31P	32P	33P	34P
La	3.46	1.90	1.34	1.64	3.98	3.08	3.79	2.63	9.14	3.75	3.12	5.28	3.19	3.64	3.89	2.68	0.93
Ce	7.57	4.06	2.96	3.02	6.43	5.56	6.75	4.97	17.40	6.56	6.56	10.98	5.78	6.41	6.73	4.46	1.67
Pr	0.99	0.57	0.40	0.35	0.67	0.63	0.76	0.56	1.91	0.98	0.80	1.41	0.68	0.79	0.79	0.48	0.20
Nd	4.14	2.34	1.61	1.26	1.98	2.17	2.54	2.14	6.39	4.04	3.35	6.09	2.52	3.08	3.06	1.77	0.86
Sm	1.13	0.60	0.42	0.33	0.36	0.40	0.50	0.52	1.02	0.90	0.73	1.54	0.56	0.69	0.63	0.40	0.29
Eu	0.20	0.10	0.08	0.13	0.25	0.16	0.35	0.20	0.15	0.11	0.18	0.41	0.17	0.29	0.38	0.18	0.06
Gd	1.00	0.62	0.49	0.33	0.26	0.43	0.44	0.48	0.98	1.02	0.72	1.33	0.60	0.70	0.61	0.38	0.28
Tb	0.17	0.11	0.09	0.06	0.04	0.07	0.08	0.08	0.14	0.16	0.14	0.22	0.10	0.12	0.09	0.06	0.06
Dy	1.09	0.74	0.63	0.45	0.22	0.50	0.52	0.58	0.85	1.07	0.92	1.32	0.62	0.73	0.56	0.43	0.39
Ho	0.21	0.15	0.12	0.10	0.04	0.09	0.10	0.12	0.18	0.20	0.18	0.25	0.15	0.16	0.12	0.10	0.09
Er	0.65	0.51	0.45	0.34	0.14	0.34	0.33	0.41	0.63	0.66	0.57	0.68	0.46	0.47	0.36	0.31	0.33
Tm	0.12	0.09	0.08	0.07	0.03	0.06	0.06	0.07	0.10	0.11	0.10	0.11	0.08	0.09	0.06	0.06	0.06
Yb	0.73	0.60	0.57	0.47	0.19	0.46	0.44	0.52	0.71	0.72	0.66	0.70	0.53	0.61	0.40	0.40	0.41
Lu	0.13	0.10	0.09	0.08	0.03	0.08	0.08	0.09	0.12	0.13	0.12	0.11	0.10	0.08	0.07	0.07	0.07

**Table E.6: Whole rock geochemistry of borehole 20/0252 obtained from ICP-MS analysis. Rare earth element concentrations in ppm.**

Thickness (m)	20.92	20.9	20.88	20.86	20.84	20.82	20.8	20.78	20.76	20.74	20.72	20.7	20.68	20.67	20.65	20.63	20.61	20.59
Sample name	35P	36P	37P	38P	39P	40P	41P	42P	43P	44P	45P	46P	47P	48P	49P	50P	51P	52P
La	3.95	2.50	2.09	1.09	0.95	0.72	0.97	1.29	1.62	2.89	2.63	1.50	1.19	1.05	1.39	1.53	1.45	1.71
Ce	7.74	3.63	3.47	2.31	2.16	1.32	1.86	2.56	2.58	4.20	4.52	2.53	1.95	1.84	2.30	2.61	2.27	2.65
Pr	0.91	0.39	0.37	0.33	0.30	0.17	0.22	0.31	0.29	0.41	0.48	0.28	0.25	0.19	0.25	0.29	0.23	0.30
Nd	3.44	1.32	1.35	1.35	1.36	0.79	0.93	1.30	1.24	1.56	1.80	1.07	1.00	0.78	0.91	1.09	0.77	1.07
Sm	0.74	0.27	0.28	0.42	0.40	0.30	0.28	0.34	0.27	0.28	0.34	0.29	0.26	0.19	0.19	0.24	0.15	0.23
Eu	0.22	0.17	0.15	0.08	0.06	0.05	0.07	0.06	0.11	0.16	0.26	0.12	0.11	0.23	0.30	0.35	0.34	0.39
Gd	0.63	0.26	0.23	0.42	0.43	0.28	0.30	0.34	0.30	0.23	0.33	0.29	0.30	0.20	0.17	0.21	0.13	0.14
Tb	0.11	0.04	0.03	0.08	0.08	0.06	0.06	0.07	0.06	0.03	0.05	0.05	0.05	0.04	0.02	0.03	0.01	0.02
Dy	0.70	0.25	0.19	0.56	0.56	0.38	0.45	0.48	0.36	0.19	0.28	0.36	0.38	0.26	0.14	0.16	0.07	0.09
Ho	0.15	0.06	0.05	0.12	0.13	0.10	0.10	0.11	0.08	0.04	0.06	0.08	0.09	0.05	0.03	0.03	0.01	0.02
Er	0.46	0.20	0.11	0.41	0.45	0.35	0.34	0.38	0.28	0.11	0.18	0.24	0.29	0.17	0.07	0.09	0.05	0.06
Tm	0.08	0.04	0.02	0.07	0.08	0.07	0.06	0.07	0.05	0.02	0.03	0.04	0.06	0.03	0.01	0.01	0.01	0.01
Yb	0.56	0.25	0.15	0.50	0.59	0.42	0.49	0.46	0.35	0.16	0.18	0.32	0.39	0.22	0.07	0.07	0.04	0.03
Lu	0.10	0.05	0.03	0.09	0.09	0.08	0.08	0.09	0.06	0.03	0.04	0.06	0.04	0.01	0.01	0.00	0.00	0.00

**Table E.7: Whole rock geochemistry of borehole BH6259 obtained from ICP-MS analysis. Rare earth element concentrations in ppm.**

Depth	1087.09	1087.11	1087.13	1087.15	1087.17	1087.19	1087.21	1087.23	1087.25	1087.27	1087.29	1087.31	1087.33	1087.35	1087.37	1087.39	1087.43
Sample	N73	N74	N75	N76	N77	N78	N79	N80	N81	N82	N83	N84	N85	N86	N87	N88	N90
La	3.87	2.58	2.76	5.80	5.69	1.27	2.44	9.55	2.65	5.01	4.81	15.24	2.91	6.88	2.28	1.37	2.65
Ce	7.50	4.90	6.15	14.46	12.27	2.38	5.50	21.67	5.63	10.01	7.77	36.11	5.23	14.90	4.57	2.65	4.44
Pr	0.94	0.62	0.84	1.97	1.55	0.29	0.77	2.67	0.71	1.34	0.79	4.65	0.65	1.87	0.57	0.33	0.47
Nd	3.68	2.55	3.71	8.45	5.93	1.14	3.24	10.05	3.00	5.76	2.76	18.57	2.51	7.24	2.37	1.19	1.81
Sm	0.77	0.53	0.98	1.94	1.06	0.27	0.77	1.85	0.75	1.53	0.54	3.38	0.64	1.35	0.61	0.32	0.45
Eu	0.19	0.17	0.19	0.26	0.19	0.12	0.17	0.24	0.18	0.36	0.23	0.42	0.19	0.33	0.16	0.14	0.17
Gd	0.80	0.61	1.03	1.72	0.98	0.31	0.83	1.59	0.85	1.53	0.55	2.75	0.78	1.34	0.63	0.35	0.56
Tb	0.13	0.11	0.17	0.27	0.14	0.06	0.14	0.22	0.14	0.24	0.10	0.36	0.12	0.17	0.12	0.07	0.10
Dy	0.95	0.77	1.25	1.56	0.95	0.37	1.12	1.19	1.02	1.62	0.76	1.81	0.98	1.22	0.77	0.45	0.72
Ho	0.18	0.16	0.24	0.29	0.17	0.08	0.23	0.24	0.23	0.30	0.16	0.33	0.20	0.22	0.18	0.10	0.15
Er	0.61	0.53	0.75	0.85	0.52	0.25	0.80	0.70	0.76	0.88	0.54	0.88	0.61	0.70	0.54	0.34	0.51
Tm	0.09	0.08	0.13	0.14	0.08	0.04	0.15	0.12	0.12	0.13	0.11	0.13	0.11	0.11	0.09	0.06	0.08
Yb	0.70	0.60	0.89	0.84	0.64	0.32	0.98	0.75	0.83	0.91	0.66	0.76	0.73	0.75	0.66	0.42	0.61
Lu	0.11	0.11	0.14	0.13	0.11	0.06	0.20	0.13	0.16	0.15	0.12	0.12	0.13	0.11	0.07	0.11	0.11
Depth	1087.45	1087.47	1087.49	1087.51	1087.53	1087.55	1087.57	1087.59	1087.61	1087.63	1087.65	1087.67	1087.69	1087.71	1087.73	1087.75	1087.77
Sample	N91	N92	N93	N94	N95	N96	N97	N98	N99	N100	N101	N102	N103	N104	N105	N106	N107
La	3.51	1.86	1.59	3.56	3.70	1.55	0.85	1.11	3.46	2.50	1.77	2.06	2.20	1.68	1.88	2.32	2.54
Ce	6.65	3.52	2.85	5.28	6.66	3.00	1.95	2.01	4.94	4.77	3.04	3.37	3.69	2.80	3.22	4.05	4.01
Pr	0.80	0.42	0.37	0.55	0.85	0.37	0.26	0.22	0.54	0.58	0.35	0.38	0.39	0.31	0.37	0.46	0.47
Nd	3.14	1.63	1.39	2.01	3.77	1.56	1.09	0.76	1.89	2.21	1.22	1.48	1.41	1.12	1.38	2.02	1.78
Sm	0.70	0.39	0.39	0.41	0.99	0.50	0.33	0.19	0.34	0.49	0.21	0.30	0.28	0.22	0.27	0.37	0.38
Eu	0.18	0.16	0.14	0.14	0.16	0.12	0.09	0.17	0.44	0.39	0.29	0.32	0.40	0.34	0.35	0.42	0.48
Gd	0.69	0.44	0.40	0.50	0.99	0.52	0.38	0.21	0.29	0.41	0.19	0.23	0.29	0.21	0.25	0.37	0.33
Tb	0.11	0.09	0.08	0.10	0.18	0.09	0.07	0.04	0.03	0.07	0.03	0.05	0.04	0.03	0.05	0.06	0.05
Dy	0.84	0.55	0.56	0.67	1.18	0.67	0.51	0.19	0.18	0.43	0.17	0.27	0.23	0.16	0.24	0.31	0.29
Ho	0.17	0.12	0.12	0.13	0.23	0.14	0.11	0.04	0.04	0.08	0.04	0.05	0.04	0.03	0.04	0.06	0.05
Er	0.54	0.40	0.42	0.45	0.76	0.47	0.38	0.17	0.08	0.22	0.11	0.16	0.10	0.12	0.12	0.16	0.17
Tm	0.09	0.07	0.07	0.09	0.12	0.08	0.07	0.02	0.01	0.04	0.02	0.03	0.02	0.02	0.02	0.03	0.03
Yb	0.62	0.46	0.50	0.62	0.79	0.60	0.47	0.13	0.06	0.21	0.13	0.20	0.17	0.16	0.14	0.16	0.16
Lu	0.11	0.08	0.10	0.10	0.13	0.10	0.08	0.02	0.01	0.03	0.02	0.04	0.02	0.03	0.02	0.02	0.03
Depth	1087.79	1087.81	1087.83	1087.85	1087.87	1087.89	1087.91	1087.93	1087.95	1087.97	1087.99	1088.01	1088.03	1088.05	1088.07	1088.09	
Sample	N108	N109	N110	N111	N112	N113	N114	N115	N116	N117	N118	N119	N120	N121	N122	N123	
La	1.88	1.73	2.15	2.20	2.34	1.91	1.84	1.97	2.01	1.88	2.35	2.00	1.95	2.06	1.99	2.11	
Ce	3.26	2.90	3.51	3.54	3.71	3.14	2.95	3.20	3.39	3.14	3.91	3.23	3.20	3.27	3.44	3.34	
Pr	0.43	0.32	0.39	0.39	0.42	0.34	0.31	0.36	0.39	0.36	0.43	0.34	0.34	0.35	0.40	0.35	
Nd	1.60	1.11	1.44	1.29	1.42	1.25	1.20	1.17	1.49	1.29	1.51	1.21	1.41	1.37	1.52	1.24	
Sm	0.41	0.24	0.26	0.30	0.29	0.24	0.23	0.23	0.28	0.29	0.27	0.21	0.32	0.28	0.40	0.27	
Eu	0.39	0.34	0.47	0.44	0.47	0.39	0.38	0.41	0.44	0.36	0.42	0.42	0.39	0.40	0.39	0.41	
Gd	0.40	0.21	0.23	0.23	0.18	0.21	0.20	0.18	0.30	0.24	0.22	0.18	0.26	0.21	0.37	0.16	
Tb	0.06	0.03	0.03	0.03	0.03	0.03	0.02	0.03	0.04	0.03	0.03	0.02	0.04	0.03	0.06	0.02	
Dy	0.42	0.18	0.16	0.14	0.14	0.16	0.13	0.17	0.20	0.20	0.14	0.07	0.21	0.15	0.30	0.09	
Ho	0.08	0.04	0.03	0.03	0.02	0.03	0.02	0.03	0.04	0.04	0.02	0.01	0.04	0.02	0.06	0.02	
Er	0.21	0.10	0.10	0.07	0.06	0.07	0.06	0.08	0.10	0.11	0.07	0.03	0.11	0.07	0.17	0.04	
Tm	0.03	0.01	0.01	0.01	0.01	0.01	0.01	0.01	0.02	0.02	0.01	0.00	0.02	0.01	0.03	0.01	
Yb	0.19	0.11	0.09	0.06	0.05	0.07	0.07	0.08	0.11	0.10	0.08	0.03	0.12	0.08	0.18	0.04	
Lu	0.03	0.02	0.01	0.01	0.01	0.01	0.01	0.01	0.02	0.02	0.01	0.01	0.02	0.01	0.03	0.01	

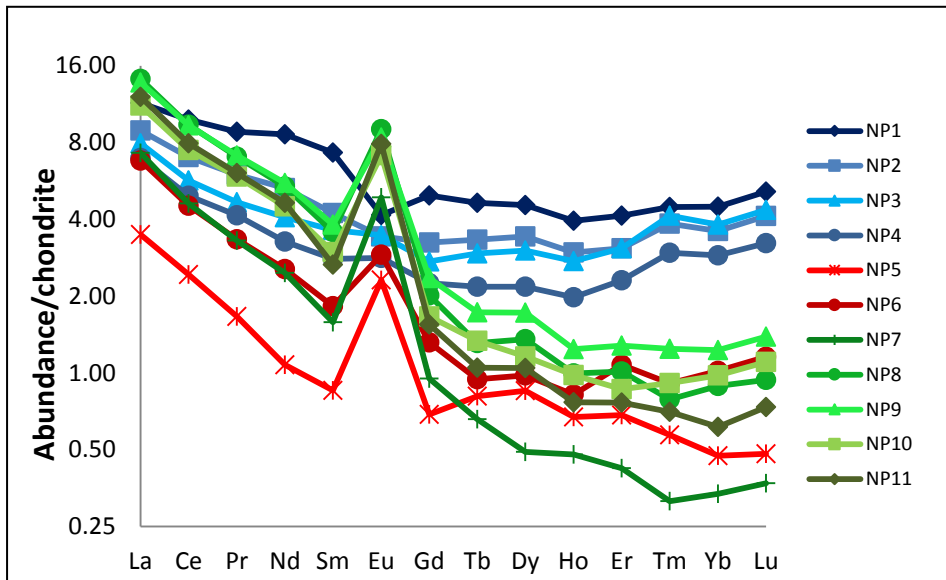


Figure E.7: Chondrite normalised REE diagrams for borehole SD14/90.  
C1 chondrite values from Lodders, 2003.

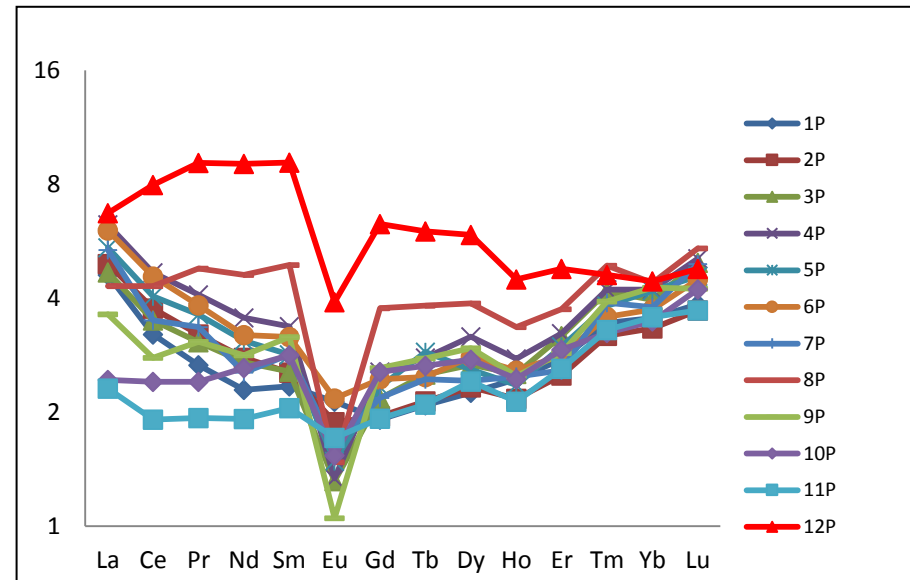


Figure E.8: Chondrite normalised REE diagrams for the hangingwall and the top chromitite stringer, from borehole 20/0252. C1 chondrite values from Lodders, 2003.

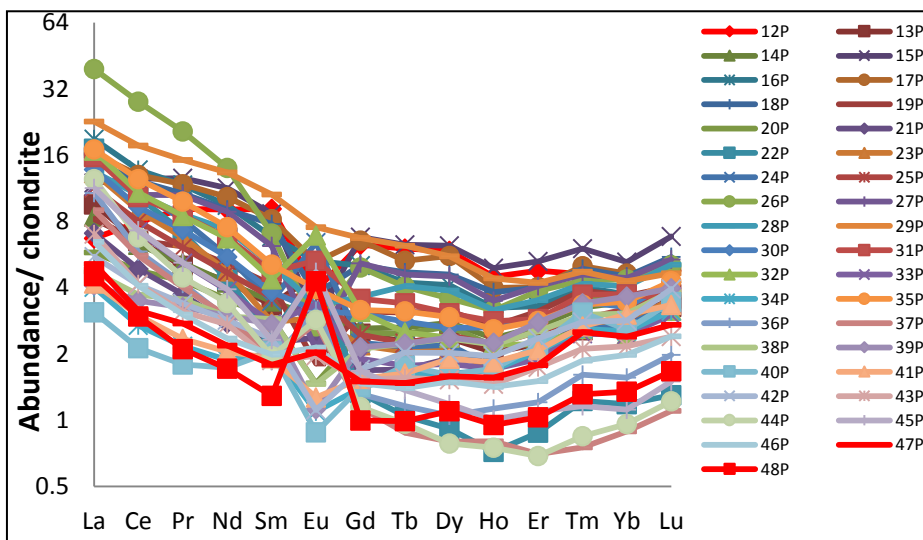


Figure E.9: Chondrite normalised REE diagrams for the top and bottom chromitite stringer and the pegmatoidal layer, from borehole 20/0252.

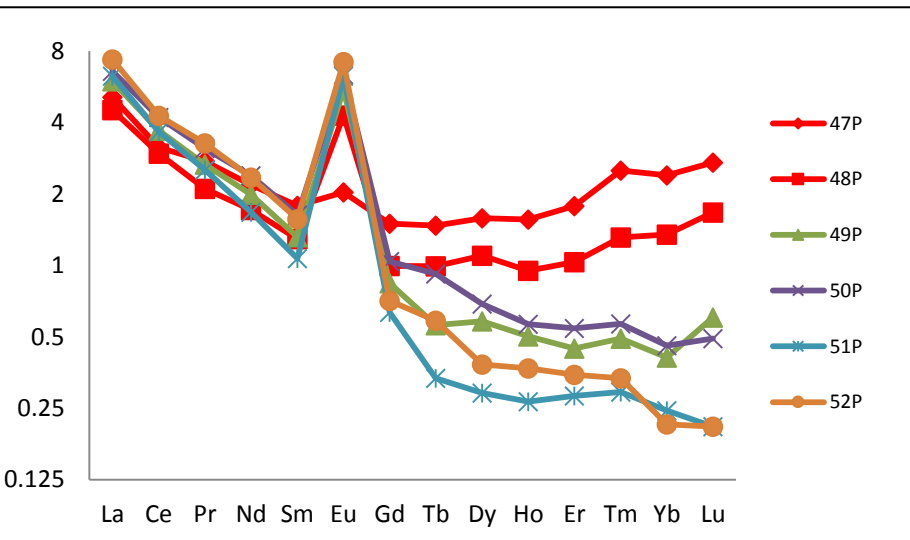


Figure E.10: Chondrite normalised REE diagrams for the bottom chromitite stringer and the footwall, from borehole 20/0252.

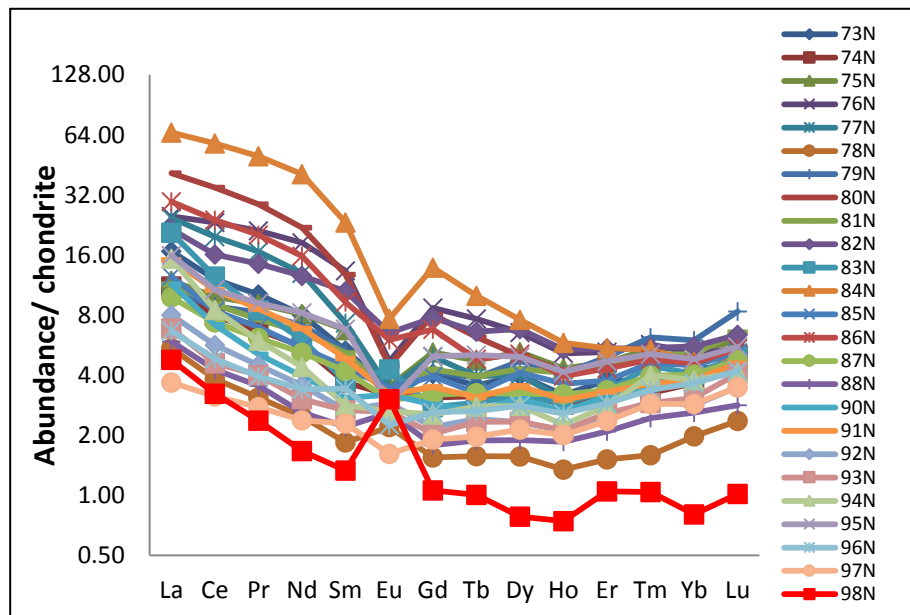


Figure E.11: Chondrite normalised REE diagrams for the chromitite stringer and the hangingwall, from borehole BH6259.

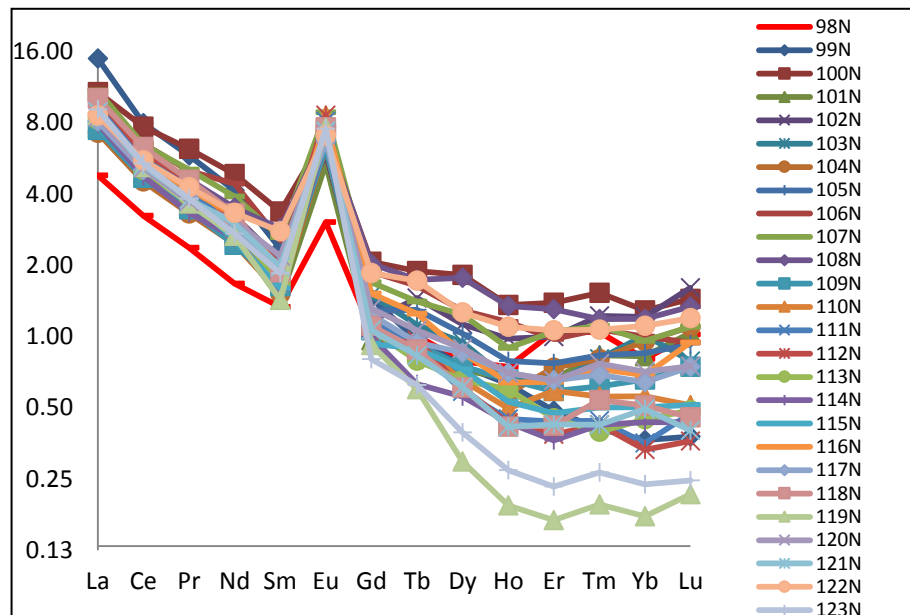


Figure E.12: Chondrite normalised REE diagrams for the chromitite stringer and the footwall, from borehole BH6259.

## Appendix F

Standard	WPR1	WMG1
<sup>189</sup> Os	0.01	0.02
<sup>193</sup> Ir	0.01	0.05
<sup>101</sup> Ru	0.02	0.03
<sup>103</sup> Rh	0.01	0.03
<sup>195</sup> Pt	0.27	0.76
<sup>106</sup> Pd	0.24	0.40
<sup>197</sup> Au	0.04	0.11

<b>NP1 – NP4: Hangingwall</b>	<b>P1 – P11: Hangingwall</b>	<b>N73 – N97: Hangingwall</b>
<b>NP5 – NP7: Chromitite layer</b>	<b>P12: Top chromitite layer</b>	<b>N98: Chromitite layer</b>
<b>NP8 – NP11: Footwall</b>	<b>P13 – P46: Pegmatoidal layer</b>	<b>N99 – N121: Footwall</b>
	<b>P47 – P48: Bottom chromitite layer</b>	
	<b>P49 – P52: Footwall</b>	

**Table F.1: PGE whole rock geochemistry of standards analysed.**

**Table F.2: Whole rock PGE analysis of the non-pegmatoidal reef, from borehole SD14/90. PGE values in ppm, Cr and S in wt%.**

Depth(m)	72.14	72.16	72.16	72.18	72.20	72.22	72.24	72.26	72.28	72.30	72.32	72.34	72.34
Sample name	NP1	NP2	NP2 Rep	NP3	NP4	NP5	NP6	NP7	NP8	NP9	NP10	NP11	NP11 Rep
Os	0.07	0.10	0.11	0.05	0.10	1.72	0.36	0.51	0.01	0.03	n.d.	n.d.	n.d.
Ir	0.11	0.15	0.16	0.13	0.33	2.70	0.76	0.81	0.02	0.05	n.d.	n.d.	n.d.
Ru	0.62	0.85	0.85	0.67	1.57	14.01	4.13	3.92	0.11	0.31	n.d.	n.d.	n.d.
Rh	0.39	0.49	0.49	0.39	1.03	8.29	2.44	2.66	0.07	0.19	n.d.	n.d.	n.d.
Pt	5.85	5.06	5.12	5.43	12.59	79.92	24.70	24.36	1.15	2.22	0.01	0.02	0.02
Pd	2.47	2.82	2.86	2.08	3.33	13.34	3.46	2.95	0.51	1.53	0.07	0.03	0.04
Au	0.26	0.37	0.37	0.42	0.31	0.25	0.16	0.07	0.04	0.10	0.01	n.d.	0.01
Cr	0.30	0.25	0.25	0.25	2.81	14.44	7.27	8.77	0.14	0.08	0.06	0.02	0.02
S	0.56	1.54	1.54	1.13	0.98	0.82	0.24	0.22	0.02	0.03	0.01	0.01	0.01

**Table F.3: Whole rock PGE analysis of the pegmatoidal reef, from borehole 20/0252. PGE values in ppm, Cr and S in wt%.**

Thickness	21.58	21.5	21.46	21.44	21.42	21.4	21.38	21.36	21.34	21.32	21.3	21.26	21.26	21.20	21.12
Sample	P2	P6	P8	P9	P10	P11	P12	P13	P14	P15	P16	P18	P18 Rep	P21	P25
Os	0.01	0.03	0.15	0.15	0.07	0.04	0.38	0.02	0.13	0.30	0.33	0.33	0.32	0.02	0.21
Ir	0.01	0.04	0.22	0.17	0.16	0.18	0.60	0.08	0.23	0.34	0.48	0.56	0.52	0.03	0.28
Ru	0.07	0.23	0.98	0.84	0.74	1.07	3.16	0.48	1.26	1.74	2.55	2.89	2.74	0.15	1.63
Rh	0.04	0.11	0.51	0.38	0.46	0.60	1.56	0.25	0.66	0.82	0.23	1.74	1.67	0.10	0.89
Pt	0.45	1.74	2.48	2.21	14.32	11.23	16.54	3.31	7.78	2.43	2.47	18.41	17.71	2.83	3.98
Pd	0.34	0.75	0.81	0.61	2.91	2.56	4.11	0.97	2.00	1.40	0.96	7.40	6.97	1.22	2.61
Au	0.13	0.15	0.24	0.36	0.86	0.49	0.57	0.13	0.30	0.41	1.77	1.08	1.18	0.13	0.22
Cr	0.32	0.32	0.37	0.37	1.44	3.70	7.95	0.32	0.31	0.37	0.17	0.29	0.29	0.33	0.21
S	0.54	0.52	1.99	1.73	1.24	1.02	0.58	0.14	0.47	1.05	0.75	0.75	0.75	0.12	0.42

Thickness (m)	21.04	21.04	20.96	20.88	20.80	20.76	20.74	20.72	20.70	20.68	20.67	20.65	20.63	20.61	20.59
Sample name	P29	P29 Rep	P33	P37	P41	P43	P44	P45	P46	P47	P48	P49	P50	P51	P52
Os	0.02	0.03	n.d.	0.04	0.08	n.d.	n.d.	n.d.	n.d.						
Ir	0.06	0.06	n.d.	n.d.	n.d.	n.d.	n.d.	n.d.	0.01	0.05	0.10	n.d.	n.d.	n.d.	n.d.
Ru	0.34	0.33	0.01	0.01	0.01	n.d.	0.02	n.d.	0.05	0.26	0.68	n.d.	n.d.	n.d.	n.d.
Rh	0.11	0.12	n.d.	n.d.	0.01	n.d.	0.01	n.d.	0.03	0.11	0.18	n.d.	n.d.	n.d.	n.d.
Pt	1.15	1.12	0.06	0.04	0.28	0.11	0.16	0.05	0.33	0.75	1.30	0.01	n.d.	0.01	n.d.
Pd	1.09	1.03	0.05	0.01	0.19	0.13	0.14	0.06	0.12	0.11	0.14	0.01	n.d.	n.d.	n.d.
Au	0.17	0.16	0.02	n.d.	0.03	0.02	0.02	0.01	0.03	0.01	0.01	n.d.	n.d.	n.d.	n.d.
Cr	0.16	0.16	0.16	0.29	0.21	0.08	0.01	0.12	0.28	1.22	3.40	0.03	0.01	n.d.	0.01
S	0.09	0.09	0.06	0.42	0.27	0.37	0.51	0.48	0.04	n.d.	n.d.	0.01	0.01	0.01	0.01

Table F.4: Whole rock PGE analysis of the non-pegmatoidal reef, from borehole BH6259. PGE values in ppm, Cr and S in wt%.

Thickness (m)	1087.15	1087.23	1087.31	1087.39	1087.47	1087.51	1087.53	1087.55	1087.57	1087.59	1087.59	1087.61	1087.63	1087.65	1087.67
Sample name	N76	N80	N84	N88	N92	N94	N95	N96	N97	N98	N98 Rep	N99	N100	N101	N102
Os	n.d.	n.d.	n.d.	0.01	0.01	0.16	0.23	0.16	0.13	0.92	1.30	0.02	0.00	n.d.	n.d.
Ir	n.d.	n.d.	n.d.	0.01	0.01	0.16	0.24	0.20	0.21	1.48	1.86	0.03	0.00	n.d.	n.d.
Ru	0.01	0.01	0.02	0.06	0.06	1.00	1.32	1.15	1.16	7.65	9.75	0.18	0.01	n.d.	0.01
Rh	n.d.	n.d.	0.01	0.03	0.02	0.40	0.28	0.51	0.54	4.56	5.60	0.10	0.01	n.d.	n.d.
Pt	0.02	0.02	0.06	0.33	0.49	4.79	5.47	8.92	3.53	45.32	57.48	1.70	0.04	0.01	0.03
Pd	0.01	0.01	0.05	0.21	0.27	1.12	1.86	3.98	2.27	9.17	11.53	0.92	0.09	0.06	0.08
Au	0.02	0.01	0.02	0.08	0.16	0.19	0.66	0.21	0.48	0.31	0.38	0.15	0.01	0.01	0.01
Cr	0.28	0.26	0.24	0.34	0.33	0.49	0.36	0.39	0.40	12.76	12.76	0.24	0.10	0.09	0.12
S	0.06	0.08	0.06	0.81	0.62	1.49	2.73	0.98	1.45	0.45	0.45	0.02	0.26	0.03	0.03

Thickness (m)	1087.69	1087.73	1087.81	1087.89	1087.97	1088.05
Sample name	N103	N105	N109	N113	N117	N121
Os	n.d.	n.d.	n.d.	n.d.	n.d.	0.02
Ir	n.d.	n.d.	0.01	n.d.	n.d.	0.03
Ru	0.01	n.d.	0.05	0.01	0.01	0.16
Rh	0.01	n.d.	0.03	0.01	0.01	0.08
Pt	0.12	0.02	0.26	0.06	0.04	1.34
Pd	0.04	0.06	0.31	0.10	0.04	0.77
Au	0.01	0.01	0.02	0.01	0.01	0.10
Cr	0.06	0.05	0.03	0.01	0.01	0.01
S	0.02	0.01	0.05	0.03	0.02	0.17

## Appendix G

**Table G.1: Sulphur analyses for non-pegmatoidal Merensky reef, from borehole SD14/90. Sulphur values in %.**

Sample name	1NP	2NP	3NP	4NP	5NP	6NP	7NP	8NP	9NP	10NP	11NP
S (%)	0.56	1.54	1.13	0.98	0.82	0.24	0.22	0.02	0.03	0.01	< 0.01

**Table G.2: Sulphur analyses for non-pegmatoidal Merensky reef, from borehole BH6259. Sulphur values in %.**

Sample	73N	74N	75N	76N	77N	78N	79N	80N	81N	82N	83N	84N	85N	86N	87N	88N	89N
S (%)	0.09	0.10	0.07	0.06	0.05	0.04	0.06	0.08	0.20	0.04	0.04	0.06	0.08	0.03	0.05	0.81	0.36
Sample	90N	91N	92N	93N	94N	95N	96N	97N	98N	99N	100N	101N	102N	103N	104N	105N	106N
S (%)	0.57	0.70	0.62	0.66	1.49	2.73	0.98	1.45	0.45	0.02	0.26	0.03	0.03	0.02	0.02	0.01	0.03
Sample	107N	108N	109N	110N	111N	112N	113N	114N	115N	116N	117N	118N	119N	120N	121N	122N	123N
S (%)	0.04	0.03	0.05	0.02	0.04	0.02	0.03	0.01	0.12	0.03	0.02	0.02	0.05	0.02	0.17	0.92	0.46

**Table G.3: Sulphur analyses for pegmatoidal Merensky reef, from borehole 20/0252. Sulphur values in %.**

Sample	1P	2P	3P	4P	5P	6P	7P	8P	9P	10P	11P	12P	13P	14P	15P	16P	17P
S (%)	0.05	0.54	0.93	0.55	0.67	0.52	0.55	1.99	1.73	1.24	1.02	0.58	0.14	0.47	1.05	0.75	0.31
Sample	18P	19P	20P	21P	22P	23P	24P	25P	26P	27P	28P	29P	30P	31P	32P	33P	34P
S (%)	0.75	0.25	0.35	0.12	0.08	0.12	0.75	0.42	0.07	0.18	0.24	0.09	0.23	2.33	1.88	0.06	0.12
Sample	35P	36P	37P	38P	39P	40P	41P	42P	43P	44P	45P	46P	47P - 49P	50P	51P	52P	
S (%)	1.42	0.75	0.42	0.08	0.09	0.19	0.27	0.10	0.37	0.51	0.48	0.04	No data	< 0.01	< 0.01	0.01	

## Appendix H.1

### Platinum group elements within the Merensky Reef: preliminary results of a high resolution mineralogical and geochemical study

Magson J1\*, Tredoux M1, Roelofse F2

1 - Department of Geology, University of the Free State [markramj1@ufs.ac.za](mailto:markramj1@ufs.ac.za)

A study of the Merensky Reef was undertaken in the south-western portion of the Western Limb of the Bushveld complex, where it occurs either as a pegmatoidal or a non-pegmatoidal reef. The mineralogy and geochemistry were described on core sections across both reef types from the area. The cores were analysed in 2 cm intervals. Samples were analysed by optical microscopy. Quantitative analysis was done using scanning electron microprobe and electron microprobe analysis. Major elements were determined by using x-ray fluorescence and trace elements by using ICP-MS (inductively coupled plasma mass spectrometry). Platinum-group elements (PGE) were determined by Ni-S fire assay with an ICP-MS finish and sulphur by an Eltra Infrared Analyser. Microscope analysis showed sulphide inclusions visible in chromite grains (Figure 1). These inclusions display negative crystal shapes imposed by the crystal structure of the host chromite. Similar trapped sulphide inclusions have been described from chromites in the Platreef by [1]. Results indicated that there is a close relationship between chromium and PGE enrichment (Figure 2). Chondrite normalized patterns showed a relative increase in Pd in the footwall with a significant decrease in the hangingwall. The opposite can be seen for Pt. REE plots suggest a small amount of local differentiation with respect to La.

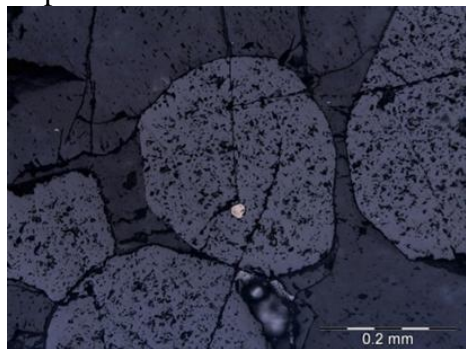


Figure 1: Microscope analysis of non-pegmatoidal Merensky Reef, sulphide inclusion visible in chromite grain.

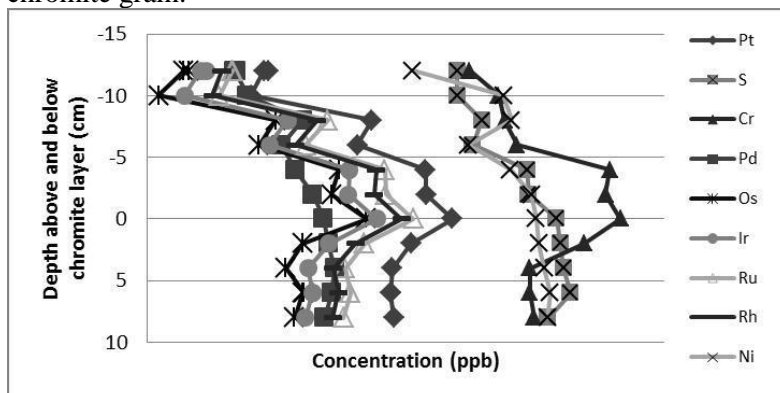


Figure 2: PGE, Cr, S and Ni concentrations vs. depth. The PGE concentrations, except for Pd, correlate with the chromite enrichment with depth, whereas Pd tends to show a better correlation with S enrichment.

[1] McDonald I. and Holwell D.A. (2011). Geology of the Northern Bushveld Complex and the Setting and Genesis of the Platreef Ni-Cu-PGE Deposit. *Reviews in Economic Geology*, 17, 297–327.

## Appendix H.2

### PLATINUM GROUP ELEMENTS WITHIN THE MERENSKY REEF: PRELIMINARY RESULTS OF A HIGH RESOLUTION MINERALOGICAL AND GEOCHEMICAL STUDY

J. Magson, M. Tredoux & F. Roelofse

<sup>1</sup>Department of Geology, University of the Free State, South Africa. [markramj1@ufs.ac.za](mailto:markramj1@ufs.ac.za)

A study of the Merensky reef was undertaken in the south western portion of the Western Limb of the Bushveld complex, where it occurs either a pegmatoidal or a non-pegmatoidal reef. The mineralogy and geochemistry were described on core sections across both reef types from the area. All three sets of core studied, corresponds to the normal Merensky 'A' type reef. The cores were analysed in 2 cm intervals. Samples were analysed by optical microscopy. Major elements were determined by using XRF (X-ray fluorescence) and trace elements by using ICP-MS (inductively-coupled plasma mass spectrometry). Platinum group elements were determined by Ni-S fire assay and sulphur by an Eltra Infrared Analyzer.

Microscope analysis showed sulphide inclusions visible in chromite grains (Fig. 1a). These inclusions display negative crystal shapes imposed by the crystal structure of the host chromite. Further investigation also showed cumulus phase plagioclase in the footwall and intercumulus plagioclase in the hangingwall, with intercumulus plagioclase overgrowing parts of the euhedral cumulus plagioclase (Fig. 1b). The sulphide inclusions found in the chromite can be used to reveal the parental composition of sulphide melts within magmatic systems. Similar trapped sulphide inclusions have been described from chromites in the Platreef by Holwell & McDonald (2011), that interpreted their presence as early PGE-rich sulphide liquids with Pt/Pd ratios close to unity that supports models of sulphide saturation and metal enrichment prior to intrusion. Results indicated that there is a close relationship between chromite and PGE enrichment (Fig. 2). Chondrite normalised patterns showed a relative increase in Pd in the footwall with a significant decrease in the hangingwall. The opposite can be seen for Pt.

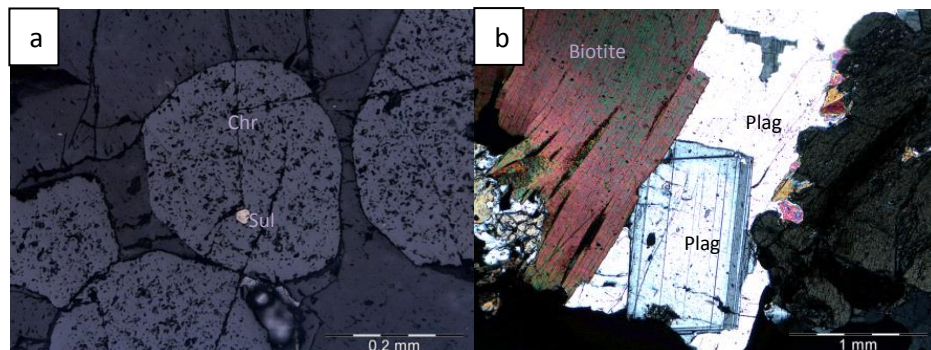


**Figure 1.** Microscope analysis of non-pegmatoidal Merensky reef (a) sulphide inclusion visible in chromite grain (b) intercumulus plagioclase overgrowing an cumulus plagioclase. Chr, chromite; Sul, sulphide; Plag, plagioclase.

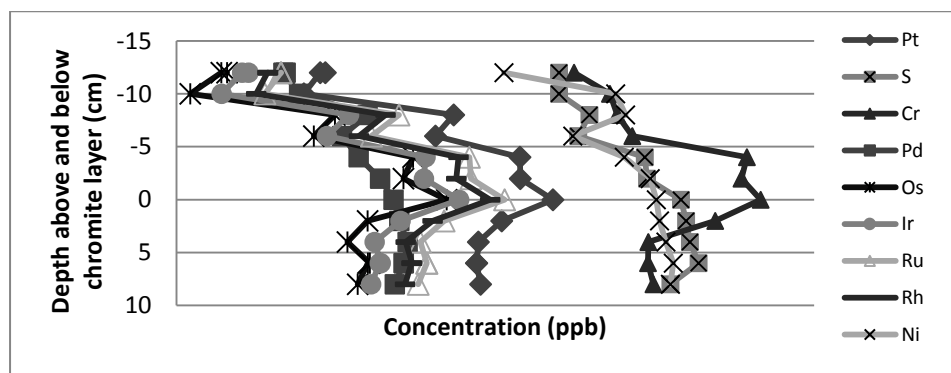


**Figure 2.** PGE, Cr, S and Ni concentrations vs depth. The PGE concentrations, except for Pd, correlate with the chromite enrichment with depth, whereas Pd tend to show a better correlation with S enrichment.

#### References

1. Holwell, D.A. and McDonald, I., 2011. Precious metal enrichment in the Platreef, Bushveld complex, South Africa: evidence from homogenized magmatic sulphide melt inclusions. *Contribution Mineral Petrology*, **161**, 1011-1026.

## Appendix H.3

### PLATINUM-GROUP ELEMENTS WITHIN THE MERENSKY REEF, WESTERN LIMB, BUSHVELD COMPLEX: RESULTS OF A HIGH RESOLUTION MINERALOGICAL AND GEOCHEMICAL STUDY

Magson, J., Tredoux, M., & Roelofse, F.

University of Free State . Nelson Mandela Str. Bloemfontein, South Africa

e-mail: markramj1@ufs.ac.za

**ABSTRACT.** Variation occur within the thickness of the Merensky reef and mineralogical and geochemical studies shows a close relationship between chromium and PGE enrichment.

A study of the Merensky reef was undertaken in the south-western portion of the Western Limb of the Bushveld complex. Variation occur in the thickness of the Merensky reef (pegmatoidal and a non-pegmatoidal reef), with the term “Merensky reef” referring to that part of the Merensky unit that is economically exploitable (Leeb-du Toit 1986). The mineralogy and geochemistry were described on core sections across both reef types (pegmatoidal and non-pegmatoidal) from the area. All three sets of core studied, corresponds to the normal Merensky ‘A’ type reef (Leeb-du Toit 1986).

The core were analysed in 2cm intervals. Samples were analysed by optical microscopy. Quantitative analysis was done using scanning electron microprobe and electron microprobe analysis. Major elements were determined by using x-ray fluorescence and trace elements by using ICP-MS (inductively coupled plasma mass spectrometry). Platinum-group elements (PGE) were determined by Ni-S fire assay with an ICP-MS finish and sulphur by an Eltra Infrared Analyser.

Microscope analysis showed sulphide inclusions visible in chromite grains (Fig. 1). These inclusions display negative crystal shapes imposed by the crystal structure of the host chromite. Similar trapped sulphide inclusions have been described from chromites in the Platreef by (Holwell & McDonald 2011).

Results indicated that there is a close relationship between chromium and PGE enrichment (Fig. 2). Chondrite normalized patterns showed a relative increase in Pd in the footwall with a significant decrease in the hangingwall. The opposite can be seen for Pt. REE plots suggests a small amount of local differentiation with respect to La.

#### REFERENCES

- HOLWELL, D.A. & MCDONALD, I. (2011): Precious metal enrichment in the Platreef, Bushveld complex, South Africa: evidence from homogenized magmatic sulphide melt inclusions. Contribution Mineral Petrology, 161, 1011-1026.  
LEEB-DU TOIT, A. (1986): The Impala Platinum Mines. In: *Mineral deposits of Southern Africa*. Edited by C.R. Anhaeusser and S. Maske. 2, 1091-1106.

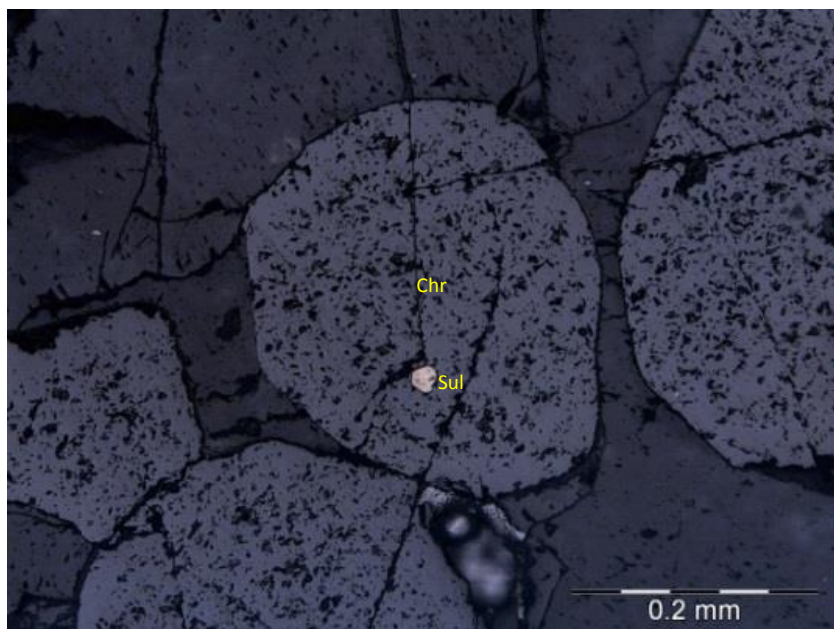


Fig 1. Microscope analysis of non-pegmatoidal Merensky reef (a) sulphide inclusion visible in chromite grain. Chr, chromite; Sul, sulphide; Plag, plagioclase.

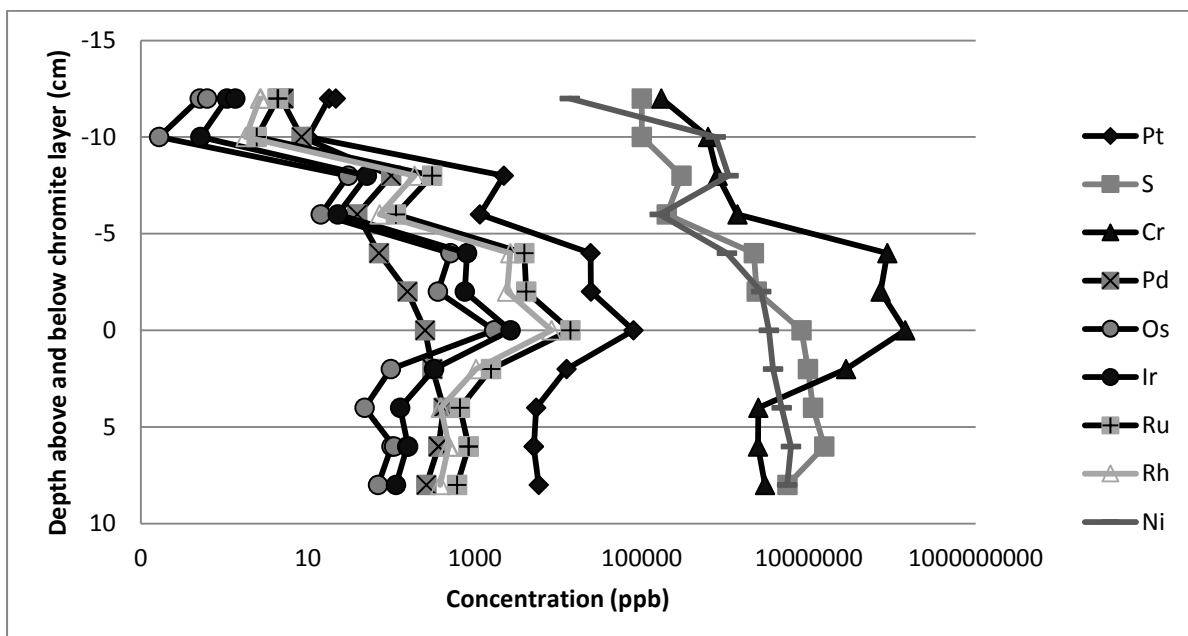


Fig 2. PGE, Cr, S and Ni concentrations vs depth of the non-pegmatoidal Merensky reef . The PGE concentrations, except for Pd, correlate with the chromite enrichment with depth, whereas Pd tend to show a better correlation with S enrichment.

## **Appendix H4**

### **Mineralogical and geochemical interpretations on the pegmatoidal and non-pegmatoidal Merensky Reef**

Justine Markram, Marian Tredoux

*University of the Free State, Department of Geology, Bloemfontein, Free State, South Africa*

This study is in the southwestern portion of the Western Limb of the Bushveld complex. The stratigraphy of the Critical Zone of the Bushveld complex consists of seven major rhythmic layered units grading from pyroxenite (with chromitite) through norite to anorthosite. The Merensky Unit is the most general and complete cyclic unit within the Critical Zone. The Merensky Reef forms the base of the sixth unit and the uppermost seventh unit commences with the Bastard Reef. Variation occurs in the thickness of the Merensky Reef. The term “Merensky Reef” refers to that part of the Merensky unit that is economically exploitable. The Merensky Reef is referred to as either a pegmatoid Reef if a pegmatoidal pyroxenite is present or pyroxenite Reef (non pegmatoidal Reef) if it is absent. In the latter the chromitite layer rests on a footwall of pure white anorthosite. In the former case, the reef is defined by a pegmatoidal (feldspathic in certain areas) pyroxenite bounded by a thin top and bottom chromitite layer. The lateral distribution of platinum group elements in the Merensky Reef is highly variable. The vertical distribution of the PGE is influenced by to a large extend by the separation between these two chromitite layers or the absence of one chromitite layer. Detailed mineralogy and geochemistry are described on two sets of core, across both reef types from the area, and how the grade or distribution of platinum is influenced by the presence or not of pegmatoidal Merensky Reef. Samples are analyzed by optical microscopy, for major mineral petrology. Mineral chemistry is investigated using detailed SEM (scanning electron microscope) work. Major elements are determined by using XRF (X-ray fluorescence) and trace elements by using ICP-MS (inductively-coupled plasma mass spectrometry).